frontiers | Research Topics

Advancements and enhancements in bioactive and biocompatible hydrogels for tissue healing and drug delivery

Edited by
Bruce Alan Bunnell and Bryan Brown

Published in
Frontiers in Bioengineering and Biotechnology

FRONTIERS EBOOK COPYRIGHT STATEMENT

The copyright in the text of individual articles in this ebook is the property of their respective authors or their respective institutions or funders. The copyright in graphics and images within each article may be subject to copyright of other parties. In both cases this is subject to a license granted to Frontiers.

The compilation of articles constituting this ebook is the property of Frontiers.

Each article within this ebook, and the ebook itself, are published under the most recent version of the Creative Commons CC-BY licence. The version current at the date of publication of this ebook is CC-BY 4.0. If the CC-BY licence is updated, the licence granted by Frontiers is automatically updated to the new version.

When exercising any right under the CC-BY licence, Frontiers must be attributed as the original publisher of the article or ebook, as applicable.

Authors have the responsibility of ensuring that any graphics or other materials which are the property of others may be included in the CC-BY licence, but this should be checked before relying on the CC-BY licence to reproduce those materials. Any copyright notices relating to those materials must be complied with.

Copyright and source acknowledgement notices may not be removed and must be displayed in any copy, derivative work or partial copy which includes the elements in question.

All copyright, and all rights therein, are protected by national and international copyright laws. The above represents a summary only. For further information please read Frontiers' Conditions for Website Use and Copyright Statement, and the applicable CC-BY licence.

ISSN 1664-8714
ISBN 978-2-83251-581-5
DOI 10.3389/978-2-83251-581-5

About Frontiers

Frontiers is more than just an open access publisher of scholarly articles: it is a pioneering approach to the world of academia, radically improving the way scholarly research is managed. The grand vision of Frontiers is a world where all people have an equal opportunity to seek, share and generate knowledge. Frontiers provides immediate and permanent online open access to all its publications, but this alone is not enough to realize our grand goals.

Frontiers journal series

The Frontiers journal series is a multi-tier and interdisciplinary set of open-access, online journals, promising a paradigm shift from the current review, selection and dissemination processes in academic publishing. All Frontiers journals are driven by researchers for researchers; therefore, they constitute a service to the scholarly community. At the same time, the *Frontiers journal series* operates on a revolutionary invention, the tiered publishing system, initially addressing specific communities of scholars, and gradually climbing up to broader public understanding, thus serving the interests of the lay society, too.

Dedication to quality

Each Frontiers article is a landmark of the highest quality, thanks to genuinely collaborative interactions between authors and review editors, who include some of the world's best academicians. Research must be certified by peers before entering a stream of knowledge that may eventually reach the public - and shape society; therefore, Frontiers only applies the most rigorous and unbiased reviews. Frontiers revolutionizes research publishing by freely delivering the most outstanding research, evaluated with no bias from both the academic and social point of view. By applying the most advanced information technologies, Frontiers is catapulting scholarly publishing into a new generation.

What are Frontiers Research Topics?

Frontiers Research Topics are very popular trademarks of the *Frontiers journals series*: they are collections of at least ten articles, all centered on a particular subject. With their unique mix of varied contributions from Original Research to Review Articles, Frontiers Research Topics unify the most influential researchers, the latest key findings and historical advances in a hot research area.

Find out more on how to host your own Frontiers Research Topic or contribute to one as an author by contacting the Frontiers editorial office: frontiersin.org/about/contact

Advancements and enhancements in bioactive and biocompatible hydrogels for tissue healing and drug delivery

Topic editors

Bruce Alan Bunnell — University of North Texas Health Science Center, United States

Bryan Brown — University of Pittsburgh, United States

Citation

Bunnell, B. A., Brown, B., eds. (2023). *Advancements and enhancements in bioactive and biocompatible hydrogels for tissue healing and drug delivery*. Lausanne: Frontiers Media SA. doi: 10.3389/978-2-83251-581-5

Table of contents

frontiers | Frontiers in Bioengineering and Biotechnology

ORIGINAL RESEARCH
published: 14 April 2022
doi: 10.3389/fbioe.2022.884036

An Injectable Platform of Engineered Cartilage Gel and Gelatin Methacrylate to Promote Cartilage Regeneration

Wei Xu[1,2,3†], *Tao Wang*[1,2,3†], *Yahui Wang*[2†], *Xiaodi Wu*[1,2,3], *Yujie Chen*[4], *Daiying Song*[1,2,3], *Zheng Ci*[5], *Yilin Cao*[2,3], *Yujie Hua*[2,3]*, *Guangdong Zhou*[1,2,3]* *and Yu Liu*[1,2,3,5]*

[1]Research Institute of Plastic Surgery, Wei Fang Medical College, Weifang, China, [2]National Tissue Engineering Center of China, Shanghai, China, [3]Shanghai Key Laboratory of Tissue Engineering, Department of Plastic and Reconstructive Surgery, Shanghai 9th People's Hospital, Shanghai Stem Cell Institute, Shanghai Jiao Tong University School of Medicine, Shanghai, China, [4]Shanghai Engineering Research Center of Nano-Biomaterials and Regenerative Medicine, College of Chemistry, Chemical Engineering and Biotechnology, Donghua University, Shanghai, China, [5]Shanghai Resthetic Bio CO., LTD, Shanghai, China

OPEN ACCESS

Edited by:
Bruce Alan Bunnell,
United States

Reviewed by:
Fengxuan Han,
Soochow University, China
Wei Wang,
Tianjin University, China

***Correspondence:**
Yujie Hua
hyj137@shsmu.edu.cn
Guangdong Zhou
guangdongzhou@126.com
Yu Liu
yuliu1211@163.com

[†]These authors have contributed equally to this work

Specialty section:
This article was submitted to Tissue Engineering and Regenerative Medicine, a section of the journal Frontiers in Bioengineering and Biotechnology

Received: 25 February 2022
Accepted: 30 March 2022
Published: 14 April 2022

Citation:
Xu W, Wang T, Wang Y, Wu X, Chen Y, Song D, Ci Z, Cao Y, Hua Y, Zhou G and Liu Y (2022) An Injectable Platform of Engineered Cartilage Gel and Gelatin Methacrylate to Promote Cartilage Regeneration. Front. Bioeng. Biotechnol. 10:884036. doi: 10.3389/fbioe.2022.884036

Cell–hydrogel constructs are frequently used as injectable platforms for irregular cartilage regeneration. However, cell–hydrogel constructs have obvious disadvantages, such as long culture times, high probability of infection, and poor cartilage formation capacity, significantly limiting their clinical translation. In this study, we aimed to develop a novel injectable platform comprising engineered cartilage gel (ECG) and gelatin methacrylate (GelMA) to improve cartilage regeneration. We first prepared an ECG by cutting the *in vitro* engineered cartilage sheet into pieces. The chondrocytes and ECG were evenly encapsulated into GelMA to form Cell-GelMA and ECG-GelMA constructs. The ECG-GelMA construct exhibited preferred gel characteristics and superior biocompatibility compared with the Cell-GelMA construct counterpart. After subcutaneous implantation in nude mice and goat, both gross views and histological evaluations showed that the ECG-GelMA construct achieved more homogenous, stable, and mature cartilage regeneration than the Cell-GelMA construct. Immunological evaluations showed that ECG-GelMA had a mitigatory immunologic reaction than the Cell-GelMA construct. Overall, the results suggest that the ECG-GelMA is a promising injectable platform for cartilage regeneration that may advance clinical translation.

Keywords: injectable platform, cell-hydrogel, cartilage regeneration, engineered cartilage gel, immune response

1 INTRODUCTION

Stable cartilage restoration still poses a tremendous clinical challenge for plastic surgeons (Zhou et al., 2018). Developments in tissue engineering technologies have provided a new avenue to achieve cartilage regeneration. When tissue-engineered cartilage is used in plastic surgery, it must create little trauma, have plasticity, be homogeneous, and effectively form cartilage tissue. The emergence of injectable cartilage may solve these problems (Liu et al., 2017).

The basic principle for the development of injectable cartilage is to inoculate chondrocytes into a fluid vehicle (Xu et al., 2020c), inject the chondrocyte-loaded fluid vehicle into the defect to form biologically active cartilage tissue, filling and repairing a defect site (Hua et al., 2021). This method is easily accepted by patients because it is simple, the injectable is malleable, and the process creates little trauma (Cakmak et al., 2013; Singh et al., 2018). Among a variety of fluid vehicles, hydrogels, such as gelatin methacrylate (GelMA), are the most frequently used platform for injectable cartilage

tissue engineering because of their remarkable characteristics, including flexibility and versatility in fabrication, variety in composition, high moldability, excellent biocompatibility, and similarity to the extracellular matrix (ECM) (Wu et al., 2020; Xu et al., 2021b). However, because of their compact structure, hydrogels can block nutrient penetration, hindering oxygen and waste exchange, and impeding cell–cell interactions, which significantly interferes with cartilage formation and limits clinical translation (Lee and Shin, 2007; Qi et al., 2015).

Our recent studies have proved that mature *in vitro* engineered cartilage can improve the stability and efficiency of regenerated cartilage *in vivo* (Xu et al., 2020a; Xu et al., 2020d). Consequently, loading hydrogels with more mature cartilage tissue instead of chondrocytes may enhance the quality of the *in vivo* engineered cartilage. Scaffold-free cartilage sheet technology is based on the theory of "chondrocyte redifferentiation in high-density culture" (Schulze-Tanzil et al., 2002; Schuh et al., 2012), and extensive experiments have demonstrated that this technology can regenerate high quality cartilage tissue *in vitro* (Ding et al., 2021). Our latest studies demonstrated that an engineered cartilage gel (ECG) produced by the cartilage sheet technology has the excellent ability to regenerate cartilage (Ci et al., 2021). As a result, we suspect that ECG may be an alternative for chondrocytes, acting as the cellular supplementation in the form of microtissues to load into the GelMA, creating a new injectable platform for cartilage regeneration.

To verify our hypothesis, goat-derived chondrocytes were used to prepare a cartilage sheet, which was further cut into pieces to form the ECG. Thereafter, both chondrocytes and ECG were evenly encapsulated into GelMA to form Cell-GelMA and ECG-GelMA constructs, respectively. We systematically compared the gelation characteristics, biocompatibility, *in vivo* cartilage formation, and inflammatory reaction of the Cell-GelMA and ECG-GelMA constructs, to determine the feasibility of developing a novel injectable platform comprising ECG and GelMA to improve cartilage regeneration.

2 MATERIALS AND METHODS

2.1 Chondrocytes Preparation

This study was approved by the Weifang Medical University Ethics Committee. Goats (2,3 months old) were purchased from Shanghai Jiagan Experimental Animal Raising Farm (Shanghai, China). Auricular cartilage obtained from a goat was fragmented into 1 × 1 mm^2 pieces and digested with 0.2% collagenase NB4 (Worthington biochemical Crop., Freehold, NJ, United States) for 8 h at 37°C on a shaker. The isolated chondrocytes were collected and cultured in Dulbecco's modified Eagle's medium (DMEM, Gibco BRL, Grand Island, NY, United States) containing 10% fetal bovine serum (FBS, Gibco BRL) and 1% antibiotic–antimycotic (Gibco BRL). Chondrocytes were passaged at >80% confluence. Chondrocytes at passage 3 (P3) were harvested for use.

2.2 ECG Formation

Cartilage sheets were prepared as previously described (Xue et al., 2018; Ci et al., 2021). Briefly, the above prepared chondrocytes were seeded in 6-well cell culture plates at a density of 1.5 × 107 cells/well and cultured in a medium of high DMEM, 10% FBS, and 1% antibiotic–antimycotic. The medium was changed every day, and cartilage sheets were harvested with cell scrapers after 5 days cultivation. ECG was obtained by cutting the obtained cartilage sheet with scissors into small pieces with *an area of 0.1–0.2 mm^2*.

2.3 Preparation of Cell-GelMA and ECG-GelMA Constructs

GelMA was synthesized as previously described (Van Den Bulcke et al., 2000). To prepare the standard hydrogels, 13% GelMA (w/v) was dissolved in phosphate buffered saline (PBS) at 50 °C to create the gel precursors, which were then mixed with 0.2% (w/v) photo-initiator (lithium phenyl-2,4,6-trimethylbenzoyl-phosphinate, LAP). The prepared GelMA solution was filtered aseptically (0.22 μm) and stored at 4°C prior to use.

The harvested chondrocytes were suspended to a concentration of 1.7 × 10^8 cells/m, and mixed with GelMA at a ratio of 1:1 by volume to achieve a Cell-GelMA construct with a final concentration of 8.5 × 10^7 cells/ml.

The collected ECG was mixed with GelMA at a ratio of 1:1 by volume, achieving a ECG-GelMA construct with a final concentration of 8.5 × 10^7 cells/mL. Both the Cell-GelMA and ECG-GelMA constructs were crosslinked by UV light irradiation (365 nm, 20 mW/cm^2) for 5 s.

2.4 Characteristics of the GelMA, Cell-GelMA, and ECG-GelMA Constructs

2.4.1 Morphology

The chondrocytes, cartilage sheet, ECG, GelMA, Cell-GelMA, and ECG-GelMA were observed using a light microscope (OLYMPUS, CKX41), and photographed using a single lens reflex camera (Nikon, Japan). The GelMA, Cell-GelMA, and ECG-GelMA constructs were freeze-dried and examined using scanning electron microscopy (SEM, Philips XL-30, Amsterdam, Netherlands) at an accelerating voltage of 15 kV.

2.4.2 *Rheological Analyses and Viscosity*

Tests of the viscosity and shear-thinning behavior of the gel precursors were performed on a HAAKE MARS Rotational Rheometer with a parallel plate geometry (P20 TiL, 20 mm diameter) at 25°C. The shear-thinning behavior was analyzed at a 0.5 mm gap from 0 1/s to 50 1/s. Dynamic rheology experiments were exposed to light irradiation (365 nm, 20 mW/cm^2) within 60 s. A time sweep oscillatory test was performed at 10% strain (CD mode), 1 Hz frequency, and a 0.5 mm gap for 120 s. The gel point was determined as the time when the storage modulus (G′) surpassed the loss modulus (G″).

2.4.3 Swelling Ratio and In Vitro Enzymatic Degradation

The initial volume of the GelMA, Cell-GelMA, and ECG-GelMA constructs was recorded as V_0, and the volume after 24 h was recorded as V. The volume swelling ratio was defined as SRv = V/V_0 (Gan et al., 2019).

$$SR_V = \frac{\pi R_1^2 \times H_1}{\pi R_0^2 \times H_0}$$

R_1 and R_0 are the radii of the various hydrogels before and after 24 h swelling, respectively, and H_0 and H_1 are the initial height and the height after 24 h swelling of the various hydrogels, respectively.

The enzymatic degradation was examined by a gravimetric method, as previously described (Xu et al., 2020d). The initial hydrogel dry weight was W_0 and the remaining hydrogel dry weight after immersing in an enzymatic solution (0.15% w/v collagenase) was recorded as W_t. The degradation ratio was defined as $W_t/W_0 \times 100\%$.

2.4.4 Mechanical Testing

The mechanical properties of the hydrogel discs (Φ 10 × 3 mm), including GelMA, Cell-GelMA, and ECG-GelMA constructs, were examined using a mechanical testing machine (Instron-5542, Instron, Canton, MA, United States), as previously described (Gan et al., 2019). Briefly, crosslinked samples were compressed at a rate of 0.5 mm/min at room temperature until 80% of the maximum deformation to obtain compressive stress–strain curves. The compressive modulus was then calculated from the slope of the stress–strain curve.

2.4.5 Biocompatibility of the Cell-GelMA and ECG-GelMA Constructs

To determine the biocompatibility of the Cell-GelMA and ECG-GelMA constructs, chondrocytes within the constructs were adjusted to a final concentration of 3.0×10^7 cells/mL. After 1, 4, and 7 days *in vitro* culture, the viability of the cells within the constructs were evaluated using a Live and Dead Cell Viability Assay (Invitrogen, United States) *via* a confocal microscope (Nikon, Japan), following the manufacturer's instructions. After imaging using the confocal microscope, ImageJ software was used to quantitatively analyze the number of dead cells.

To observe the chondrocytes and ECG morphology within GelMA, samples after 7 days *in vitro* culture were washed thrice in PBS and the samples were fixed in 4% paraformaldehyde (PFA) at room temperature for 30 min. The fixed samples were washed thrice in PBS and immersed in a permeabilization and blocking buffer (1% bovine serum albumin and 0.1% Triton in PBS) for 30 min. To stain the actin cytoskeleton, a diluted methanolic solution of Alexa Fluor 546 phalloidin (Invitrogen) in the blocking buffer was incubated with the fixed samples at room temperature in the dark for 30 min. All samples were washed with PBS and the nuclei was counterstained with 4, 6-diamidino-2-phenylindole dihydrochloride (DAPI). All samples were sealed with a solution containing an anti-fluorescence quenching agent. The images were acquired using a confocal microscope equipped with the appropriate excitation and emission filters.

The DNA content was extracted from the samples using 250 μg/ml Protease K, and then quantified with the PicoGreen dsDNA assay (Invitrogen) according to the manufacturer's protocol to determine the chondrocytes proliferation within the constructs.

2.6 Subcutaneous Injection Into Nude Mice and Goats

Cell-GelMA and ECG-GelMA constructs were subcutaneously injected into the dorsal area of nude mice at a total volume of 0.15 ml via a syringe with an 18-gauge needle. Samples were harvested 8 weeks post-implantation. Cell-GelMA, ECG, and ECG-GelMA constructs were also subcutaneously injected into the dorsal area of goats at a total volume of 0.4 ml. Samples were harvested at 1, 2, and 12 weeks post-implantation.

2.7 Quantitative Polymerase Chain Reaction (qPCR)

The expression of cartilage-related genes (ACAN, COL-2, and Sox-9) and inflammation-related genes (CD3 and CD68) were analyzed by qPCR. The total RNA was extracted with Tiazol reagent (Invitrogen), and then reverse transcribed using Moloney murine leukemia virus reverse transcriptase (Invitrogen). qPCR was performed using a Fast Synergy Brands Green Master Kit and Light Cycler 480 system (Roche) in accordance with the manufacturer's instructions. The results were analyzed using the comparative threshold cycle method and normalized to endogenous reference gene GAPDH. The primer sequences are listed in **Table 1**.

2.8 Histological and Immunohistochemical Analyses

Samples were fixed in 4% paraformaldehyde and embedded in paraffin for sectioning into 5-μm thick slices that were then mounted on glass slides. Sections were stained with hematoxylin and eosin (HE) and safranin-O (SO). For immunohistochemical analysis, a rabbit anti-human monoclonal antibody against collagen II (COL-2) was used with a horseradish peroxidase (HRP)-conjugated anti-rabbit antibody (1:400 in PBS, Santa Cruz) as the secondary antibody. CD3 was detected using a rabbit anti-human CD3 monoclonal antibody (1:100 in PBS, Santa Cruz Biotechnology, Santa Cruz, CA, United States). CD68 was detected using a rabbit anti-human CD68 monoclonal antibody (1:1,000 in PBS, Santa Cruz Biotechnology). Color development was conducted with diaminobenzidine tetrahydrochloride (Santa Cruz Biotechnology).

2.9 Biochemical and Biomechanical Determination

Quantitative biochemical analysis of regenerated cartilage was performed as described previously (Wang et al., 2020; Chen

TABLE 1 | Primer sequences of related genes.

Gene	Accession number	Primer sequence
ACAN	XM_018066613.1	CAGAGGCAACCACAACAGACA AGCTGGGAAGGCATAAGCATG
COL-2	XM_018047868.1	GCATTGCCTACCTGGACGAAG TCACAGTCTCGCCCCACTTAC
Sox-9	XM_018063905.1	AAGAACAAGCCGCACGTCAA CCGTTCTTCACCGACTTCCTC
CD3	XM_005689508.3	TTATCAGTGCCTCGCAACCG CTTTCGGCTCTTGCTCCAGTA
CD68	XM_005693517.3	AGCCCAGATTCAGATGCGAGT GATCCTGTTTGAATCCGAAGCT

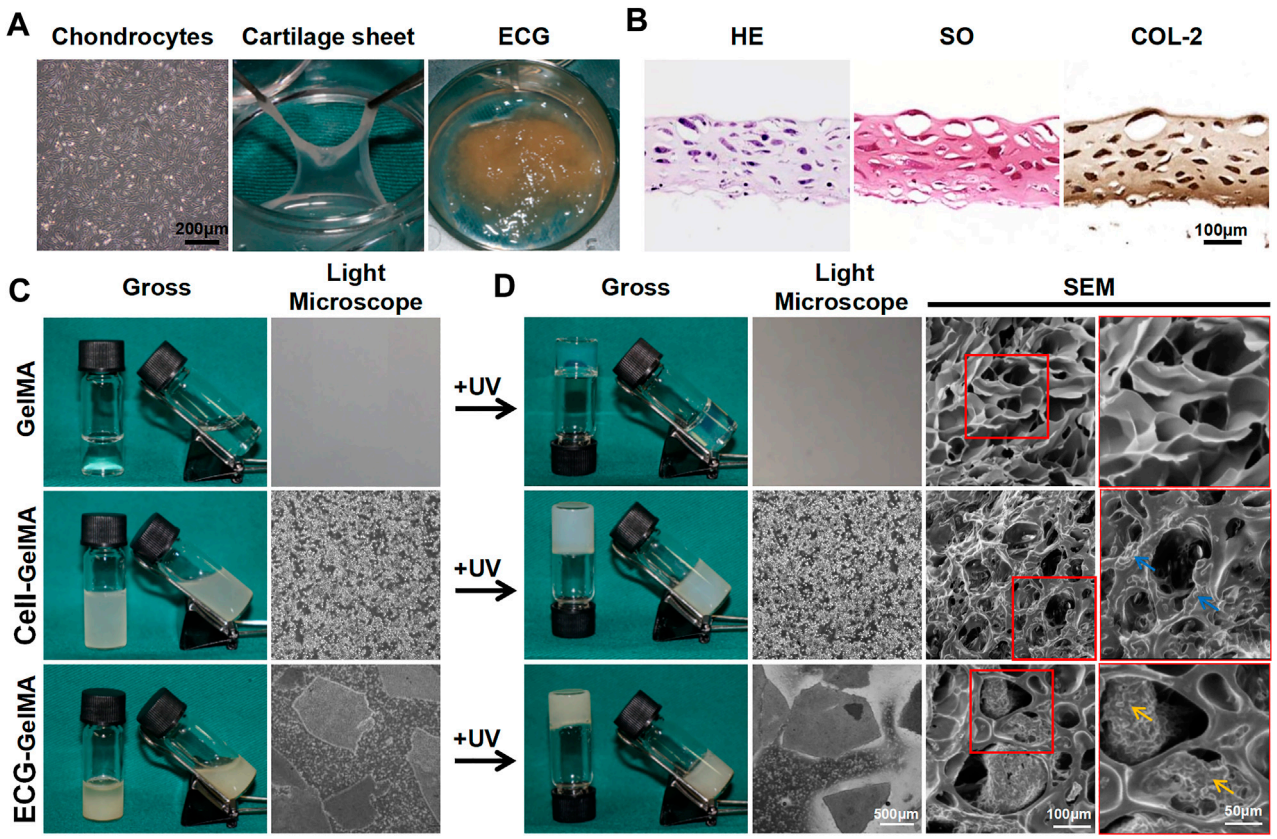

FIGURE 1 | The synthesis and gel properties of ECG-GelMA. The light microscope image of chondrocytes at P3, gross image of cartilage sheet after 5 days *in vitro* cultured, and gross image of ECG derived from chopped cartilage sheet **(A)**. HE, SO, and COL-2 staining of cartilage sheet **(B)**. The gross and light microscope images of GelMA, Cell-GelMA, and ECG-GelMA before UV crosslinking **(C)**. The gross, light microscope, and SEM images of GelMA, Cell-GelMA, and ECG-GelMA after UV crosslinking **(D)**. The blue arrows indicate cells, and the orange arrows indicate ECG.

et al., 2021). Briefly, samples were weighed using an electronic balance. The volume of each sample was measured using a water displacement method. The GAG content in the samples was quantified using Alcian Blue. The total collagen content was detected using a hydroxyproline assay. The DNA content was determined as described above. *The amount of COL-1 and COL-2 was measured by an ELISA.*

Young's modulus was analyzed using a constant compressive strain rate in a biomechanical analyzer (Instron-5969, Canton, MA, United States), as previously described (Xu et al., 2020b). The Young's modulus was calculated using the slope of the stress–strain curve.

2.10 Statistical Analysis

All samples were test at least three times. Differences in quantitative data were analyzed using SPSS23. A p value < 0.05 was considered statistically significant.

3 RESULTS

3.1 Characterizations of ECG, Cell-GelMA, and ECG-GelMA Constructs

As shown in the light microscopy images in **Figure 1A**, P3 chondrocytes had polygonal morphology, indicating viability.

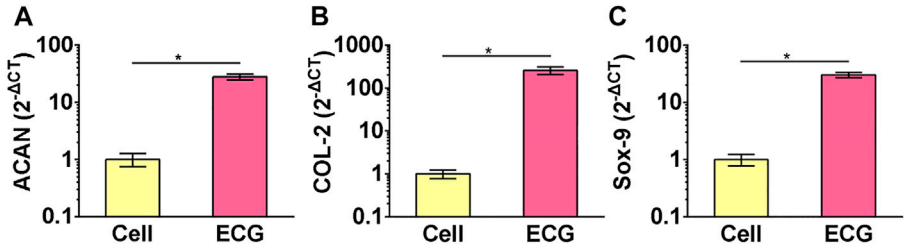

FIGURE 2 | QPCR analysis of chondrocytes and ECG. Gene expression of ACAN **(A)**, COL-2 **(B)** and Sox-9 **(C)** in chondrocytes and ECG after 5 days *in vitro* culture. *$p < 0.05$.

The chondrocytes were cultured in 6-well culture plates at a density of 1.5×10^7 cells/well for 5 days, successfully achieving a cartilage sheet with pink-white appearance and soft texture. The generated cartilage sheet had lacunae structures and preliminary cartilage-specific ECM deposition, as confirmed by superficial SEM examination (**Supplementary Figure S1A**), as well as positive SO and COL-2 staining (**Figure 1B**). Phalloidine staining further revealed that the cartilage sheet displayed extensive F-actin (**Supplementary Figure S1B**), indicating favorable viability.

Thereafter, the generated cartilage sheet was cut into pieces to achieve ECG, which had satisfactory gel properties and could be collected using a 5 ml syringe (**Supplementary Figure S2** and **Supplementary Videos S1**). The P3 chondrocytes and ECG were evenly blended with GelMA to form Cell-GelMA and ECG-GelMA constructs, respectively. Our results confirmed that both the Cell-GelMA and ECG-GelMA constructs exhibited gel properties (**Supplementary Videos S2,S3**).

As shown in the gross view and light microscope images (**Figure 1C**), a uniform distribution of chondrocytes and ECG were clearly observed inside the GelMA, and the same results were observed after being exposed to UV light irradiation (**Figure 1D**). SEM images revealed that the freeze-dried pure GelMA exhibited highly interconnected micropores with smooth pore walls, whereas chondrocytes aggregated on the pore walls in the Cell-GelMA group and minced ECG was distributed in the pores in the ECG-GelMA group.

The gene expression of the chondrocyte and ECG groups were examined using qPCR. The expression of cartilage-related genes, including ACAN, COL-2, and Sox-9, was significantly greater in the ECG than in chondrocytes after 5 days *in vitro* culture (**Figures 2A–C**).

The Cell-GelMA and ECG-GelMA constructs exhibited injectable gel modality with suitable viscosity, and the addition of ECG into GelMA enhanced the viscosity of the hydrogel (**Supplementary Figure S3A**). Time-sweep rheological analyses further confirmed fast gelation at approximately 5 s, indicating satisfactory photo-crosslinked performance of gel precursors (**Supplementary Figure S3B**). Adding ECG to the GelMA hydrogel significantly enhanced the storage moduli (**Supplementary Figure S3C**), whereas it did not affect the compressive moduli (**Supplementary Figure S3D**). The GelMA, Cell-GelMA, and ECG-GelMA groups displayed a consistent low swelling ratio (**Supplementary Figure S3E**), which is beneficial for *in vivo* implantation and shape maintenance. *In vitro* degradation experiments showed that all samples significantly degraded over the initial 8 h (**Supplementary Figure S3F**), suggesting favorable biodegradability for cartilage regeneration. Furthermore, our results confirmed that both the Cell-GelMA and ECG-GelMA constructs were quickly crosslinked from the solution to the sol state upon light irradiation (365 nm, 20 mW/cm^2) within 60 s (**Supplementary Figure S4**). Alternatively, pure ECG failed to form a gel state under identical light irradiation. Collectively, the results indicate the successful preparation of Cell-GelMA and ECG-GelMA constructs that may be ideal injectable gel modalities for cartilage regeneration.

3.2 Biocompatibility

Cell viability assays showed that chondrocytes grew well in both Cell-GelMA and ECG-GelMA with significant proliferation rates and few dead cells at 1, 4, and 7 days (**Figure 3A**). Notably, significantly more dead cells were observed in the Cell-GelMA group, whereas few dead cells were displayed in the ECG-GelMA group, as further confirmed by quantitative analysis of the dead cells (**Figure 3B**). In addition, the cell proliferation test demonstrated that the total DNA content in both the Cell-GelMA and ECG-GelMA groups gradually increased with increasing culture time, and more DNA was observed in the ECG-GelMA group than in the Cell-GelMA group (**Figure 3C**). Phalloidine staining showed that the ECG-GelMA construct displayed extensively more F-actin and stretched more than the Cell-GelMA construct (**Figure 3D**). Collectively, these results indicate that ECG had better biocompatibility than the cells (chondrocytes) when encapsulated within GelMA.

3.3 Cartilage Regeneration in a Nude Mice Model

The feasibility of cartilage regeneration was primary tested in nude mice. After 8 weeks subcutaneous implantation, both Cell-GelMA and ECG-GelMA successfully generated cartilage-like tissues with an ivory-white appearance (**Figure 4A1** and B1). Histological analysis further confirmed that samples in all groups formed cartilage-specific ECM distributions with abundant lacuna structures (**Figure 4A2**-A8 and B2-B8). Notably, the ECG-GelMA group exhibited a significantly robust appearance with larger volume

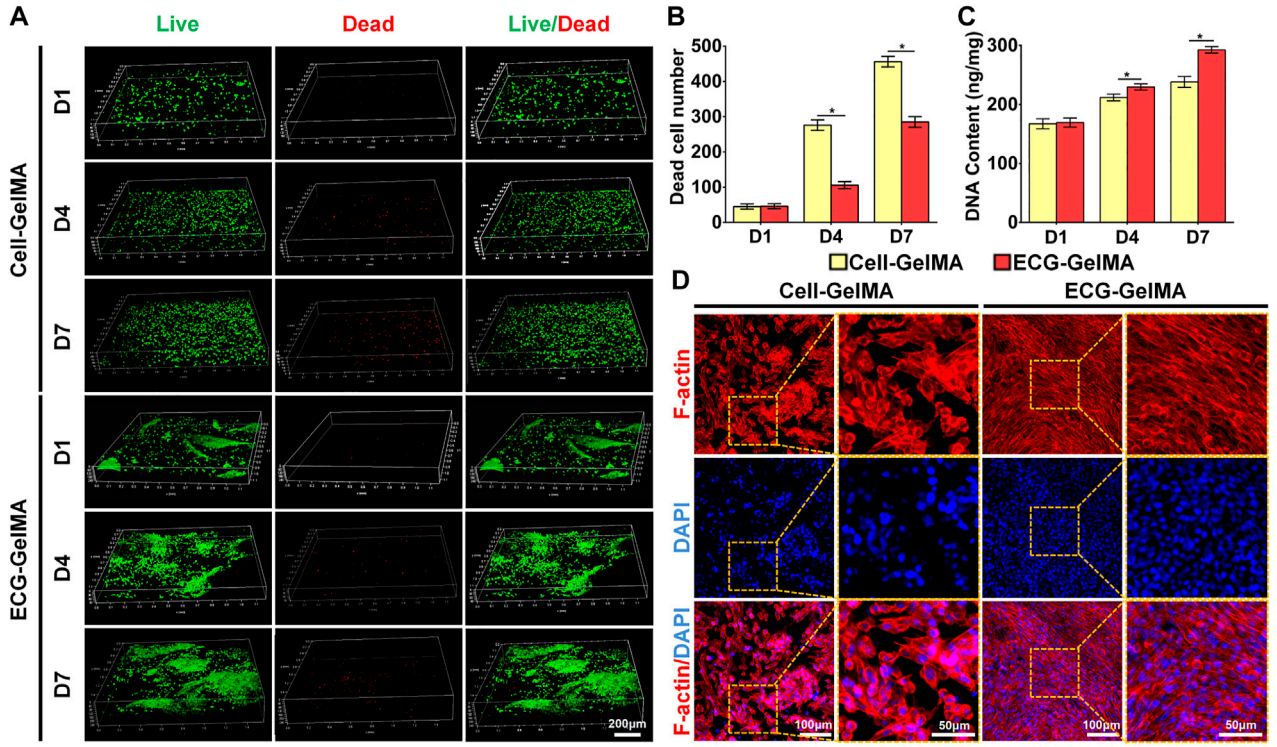

FIGURE 3 | Biocompatibility evaluation of Cell-GelMA and ECG-GelMA. Live/dead staining images **(A)**, as well as quantitative analysis of dead cell number **(B)** and DNA content **(C)** in Cell-GelMA and ECG-GelMA groups at 1–7 days. Phalloidin staining images in Cell-GelMA and ECG-GelMA groups at 7 days **(D)**. *$p < 0.05$.

and homogeneous cartilage ECM deposition than the Cell-GelMA group (**Supplementary Figure S5**). Additionally, heterogeneous cartilage ECM distribution and fibrous-like tissue were observed in Cell-GelMA (**Figure 4A2**), especially in the inner zone (**Figure 4A4**, A6, and A8). Consistent with the gross and histological staining, the quantitative analysis showed that the wet weight, volume, Young's modulus, DNA content, GAG content, total collagen content and *COL-2 content* presented a trend of ECG-GelMA > Cell-GelMA (**Figures 5A–G**). COL-1 content showed ECG-GelMA group were less than Cell-GelMA group (**Figure 5H**). The data suggests that ECG-GelMA outperformed the Cell-GelMA group in terms of cartilage regeneration in nude mice.

3.4 Immune Response

The immunological response of the Cell-GelMA and ECG-GelMA groups were compared in an immunocompetent goat model. After 1 week of subcutaneous implantation, samples in the Cell-GelMA group showed tremendous inflammatory cell infiltration, indicated by positive immunohistochemical staining for CD3 and CD68 (**Figure 6A1**-A5). In contrast, little inflammatory cell infiltration was observed in ECG-GelMA (**Figure 6**B1-B5). Although the inflammatory reaction was significantly reduced in both groups after 2 weeks implantation (**Figure 6**C1-C5 and D1-D5), obvious inflammatory cells were observed in samples at the Cell-GelMA group, whereas they nearly disappeared in the ECG-GelMA group. qPCR analysis of the inflammation-associated genes was used to evaluate the immune response to xenogeneic tissue (**Figures 6E,F**). Expression levels of CD3 and CD68 in the Cell-GelMA was much greater than those in the ECG-GelMA after 1 and 2 weeks *in vivo*. The expression levels of CD3 and CD68 in both samples gradually decreased over the *in vivo* period and were nearly undetectable in the ECG-GelMA group after 2 weeks implantation. The ECG-GelMA had negligible inflammatory reaction compared with the Cell-GelMA group.

3.5 Cartilage Regeneration in a Goat Model

The cartilage regeneration abilities of Cell-GelMA and ECG-GelMA were evaluated by subcutaneously injecting the samples into autologous goats. As the *in vivo* period increased, Cell-GelMA and ECG-GelMA gradually matured, as evidenced by the switch from a reddish appearance and less ECM deposition at 1 and 2 weeks to an ivory-white appearance and mature ECM deposition at 12 weeks (**Figures 6**, **7**). Notably, gross and panorama HE staining revealed that the Cell-GelMA construct shrunk during the *in vivo* period, whereas ECG-GelMA showed limited shrinkage (**Figure 7A1**, B1, A2, B2). Histological results further demonstrated that the regenerated tissues gradually matured over 12 weeks implantation, and GelMA in all groups degraded over time (**Supplementary Figure S6**). Additionally,

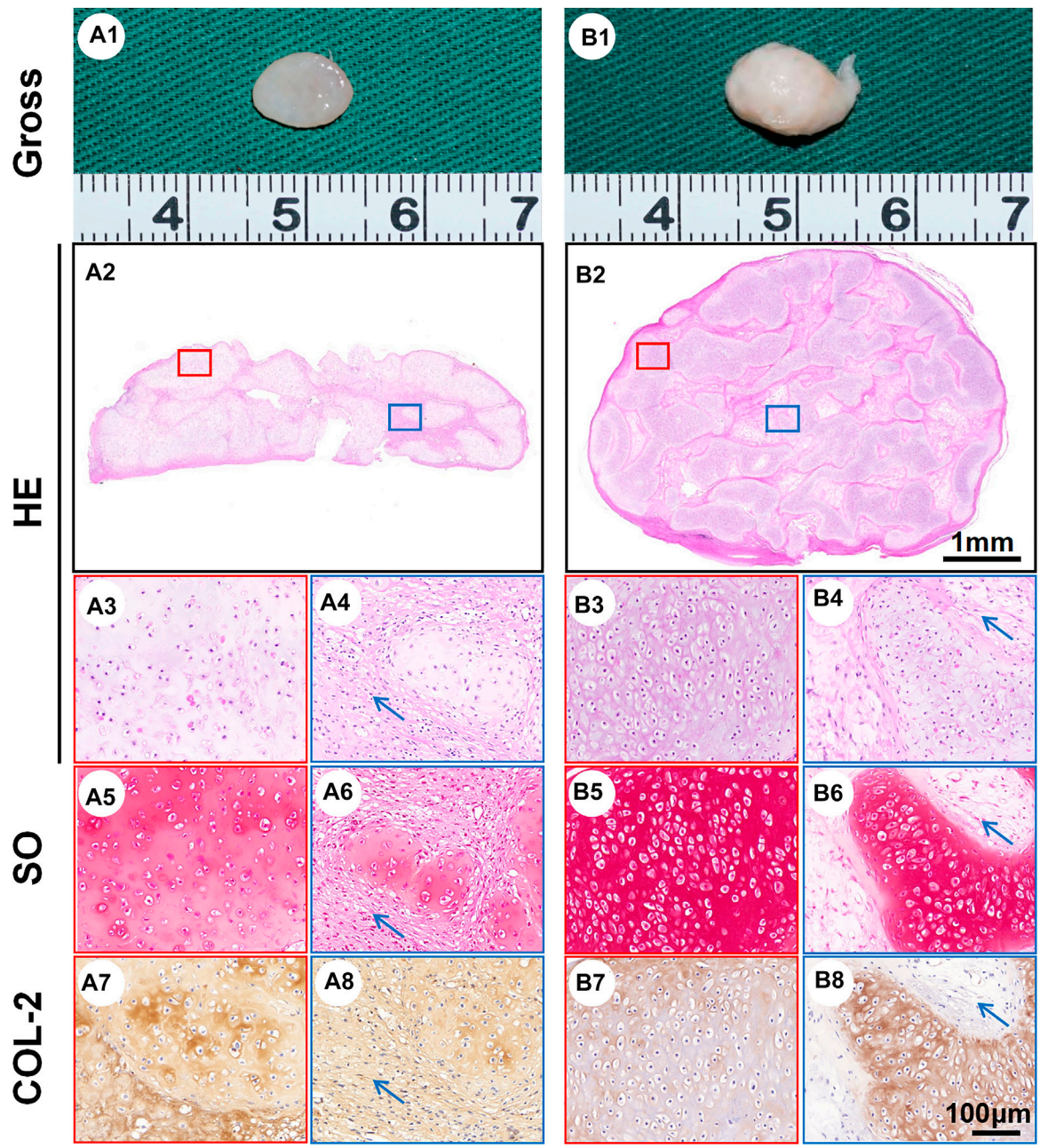

FIGURE 4 | Gross view and histological examination of regenerated cartilage in Cell-GelMA and ECG-GelMA after 8 weeks implantation in nude mice. Gross view (A1 and B1), HE (A2-A4 and B2-B4), SO (A5-A6 and B5-B6), and immunohistochemical COL-2 (A7-A8 and B7-B8) staining in Cell-GelMA and ECG-GelMA groups. The blue box represents magnified images at inner zone of regenerated cartilage, and the red box represents magnified images at peripheral zone of regenerated cartilage. The blue arrows indicate fibrous tissue.

immature cartilage-like tissue and undegraded GelMA were observed inside the Cell-GelMA (**Figure 7A2**-A8), whereas mature and homogeneously distributed cartilage-like tissue was observed in the ECG-GelMA group (**Figure 7B2-B8**). The biomechanical and biochemical results further indicated that *the wet weight, volume, Young's modulus, DNA content, GAG content, total collagen and COL-2 content presented a trend of ECG-GelMA > Cell-GelMA* (**Figure 8A**-G), meanwhile, COL-1 content showed ECG-GelMA group were less than Cell-GelMA group *(***Figure 8H***)*, indicating the advantages of ECG-GelMA for cartilage regeneration in an immunocompetent goat.

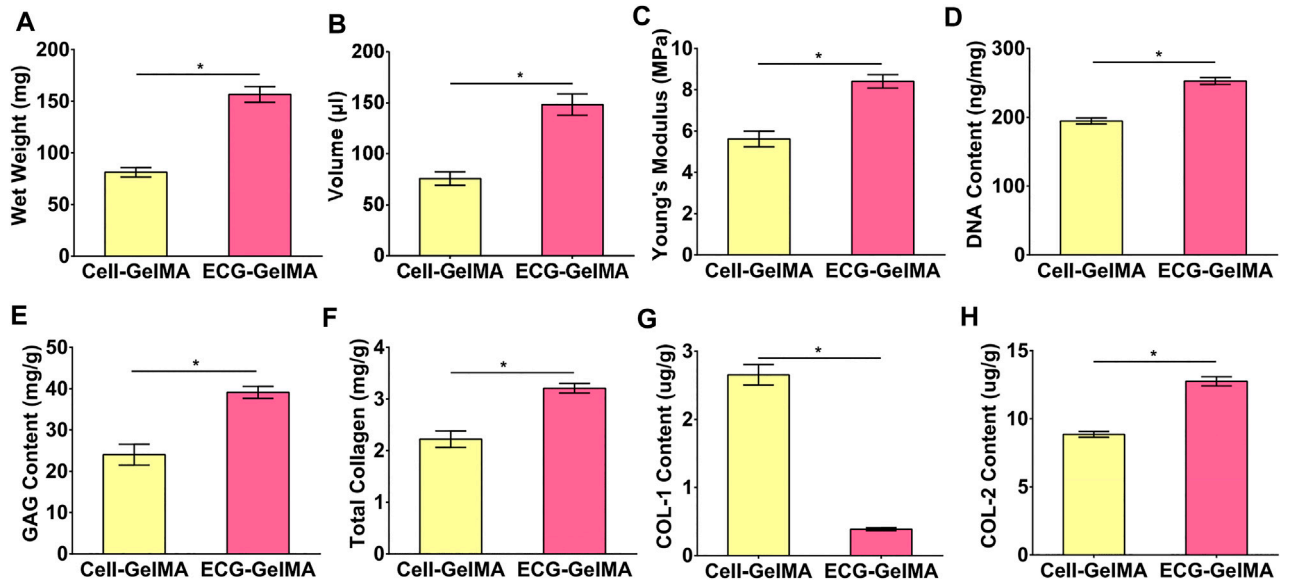

FIGURE 5 | Quantitative analysis of the regenerated cartilage in Cell-GelMA and ECG-GelMA groups after 8 weeks implantation in nude mice. Quantitative analysis of wet weight **(A)**, volume **(B)**, Young's modulus **(C)**, DNA content **(D)**, GAG content **(E)**, total collagen **(F)**, COL-1 content **(G)**, and COL-2 content **(H)** in Cell-GelMA and ECG-GelMA groups. $^{*}p < 0.05$.

4 DISCUSSION

Various types of irregular cartilage tissue deficiencies are common clinically, especially in plastic surgery, such as head and face cartilage defects or dysplasia (Pascual-Garrido et al., 2018). Autologous bone, cartilage, and various artificial materials are frequently used to repair cartilage defects or simply improve the morphology by transplantation or injection filling; however, these methods have not been widely used because of their limitations (Schuurman et al., 2013; Wei et al., 2021). Herein, we introduce a new injectable platform for cartilage regeneration that includes cutting an *in vitro* engineered cartilage sheet into pieces to achieve ECG and encapsulating the ECG into GelMA to form an injectable ECG-GelMA construct. Thereafter, the ECG-GelMA construct could be injected *in situ* for *in vivo* cartilage restoration. Our results confirmed that the ECG-GelMA construct supported better cartilage regeneration than a traditional Cell-GelMA construct.

In recent years, injectable cartilage has been easily accepted by patients and has broad application prospects because of unique advantages such as minimal trauma, injection moldability, and convenient operation. Cell–hydrogel constructs are frequently used in the research on injectable cartilage. However, cell–hydrogel constructs still have obvious disadvantages such as long culture times, high probability of infection, and poor cartilage formation capacity (Bryant et al., 2007; Mashingaidze et al., 2013; Ni et al., 2014).

A cartilage sheet is an ideal tissue for tissue-engineered cartilage regeneration, and a photocrosslinkable hydrogel is a promising scaffold for cartilage regeneration. However, using ECG in combination with photo-crosslinked hydrogels *in vitro* to construct injectable cartilage patterns has not been demonstrated. Our current study showed that the ECG-GelMA constructs supported satisfactory chondrogenesis, and was used as an injectable hydrogel for cartilage regeneration.

ECG-GelMA regenerated better quality cartilage with more efficiency than traditional a Cell-GelMA. The ECG-GelMA group had more mature chondrocyte formation than the Cell-GelMA group after 8 weeks implantation in nude mice and 12 weeks in goats. We suggested that the ECG-GelMA is a promising method for cartilage regeneration. The regeneration process and principle are mainly as follows: 1) the ECG was made of tissue pieces from a cartilage sheet cultured *in vitro*, in which genes (ACAN, COL-2, Sox-9) were up-regulated and ECM was preliminary deposited. In the active stage of cartilage regeneration, the implantation can adapt to the internal environment more quickly *in vivo*, and cartilage regeneration is more stable; 2) ECG contains cartilage-specific ECM, allowing chondrocytes to be housed in an environment that mimics their natural growth process and cells may sense the resistance of matrix through attachment to their own ECM, in order to appropriately induce cellular differentiation and tissue remodeling. (Schulze-Tanzil et al., 2002; Xu et al., 2021a); 3) cells are effectively "caged" away from one another by the hydrogel (Zhang et al., 2016), resulting in interference with the fluidity and interaction of chondrocytes in the Cell-GelMA group. In contrast, ECG is a microscale tissue with integrated structure that does not affect cell interaction and is more conducive to cartilage tissue regeneration. 4) Our results confirmed that ECG-GelMA group exhibited mitigative inflammatory reaction compared to Cell-GelMA group, which was obvious conducive for cartilage formation.

The stability of injectable cartilage regeneration in immunocompetent large animals is still a bottleneck because the scaffold materials cause inflammation, which hinders

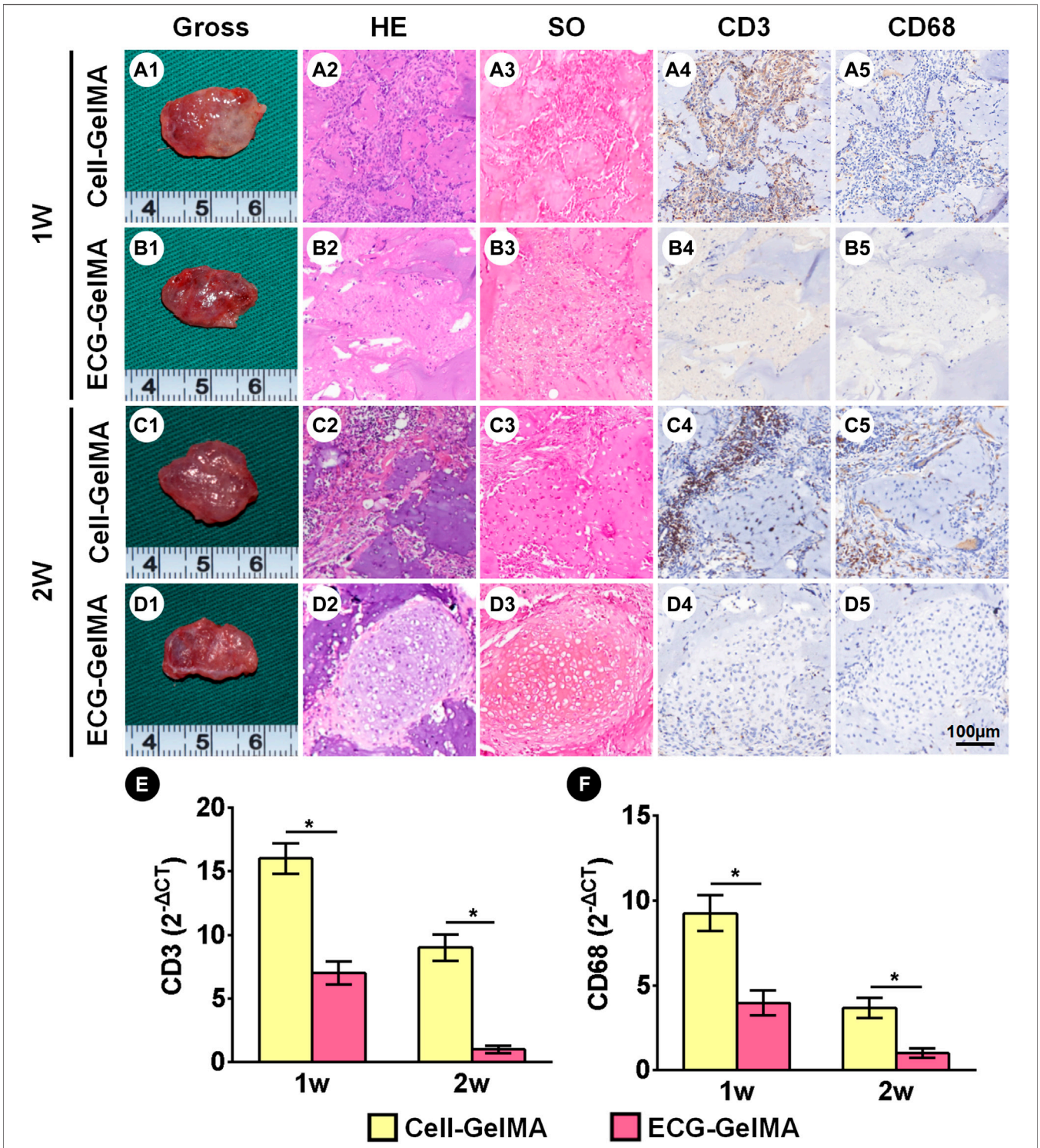

FIGURE 6 | Inflammatory response evaluations of Cell-GelMA and ECG-GelMA constructs subcutaneously implanted into goats for 1 and 2 weeks. Gross view of samples in Cell-GelMA, ECG, and ECG-GelMA groups subcutaneously implanted into goats for 1 week (A1-B1) and 2 weeks (C1-D1). HE (A2-D2), SO (A3-D3), immunohistochemical CD3 (A4-D4) and CD68 (A5-D5) staining of samples in Cell-GelMA, ECG, and ECG-GelMA groups subcutaneously implanted into goats for 1 and 2 weeks. Expression of CD3 (E) and CD68 (F) genes Cell-GelMA, ECG, and ECG-GelMA groups subcutaneously implanted into goats for 1 and 2 weeks $^{*}p < 0.05$.

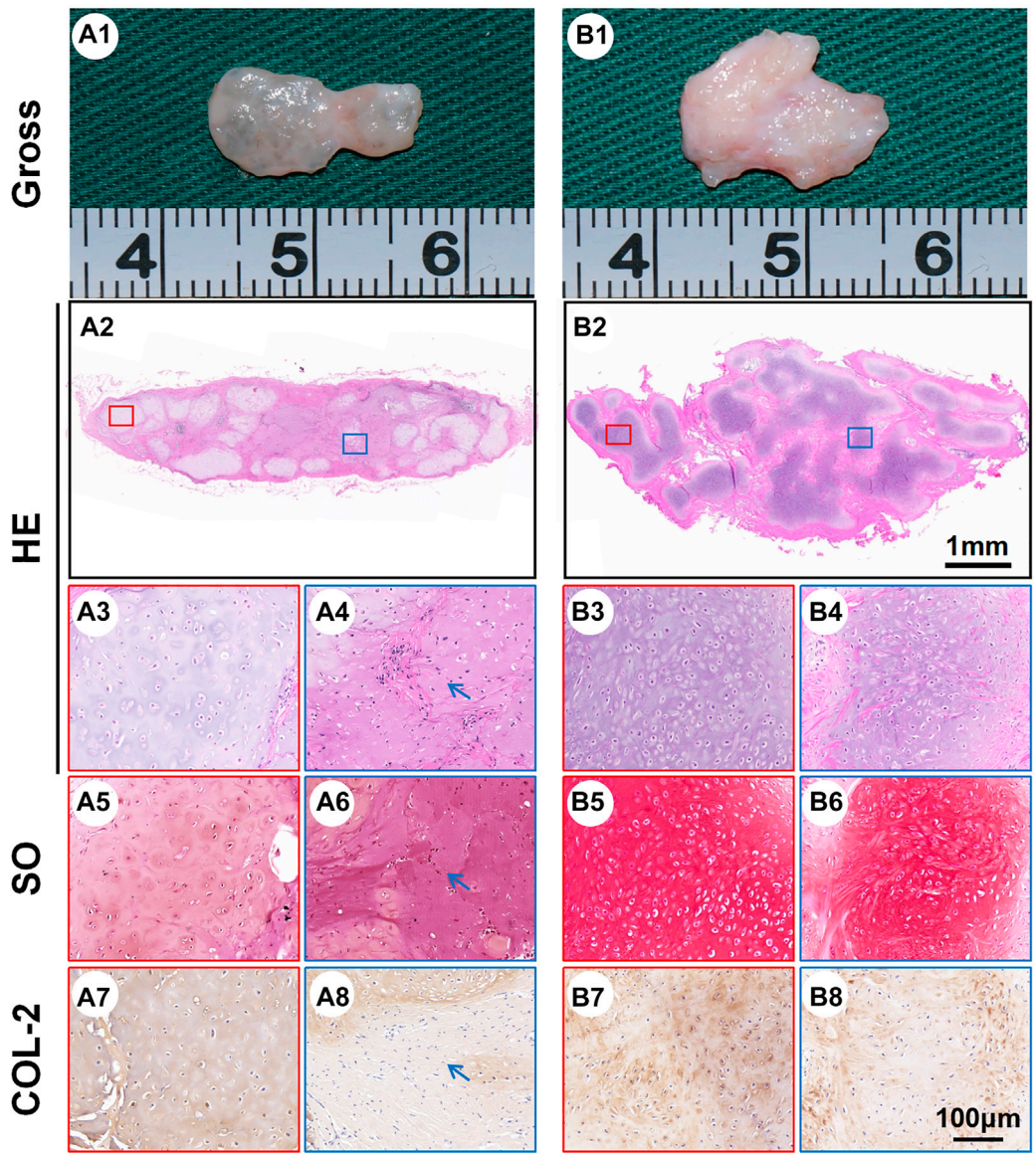

FIGURE 7 | Cartilage regeneration of Cell-GelMA and ECG-GelMA subcutaneously implanted in goat for 12 weeks. Gross view (A1 and B1), HE (A2-A4, and B2-B4), SO (A5-A6 and B5-B6), and immunohistochemical COL-2 (A7-A8 and B7-B8) staining of Cell-GelMA **(A)**, and ECG-GelMA **(B)**. The blue box represents magnified images at inner zone of regenerated cartilage, and the red box represents magnified images at peripheral zone of regenerated cartilage. The blue arrows indicate fibrous tissue.

cartilage regeneration (Luo et al., 2009). Prolonged *in vitro* cultivation supports the formation of a mature cartilaginous graft to resist the acute host response and promotes stable subcutaneous cartilage formation in autologous immunocompetent animals (Liu et al., 2016). However, a long-term *in vitro* cultured cell–hydrogel construct still cannot achieve satisfactory cartilage regeneration *in vivo*, mainly because the scaffold degradation is incomplete. The cartilage sheet can improve cartilage regeneration *in vivo* (Wu et al., 2020). However, our previous study found that ECG had a certain degree of absorption in large animals, which may be related to the slight inflammation caused by surgical trauma during the early stages of implantation. A scaffold that can protect ECG from inflammatory cells in the early stages *in vivo* is needed. Herein, we confirmed that the incorporation of GelMA allowed the construct to serve as an immune barrier against the immune response during the initial implantation.

ECG has unique advantages in clinical translation because of its scaffold-free nature; however, whether the ECG can effectively avoid the inflammatory reaction and steadily maintain the cartilage phenotype in large and immunocompetent animals still needs to be investigated (Wu et al., 2020). We speculate

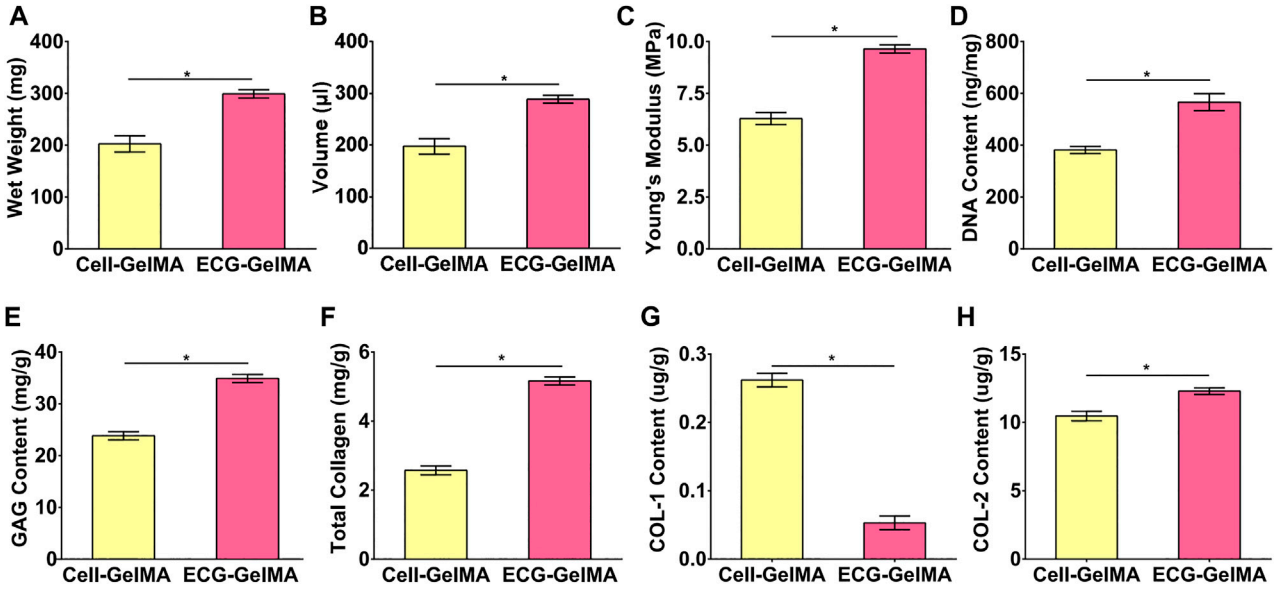

FIGURE 8 | Quantitative analysis of the regenerated cartilage in Cell-GelMA and ECG-GelMA groups after 12 weeks subcutaneously implantation in a goat. Quantitative analysis of wet weight **(A)**, volume **(B)**, Young's modulus **(C)** DNA content **(D)**, GAG content **(E)**, total collagen **(F)**, COL-1 content **(G)**, and COL-2 content **(H)** in Cell-GelMA and ECG-GelMA groups. *$p < 0.05$.

that GelMA may protect chondrocytes from inflammatory cells. The reasons are as follows. 1) Inflammatory cells were mainly distributed in the periphery of the tissue and very few entered the tissue. 2) A significantly reduced inflammatory response was observed in both of the groups at 2 weeks. In addition, our study demonstrated that the ECG-GelMA group had low inflammatory response and a high cartilage survival rate. We suppose the main reasons are as follows: 1) Numerous studies have confirmed that chondrocytes caused inflammatory responses, while cartilage-specific ECM was inflammatory inert. Compared to the chondrocytes in Cell-GelMA group, chondrocytes in ECG-GelMA group were enveloped by a layer of cartilage-specific ECM in ECG, thus protecting chondrocytes from inflammatory invasion (Yang et al., 2005; Wu et al., 2007; Weidenbecher et al., 2008). 2) qPCR analysis demonstrated that the expression of cartilage-related genes, including ACAN, COL-2, and Sox-9 of the ECG was significantly up-regulated, which also promoted the deposition of ECM. The ECM surrounding the cells in ECG function as a natural barrier to make them less vulnerable to inflammatory cells (Xu et al., 2019). 3) The ECM in ECG-GelMA also provides a suitable microenvironment for cells to reside, and would be more conducive to keep stable cartilage phenotype and lower inflammatory response after implantation compared with Cell-GelMA.

Although cartilage can be regenerated in immunocompetent animals, how to solve the problem of early inflammation, and how to adjust the ECG construction and hydrogel selection need to be investigated. Furthermore, the generated cartilage was nearly an island structure, which may relate to the ingrowth of connective tissue after injection into the body. The island cartilage is an absorption risk that needs to be solved. Although ECG-GelMA at a 1:1 ratio is reported in this study, whether a higher ECG concentration can produce better regenerated cartilage has not been investigated. In addition, some important questions, including how to precisely control the shape after injection and achieve stable regenerated cartilage, still need to be studied.

5 CONCLUSION

This study establishes and demonstrates a new concept for cartilage regeneration on the basis of an injectable platform of a ECG-GelMA construct. The ECG-GelMA construct has preferred gel characteristics, superior biocompatibility, enhanced cartilage formation capacity, and enhanced mitigatory immunologic reaction compared with a traditional Cell-GelMA construct. The results of this study provide a new strategy for injectable cartilage regeneration with the potential for clinical translation.

DATA AVAILABILITY STATEMENT

The original contributions presented in the study are included in the article/**Supplementary Material**, further inquiries can be directed to the corresponding authors.

ETHICS STATEMENT

The animal study was reviewed and approved by Weifang Medical University Ethics Committee.

AUTHOR CONTRIBUTIONS

WX, culture cells and editing. TW and XW, scaffolds formation and SEM test. YW and YC revision. DS and ZC, animal operation. YC, YH, scaffolds formation and machine test. GZ, editing. YL, funding aquisiton and Review; editing.

FUNDING

This work was supported by Science and Technology Commission of Shanghai Municipality (19441902600, 20S31900900, 20DZ2254900), the National Key Research and Development Program of China (2017YFC1103900), the National Natural Science Foundation of China (81871502, 81701843, and 81671837), the Shanghai Excellent Technical Leader (18XD1421500), the Program of Shanghai Academic/Technology Research Leader (19XD1431100), the Shanghai Collaborative Innovation Program on Regenerative Medicine and Stem Cell Research (2019CXJQ01), and the Clinical Research Plan of SHDC (SHDC2020CR 2045B).

SUPPLEMENTARY MATERIAL

The Supplementary Material for this article can be found online at: https://www.frontiersin.org/articles/10.3389/fbioe.2022.884036/full#supplementary-material

REFERENCES

Bryant, S. J., Cuy, J. L., Hauch, K. D., and Ratner, B. D. (2007). Photo-Patterning of Porous Hydrogels for Tissue Engineering. *Biomaterials* 28 (19), 2978–2986. doi:10.1016/j.biomaterials.2006.11.033

Cakmak, O., Babakurban, S. T., Akkuzu, H. G., Bilgi, S., Ovalı, E., Kongur, M., et al. (2013). Injectable Tissue-Engineered Cartilage Using Commercially Available Fibrin Glue. *Laryngoscope* 123 (12), 2986–2992. doi:10.1002/lary.24156

Chen, Y., Xu, W., Shafiq, M., Tang, J., Hao, J., Xie, X., et al. (2021). Three-Dimensional Porous Gas-Foamed Electrospun Nanofiber Scaffold for Cartilage Regeneration. *J. Colloid Interf. Sci* 603, 94–109. doi:10.1016/j.jcis.2021.06.067

Ci, Z., Zhang, Y., Wang, Y., Wu, G., Hou, M., Zhang, P., et al. (2021). 3D Cartilage Regeneration with Certain Shape and Mechanical Strength Based on Engineered Cartilage Gel and Decalcified Bone Matrix. *Front. Cel Dev. Biol.* 9, 638115. doi:10.3389/fcell.2021.638115

Ding, J., Bao, S., Qian, W., and Zhao, H. (2021). Subcutaneous Regeneration of Engineered Cartilage: A Comparison of Cell Sheets and Chondrocyte-Scaffold Constructs in a Porcine Model. *Plast. Reconstr. Surg.* 147 (3), 625–632. doi:10.1097/PRS.0000000000007670

Gan, D., Wang, Z., Xie, C., Wang, X., Xing, W., Ge, X., et al. (2019). Mussel-Inspired Tough Hydrogel with *In Situ* Nanohydroxyapatite Mineralization for Osteochondral Defect Repair. *Adv. Healthc. Mater.* 8 (22), 1901103. doi:10.1002/adhm.201901103

Hua, Y., Xia, H., Jia, L., Zhao, J., Zhao, D., Yan, X., et al. (2021). Ultrafast, Tough, and Adhesive Hydrogel Based on Hybrid Photocrosslinking for Articular Cartilage Repair in Water-Filled Arthroscopy. *Sci. Adv.* 7 (35), eabg0628. doi:10.1126/sciadv.abg0628

Lee, S.-H., and Shin, H. (2007). Matrices and Scaffolds for Delivery of Bioactive Molecules in Bone and Cartilage Tissue Engineering. *Adv. Drug Deliv. Rev.* 59 (4-5), 339–359. doi:10.1016/j.addr.2007.03.016

Liu, Y., Li, D., Yin, Z., Luo, X., Liu, W., Zhang, W., et al. (2016). Prolonged *In Vitro* Precultivation Alleviates Post-Implantation Inflammation and Promotes Stable Subcutaneous Cartilage Formation in a Goat Model. *Biomed. Mater.* 12 (1), 015006. doi:10.1088/1748-605X/12/1/015006

Liu, M., Zeng, X., Ma, C., Yi, H., Ali, Z., Mou, X., et al. (2017). Injectable Hydrogels for Cartilage and Bone Tissue Engineering. *Bone Res.* 5, 17014. doi:10.1038/boneres.2017.14

Luo, X., Zhou, G., Liu, W., Zhang, W. J., Cen, L., Cui, L., et al. (2009). *In Vitro* precultivation Alleviates Post-Implantation Inflammation and Enhances Development of Tissue-Engineered Tubular Cartilage. *Biomed. Mater.* 4 (2), 025006. doi:10.1088/1748-6041/4/2/025006

Mashingaidze, F., Choonara, Y. E., Kumar, P., du Toit, L. C., Maharaj, V., Buchmann, E., et al. (2013). Exploration of the Biomacromolecular Interactions of an Interpenetrating Proteo-Saccharide Hydrogel Network at the Mucosal Interface. *J. Biomed. Mater. Res.* 101 (12), 3616–3629. doi:10.1002/jbm.a.34664

Ni, P., Ding, Q., Fan, M., Liao, J., Qian, Z., Luo, J., et al. (2014). Injectable Thermosensitive PEG-PCL-PEG Hydrogel/Acellular Bone Matrix Composite for Bone Regeneration in Cranial Defects. *Biomaterials* 35 (1), 236–248. doi:10.1016/j.biomaterials.2013.10.016

Pascual-Garrido, C., Rodriguez-Fontan, F., Aisenbrey, E. A., Payne, K. A., Chahla, J., Goodrich, L. R., et al. (2018). Current and Novel Injectable Hydrogels to Treat Focal Chondral Lesions: Properties and Applicability. *J. Orthop. Res.* 36 (1), 64–75. doi:10.1002/jor.23760

Qi, C., Yan, X., Huang, C., Melerzanov, A., and Du, Y. (2015). Biomaterials as Carrier, Barrier and Reactor for Cell-Based Regenerative Medicine. *Protein Cell* 6 (9), 638–653. doi:10.1007/s13238-015-0179-8

Schuh, E., Hofmann, S., Stok, K., Notbohm, H., Müller, R., and Rotter, N. (2012). Chondrocyte Redifferentiation in 3D: The Effect of Adhesion Site Density and Substrate Elasticity. *J. Biomed. Mater. Res.* 100A (1), 38–47. doi:10.1002/jbm.a.33226

Schulze-Tanzil, G., de Souza, P., Villegas Castrejon, H., John, T., Merker, H. J., Scheid, A., et al. (2002). Redifferentiation of Dedifferentiated Human Chondrocytes in High-Density Cultures. *Cel Tissue Res.* 308 (3), 371–379. doi:10.1007/s00441-002-0562-7

Schuurman, W., Levett, P. A., Pot, M. W., van Weeren, P. R., Dhert, W. J. A., Hutmacher, D. W., et al. (2013). Gelatin-Methacrylamide Hydrogels as Potential Biomaterials for Fabrication of Tissue-Engineered Cartilage Constructs. *Macromol. Biosci.* 13 (5), 551–561. doi:10.1002/mabi.201200471

Singh, Y. P., Moses, J. C., Bhardwaj, N., and Mandal, B. B. (2018). Injectable Hydrogels: A New Paradigm for Osteochondral Tissue Engineering. *J. Mater. Chem. B* 6 (35), 5499–5529. doi:10.1039/c8tb01430b

Van Den Bulcke, A. I., Bogdanov, B., De Rooze, N., Schacht, E. H., Cornelissen, M., and Berghmans, H. (2000). Structural and Rheological Properties of Methacrylamide Modified Gelatin Hydrogels. *Biomacromolecules* 1 (1), 31–38. doi:10.1021/bm990017d

Wang, Y., Xu, Y., Zhou, G., Liu, Y., and Cao, Y. (2020). Biological Evaluation of Acellular Cartilaginous and Dermal Matrixes as Tissue Engineering Scaffolds for Cartilage Regeneration. *Front. Cel Dev. Biol.* 8, 624337. doi:10.3389/fcell.2020.624337

Wei, W., Ma, Y., Yao, X., Zhou, W., Wang, X., Li, C., et al. (2021). Advanced Hydrogels for the Repair of Cartilage Defects and Regeneration. *Bioactive Mater.* 6 (4), 998–1011. doi:10.1016/j.bioactmat.2020.09.030

Weidenbecher, M., Tucker, H. M., Awadallah, A., and Dennis, J. E. (2008). Fabrication of a Neotrachea Using Engineered Cartilage. *Laryngoscope* 118 (4), 593–598. doi:10.1097/MLG.0b013e318161f9f8

Wu, W., Cheng, X., Zhao, Y., Chen, F., Feng, X., and Mao, T. (2007). Tissue Engineering of Trachea-Like Cartilage Grafts by Using Chondrocyte Macroaggregate: Experimental Study in Rabbits. *Artif. Organs* 31 (11), 826–834. doi:10.1111/j.1525-1594.2007.00474.x

Wu, J., Chen, Q., Deng, C., Xu, B., Zhang, Z., Yang, Y., et al. (2020). Exquisite Design of Injectable Hydrogels in Cartilage Repair. *Theranostics* 10 (21), 9843–9864. doi:10.7150/thno.46450

Xu, Y., Li, Y., Liu, Y., Li, H., Jia, Z., Tang, Y., et al. (2019). Surface Modification of Decellularized Trachea Matrix with Collagen and Laser Micropore Technique to Promote Cartilage Regeneration. *Am. J. Transl Res.* 11 (9), 5390–5403.

Xu, Y., Duan, L., Li, Y., She, Y., Zhu, J., Zhou, G., et al. (2020a). Nanofibrillar Decellularized Wharton's Jelly Matrix for Segmental Tracheal Repair. *Adv. Funct. Mater.* 30 (14), 1910067. doi:10.1002/adfm.201910067

Xu, Y., Guo, Y., Li, Y., Huo, Y., She, Y., Li, H., et al. (2020b). Biomimetic Trachea Regeneration Using a Modular Ring Strategy Based on Poly(Sebacoyl Diglyceride)/Polycaprolactone for Segmental Trachea Defect Repair. *Adv. Funct. Mater.* 30 (42), 2004276. doi:10.1002/adfm.202004276

Xu, Y., Jia, L., Wang, Z., Jiang, G., Zhou, G., Chen, W., et al. (2020c). Injectable Photo-Crosslinking Cartilage Decellularized Extracellular Matrix for Cartilage Tissue Regeneration. *Mater. Lett.* 268, 127609. doi:10.1016/j.matlet.2020.127609

Xu, Y., Xu, Y., Bi, B., Hou, M., Yao, L., Du, Q., et al. (2020d). A Moldable Thermosensitive Hydroxypropyl Chitin Hydrogel for 3D Cartilage Regeneration *In Vitro* and *In Vivo*. *Acta Biomater.* 108, 87–96. doi:10.1016/j.actbio.2020.03.039

Xu, Y., Dai, J., Zhu, X., Cao, R., Song, N., Liu, M., et al. (2021a). Biomimetic Trachea Engineering via a Modular Ring Strategy Based on Bone-Marrow Stem Cells and Atelocollagen for Use in Extensive Tracheal Reconstruction. *Adv. Mater.* 34, 2106755. doi:10.1002/adma.202106755

Xu, Y., Wang, Z., Hua, Y., Zhu, X., Wang, Y., Duan, L., et al. (2021b). Photocrosslinked Natural Hydrogel Composed of Hyaluronic Acid and Gelatin Enhances Cartilage Regeneration of Decellularized Trachea Matrix. *Mater. Sci. Eng. C* 120, 111628. doi:10.1016/j.msec.2020.111628

Xue, J., He, A., Zhu, Y., Liu, Y., Li, D., Yin, Z., et al. (2018). Repair of Articular Cartilage Defects with Acellular Cartilage Sheets in a Swine Model. *Biomed. Mater.* 13 (2), 025016. doi:10.1088/1748-605X/aa99a4

Yang, J., Yamato, M., Kohno, C., Nishimoto, A., Sekine, H., Fukai, F., et al. (2005). Cell Sheet Engineering: Recreating Tissues without Biodegradable Scaffolds. *Biomaterials* 26 (33), 6415–6422. doi:10.1016/j.biomaterials.2005.04.061

Zhang, Z., Eyster, T. W., and Ma, P. X. (2016). Nanostructured Injectable Cell Microcarriers for Tissue Regeneration. *Nanomedicine* 11 (12), 1611–1628. doi:10.2217/nnm-2016-0083

Zhou, G., Jiang, H., Yin, Z., Liu, Y., Zhang, Q., Zhang, C., et al. (2018). *In Vitro* Regeneration of Patient-Specific Ear-Shaped Cartilage and its First Clinical Application for Auricular Reconstruction. *EBioMedicine* 28, 287–302. doi:10.1016/j.ebiom.2018.01.011

Conflict of Interest: Author ZC was employed by the company Shanghai Resthetic Bio CO., LTD.

The remaining authors declare that the research was conducted in the absence of any commercial or financial relationships that could be construed as a potential conflict of interest.

Publisher's Note: All claims expressed in this article are solely those of the authors and do not necessarily represent those of their affiliated organizations, or those of the publisher, the editors, and the reviewers. Any product that may be evaluated in this article, or claim that may be made by its manufacturer, is not guaranteed or endorsed by the publisher.

Copyright © 2022 Xu, Wang, Wang, Wu, Chen, Song, Ci, Cao, Hua, Zhou and Liu. This is an open-access article distributed under the terms of the Creative Commons Attribution License (CC BY). The use, distribution or reproduction in other forums is permitted, provided the original author(s) and the copyright owner(s) are credited and that the original publication in this journal is cited, in accordance with accepted academic practice. No use, distribution or reproduction is permitted which does not comply with these terms.

frontiers | Frontiers in Bioengineering and Biotechnology

ORIGINAL RESEARCH
published: 12 May 2022
doi: 10.3389/fbioe.2022.884601

Silk Hydrogel-Mediated Delivery of Bone Morphogenetic Protein 7 Directly to Subcutaneous White Adipose Tissue Increases Browning and Energy Expenditure

Kristy L. Townsend[1,2], Eleanor Pritchard[3†], Jeannine M. Coburn[3†], Young Mi Kwon[1], Magdalena Blaszkiewicz[1,2], Matthew D. Lynes[1,4], David L. Kaplan[3] and Yu-Hua Tseng[1]**

[1]Integrative Physiology and Metabolism, Joslin Diabetes Center, Harvard Medical School, Boston, MA, United States, [2]Department of Neurological Surgery, The Ohio State University, Wexner Medical Center, Columbus, OH, United States, [3]Department of Biomedical Engineering, Tufts University, Medford, MA, United States, [4]Center for Molecular Medicine, Maine Medical Center Research Institute, Scarborough, ME, United States

Objective: Increasing the mass and/or activity of brown adipose tissue (BAT) is one promising avenue for treating obesity and related metabolic conditions, given that BAT has a high potential for energy expenditure and is capable of improving glucose and lipid homeostasis. BAT occurs either in discrete "classical" depots, or interspersed in white adipose tissue (WAT), termed "inducible/recruitable" BAT, or 'beige/brite' adipocytes. We and others have demonstrated that bone morphogenetic protein 7 (BMP7) induces brown adipogenesis in committed and uncommitted progenitor cells, resulting in increased energy expenditure and reduced weight gain in mice. BMP7 is therefore a reliable growth factor to induce browning of WAT.

Methods: In this study, we sought to deliver BMP7 specifically to subcutaneous (sc)WAT in order to induce tissue-resident progenitor cells to differentiate into energy-expending recruitable brown adipocytes, without off-target effects like bone formation, which can occur when BMPs are in the presence of bone progenitor cells (outside of WAT). BMP7 delivery directly to WAT may also promote tissue innervation, or directly activate mitochondrial activity in brown adipocytes, as we have demonstrated previously. We utilized silk protein in the form of an injectable hydrogel carrying BMP7. Silk scaffolds are useful for *in vivo* delivery of substances due to favorable material properties, including controlled release of therapeutic proteins in an active form, biocompatibility with minimal immunogenic response, and prior FDA approval for some medical materials. For this study, the silk was engineered to meet desirable release kinetics for BMP7 in order to mimic our prior *in vitro* brown adipocyte differentiation studies. Fluorescently-labeled silk hydrogel loaded with BMP7 was directly injected into WAT through the skin and monitored by non-invasive *in vivo* whole body imaging, including in UCP1-luciferase reporter mice, thereby enabling an approach that is translatable to humans.

OPEN ACCESS

Edited by:
Bruce Alan Bunnell, University of North Texas Health Science Center, United States

Reviewed by:
Christian Dani, INSERM U1091 Institut de Biologie de Valrose, France
Hongshuai Li, The University of Iowa, United States

***Correspondence:**
Kristy L. Townsend
kristy.townsend@osumc.edu
Yu-Hua Tseng
yu-hua.tseng@joslin.harvard.edu

†*These authors have contributed equally to this work*

Specialty section:
This article was submitted to Tissue Engineering and Regenerative Medicine, a section of the journal Frontiers in Bioengineering and Biotechnology

Received: *26 February 2022*
Accepted: *28 April 2022*
Published: *12 May 2022*

Citation:
Townsend KL, Pritchard E, Coburn JM, Kwon YM, Blaszkiewicz M, Lynes MD, Kaplan DL and Tseng Y-H (2022) Silk Hydrogel-Mediated Delivery of Bone Morphogenetic Protein 7 Directly to Subcutaneous White Adipose Tissue Increases Browning and Energy Expenditure. Front. Bioeng. Biotechnol. 10:884601. doi: 10.3389/fbioe.2022.884601

Results: Injection of the BMP7-loaded silk hydrogels into the subcutaneous WAT of mice resulted in "browning", including the development of multilocular, uncoupling protein 1 (UCP1)-positive brown adipocytes, and an increase in whole-body energy expenditure and skin temperature. In diet-induced obese mice, BMP7-loaded silk delivery to subcutaneous WAT resulted in less weight gain, reduced circulating glucose and lower respiratory exchange ratio (RER).

Conclusions: In summary, BMP7 delivery via silk scaffolds directly into scWAT is a novel translational approach to increase browning and energy expenditure, and represents a potential therapeutic avenue for delivering substances directly to adipose depots in pursuit of metabolic treatments.

Keywords: silk hydrogel, adipose tissue, browning, thermogenesis, BMP7, intraadipose delivery

HIGHLIGHTS

- BMP7 delivery to scWAT using protein-loaded silk scaffolds allows targeted browning without undesirable bone-formation.
- Silk scaffolds for drug delivery to scWAT can be done via direct injections through the skin with a hypodermic needle.
- Silk can be loaded with fluorescent tags to non-invasively monitor.
- BMP7 delivery to scWAT increased energy expenditure concurrent with increased tissue UCP1 expression.

INTRODUCTION

Obesity and related metabolic conditions such as type 2 diabetes mellitus (T2DM) and cardiovascular disease (CVD) currently exist as global pandemics, and cardiometabolic disease is a leading cause of death worldwide. Obesity is a difficult condition to treat and reverse, due to the complex pathophysiology that involves both genetic predisposition and environmental factors such as diet, as well as dysfunction in numerous tissues and organs. Therapies that act on appetite centers of the brain are met with undesirable psychiatric side effects, thus, an approach that instead targets unhealthy adipose tissue itself is an appealing alternative option to not only reduce adipose mass, but prevent other metabolic comorbidities by improving adipose tissue function. Improvement of obesity can mitigate resulting co-morbidities such as T2DM, CVD and cardiometabolic diseases.

Bone morphogenetic protein 7 (BMP7) is capable of inducing a range of metabolically beneficial effects, including: 1) promotion of stem and progenitor cell commitment to the brown adipocyte lineage (Tseng et al., 2008); 2) differentiating brown preadipocytes into mature, uncoupling 1 (UCP1)-positive brown adipocytes (Tseng et al., 2008; Boon et al., 2013; Elsen et al., 2014; Okla et al., 2015)); 3) increasing mitochondrial activity and fatty acid utilization in brown adipocytes (Townsend et al., 2013); 4) increasing whole-body energy expenditure (Townsend et al., 2012; Boon et al., 2013; Saini et al., 2015; Townsend et al., 2017); 5) decreasing appetite (Townsend et al., 2012; Townsend et al., 2017); and 6) promoting neural plasticity (reviewed in (Jensen et al., 2021)). Since brown adipocytes are so metabolically healthy, with both anti-obesity and anti-diabetes functions (Townsend and Tseng, 2014) (Jensen et al., 2021), there is great interest in the potential therapeutic benefits of increasing brown adipose tissue (BAT) mass and/or activity in humans. Therefore, the utilization of BMP7 for the treatment or mitigation of obesity and its co-morbidities, such as T2DM and CVD, is of interest.

BMP7 is currently FDA-approved (marketed as OP-1 by Stryker Biotech), under the Humanitarian Device Exemption, for utilization in long bone nonunions and recalcitrant nonunions (White et al., 2007), but has not yet been used in human clinical trials as a weight-loss or anti-diabetes drug. While systemic administration of BMP7 has been shown to be effective at reversing diet- and genetically-induced obesity and diabetes in mice (Townsend et al., 2012), systemic administration in humans will be met with a number of obstacles, including the potential for bone-formation at higher doses (Luo et al., 1995) (Lavery et al., 2009), and the short half-life of BMP7 in circulation (Vukicevic et al., 1998). Therefore, direct and continuous release of BMP7 discretely in subcutaneous white adipose tissue (scWAT) should result in several beneficial effects of BMP7 treatment, as indicated by prior mouse studies (Tseng et al., 2008; Boon et al., 2011; Boon et al., 2013) (Townsend et al., 2012) (Townsend et al., 2017). These benefits include an increase in brown adipogenesis, reduction of white fat mass, activation of brown adipocyte energy expenditure, and weight loss, while avoiding the potentially harmful side effects of systemic administration such as osteogenesis in niches where bone progenitor cells are found.

Thermogenic adipose tissue consists of classical BAT depots, such as the interscapular depot in rodents and human babies, as well as inducible/recruitable cells that can be stimulated to appear in white fat depots, termed either 'beige' or 'brite', through the process of 'browning' (Townsend and Tseng, 2014). One of the most prominent thermogenic systems in brown and beige adipocytes is the regulated uncoupling of oxidative phosphorylation from ATP synthesis by uncoupling protein 1 (UCP1), a protein specifically expressed in the mitochondria of mammalian brown and beige adipocytes. UCP1 offers an efficient

way to expend excess energy, although there also exist UCP1-independent means of heat production (Roesler and Kazak, 2020). UCP1 activity requires fatty acid fuels, which are in part released from white adipocytes through lipolysis. Browning may occur either via transdifferentiation of a mature white adipocyte to a UCP1-positive brown adipocyte, or via *de novo* adipogenesis differentiated from tissue-resident progenitors (Townsend and Tseng, 2014). Several growth factors, including BMP7, have been shown to promote the browning process, as does beta-adrenergic stimulation, such as with norepinephrine release to WAT and BAT after cold exposure (Townsend and Tseng, 2014). In humans, browning of scWAT was demonstrated by the presence of UCP1 in multilocular adipocytes, with increased presence of mitochondria and respiratory capacity after burn trauma (Sidossis et al., 2015), or after treatment with pharmacological agents (reviewed in (Herz and Kiefer, 2019)). Cold exposure or treatment with beta-adrenergic agonists in humans have been pursued as a means to increase browning, but may also lead to increased appetite, in addition to discomfort and potential cardiovascular risks (Schellen et al., 2012). Therefore, new non-sympathetic modes of increasing brown fat mass and activity are appealing options, especially if these therapies can also stimulate UCP1 activity and other metabolically healthy processes in adipose tissues.

Bioengineered silk protein delivery vehicles are an appealing candidate for mediating BMP7 delivery to WAT, as silk is a readily available natural resource (such as from silkworm production), is non-immunogenic, and is able to be engineered into microspheres, hydrogels and other drug delivery systems that protect the 'drug' from degradation, but are able to be regulated to control drug release kinetics ((Guziewicz et al., 2011; Hines and Kaplan, 2011; Pritchard et al., 2013a; Pritchard et al., 2013b; Guziewicz et al., 2013; Coburn et al., 2015; Lovett et al., 2015; Kluge et al., 2016; Zhang et al., 2017)). Silk-mediated delivery of BMP2 has already been optimized *in vitro* and in mouse models (Diab et al., 2012; Shi et al., 2013; Zhang et al., 2014; Koolen et al., 2016; Shen et al., 2016).

As we demonstrate here, specific delivery of BMP7 to subcutaneous (sc)WAT by silk-hydrogel delivery directly through the skin led to induction of browning of white fat. Silk-mediated, scWAT-specific, delivery of BMP7 also appears able to increase energy expenditure and reverse diet-induced adiposity, without the problem of bone formation that may occur with systemic administration, making it an appealing candidate for treatments aimed at augmenting brown fat amount and function.

MATERIALS AND METHODS

Mouse Studies

Mice were C57BL6/J males or UCP1-Cre mated to Rosa-Luciferase males, and all were adults over 7 weeks old and housed in a standard 12/12 light/dark cycle starting at 7a.m., and were held at room temperature unless otherwise indicated. Those undergoing a high fat diet were fed 45% kcal from fat diet (part of the diet-induced obesity diet series) from Research Diets. Metabolic phenotyping included measurements in a Columbus Instruments Comprehensive Laboratory Animal Monitoring System (CLAMS) for assessment of VO2, VCO2, RER and Heat, using the Joslin Diabetes Center Metabolic Phenotyping Core, and these measurements were conducted just prior to tissue collection. DEXA scans (dual-energy X-ray absorptiometry) were used to quantify tissue composition (fat *vs.* lean), and was conducted the first day of CLAMS. An IVIS-CT small animal imager was used to image tissue levels of fluorescent or luciferase signals in live, anesthetized animals. Circulating insulin and glucose were measured by commercially available ELISAs in the Joslin Specialized Assay Core. All mouse studies were conducted similar to previously described methods (Townsend et al., 2012; Townsend et al., 2017). N = 6-8 mice were used per study, except IVIS imaging which included N = 3-4 mice per group. Separate cohorts were used for ipsilateral/contralateral measurements of changes to skin temperature and for imaging of silk injections, versus cohorts used for whole body metabolic assessments where bilateral silk injections were given directly through the skin to flank/inguinal scWAT.

IVIS-CT

For acquisition of fluorescent and bioluminescent images an IVIS-Spectrum CT imaging system equipped with a CCD camera (Caliper Life Sciences) was used. Mice were sedated with 2% isoflurane, then fluorescent images and microCT images were captured. Silk hydrogels were labeled using DyLite800 beads and were imaged using the 735 nm excitation filter and the 800 nm emission filter. Fluorescent data was projected onto microCT imaging using Living Image software to generate 3 dimensional projections. Immediately after fluorescent imaging, D-Luciferin (Perkin Elmer) was diluted to 3 mg/100 μL in normal saline and 0.6 mg of D-Luciferin was administrated intraperitoneally. 15 min after D-Luciferin injection, bioluminsecent images were captured without an emission filter or any excitation light.

Extraction of Silk Fibroin

Silk fibroin from B. mori silkworm cocoons was isolated as previously described (Rockwood et al., 2011). Briefly, cocoons were cut to approximately 1 cm^2 pieces and boiled in 0.02 M Na_2CO_3 solution for 30, 40, 60 min to extract the silk fibroin (referred to as silk). The silk fibers were washed using deionized water (PicoPure® water purification system, Hydro Service and Supplies, Durham, NC) and air dried. The dried silk fibers (5 g) were dissolved in 20 ml 9.3 M LiBr at 60°C for 3 h followed by dialysis (Pierce 3.4 kDa MWCO dialysis cassette; Fisher Scientific, Pittsburg, PA) for 2 days with at least 6 water exchanges. The resulting aqueous silk solution was stored at 4°C for future use.

BMP7 Loaded Silk Formulations

For BMP7 loaded silk particles embedded within silk hydrogels, BMP-7 loaded silk microparticles were fabricated following a previously published poly (vinyl alcohol) ((PVA)/silk particle formulation procedures (Wang et al., 2010)). A 1% 60 min extract

silk solution, 1% 40 min extract silk solution, and 1% PVA was sterile filter and handled aseptically thereafter. To prepare the particles, equal volumes of 1% 60 min extract silk solution and 1% 40 min extract silk solution were combined to a final volume of 50 ml. To this solution, 0.5 ml of 5 mg/ml sterile bovine serum albumin (BSA) was added. To 30 ml of this silk/BSA solution, 0.5 ml of 1 mg/ml BMP-7 was added; this solution was combined with 120 ml 1% PVA solution and allowed to mix for 2 h at room temperature. The solution was transferred to Petri dishes to allow for particle formation and solvent evaporation. After complete solvent evaporation, the resulting film was removed from the Petri dish using sterile forceps and transferred to a 50 ml conical tube to which 45 ml sterile deionized water was added to isolate the particles. The particle suspension was centrifuged for 10 min, the aqueous phase removed, and the particles washed two more times with ultrapure water. The resulting particles were allowed to air dry. For the pilot animal study, the particles were resuspended in sterile PBS at 15 mg/ml and centrifuged for 3 min. The particles were resuspended at 150 mg/ml. Separately, 6% 60 min extracted silk was probe sonicated, as described below, and placed on ice to form a pre-gelled silk solution. The pre-gelled silk solution was mixed 2:1 with the silk particles and maintained on ice. Ten microliters (0.5 mg silk particles) of the particle-loaded pre-gelled silk solution was injected.

To generate BMP7-loaded silk hydrogels, 2 ml of 3% or 6% silk solution was probe sonicated (Branson 450 Probe Sonifier, Branson Ultrasonics, Danbury, CT) at 30% amplitude for 30 min for two cycles to form a pre-gelled solution maintaining on ice between cycles and after sonification. BMP7 was added to the pre-gelled silk solutions at a final concentration of 120 μg/ml and maintained on ice for *in vivo* studies.

In vitro BMP7 Release Studies

For silk particles loaded with BMP7 and suspended in silk hydrogel, 10 μL was transferred to low-protein bind Eppendorf tubes and allowed to gel at room temperature.

For silk hydrogels loaded with BMP7, 20 μL of the BMP7-loaded pre-gelled solution (2.4 μg BMP7) was transferred to low-protein bind Eppendorf tubes and allowed to gel at room temperature for 4 h and stored at 4°C overnight. *In vitro*, BMP7 release studies were performed by adding 1 ml PBS to each Eppendorf tube containing the BMP7-loaded hydrogels. At periodic time points, 0.950 ml PBS was removed and replaced with fresh PBS to continue the release study. BMP7 release was determined using a BMP7 ELISA kit (R&D Systems Inc., Minneapolis, MN, United States) following the manufacturers protocol.

For *in vivo* studies, 10 μL of the 3% silk formulation (1.2 μg BMP7 or empty silk control) was prepared aseptically after sterile filtration of the silk solution. The pre-gelled solutions were loaded into insulin syringes. Syringes were maintained at room temperature for 2 h (time required to observe gelation of test tube sample via inversion testing) to allow for gelation and stored at 4°C.

For *in vivo* imaging, soluble silk was labeled with a DyLight 800 antibody labeling kit (ThermoFisher, Waltham, MA, United States) following the manufacturer's protocol. The labeled silk was combined 1:100 with unlabeled silk and subsequently used for fabricating silk hydrogels.

Adipose Histology and Immunostaining

Tissues were fixed in 10% normal buffered formalin followed by paraffin-embedding and slicing at 7uM in a microtome. Tissue sections were mounted on slides for immunostaining, including hematoxylin to assess tissue histology, UCP1 (as described in (Townsend et al., 2012; Townsend et al., 2017)) and the nuclear fluorophore DAPI.

Statistics

Statistics were conducted as described in (Townsend et al., 2012; Townsend et al., 2017), with ANOVA (continuous data in line graphs) or student's *t*-test with Fisher post-hoc (bar graphs) as appropriate.

RESULTS

Engineered BMP7 Silk Hydrogel Delivered Directly to scWAT in Mice

In order to avoid undesirable effects of BMP7, including bone formation, we sought a method to deliver BMP7 directly to scWAT depots in order to promote brown adipogenesis. To start, we employed silk microspheres, which were loaded with BMP7 or vehicle. *In vitro* BMP7 release rate from the microspheres measured by ELISA mimicked the dose we utilized to promote brown adipogenesis from progenitor cells in culture (Townsend et al., 2013). After optimization, *in vivo* studies were employed. Aqueous silk hydrogel solution was loaded with vehicle or BMP7 microspheres and sonicated in order to start the gelation process. While silk is kept cold, gelation is slow, but when the silk reaches body temperature gelation speeds up and allows the solution to firm itself in place at the site of delivery (**Supplementary Figure S1A**).

Surgical incisions above the flank/inguinal scWAT depot allowed delivery of the silk microspheres to the adipose. The right contralateral scWAT depot received BMP7 and the left contralatel depot received vehicle-loaded microspheres. Silk microsphere *in vitro* release kinetics are presented in **Supplementary Figure S1B** to the left. Skin temperature was compared between the left and right side 30 days after silk delivery, and 5 out of 6 mice had higher flank skin temperatures on the side that received BMP7 (**Supplementary Figure S1B**, right panel). Histological analysis of the scWAT depots at the conclusion of the study demonstrated an increase in multilocular (**Supplementary Figure S1C**) and UCP1-positive (**Supplementary Figure S1D**) cells in the depot that received BMP7.

Since the microsphere delivery method is more labor intensive and does not allow the silk to be injected inside the scWAT depot less invasively through the skin without a silk hydrogel carrier, we moved to loading BMP7 directly into a silk hydrogel solution. This approach also allows the particles to be delivered more homogeneously to the tissue, without settling of microspheres

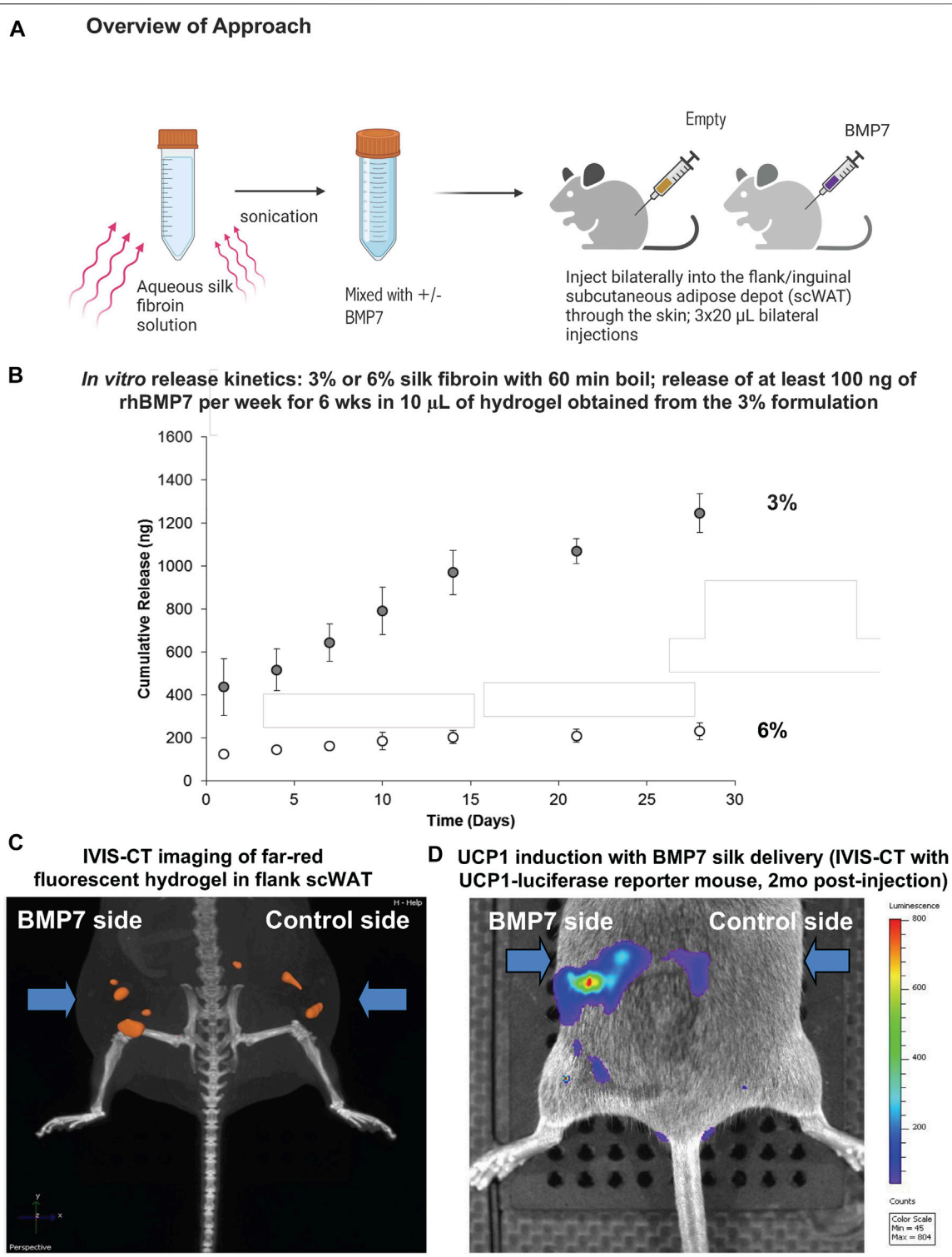

FIGURE 1 | Silk hydrogels for direct delivery of BMP7 to scWAT. **(A)** Overview of the approach: aqueous silk fibroin solution is mixed with either BMP7 or vehicle in advance. On the day of the injection, the solution is sonicated in order to start the gelation process. The hydrogel remains fluid when kept on ice. Injections are performed through the skin, and we deliver three 20uL volumes of hydrogel per side, distributed anterior to posterior along the flank adipose depot. When the hydrogel reaches body temperature, it gels into place. **(B)** *In vitro* release kinetics confirmed that BMP7-loaded silk hydrogel released the target of at least 100 ng rhBMP7 per week for a period of 6 weeks when using a 10 µL hydrogel sample (ELISA data for BMP7). Data reported is for a 20 µL hydrogel. The 3% silk hydrogel formulation achieves the desired release outcomes. **(C)** IVIS-CT imaging of a UCP1-Cre/Rosa-luciferase reporter mouse, showing the far-red fluorescence of the injected silk hydrogel in the flank scWAT depots bilaterally. Representative image from N = 3 mice. **(D)** IVIS-CT imaging of a UCP1-Cre/Rosa-luciferase reporter mouse, showing UCP1 induction on the BMP7 side only (highest expression in red), 2 months post-injection. Representative image from N = 3 mice.

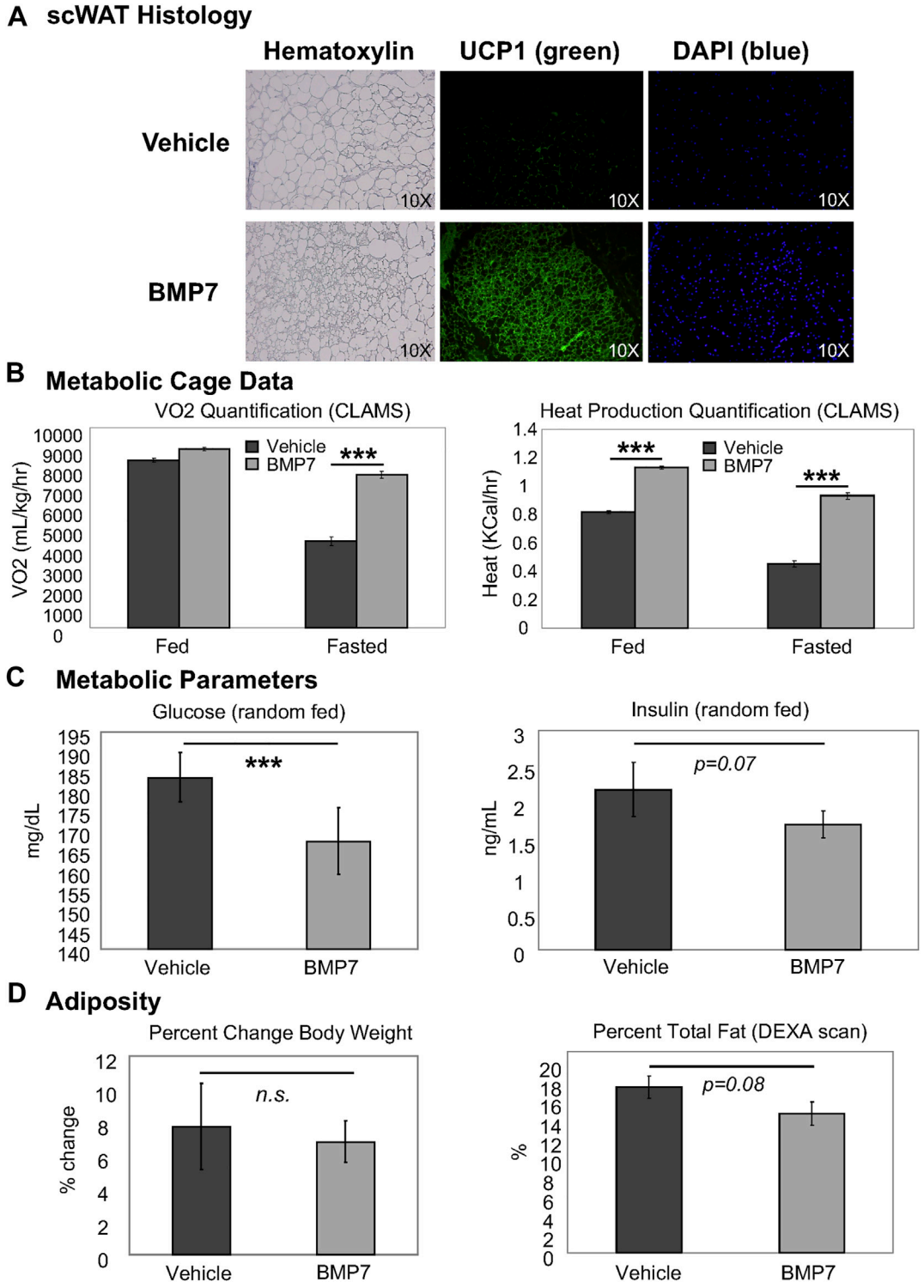

FIGURE 2 | BMP7 delivery to scWAT increases UCP1+ browning and improved metabolic parameters. **(A)** Mice treated with BMP7 hydrogel to the flank scWAT depot displayed adipose histology indiciative of 'browning', including increased presence of multilocular cells (hematoxylin, left panels) and UCP1 positive cells (green immunostaining, middle panels). DAPI (blue, far right panels) is used to show cell nuclei. For these studies, N = 6-8 mice per group (BMP7 or empty silk hydrogel) were used. **(B)** CLAMS metabolic cages were used to measure whole body energy utilization in mice treated with vehicle or BMP7-loaded silk hydrogel to scWAT. A significant increase in VO2 was observed in BMP7-treated mice in the fasted state only, but heat was higher for BMP7-treated mice in both the fed and fasted state. **(C)** ELISA assays were used to measure circulating glucose and insulin in random-fed animals, and glucose was significantly lower in BMP7-treated animals (left panel), while insulin showed a trend to be reduced (right panel). **(D)** Across the study, chow-fed animals showed no difference in body weight with BMP7 treatment (left panel), but a trend for reduced total adiposity (body fat measured in a DEXA scan; right panel).

into high-concentration areas. Similar to the microsphere experiment, the hydrogel solution is sonicated to begin the gelation process, followed by the addition of BMP7 into the pre-gelled solution, and direct injection through the skin to the flank scWAT depot (**Figure 1A**). Three 20 μL injections were delivered to each depot (anterior, mid, posterior in the flank depot). Hydrogel release kinetics were confirmed in preliminary studies via *in vitro* ELISA assays, with the target of releasing at least 100 ng of recombinant human BMP7 (rhBMP7) per week for a 6-week period per 10 μL hydrogel (**Figure 1B**). Initial tests in IVIS also confirmed that 1:100 was an optimal concentration (**Supplementary Figure S2**).

For initial pilot experiments, UCP1-Cre/Rosa-luficerase reporter mice were utilized (N = 3) and BMP7-loaded hydrogel was injected to the flank/inguinal scWAT, with vehicle-loaded hydrogel on the contralateral side. These hydrogels were fluorescent, which allowed us to visualize the silk placement *in vivo* using IVIS-CT intravital whole-animal imaging (**Figure 1C**). In addition to confirming that injections stayed in place in the scWAT depot, we were able to observe an increase in UCP1 induction via luciferase signal on the BMP7-treated side only, that persisted to 2-months post-injection (**Figure 1D**).

BMP7-Loaded Silk Hydrogel Delivered to scWAT Led to Browning and Improved Metabolic Parameters in Chow-Fed Mice

In chow-fed mice, BMP7 silk hydrogel treatment to scWAT led to increased multilocularity and UCP1 expression, including an increase in density of UCP1-positive cells, and increased cellularity as indicated by DAPI nuclear stain, per frame of view (**Figure 2A**). This indicated increased browning in the white fat with BMP7 treatment versus empty silk. Importantly, no bone formation was observed in any of the adipose depots receiving BMP7-loaded silk, and at day 20 after silk hydrogel injections circulating levels of hBMP7 measured by ELISA were undetectable (below the limit of detection for this assay's standard curve). In separate animals during initial proof of concept studies, a subset of injections went into the leg outside of the adipose tissue, and in these animals bone formation was observed, demonstrating BMP7 bioactivity and underscoring the importance of injections directly to scWAT to avoid off-target osteogenesis. In subsequent studies with adipose delivery of BMP7, no bone formation was ever observed visually or in histological sections.

In accordance with this increase in the presence of thermogenic, energy-expending cells, the BMP7-treated mice also had higher whole body energy expenditure, as measured by VO2 (fasted state only) and heat production (both fed and fasted states; **Figure 2B**). Random fed glucose was reduced in BMP7-treated mice (**Figure 2C**) without significantly affecting insulin levels, fitting with observations that increased brown fat activity improves glucose and insulin regulation and may have anti-diabetic effects. Finally, although BMP7-treated animals did not display a reduction in body weight, they did have a trend for decreased total fat mass, as measured in a DEXA scan (**Figure 2D**).

BMP7-Loaded Silk Hydrogel Improved Metabolic Health in Obese Mice Fed a High-Fat Diet

To examine whether BMP7-loaded silk hydrogel could counteract obesity and its sequelae, we fed mice with a high fat diet containing 45 kcal% fat for 3 months. BMP7 silk hydrogel delivery to scWAT at this obese timepoint led to reduced weight gain between days 28–45 of the treatment (**Figure 3A**, left panel, which resulted in an approximately 5% reduction in body weight across the study (**Figure 3A**, right panel). Early weight loss in both groups is attributed to the stress of handling and drug delivery and was not significantly different between BMP7 or vehicle treated mice. The overall weight loss due to BMP7 treatment was not due to changes in food intake (**Figure 3B**, left panel). Circulating glucose levels in the fasted state were significantly reduced in the BMP7-treated mice (**Figure 3B**, middle panel), but there was no difference in circulating insulin (**Figure 3B**, right panel). Energy expenditure as measured in CLAMS metabolic cages indicated increased VO2 in BMP7-treated animals in the fed state, and a reduction in respiratory exchange ration, or RER (**Figure 3C**). A reduction in RER from 1 to closer to 0.7 indicates a greater utilization of lipids as fuel, which would be expected with higher BAT activity.

DISCUSSION

Obesity and diabetes are currently global pandemics, and treatment options have thus far proven to be largely unsuccessful. Most pharmacological approaches or lifestyle modifications are met with limited success, as either side effects are high or adherence is low, respectively. Novel treatment strategies that could bypass the brain are also appealing, since many therapies targeting central appetite pathways lead to risky psychological effects. Since the rediscovery of metabolically active brown adipose tissue in adult humans, increasing the amount or activity of this thermogenic and energy-expending tissue offers an attractive way to offset the metabolic consequences of obesity and diabetes. Given its great capacity in utilizing glucose and lipids, enhanced BAT activity may be appealing for its anti-diabetic actions and improvements in metabolic phenotype, regardless of impacts on body weight and adiposity.

Given the success of silk hydrogels in delivering drugs, they also have numerous appealing characteristics for use in humans, including: eliciting minimal inflammatory response, being biocompatible and biodegradable (Li et al., 2003; Panilaitis et al., 2003; Meinel et al., 2005; Wang et al., 2008; Brown et al., 2015), representing a readily available natural resource, and existing as an FDA-approved biomaterial. Previously, silk microspheres have been used for encapsulation of BMP2 (Li et al., 2006), which remained bioactive after release and was able to induce osteogenesis of precursor cells. (BMP2 does not promote browning, but is a similar protein to BMP7.) In this study, we demonstrated that BMP7 delivery to scWAT of mice using a silk hydrogel provided an efficient means to promote browning and

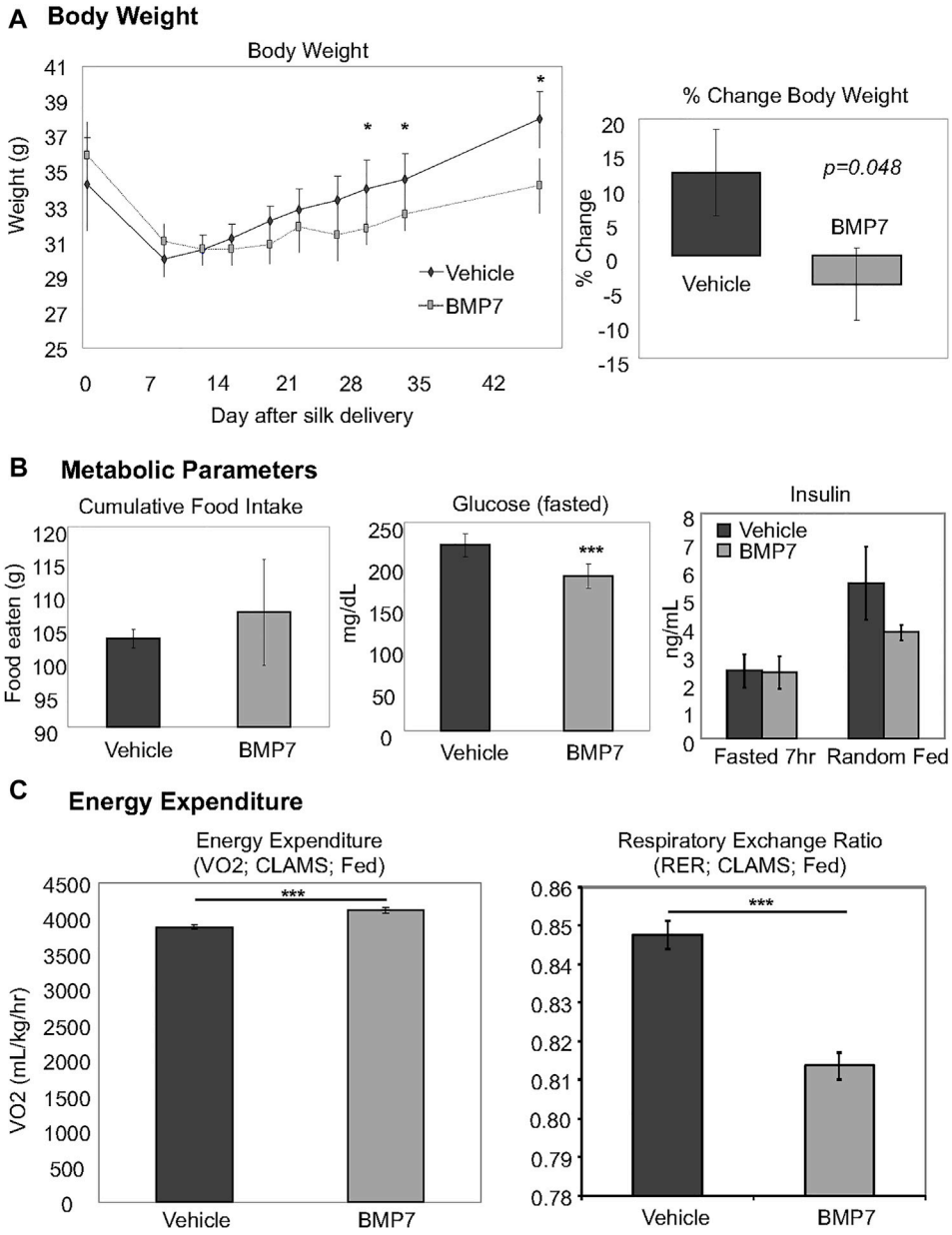

FIGURE 3 | Improved metabolism in obese mice treated with BMP7 hydrogels. **(A)** BMP7-treated mice fed a 45% high-fat diet for 3 months prior to hydrogel delivery lost more weight starting at 28–45 days post-injections. For these studies, N = 6-8 mice per group were used. **(B)** BMP7-treated mice did not change food intake across the study (left panel), and showed a significant reduction in fasted blood glucose levels (middle panel) with no changes in blood insulin (far right panel). **(C)** CLAMS data indicated an increase in VO2 and a decrease in RER in mice treated with BMP7 hydrogel. A reduction in RER from 1 to closer to 0.7 indicates a greater utilization of lipids as fuel, which would be expected with higher BAT activity.

an improved metabolic phenotype. BMP7 has been FDA approved under the Humanitarian Device Exemption for spinal fusion surgeries, and given its numerous beneficial effects on metabolism, BMP7 is a promising candidate for human browning induction. In fact, in all of our studies, including pilot studies leading up to these published data, we did not observe any bone formation in WAT after BMP7-delivery, and we consistenly observed browning and improvement in metabolic parameters.

The duration of BMP7s effects is currently unclear, but in UCP1-reporter mice we observed UCP1 induction on the BMP7-treated side 2 months later, and high-fat fed mice displayed weight loss at 1.5 months post-treatment. Clinical studies are required to determine the optimal dosage and duration in order to sustain weight loss effects and continued improvements in metabolism. Nevertheless, the proof-of-concept studies reported here pave the way to develop effective approaches for the treatment of obesity-related metabolic diseases. It may be that

humans need to receive numerous injections over time in order to sustain weight loss effects and continue to promote browning. Or, localized delivery of BMP7 may promote enough remodeling (browning and other effects) of the WAT, that systemic results are achieved through tissue cross-talk or release of BATokines to the circulation. Overall, the gradual weight loss we observed in these studies may be preferential to a more significant initial decline in adiposity, which could prevent the hypothalamus from establishing a new set point and drive up appetite counter-regulatory pathways; the more gradual weight loss we observe here could be more advantageous for longer-term sustainability. Future experiments can determine the duration of the effect and optimize treatment re-delivery strategies.

Finally, given that the research literature clearly demonstrates the importance of adipose innervation and nerve activation (in particular, norepinephrine release from adipose sympathetic nerve endings) for maintenance of UCP1-mediated thermogenesis, as well as research literature support for a neural plasticity role for BMPs (Jensen et al., 2021), we can not rule out the possibility that BMP7 is promoting innervation and neural activation of brown adipocytes after driving brown adipogenesis in scWAT. This would explain the sustained increase in energy expenditure that led to weight loss, without affecting appetite, and this would represent another benefit of BMP7 treatment, but it warrants further future exploration. In addition, further studies are needed to determine if silk-mediated BMP7 delivery is sufficient to prevent, as well as reverse, diet-induced obesity and to determine whether or not there are any potential long-term side effects. Silk hydrogel injections to scWAT through the skin may also be an avenue to deliver other treatments directly to adipose tissues, potentially as combinatorial therapies that help sustain tissue energy expenditure over longer periods.

CONCLUSION

In conclusion, we provide a translational approach to deliver bioactive BMP7 protein directly through the skin to scWAT as a means of promoting browning and increased thermogenic energy expenditure, with resulting improvements to metabolic health.

DATA AVAILABILITY STATEMENT

The original contributions presented in the study are included in the article/**Supplementary Material**, further inquiries can be directed to the corresponding authors.

ETHICS STATEMENT

The animal study was reviewed and approved by Joslin Diabetes Center IACUC.

AUTHOR CONTRIBUTIONS

KT conceived of the experiments, coordinated the multi-lab collaboration, designed experiments, collected and analyzed data and wrote the manuscript. EP, JC, and DK engineered the silk microspheres and hydrogels, tested *in vitro* BMP7 release, and provided the silk materials for the *in vivo* studies. YK and MB assisted with data collection and analysis. ML assisted with IVIS-CT imaging. Y-HT funded the experiments, designed experiments, and oversaw the project.

FUNDING

This work was supported in part by US National Institutes of Health (NIH) grants R01DK077097 (to Y-HT) and P30DK036836 (to Joslin Diabetes Center's Diabetes Research Center). KT was funded by grants NIH T32-DK007260-33 and NIH F32-DK091996 and a Junior Faculty Award from the American Diabetes Association (1-14-JF-55). DLK was funded by NIH P41EB027062.

ACKNOWLEDGMENTS

The authors would like to thank technical assistants in the Tseng, Townsend and Kaplan laboratories, including Lindsay MacDougall, Tian Lian Huang, and Sabrina DiPietro. We also thank the Joslin Specialized Assay Core for ELISA data and the Metabolic Phenotyping Core for CLAMS data.

SUPPLEMENTARY MATERIAL

The Supplementary Material for this article can be found online at: https://www.frontiersin.org/articles/10.3389/fbioe.2022.884601/full#supplementary-material

Supplementary Figure S1 | (A) Approach: Pilot data using silk microspheres pre-loaded with either vehicle or BMP7. Hydrogels were surgically implanted onto the flank scWAT depot, unilaterally. **(B)** In vitro release kinetics (measured by hBMP7 ELISA) for the silk microspheres is presented on the left panel. To the right, the skin surface temperature was measured using a flat Sable systems thermocouple probe, and 5 out of 6 mice displayed higher skin temperatures on the BMP7-treated side than the vehicletreated side. **(C)** On the side receiving BMP7-loaded silk microspheres, an increase in multilocular cells was observed in the scWAT (hematoxylin) versus the vehicle-treated side. **(D)** The multilocular cells observed in the BMP7-treated side were UCP1-positive (green immunostaining), indicating they are brown adipocytes.

Supplementary Figure S2 | (A) Transillumination biofluorescent imaging of DyLight800 in silk hydrogels injected through the skin to inguinal scWAT (unilateral on mouse right side), at 3 different concentrations ranging from 1 :10,000 to 1 :1000 and 1 :100. **(B)** Fluorescent tomography imaging of DyLight800 in silk hydrogels injected in the same mice as A, overlaid onto x-ray computed tomography to localize the signal in 3 dimensions in the adipose depot, confirming appropriate placement of the injection.

REFERENCES

Boon, M. R., van den Berg, S. A. A., Wang, Y., van den Bossche, J., Karkampouna, S., Bauwens, M., et al. (2013). BMP7 Activates Brown Adipose Tissue and Reduces Diet-Induced Obesity Only at Subthermoneutrality. *PLOS One* 8 (9), e74083. doi:10.1371/journal.pone.0074083

Boon, M. R., van der Horst, G., van der Pluijm, G., Tamsma, J. T., Smit, J. W. A., and Rensen, P. C. N. (2011). Bone Morphogenetic Protein 7: A Broad-Spectrum Growth Factor with Multiple Target Therapeutic Potency. *Cytokine & Growth Factor Rev.* 22 (4), 221–229. doi:10.1016/j.cytogfr.2011.08.001

Brown, J., Lu, C.-L., Coburn, J., and Kaplan, D. L. (2015). Impact of Silk Biomaterial Structure on Proteolysis. *Acta Biomater.* 11, 212–221. doi:10.1016/j.actbio.2014.09.013

Coburn, J. M., Na, E., and Kaplan, D. L. (2015). Modulation of Vincristine and Doxorubicin Binding and Release from Silk Films. *J. Control. Release* 220 (Pt A), 229–238. doi:10.1016/j.jconrel.2015.10.035

Diab, T., Pritchard, E. M., Uhrig, B. A., Boerckel, J. D., Kaplan, D. L., and Guldberg, R. E. (2012). A Silk Hydrogel-Based Delivery System of Bone Morphogenetic Protein for the Treatment of Large Bone Defects. *J. Mech. Behav. Biomed. Mater.* 11, 123–131. doi:10.1016/j.jmbbm.2011.11.007

Elsen, M., Raschke, S., Tennagels, N., Schwahn, U., Jelenik, T., Roden, M., et al. (2014). BMP4 and BMP7 Induce the White-To-Brown Transition of Primary Human Adipose Stem Cells. *Am. J. Physiology-Cell Physiology* 306 (5), C431–C440. doi:10.1152/ajpcell.00290.2013

Guziewicz, N. A., Massetti, A. J., Perez-Ramirez, B. J., and Kaplan, D. L. (2013). Mechanisms of Monoclonal Antibody Stabilization and Release from Silk Biomaterials. *Biomaterials* 34 (31), 7766–7775. doi:10.1016/j.biomaterials.2013.06.039

Guziewicz, N., Best, A., Perez-Ramirez, B., and Kaplan, D. L. (2011). Lyophilized Silk Fibroin Hydrogels for the Sustained Local Delivery of Therapeutic Monoclonal Antibodies. *Biomaterials* 32 (10), 2642–2650. doi:10.1016/j.biomaterials.2010.12.023

Herz, C. T., and Kiefer, F. W. (2019). Adipose Tissue Browning in Mice and Humans. *J. Endocrinol.* 241 (3), R97–R109. doi:10.1530/joe-18-0598

Hines, D. J., and Kaplan, D. L. (2011). Mechanisms of Controlled Release from Silk Fibroin Films. *Biomacromolecules* 12 (3), 804–812. doi:10.1021/bm101421r

Jensen, G. S., Leon-Palmer, N. E., and Townsend, K. L. (2021). Bone Morphogenetic Proteins (BMPs) in the Central Regulation of Energy Balance and Adult Neural Plasticity. *Metabolism* 123, 154837. doi:10.1016/j.metabol.2021.154837

Kluge, J. A., Li, A. B., Kahn, B. T., Michaud, D. S., Omenetto, F. G., and Kaplan, D. L. (2016). Silk-based Blood Stabilization for Diagnostics. *Proc. Natl. Acad. Sci. U.S.A.* 113 (21), 5892–5897. doi:10.1073/pnas.1602493113

Koolen, P. G. L., Haas, D., Kim, K., Fox, S., Ibrahim, A. M. S., Kim, P., et al. (2016). Increased Osteoid Formation in BMP-2-Loaded Silk-Based Screws. *Plastic Reconstr. Surg.* 137 (5), 808e–817e. doi:10.1097/prs.0000000000002080

Lavery, K., Hawley, S., Swain, P., Rooney, R., Falb, D., and Alaoui-Ismaili, M. H. (2009). New Insights into BMP-7 Mediated Osteoblastic Differentiation of Primary Human Mesenchymal Stem Cells. *Bone* 45 (1), 27–41. doi:10.1016/j.bone.2009.03.656

Li, C., Vepari, C., Jin, H.-J., Kim, H. J., and Kaplan, D. L. (2006). Electrospun Silk-BMP-2 Scaffolds for Bone Tissue Engineering. *Biomaterials* 27 (16), 3115–3124. doi:10.1016/j.biomaterials.2006.01.022

Li, M., Ogiso, M., and Minoura, N. (2003). Enzymatic Degradation Behavior of Porous Silk Fibroin Sheets. *Biomaterials* 24 (2), 357–365. doi:10.1016/s0142-9612(02)00326-5

Lovett, M. L., Wang, X., Yucel, T., York, L., Keirstead, M., Haggerty, L., et al. (2015). Silk Hydrogels for Sustained Ocular Delivery of Anti-vascular Endothelial Growth Factor (Anti-VEGF) Therapeutics. *Eur. J. Pharm. Biopharm.* 95 (Pt B), 271–278. doi:10.1016/j.ejpb.2014.12.029

Luo, G., Hofmann, C., Bronckers, A. L., Sohocki, M., Bradley, A., and Karsenty, G. (1995). BMP-7 Is an Inducer of Nephrogenesis, and Is Also Required for Eye Development and Skeletal Patterning. *Genes Dev.* 9 (22), 2808–2820. doi:10.1101/gad.9.22.2808

Meinel, L., Hofmann, S., Karageorgiou, V., Kirker-Head, C., McCool, J., Gronowicz, G., et al. (2005). The Inflammatory Responses to Silk Films *In Vitro* and *In Vivo*. *Biomaterials* 26 (2), 147–155. doi:10.1016/j.biomaterials.2004.02.047

Okla, M., Wang, W., Kang, I., Pashaj, A., Carr, T., and Chung, S. (2015). Activation of Toll-like Receptor 4 (TLR4) Attenuates Adaptive Thermogenesis via Endoplasmic Reticulum Stress. *J. Biol. Chem.* 290 (44), 26476–26490. doi:10.1074/jbc.m115.677724

Panilaitis, B., Altman, G. H., Chen, J., Jin, H.-J., Karageorgiou, V., and Kaplan, D. L. (2003). Macrophage Responses to Silk. *Biomaterials* 24 (18), 3079–3085. doi:10.1016/s0142-9612(03)00158-3

Pritchard, E. M., Hu, X., Finley, V., Kuo, C. K., and Kaplan, D. L. (2013). Effect of Silk Protein Processing on Drug Delivery from Silk Films. *Macromol. Biosci.* 13 (3), 311–320. doi:10.1002/mabi.201200323

Pritchard, E. M., Valentin, T., Panilaitis, B., Omenetto, F., and Kaplan, D. L. (2013). Antibiotic-Releasing Silk Biomaterials for Infection Prevention and Treatment. *Adv. Funct. Mat.* 23 (7), 854–861. doi:10.1002/adfm.201201636

Rockwood, D. N., Preda, R. C., Yücel, T., Wang, X., Lovett, M. L., and Kaplan, D. L. (2011). Materials Fabrication from *Bombyx mori* Silk Fibroin. *Nat. Protoc.* 6 (10), 1612–1631. doi:10.1038/nprot.2011.379

Roesler, A., and Kazak, L. (2020). UCP1-independent Thermogenesis. *Biochem. J.* 477 (3), 709–725. doi:10.1042/bcj20190463

Saini, S., Duraisamy, A. J., Bayen, S., Vats, P., and Singh, S. B. (2015). Role of BMP7 in Appetite Regulation, Adipogenesis, and Energy Expenditure. *Endocrine* 48 (2), 405–409. doi:10.1007/s12020-014-0406-8

Schellen, L., Loomans, M. G. L. C., de Wit, M. H., Olesen, B. W., and Lichtenbelt, W. D. v. M. (2012). The Influence of Local Effects on Thermal Sensation under Non-uniform Environmental Conditions - Gender Differences in Thermophysiology, Thermal Comfort and Productivity during Convective and Radiant Cooling. *Physiology Behav.* 107 (2), 252–261. doi:10.1016/j.physbeh.2012.07.008

Shen, X., Zhang, Y., Gu, Y., Xu, Y., Liu, Y., Li, B., et al. (2016). Sequential and Sustained Release of SDF-1 and BMP-2 from Silk Fibroin-Nanohydroxyapatite Scaffold for the Enhancement of Bone Regeneration. *Biomaterials* 106, 205–216. doi:10.1016/j.biomaterials.2016.08.023

Shi, P., Abbah, S. A., Saran, K., Zhang, Y., Li, J., Wong, H.-K., et al. (2013). Silk Fibroin-Based Complex Particles with Bioactive Encrustation for Bone Morphogenetic Protein 2 Delivery. *Biomacromolecules* 14 (12), 4465–4474. doi:10.1021/bm401381s

Sidossis, L. S., Porter, C., Saraf, M. K., Børsheim, E., Radhakrishnan, R. S., Chao, T., et al. (2015). Browning of Subcutaneous White Adipose Tissue in Humans after Severe Adrenergic Stress. *Cell Metab.* 22 (2), 219–227. doi:10.1016/j.cmet.2015.06.022

Townsend, K. L., An, D., Lynes, M. D., Huang, T. L., Zhang, H., Goodyear, L. J., et al. (2013). Increased Mitochondrial Activity in BMP7-Treated Brown Adipocytes, Due to Increased CPT1- and CD36-Mediated Fatty Acid Uptake. *Antioxidants Redox Signal.* 19 (3), 243–257. doi:10.1089/ars.2012.4536

Townsend, K. L., Madden, C. J., Blaszkiewicz, M., McDougall, L., Tupone, D., Lynes, M. D., et al. (2017). Reestablishment of Energy Balance in a Male Mouse Model with POMC Neuron Deletion of BMPR1A. *Endocrinology* 158 (12), 4233–4245. doi:10.1210/en.2017-00212

Townsend, K. L., Suzuki, R., Huang, T. L., Jing, E., Schulz, T. J., Lee, K., et al. (2012). Bone Morphogenetic Protein 7 (BMP7) Reverses Obesity and Regulates Appetite through a Central mTOR Pathway. *FASEB J.* 26 (5), 2187–2196. doi:10.1096/fj.11-199067

Townsend, K. L., and Tseng, Y.-H. (2014). Brown Fat Fuel Utilization and Thermogenesis. *Trends Endocrinol. Metabolism* 25 (4), 168–177. doi:10.1016/j.tem.2013.12.004

Tseng, Y.-H., Kokkotou, E., Schulz, T. J., Huang, T. L., Winnay, J. N., Taniguchi, C. M., et al. (2008). New Role of Bone Morphogenetic Protein 7 in Brown Adipogenesis and Energy Expenditure. *Nature* 454 (7207), 1000–1004. doi:10.1038/nature07221

Vukicevic, S., Basic, V., Rogic, D., Basic, N., Shih, M. S., Shepard, A., et al. (1998). Osteogenic Protein-1 (Bone Morphogenetic Protein-7) Reduces Severity of Injury after Ischemic Acute Renal Failure in Rat. *J. Clin. Invest.* 102 (1), 202–214. doi:10.1172/jci2237

Wang, X., Yucel, T., Lu, Q., Hu, X., and Kaplan, D. L. (2010). Silk Nanospheres and Microspheres from Silk/pva Blend Films for Drug Delivery. *Biomaterials* 31 (6), 1025–1035. doi:10.1016/j.biomaterials.2009.11.002

Wang, Y., Rudym, D. D., Walsh, A., Abrahamsen, L., Kim, H. J., Kim, H. S., et al. (2008). *In Vivo* degradation of Three-Dimensional Silk Fibroin Scaffolds. *Biomaterials* 29 (24-25), 3415–3428. doi:10.1016/j.biomaterials.2008.05.002

White, A. P., Vaccaro, A. R., Hall, J. A., Whang, P. G., Friel, B. C., and McKee, M. D. (2007). Clinical Applications of BMP-7/OP-1 in Fractures, Nonunions and Spinal Fusion. *Int. Orthop.* 31 (6), 735–741. doi:10.1007/s00264-007-0422-x

Zhang, L., Herrera, C., Coburn, J., Olejniczak, N., Ziprin, P., Kaplan, D. L., et al. (2017). Stabilization and Sustained Release of HIV Inhibitors by Encapsulation in Silk Fibroin Disks. *ACS Biomater. Sci. Eng.* 3 (8), 1654–1665. doi:10.1021/acsbiomaterials.7b00167

Zhang, W., Zhu, C., Zhu, C., Wu, Y., Ye, D., Wang, S., et al. (2014). VEGF and BMP-2 Promote Bone Regeneration by Facilitating Bone Marrow Stem Cell Homing and Differentiation. *eCM* 27, 1–12. doi:10.22203/ecm.v027a01

Conflict of Interest: The authors declare that the research was conducted in the absence of any commercial or financial relationships that could be construed as a potential conflict of interest.

Publisher's Note: All claims expressed in this article are solely those of the authors and do not necessarily represent those of their affiliated organizations, or those of the publisher, the editors and the reviewers. Any product that may be evaluated in this article, or claim that may be made by its manufacturer, is not guaranteed or endorsed by the publisher.

Copyright © 2022 Townsend, Pritchard, Coburn, Kwon, Blaszkiewicz, Lynes, Kaplan and Tseng. This is an open-access article distributed under the terms of the Creative Commons Attribution License (CC BY). The use, distribution or reproduction in other forums is permitted, provided the original author(s) and the copyright owner(s) are credited and that the original publication in this journal is cited, in accordance with accepted academic practice. No use, distribution or reproduction is permitted which does not comply with these terms.

frontiers | Frontiers in Bioengineering and Biotechnology

REVIEW
published: 15 June 2022
doi: 10.3389/fbioe.2022.851660

Hydrogel Development for Rotator Cuff Repair

Zhengyu Xu[1†], *Yifei Fang*[1†], *Yao Chen*[1], *Yushuang Zhao*[1], *Wei Wei*[1,2*] *and Chong Teng*[1*]

[1]*Department of Orthopaedics, The Fourth Affiliated Hospital, Zhejiang University School of Medicine, Yiwu, China,* [2]*Key Laboratory of Tissue Engineering and Regenerative Medicine of Zhejiang Province, Dr. Li Dak Sum & Yip Yio Chin Center for Stem Cells and Regenerative Medicine, Zhejiang University School of Medicine, Hangzhou, China*

Rotator cuff tears (RCTs) are common in shoulder disease and disability. Despite significant advances in surgical repair techniques, 20–70% of patients still have postoperative rotator cuff dysfunction. These functional defects may be related to retear or rotator cuff quality deterioration due to tendon retraction and scar tissue at the repair site. As an effective delivery system, hydrogel scaffolds may improve the healing of RCTs and be a useful treatment for irreparable rotator cuff injuries. Although many studies have tested this hypothesis, most are limited to laboratory animal experiments. This review summarizes differences in hydrogel scaffold construction, active ingredients, and application methods in recent research. Efforts to determine the indications of hydrogel scaffolds (with different constructions and cargos) for various types of RCTs, as well as the effectiveness and reliability of application methods and devices, are also discussed.

Keywords: hydrogel, rotator cuff, tissue engineering, regeneration medicine, cytokine

OPEN ACCESS

Edited by:
Bruce Alan Bunnell,
University of North Texas Health Science Center, United States

Reviewed by:
Huacheng He,
Wenzhou University, China
Giovanni Vozzi,
University of Pisa, Italy
Ahmed El-Fiqi,
Dankook University, South Korea

****Correspondence:***
Wei Wei
zjewwei@zju.edu.cn
Chong Teng
tengchong1984@zju.edu.cn

†These authors have contributed equally to this work

Specialty section:
This article was submitted to Tissue Engineering and Regenerative Medicine, a section of the journal Frontiers in Bioengineering and Biotechnology

Received: *10 January 2022*
Accepted: *31 May 2022*
Published: *15 June 2022*

Citation:
Xu Z, Fang Y, Chen Y, Zhao Y, Wei W and Teng C (2022) Hydrogel Development for Rotator Cuff Repair. Front. Bioeng. Biotechnol. 10:851660. doi: 10.3389/fbioe.2022.851660

1 INTRODUCTION

The rotator cuff is a complex of the supraspinatus, teres minor, infraspinatus, and subscapularis muscles and their tendons. They form a cuff-like structure around the humerus head and coordinate to complete complex shoulder movements (Craig et al., 2017). Rotator cuff injury and especially tear tends to occur with extrinsic factors such as age, trauma and strain, as well as intrinsic factors such as tendon degeneration, insufficient blood supply, and subacromial impingement (Nho et al., 2008; Yadav et al., 2009). This can lead to shoulder pain, reduced strength, and motion range restriction (Chakravarty and Webley, 1993; Colvin et al., 2012).

Rotator cuff tears (RCTs) require surgical repair, and outcomes have continuously improved with the development of medical techniques (Gurnani et al., 2015; Deprés-tremblay et al., 2016). Most patients have pain relief and improved shoulder function following surgery, but 20–70% complain about postoperative function (Tashjian et al., 2010; Koh et al., 2011; Toussaint et al., 2011). Some patients' disability may be related to rotator cuff retear that appears as discontinuity on magnetic resonance imaging; however, patients with intact structures can still present dysfunction and weakness that may be related to tendon unit retraction, scar insertion, and adipose infiltration (Goutallier et al., 1994; Liem et al., 2007; Sugaya et al., 2007; Kuzel et al., 2013). Therefore, the "healing" concept of rotator cuff repair should be defined more prudently and include structural integrity and functionality.

Most RCTs occur at the tendon-bone interface where the surgery reconstruction takes place (Thorsness and Romeo, 2016; Oh et al., 2018), and this site is the key for rotator cuff healing (Li et al., 2019; Chae et al., 2020; Huang et al., 2020). For better understanding of the rotator cuff healing process, we need more knowledge about the histological structure. The tendon-bone interface is a gradient region that includes the tendon, uncalcified fibrocartilage, calcified fibrocartilage, and bone

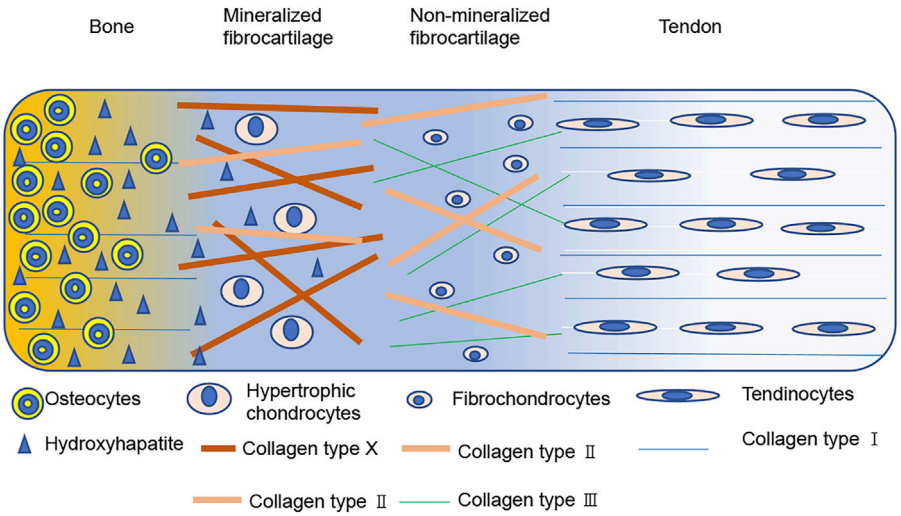

FIGURE 1 | Diagram of the four zones at the bone-tendon interface.

with different cells, structures, and mechanical aspects (Bonnevie and Mauck, 1545). The tendinocytes are distributed in the tendon tissue and contain type I collagen, while fibrochondrocytes are arranged along the long axis of collagen fibers and distributed in the non-mineralized fibrocartilage containing types I, II, and III collagen. Hypertrophic chondrocytes arranged in a columnar pattern exist in the mineralized fibrocartilage and contain type I, II, and X collagen. Finally, osteocytes, osteoblasts, and osteoclasts can be seen in bone and contain type I collagen (**Figure 1**). In addition, mineral contents and proteoglycan species vary among the different regions, and this natural heterogeneity results in varied mechanical and biological properties of the interface tissue, effectively reducing stress and allowing loads to be transferred from the tendon to the bone (Spalazzi et al., 1932; Rossetti et al., 1476).

Increasing attention has been paid to the application of interfacial tissue engineering for rotator cuff injury repair. Engineered interfacial tissue is mainly composed of seed cells, growth factors, and biomaterials. Seed cells provide the source of regeneration of the defect tissue through migration, adhesion, proliferation, and differentiation (Park et al., 2016; Liu et al., 2019). Growth factors regulate specific signaling pathways to affect a variety of cell behaviors (Prabhath et al., 2018; Han et al., 2020). Biomaterials serve as bridges that can provide a suitable growth environment for seed cells and growth factors to interact (Zhao et al., 2017; Chae et al., 2020; Veronesi et al., 2020).

Hydrogel is a 3D network structure of hydrophilic polymer chains (Oliva et al., 2017; Dimatteo et al., 2018). The polymer system of hydrogel scaffolds provides a good substrate with potential for cell transplantation and differentiation, endogenous regeneration, biological repair, and continuous delivery of growth factors and active substances (Ma et al., 2018; Tang et al., 2018; Marycz et al., 2019). In order to promote tendon-bone interface healing for rotator cuff repair, these hydrogel scaffolds should meet several requirements. First, they must reproduce the multi-regional structure of tissue interface as much as possible, including matrix composition, microstructure, and mechanical characteristics. Second, scaffolds can support the adhesion, proliferation, and differentiation of specific phenotypes of different stem cells or progenitor cells. Thirdly, scaffolds should be degradable at a rate is similar to the tissue regeneration rate to continue releasing physiological load. Finally, the scaffold design should also consider clinical use and match with the corresponding reconstructive surgery.

2 CLASSIFICATIONS AND CHARACTERIZATION OF HYDROGELS APPLIED IN ROTATOR CUFF REPAIR

2.1 Classification of Hydrogels

Hydrogels is a big class of biomaterials and can be classified according to different bases. The first one is whether their source is natural or synthetic. Natural hydrogels are obtained from plants or animals consisting of proteins and polysaccharides. They usually have good biocompatibility and biodegradability but poor mechanical strength. In recent years, synthetic hydrogels have gradually replaced natural hydrogels as they have better water absorption capacity, greater strength, and longer service life. However, synthetic hydrogels are inferior to natural ones in biological recognition, intercellular response, and cell-induced remodeling. Nichol et al. invented a hydrogel called gelatin methacryloyl (GelMA) that is a hybrid consisting of gelatin and methacryloyl (Nichol et al., 2010). Its biocompatibility is much better than gelatin and is similar to collagen, but with better formability. In the repair of rotator cuff injury, it is often used as a therapeutic substance carrier in rotator cuff injury repair (Cao et al., 2020; Huang et al., 2021). Another hydrogel classification is based on polymer constituents. Homopolymer hydrogels are derived from a single species of hydrophilic polymer or copolymer. Multipolymers hydrogels consist of two independent polymers or interpenetrating polymer networks. Besides, hydrogels can be

TABLE 1 | Hydrogel classification.

Source	Natural Synthetic	Collagen, Gelatin, Chitosan, Hyaluronic acid, N-isopropyl Acrylamide (PNIPAM), Polyethylene Glycol (PEG), PoloxamerEtc.
Preparation	Homopolymer	A single species of polymer or copolymer
	Multipolymer	Two independent crosslinked components
Response	Chemical	pH response, oxidant response, glucose response
	Physical	Temperature response, pressure response, light response
	Biochemical	Enzyme response, ligand response, antigen response

TABLE 2 | Overview of hydrogels applied for rotator cuff repair.

Hydrogel Name (Abbreviation)	Hydrogel Features/Advantages for Rotator Cuff Repair Engineering	Limitations	Refs
Gelatin hydrogel	Biodegradable, thermo-responsive, elastic, injectable	Poor mechanical properties faster degradation rate	Tokunaga et al. (2015a); Tokunaga et al. (2015b); Kabuto et al. (2015); Tokunaga et al. (2017)
Collagen hydrogel	Natural ECM protein, reasonable biomechanical properties, injectable	Limited number of functional groups for crosslinking	Hee et al. (2011); Jiang et al. (2020)
Fibrin hydrogel	Easy to be functionalized impressive stiffness, injectable	Immune response	Janmey et al. (2009); Rothrauff et al. (2019); Jiang et al. (2020)
Gelatin methacryloyl hydrogel (GelMA)	Self-sterilization, low cost, Photopolymerized, high compatibility, injectable	poor tissue adhesivity	Rothrauff et al. (2019); Cao et al. (2020); Huang et al. (2021)
Hyaluronic acid hydrogel (HA)	Biocompatible, biodegradable, noncytotoxic, nonimmunogenic	Do not support cell attachment	Lin et al. (2021)
Alginate hydrogel	Quick cross-linking, mechanically strong	Non-biodegradable and elicit immunological responses	Thankam et al. (2021)
Chitosan hydrogel	Therapeutic substance delivery capacity, injectable	Low solubility and high viscosity	Funakoshi et al. (2005)
Chitosan-4-thiobutylamidine hydrogel (CS-TBA)	Biocompatible, highly absorbent, injectable, structurally similar to natural ECM	Low solubility, high viscosity, difficult for preparation	Teng et al. (2021)
Human tendon-derived collagen hydrogel (tHG)	Thermo-responsive, injectable, type I collagen-rich	xenogeneic immune response	Kaizawa et al. (2019a); Kaizawa et al. (2019b)
Ion-based hydrogels	Anti-inflammatory	Rapid ion release rate	Chen et al. (2021); Yang et al. (2021)
Polyethylene glycol diacrylate (PEGDA)	Biocompatible, degradable, Easily manipulated, non-immunogenic, injectable	Limited microenvironment control, Poor toughness	Chen et al. (2011)
Polyvinyl alcohol (PVA)	Mechanically strong, MSC chondrogenic differentiation	Biologically inert	Thankam et al. (2021)
Poly-lactic-co-glycolic acid (PLGA)	Biocompatibility, easy handling, Similar mechanical properties with tendon	potential toxicity from dose dumping, inconsistent drug release and drug-polymer interactions	Moffat et al. (2009); Xie et al. (2010)

classified based on whether they could responsive to environmental stimuli such as temperature, pH values, light, ionic strength, and magnetic fields. For example, ultraviolet light can stimulate the curing reaction of GelMA and form a three-dimensional structure suitable for cell growth and differentiation with good strength that provides a suitable extracellular microenvironment for stem cells used in rotator cuff repair (Cao et al., 2020). The classification types are shown in **Table 1**.

2.2 Characterization of Hydrogels Applied in Rotator Cuff Repair

The main characterizations of hydrogels include swelling, self-healing, degradation and biocompatibility abilities. The physicochemical properties of hydrogels must be considered for appropriate application in rotator cuff repair. Stem cell differentiation, the loading of active substances and cytokines, and mimicking the multilayer structure of tendon-bone interface

are all critical issues. The characterization and properties of hydrogels applied for rotator cuff repair are summarized in **Table 2**.

2.2.1 Physicochemical Properties

Physicochemical properties such as swelling and stiffness are basic characteristics of hydrogels. Swelling property comes from hydrophilic groups such as hydroxyl and carboxyl groups in the polymer networks (Cui et al., 2019). The hydrogel is hydrated in water, allowing soluble molecules to enter the gel and remain stable, eventually reaching a state of equilibrium. Hydrogen bonds formed between hydrophilic groups and water molecules in the polymer chains can stabilize the hydrogel structure and effectively encapsulate active substances. In the case of rotator cuff injury, the hydrogel can be used to load cytokines, active substances, or even stem cells to promote rotator cuff healing. Hydrogel stiffness is also crucial for cell function and differentiation. Pelham and Wang first claimed that the stiffness of biomimetic extracellular matrix (ECM) molecules could be a key factor in regulating cell shape, motility, and spreading (Pelham and Wang, 1998). Self-healing hydrogel could fuse together after being broken into fragments due to new bonds spontaneously formed. Since rotator cuff repair surgery is mostly performed arthroscopically, the hydrogel must have good rheological and mechanical properties. Some hydrogels can be injected through a tube or syringe with no performance change (Patil et al., 2018).

2.2.2 Biodegradation and Biocompatibility

The degradation process of hydrogel must meet biological requirements. *In vivo* degradation should be considered during hydrogel preparation. The ideal preparation method must meet basic requirements for *in vivo* use, including no introduction of small molecule cross-linking agents and mild cross-linking without toxic by-products, (Huebsch et al., 2010; Toh et al., 2012; Toda et al., 2016). In addition to the physicochemical properties and functions of existing hydrogels, residual functional groups (not involved in network crosslinking) can be used to imbue different hydrogel functions. These groups can be added directly to the hydrogel to avoid adding these substances to the cell culture medium. Despite these advantages, covalent bonding is complex and more likely to produce toxic small molecules. This is due to purification techniques and insufficient degradation of cross-linked groups, which must be taken into account when designing hydrogel precursors. In general, materials using physically linked thermo-gelling and cryo-gelling showed low cytotoxicity compared to traditional photopolymerized hydrogels (Park et al., 2016).

The biomechanical stability of hydrogels is critical for therapy cargo reasonable release. Natural hydrogel's biomechanical stability is poorer than the synthetic biomaterial hydrogel for which is always damaged by cellular enzyme. However, there are also some studies to improve the biomechanical stability of hydrogels by modifying the hydrogels from natural sources. Shi et al. add bisphosphonates (BPs) into hyaluronan (HA) and they find it`s enzymatic degradation rate is lower than the control HA hydrogel *in vitro*. The mechanism may be that the covalent incorporation between BPs and HA increases the hydrogel`s stiffness compared to the unmodified HA hydrogel. (Shi et al., 2018). Lee et al. find that the hyaluronidase inhibition activity can be inhibited by TA (tannic acid) and the HA-TA hydrogels' enzymatic stability is significantly increased when compared with the control group (Lee et al., 2018).

Natural polymers (chitosan, collagen, alginate) and synthetic polymers (polylactic acid [PLA], polylactic hydroxyacetic acid [PLGA]) have been widely used in drug delivery for their biocompatibility, mechanical properties, and ease of handling. Synthetic hydrogels are robust and provide stability, repeatability and acceptability of cells for microenvironments. Material modification can promote cell adhesion and differentiation and maintain multiple potentials. For example, amino acids and bromo groups can promote the transformation of adipose-derived stem/stromal cells (ADSCs) into bone cells and adipose cells, respectively (Benoit et al., 2008; Liu et al., 2013). Phenyl and sulfhydryl groups have the potential to promote ADSC differentiation into chondrocytes (Ingber, 2003). Excipients can be added by manipulating the functional groups of hydrogel precursors to guide cell behavior and differentiation.

2.2.3 Mechanical Properties

As the delivery system for the therapy cells, hydrogels mechanical properties are the critical parameters which regulate mechanotransduction signal-mediated cellular behaviors (Sieminski et al., 2007; Huebsch and Mooney, 2009). For example, the cell behaviors were widely regulated by the substrate stiffness (Wen et al., 2014). Most type of cells benefit from stiffer substrates for more organized cytoskeletons. Mechanical stimulation can induce MSCs to differentiate into tendon-bone cell lineage which is critical for rotator cuff repair (Visser et al., 2015).

Hydrogel scaffold used for rotator cuff repair and augmentation should meet the native biomechanical properties. Kristen et al. report that their PLGA scaffold has the similar mechanical properties with the tendon. The tensile modulus of the unaligned and aligned scaffolds averaged 107 and 341 MPa, respectively, while the mean ultimate tensile strength ranging from 3.7 to 12.0 MPa (Moffat et al., 2009).

For mild rotator cuff lesion, patients prefer conservative treatment. Therefore, these injectable hydrogels as the carrier of therapy cargos and cells have a good prospect for clinical application. Natural injectable hydrogels including collagen, fibrin, gelatin, chitosan. They usually have good biocompatibility while limited in the mechanical prosperity and immune response (**Table 2**). Synthetic biomaterial hydrogels such as PEGDA have better tunability, almost no immune response and stronger mechanical properties.

3 THE FUNCTIONS OF HYDROGEL USED IN ROTATOR CUFF REPAIR

Hydrogels can serve as delivery systems to carry multiple therapeutic components including Anti-inflammatory cargos,

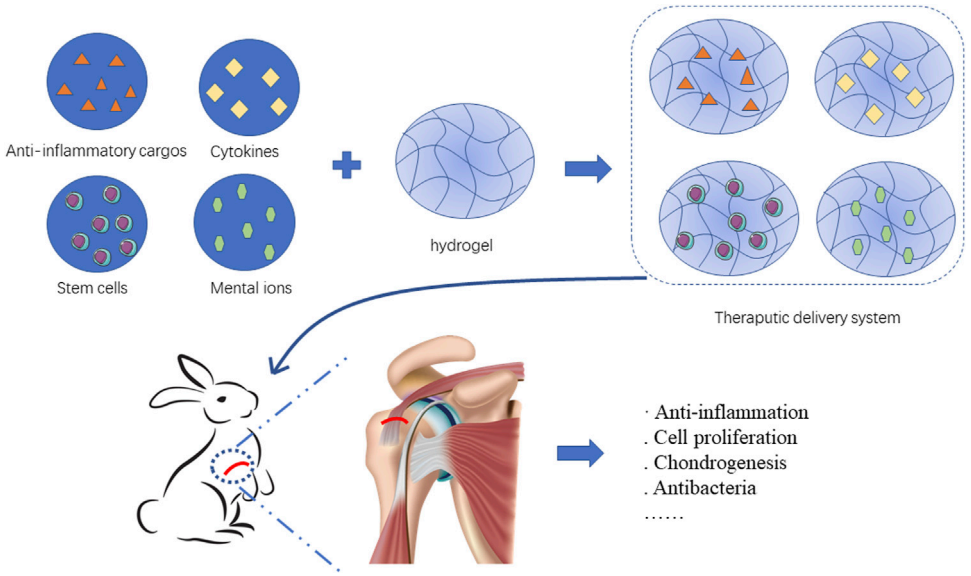

FIGURE 2 | Hydrogels load therapeutic cargos such as Anti-inflammatory cargos, cytokines, stem cells and mental ions to facilitate rotator cuff healing.

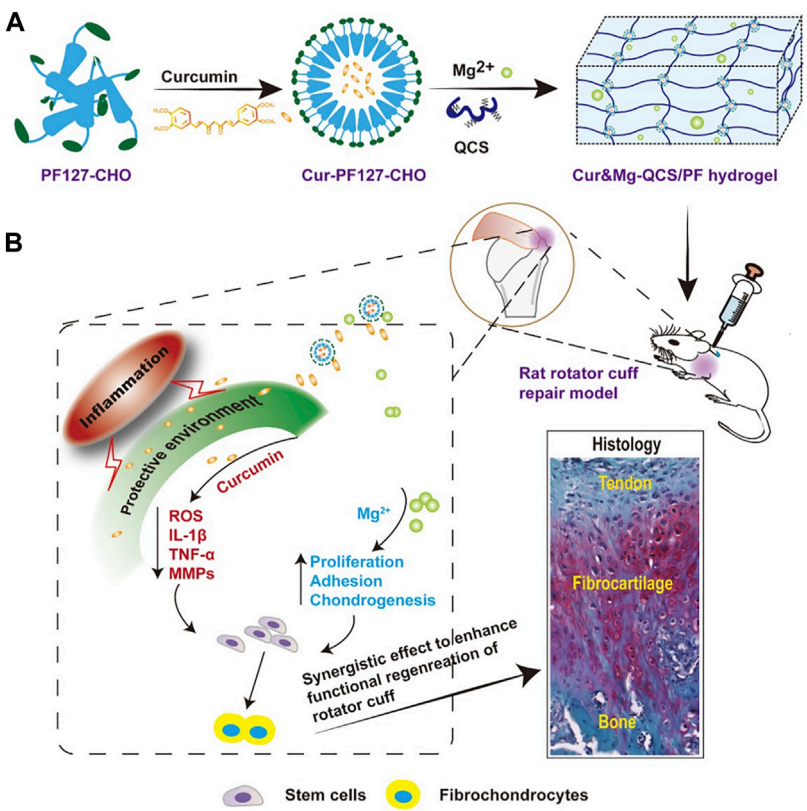

FIGURE 3 | (A) Synthesis of Cur&Mg-QCS/PF hydrogels. **(B)** *In vivo* application and evaluation of Cur&Mg-QCS/PF hydrogels. (Reprinted from (Lin et al., 2021) with permission from Theranostics).

cytokines, stem cells and mental ions. These cargos benefit rotator cuff healing by different pattern such as anti-inflammation, cell proliferation, and chondrogenesis. (**Figure 2**).

3.1 Anti-Inflammatory Effects *via* its Therapeutic Cargo

Acute inflammation is the natural response in the early state of rotator cuff injury, while chronic inflammation is a major cause of rotator cuff quality deterioration, non-healing, or re-tearing after repair. Inhibiting chronic inflammation is an effective means to improve rotator cuff quality, promote healing, and prevent retear after surgical repair (Childress et al., 2013; Kuo et al., 1932). The hydrogel itself, such as HA or methacrylated collagen hydrogel or its therapeutic cargo, such as farnesol and curcumin, can be used to inhibit chronic inflammation after rotator cuff repair.

Matrix metalloproteinases (MMPs) are calcium and zinc dependent proteinases that break down ECM proteins. Elevated levels of metalloproteinases have been correlated with several inflammatory states including delayed healing wounds, malignant tumors and rotator cuff tears. In patients with massive rotator cuff tears, high levels of MMPs are found in the synovial fluid samples from glenohumeral joints (Jacob et al., 2012; Shih et al., 2018). With the goal of achieving inherent and long-term MMP regulation, Liang et al. developed an methacrylated collagen-HA hydrogel with controlled enzymatic degradability for MMP regulation. This novel strategy provides new insight into the hydrogel design for rotator cuff repair (Liang et al., 2018).

Farnesol is a sesquiterpene compound from fruits that exerts anti-inflammatory and antioxidative effects and promotes the synthesis of collagen. Lin et al. designed farnesol containing hydrogel membranes based on gellan gum and HA. The membranes could swell rapidly and adhere to the tear site, acting as a barrier and farnesol source during the repair period. Results indicated that farnesol enhanced collagen production and the hydrogel membranes was promising in the repair of rotator cuff injuries (Lin et al., 2021).

Curcumin is a natural compound with favorable anti-inflammatory properties. Chen et al. developed a novel hydrogel termed Cur&Mg-QCS/that could release curcumin in a controlled and highly efficient manner (Chen et al., 2021). The synthesis pathways is demonstrated in **Figure 3A**. Curcumin released at the repair site provided appropriate extracellular environment for stem cells by exerting antioxidative and anti-inflammatory effects to regulate levels of reactive oxygen species, IL-1β, TNF-α, and MMPs (**Figure 3B**).

3.2 Cytokine Delivery System

Cytokines are small peptides or glycoproteins produced by a variety of tissue cells. Cytokines include vascular endothelial growth factor (VEGF), transforming growth factor (TGF)-β, platelet-derived growth factor (PDGF), epidermal growth factor (EGF), and insulin-like growth factor (IGF). Cytokines can mediate cellular interactions and promote cell growth, collagen deposition, and angiogenesis to facilitate rotator cuff injury repair (Wu et al., 2017). Effectively transporting cytokines to the injury rotator cuff has become a research focus. The ideal delivery system should be easy to use, non-toxic, and biocompatible.

Arimura et al. confirmed that loading TGF-β1 with gelatin hydrogel inhibited MMP-9 and MMP-13 expression, thus increasing collagen accumulation and enhancing the formation of tough fibrous tissue at the healing site (Arimura et al., 2017). Fibroblast growth factor 2 (FGF-2) can improve rotator cuff healing after surgical repair. Tokunaga et al. found that the application of an FGF-2 impregnated gelatin hydrogel sheet (GHS) into the bone groove of the greater tubercles is conducive to the healing of rotator cuff in a rabbit model (Tokunaga et al., 2015b; Tokunaga et al., 2017). Previously, our group fabricated a dual-factor releasing sulfhydrylated chitosan hydrogel to deliver FGF-2 and Kartogenin (KGN) for the fast healing of the tendon-bone interface. KGN is a kind of small molecules which is believed to promote the chondrogenic differentiation of bone marrow-derived mesenchymal stem cells (BMSCs) (Johnson et al., 2012). KGN upgrades the expression of TGFβ1 while TGFβ1 stimulated cartilage nodule formation. Besides, KGN significantly increased the levels of phosphor-Smads that mediate TGFβ and BMP signaling (Decker et al., 2014). We found the FGF-2/KGN-loaded hydrogel could be a promising biomaterial to promote healing rotator cuff (Teng et al., 2021).

Bone morphogenetic protein (BMP)-7 promotes osteogenesis of chondrocytes and tendinocytes, as well as matrix formation. However, retaining local concentrations of BMP-7 is difficult due to its short half-life. Kabuto et al. studied continuous BMP-7 release using a GHS to stimulate the repair of rotator cuff at the tendon-bone insertion site (Kabuto et al., 2015). Tokunaga and colleagues used acidic GHS as a long-term delivery system for PDGF-BB. The PDGF-BB containing hydrogel attached supraspinatus tendon and induced superior collagen fiber orientation than the PDGF-BB free hydrogel (Tokunaga et al., 2015a).

Platelet-rich plasma (PRP) contains high concentrations of platelets obtained from the whole blood of animals or human after centrifugation. PRP also contains a variety of cytokines. Some groups have claimed that PRP has limited repair effect for rotator cuff injury, possibly because its release process is too rapid (Barber, 2018; Cavendish et al., 2020). Kim and colleagues designed a hydrogel loaded with PRP and self-assembled peptide (SAP) for RCT healing in a rat model.

SAP is an injectable hydrogel that can be injected into the body without surgery. The low toxicity and biodegradability make SAP become popular. Compared with traditional PRP injection, SAP has a nanofiber structure that can delay the release of factors contained in physiological environment which promote collagen production. They found that PRP can promote RCT healing by improving the collagen arrangement and inhibiting apoptosis and inflammatory changes (Kim et al., 2017).

3.3 Cellular Delivery System

As the seed of the tissue regeneration, stem cells have been clinically applied for over 20 years. The most common used stem cells for rotator cuff repair and regeneration are BMSCs, ADSCs, and tendon stem cells (Liu et al., 2013).

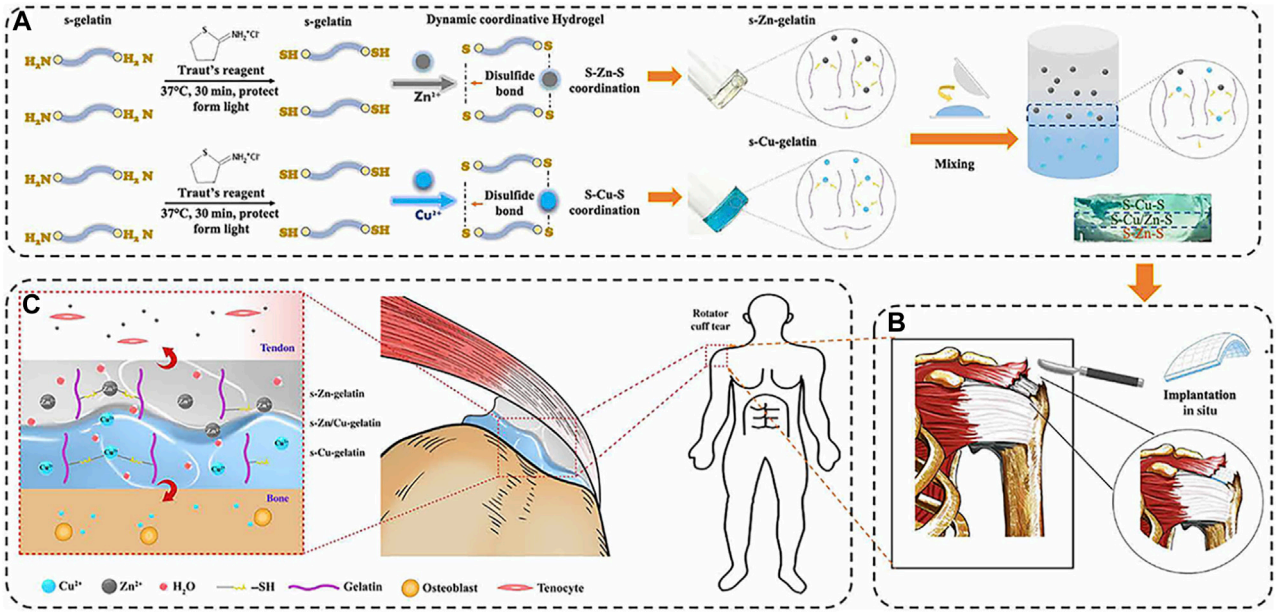

FIGURE 4 | (A) The fabrication of gradient bimetallic hydrogels. **(B)** The application of the gradient bimetallic hydrogel for RCT. **(C)** The mechanism of gradient bimetallic hydrogel for the regeneration of tendon-bone interface. (Reprinted from (Yang et al., 2021) with permission from Science Advances).

Hydrogels commonly used to deliver stem cells include tendon-derived collagen hydrogel (tHG), GelMa, and collagen. The mechanisms by which hydrogel with stem cells promotes rotator cuff healing include: 1) providing ECM materials to the damaged tendon, 2) hydrogel monomer functional groups can be modified to promote stem cell differentiation, 3) and hydrogel delivery systems can also deliver cytokines to promote stem cell differentiation (Toh et al., 2012; Park et al., 2016).

Cao et al. added osteoblasts, fibroblasts, and BMSCs separately in GelMA and sequentially loaded them on a 3D-printed multilayered scaffold to mimic the structure of tendon-bone interface. Chondrogenic differentiation was observed after *in vivo* implantation, suggesting that cells in a GelMA-multiphasic scaffold may be a new strategy to promote the healing of tendon-bone interface.

Kaizawa et al. invented a type I collagen-rich hydrogel based on human tendons, combining with ADSCs to improved mechanical strength of the tendon-bone interface (Kaizawa et al., 2019a; Kaizawa et al., 2019b). However, another group using the same model concluded that no biomechanical advantage was gained (Kaizawa et al., 2019a). Rothrauff et al. studied the effect of TGF-β3 and ADSCs delivered in fibrin and GelMA hydrogel on the healing after repairing acute or chronic massive RCTs in rats. They found the bone mineral density was improved with the application of fibrin, GelMA and ADSCs (Rothrauff et al., 2019).

Chen and colleagues developed an injectable hydrogel prepared by periosteal progenitor cells (PPCs) and polyethylene glycol diacrylate (PEGDA) with BMP-2 (Chen et al., 2011). They showed that BMP-2-loaded hydrogels could promote the differentiation of PPCs into osteoblasts and thus improve the success rate of tendon and bone healing. As a widely used biomaterial, PEGDA can provide a suitable microenvironment for mesenchymal stem cells (MSCs). In addition, bioactive cargos can be physically encapsulated in PEGDA hydrogels with MSCs as well.

3.4 Metal Ion Delivery System

Increasing attention has been paid to the role of metal ions in tendon-bone interface repair, including their anti-inflammatory, antibacterial, and cell differentiation-promoting abilities (Wang et al., 2021). Transporting metal ions and then slowly releasing them at the site of rotator cuff repair remain challenges.

Yang et al. constructed a gradient bimetal ion-based hydrogel for the first time by crosslinking sulfhydryl groups with zinc and copper ions for microstructural tendon-bone insertion reconstruction (**Figure 4**) (Yang et al., 2021). In this bimetallic hydrogel system, zinc and copper ions act as crosslinkers for the hydrogel and provide antibacterial effects and induce regeneration in the same time. The zinc and copper ions gradient layer were demonstrated to induce the arrangement of collagen and fibrocartilage at the tendon-bone interface. The gradient bimetallic ion-based hydrogels provide new insights into the regeneration of rotator cuff.

Magnesium ions promote cell adhesion, proliferation and fibrocartilage (Zhang et al., 2019; da Silva Lima et al., 2018; Hagandora et al., 2012). Besides, it can also regulate immune response which is essential for tendon-bone healing (Cheng et al., 2016). However, how to achieve the sustained release of magnesium ions is the key challenge. Chen et, al. reported a quaternized chitosan/Pluronic (QCS/PF) hydrogel delivering

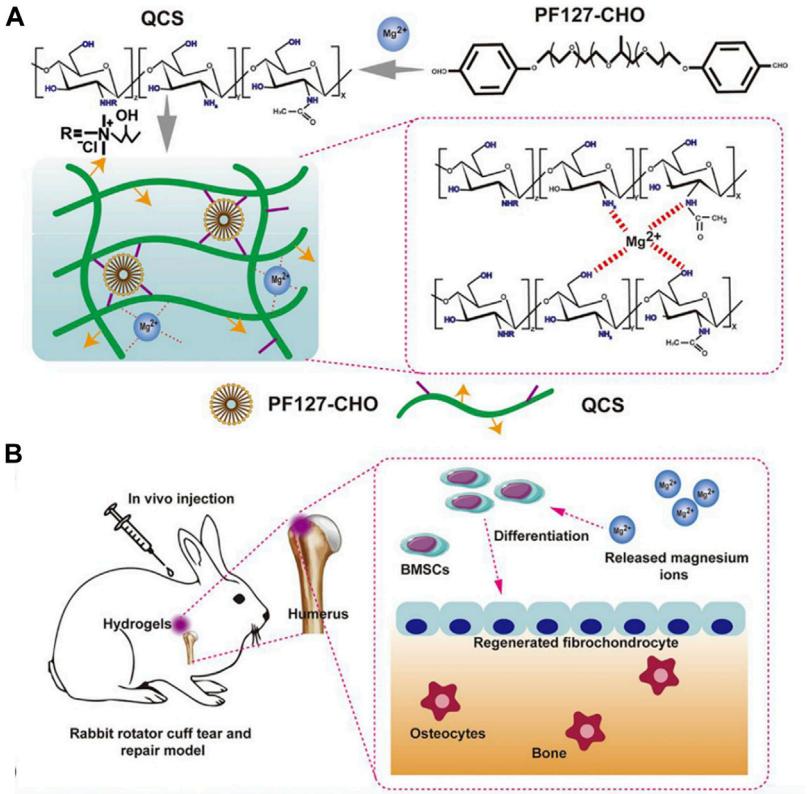

FIGURE 5 | (A) Scheme of the fabrication of QCS/PF hydrogels and the interaction between Mg^{2+} and QCS; **(B)** Application of QCS/PF hydrogels delivering Mg^{2+} *in situ* to promote tendon-bone interface regeneration in the rabbit RCT model; (Reprinted from (Chen et al., 2020)with permission from Science Advances).

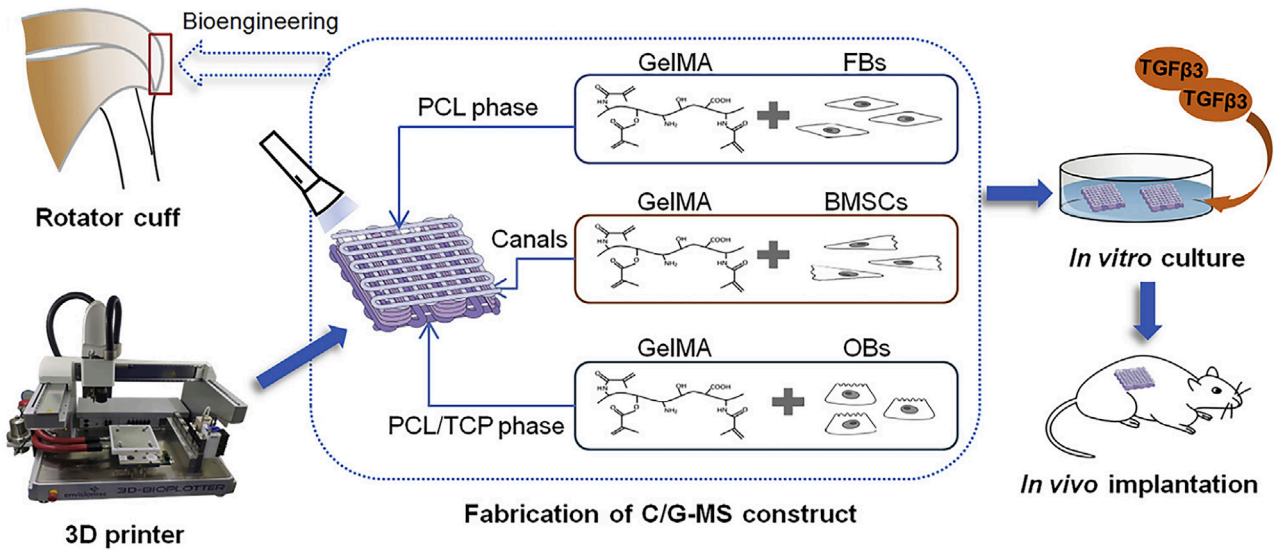

FIGURE 6 | Illustration of 3D printing multiphasic scaffold for tendon-bone interface engineering. (Reprinted from (Cao et al., 2020) with permission from Elsevier).

magnesium ions through metal coordination for RCT (**Figure 5**) (Chen et al., 2020). The self-healing property of this hydrogel ensured the safety of application in the RCT repair under external mechanical force, and the adhesive property increased the stability of material at the tendon-bone interface.

4 MULTILAYER COMPOSITE HYDROGEL SCAFFOLD FOR ROTATOR CUFF REPAIR

Jiang et al. developed a new method for RCT repair through combining a cell-laden collagen-fibrin hydrogel with a 3D printed PLGA scaffold (Jiang et al., 2020). This approach effectively supported human ADSCs' proliferation and tenogenic differentiation. The innovation of this work lies in the good biocompatibility of PLGA scaffolds fabricated by 3D printing technology for rotator cuff tendon defect repair.

Cao et al. used 3D printing technology to fabricate a multiphasic porous scaffold based on poly (ε-caprolactone) (PCL), PCL/tricalcium phosphate, and PCL/tricalcium phosphate. The three phases were designed to mimic the microstructure of tendon-bone interface. Osteoblasts, fibroblasts, and BMSCs and were separately encapsulated in GelMA hydrogel and sequentially loaded on the relevant scaffold phases (**Figure 6**). They found that 3D printing is an efficient method to develop multiphasic scaffold for tendon-bone interface engineering (Cao et al., 2020).

5 CONCLUSION AND OUTLOOK

RCTs are a common injury, and this repair is the most common shoulder operation. Tendon-bone healing following repair is influenced by the surgical technique, repair method, rotator cuff quality, and the biological healing process. This review covered hydrogels loaded with therapeutic cargoes such as cytokines, stem cells and bioactive materials that encourage rotator cuff healing. We recognize that this is a complex process dependent on numerous cellular signaling pathways involving different cytokines such as FGF-2, KGN, BMP-2, BMP-7, and PDGF-BB. Two recent studies have applied exosomes to rotator cuff injury; they can release a variety of cytokines that prevent inflammation and promote cell differentiation and fibrosis through a series of signaling pathways (Connor et al., 2019; Fu et al., 2021). Hydrogels loaded with exosomes for wound healing, bone regeneration, and cartilage repair have been studied (Hu et al., 2020; Wang et al., 2020; Zhao et al., 2020), but it is not clear whether they can promote rotator cuff healing, which may be worthy of investigation.

Besides tendon-bone healing, irreparable RCT management is another hot research topic. Surgeons encounter many challenges such as fatty infiltration, muscle atrophy, and tendon retraction in patients with irreparable RCT (Proctor, 2014; Lenart et al., 2015). Despite a substantial amount of research into rotator cuff patches, they have not applied been widely applied in the clinic. Patching the tendon-bone interface to promote rotator cuff-patch healing is difficult due to the complex gradual interface from bone tissue to tendon fiber tissue. Gradient layers of a composite hydrogel scaffold may be useful in this setting. These patches can experience stress in the early stage, but as cells migrate and the tendon fiber tissue grows, there is bionic healing between the bone and tendon.

The commercial application of hydrogel in wound dressing, drug delivery, and tissue engineering is quite successful. However, its application in shoulder is relatively rare. The possible factors are considered as follows: on the one hand, shoulder administration needs to be administered by injection or arthroscopy, which has high requirements on the physical and chemical properties of hydrogel or surgical techniques. Therefore, injectable hydrogels have great development potential. On the other hand, rotator cuff is consisted of tenacious tendons and construct the basic shoulder function. The hydrogel patch for rotator cuff tear need to achieve the similar toughness and strength. At present, the commercial application of some hydrogel materials to promote bone and cartilage repair provides ideas for the potential application in rotator cuff injury.

AUTHOR CONTRIBUTIONS

WW and CT conceived the idea. ZX and YF drafted the manuscript. YC and YZ revised the paper.

FUNDING

This work was supported by Zhejiang medical and health science and technology project (No. 2022493383) and Key Disciplines of Jinhua.

REFERENCES

Arimura, H., Shukunami, C., Tokunaga, T., Karasugi, T., Okamoto, N., Taniwaki, T., et al. (2017). TGF-β1 Improves Biomechanical Strength by Extracellular Matrix Accumulation without Increasing the Number of Tenogenic Lineage Cells in a Rat Rotator Cuff Repair Model. *Am. J. Sports Med.* 45 (10), 2394–2404. doi:10.1177/0363546517707940

Barber, F. A. (2018). PRP as an Adjunct to Rotator Cuff Tendon Repair. *Sports Med. Arthrosc. Rev.* 26 (2), 42–47. doi:10.1097/jsa.0000000000000193

Benoit, D. S. W., Schwartz, M. P., Durney, A. R., and Anseth, K. S. (2008). Small Functional Groups for Controlled Differentiation of Hydrogel-Encapsulated Human Mesenchymal Stem Cells. *Nat. Mater* 7 (10), 816–823. doi:10.1038/nmat2269

Bonnevie, E. D., and Mauck, R. L. Physiology and Engineering of the Graded Interfaces of Musculoskeletal Junctions. *Annu. Rev. Biomed. Eng.* 20, 1545–4274. (Electronic)). doi:10.1146/annurev-bioeng-062117-121113

Cao, Y., Yang, S., Zhao, D., Li, Y., Cheong, S. S., Han, D., et al. (2020). Three-dimensional Printed Multiphasic Scaffolds with Stratified Cell-Laden Gelatin Methacrylate Hydrogels for Biomimetic Tendon-To-Bone Interface Engineering. *J. Orthop. Transl.* 23, 89–100. doi:10.1016/j.jot.2020.01.004

Cavendish, P. A., Everhart, J. S., DiBartola, A. C., Eikenberry, A. D., Cvetanovich, G. L., and Flanigan, D. C. (2020). The Effect of Perioperative Platelet-Rich Plasma Injections on Postoperative Failure Rates Following Rotator Cuff Repair: a Systematic Review with Meta-Analysis. *J. shoulder Elb. Surg.* 29 (5), 1059–1070. doi:10.1016/j.jse.2020.01.084

Chae, S., Sun, Y., Choi, Y. J., Ha, D. H., Jeon, I. H., and Cho, D. W. (2020). 3D Cell-Printing of Tendon-Bone Interface Using Tissue-Derived Extracellular Matrix Bioinks for Chronic Rotator Cuff Repair. *Biofabrication* 13 (3), abd159. doi:10.1088/1758-5090/abd159

Chakravarty, K., and Webley, M. (1993). Shoulder Joint Movement and its Relationship to Disability in the Elderly. *J. Rheumatol.* 20 (8), 1359–1361.

Chen, B., Liang, Y., Bai, L., Xu, M., Zhang, J., Guo, B., et al. (2020). Sustained Release of Magnesium Ions Mediated by Injectable Self-Healing Adhesive

Hydrogel Promotes Fibrocartilaginous Interface Regeneration in the Rabbit Rotator Cuff Tear Model. *Chem. Eng. J.* 396. doi:10.1016/j.cej.2020.125335

Chen, B., Liang, Y., Zhang, J., Bai, L., Xu, M., Han, Q., et al. (2021). Synergistic Enhancement of Tendon-To-Bone Healing via Anti-inflammatory and Pro-differentiation Effects Caused by Sustained Release of Mg2+/curcumin from Injectable Self-Healing Hydrogels. *Theranostics* 11 (12), 5911–5925. doi:10.7150/thno.56266

Chen, C.-H., Chang, C.-H., Wang, K.-C., Su, C.-I., Liu, H.-T., Yu, C.-M., et al. (2011). Enhancement of Rotator Cuff Tendon-Bone Healing with Injectable Periosteum Progenitor Cells-BMP-2 Hydrogel *In Vivo*. *Knee Surg. Sports Traumatol. Arthrosc.* 19 (9), 1597–1607. doi:10.1007/s00167-010-1373-0

Cheng, P., Han, P., Zhao, C., Zhang, S., Wu, H., Ni, J., et al. (2016). High-purity Magnesium Interference Screws Promote Fibrocartilaginous Entheses Regeneration in the Anterior Cruciate Ligament Reconstruction Rabbit Model via Accumulation of BMP-2 and VEGF. *BIOMATERIALS* 81, 14–26. doi:10.1016/j.biomaterials.2015.12.005

Childress, M. A., Beutler, A., Kuo, L. A.-O., Chen, H. M., Yu, P. A., Chen, C. L., et al. (2013). Management of Chronic Tendon Injuries. *Am. Fam. Physician* 87 (7), 486–490.

Colvin, A. C., Egorova, N., Harrison, A. K., Moskowitz, A., and Flatow, E. L. (2012). National Trends in Rotator Cuff Repair. *J. Bone Jt. Surgery-American Volume* 94 (3), 227–233. doi:10.2106/jbjs.j.00739

Connor, D. E., Paulus, J. A., Dabestani, P. J., Thankam, F. K., Dilisio, M. F., Gross, R. M., et al. (2019). Therapeutic Potential of Exosomes in Rotator Cuff Tendon Healing. *J. Bone Min. Metab.* 37 (5), 759–767. doi:10.1007/s00774-019-01013-z

Craig, R., Holt, T., and Rees, J. L. (2017). Acute Rotator Cuff Tears. *Bmj* 359, j5366. doi:10.1136/bmj.j5366

Cui, X., Lee, J. J. L., and Chen, W. N. (2019). Eco-friendly and Biodegradable Cellulose Hydrogels Produced from Low Cost Okara: towards Non-toxic Flexible Electronics. *Sci. Rep.* 9, 18166. doi:10.1038/s41598-019-54638-5

da Silva Lima, F., da Rocha Romero, A. B., Hastreiter, A., Nogueira-Pedro, A., Makiyama, E., Colli, C., et al. (2018). An Insight into the Role of Magnesium in the Immunomodulatory Properties of Mesenchymal Stem Cells. *J. Nutr. Biochem.* 55, 200–208. doi:10.1016/j.jnutbio.2018.02.006

Decker, R. S., Koyama, E., Enomoto-Iwamoto, M., Maye, P., Rowe, D., Zhu, S., et al. (2014). Mouse Limb Skeletal Growth and Synovial Joint Development Are Coordinately Enhanced by Kartogenin. *Dev. Biol.* 395 (2), 255–267. doi:10.1016/j.ydbio.2014.09.011

Deprés-tremblay, G., Chevrier, A., Snow, M., Hurtig, M. B., Rodeo, S., and Buschmann, M. D. (2016). Rotator Cuff Repair: a Review of Surgical Techniques, Animal Models, and New Technologies under Development. *J. shoulder Elb. Surg.* 25 (12), 2078–2085. doi:10.1016/j.jse.2016.06.009

Dimatteo, R., Darling, N. J., and Segura, T. (2018). *In Situ* forming Injectable Hydrogels for Drug Delivery and Wound Repair. *Adv. Drug Deliv. Rev.* 127, 167–184. doi:10.1016/j.addr.2018.03.007

Fu, G., Lu, L., Pan, Z., Fan, A., and Yin, F. (2021). Adipose-derived Stem Cell Exosomes Facilitate Rotator Cuff Repair by Mediating Tendon-Derived Stem Cells. *Regen. Med.* 16 (4), 359–372. doi:10.2217/rme-2021-0004

Funakoshi, T., Majima, T., Iwasaki, N., Suenaga, N., Sawaguchi, N., Shimode, K., et al. (2005). Application of Tissue Engineering Techniques for Rotator Cuff Regeneration Using a Chitosan-Based Hyaluronan Hybrid Fiber Scaffold. *Am. J. Sports Med.* 33 (8), 1193–1201. doi:10.1177/0363546504272689

Goutallier, D., Postel, J.-M., Bernageau, J., Lavau, L., and Voisin, M.-C. (1994). Fatty Muscle Degeneration in Cuff Ruptures. *Clin. Orthop. Relat. Res.* 304, 78–83. doi:10.1097/00003086-199407000-00014

Gurnani, N., van Deurzen, D. F., Flipsen, M., Raven, E. E., and van den Bekerom, M. P. (2015). Efficacy of Different Rotator Cuff Repair Techniques. *Surg. Technol. Int.* 26, 295–300.

Hagandora, C. K., Tudares, M. A., and Almarza, A. J. (2012). The Effect of Magnesium Ion Concentration on the Fibrocartilage Regeneration Potential of Goat Costal Chondrocytes. *Ann. Biomed. Eng.* 40 (3), 688–696. doi:10.1007/s10439-011-0433-z

Han, B., Jones, I. A., Yang, Z., Fang, W., and Vangsness, C. T., Jr. (2020). Repair of Rotator Cuff Tendon Defects in Aged Rats Using a Growth Factor Injectable Gel Scaffold. *Arthrosc. J. Arthrosc. Relat. Surg.* 36 (3), 629–637. doi:10.1016/j.arthro.2019.09.015

Hee, C. K., Dines, J. S., Dines, D. M., Roden, C. M., Wisner-Lynch, L. A., Turner, A. S., et al. (2011). Augmentation of a Rotator Cuff Suture Repair Using rhPDGF-BB and a Type I Bovine Collagen Matrix in an Ovine Model. *Am. J. Sports Med.* 39 (8), 1630–1640. doi:10.1177/0363546511404942

Hu, H., Dong, L., Bu, Z., Shen, Y., Luo, J., Zhang, H., et al. (2020). miR-23a-3p-abundant Small Extracellular Vesicles Released from Gelma/nanoclay Hydrogel for Cartilage Regeneration. *J. Extracell. vesicles* 9 (1), 1778883. doi:10.1080/20013078.2020.1778883

Huang, C., Zhang, X., Luo, H., Pan, J., Cui, W., Cheng, B., et al. (2021). Effect of Kartogenin-Loaded Gelatin Methacryloyl Hydrogel Scaffold with Bone Marrow Stimulation for Enthesis Healing in Rotator Cuff Repair. *J. shoulder Elb. Surg.* 30 (3), 544–553. doi:10.1016/j.jse.2020.06.013

Huang, Y., He, B., Wang, L., Yuan, B., Shu, H., Zhang, F., et al. (2020). Bone Marrow Mesenchymal Stem Cell-Derived Exosomes Promote Rotator Cuff Tendon-Bone Healing by Promoting Angiogenesis and Regulating M1 Macrophages in Rats. *Stem Cell. Res. Ther.* 11 (1), 496. doi:10.1186/s13287-020-02005-x

Huebsch, N., Arany, P. R., Mao, A. S., Shvartsman, D., Ali, O. A., Bencherif, S. A., et al. (2010). Harnessing Traction-Mediated Manipulation of the Cell/matrix Interface to Control Stem-Cell Fate. *Nat. Mater* 9 (6), 518–526. doi:10.1038/nmat2732

Huebsch, N., and Mooney, D. J. (2009). Inspiration and Application in the Evolution of Biomaterials. *NATURE* 462 (7272), 426–432. doi:10.1038/nature08601

Ingber, D. E. (2003). Tensegrity I. Cell Structure and Hierarchical Systems Biology. *J. Cell. Sci.* 116 (7), 1157–1173. doi:10.1242/jcs.00359

Jacob, J., Eisemon, E., Sheibani-Rad, S., Patel, A., Jacob, T., and Choueka, J. (2012). Matrix Metalloproteinase Levels as a Marker for Rotator Cuff Tears. *Orthopedics* 35 (4), e474–8. doi:10.3928/01477447-20120327-18

Janmey, P. A., Winer, J. P., and Weisel, J. W. (2009). Fibrin Gels and Their Clinical and Bioengineering Applications. *J. R. Soc. Interface.* 6 (30), 1–10. doi:10.1098/rsif.2008.0327

Jiang, X., Wu, S., Kuss, M., Kong, Y., Shi, W., Streubel, P. N., et al. (2020). 3D Printing of Multilayered Scaffolds for Rotator Cuff Tendon Regeneration. *Bioact. Mater.* 5 (3), 636–643. doi:10.1016/j.bioactmat.2020.04.017

Johnson, K., Zhu, S., Tremblay, M. S., Payette, J. N., Wang, J., Bouchez, L. C., et al. (2012). A Stem Cell-Based Approach to Cartilage Repair. *Science* 336 (6082), 717–721. doi:10.1126/science.1215157

Spalazzi, J. P., Boskey Al Fau - Pleshko, N., Fau - Lu, H. H. Pleshko. N., and Lu, H. H., Quantitative Mapping of Matrix Content and Distribution across the Ligament-To-Bone Insertion, (1932) 8(9):e74349 (Electronic)). doi:10.1371/journal.pone.0074349

Kabuto, Y., Morihara, T., Sukenari, T., Kida, Y., Oda, R., Arai, Y., et al. (2015). Stimulation of Rotator Cuff Repair by Sustained Release of Bone Morphogenetic Protein-7 Using a Gelatin Hydrogel Sheet. *Tissue Eng. Part A* 21 (13-14), 2025–2033. doi:10.1089/ten.TEA.2014.0541

Kaizawa, Y., Leyden, J., Behn, A. W., Tulu, U. S., Franklin, A., Wang, Z., et al. (2019). Human Tendon-Derived Collagen Hydrogel Significantly Improves Biomechanical Properties of the Tendon-Bone Interface in a Chronic Rotator Cuff Injury Model. *J. Hand Surg. Am.* 44 (10), 899–e11. doi:10.1016/j.jhsa.2018.11.021

Kaizawa, Y., Franklin, A., Leyden, J., Behn, A. W., Tulu, U. S., Sotelo Leon, D., et al. (2019). Augmentation of Chronic Rotator Cuff Healing Using Adipose-derived Stem Cell-seeded Human Tendon-derived Hydrogel. *J. Orthop. Res.* 37 (4), 877–886. doi:10.1002/jor.24250

Kim, S. J., Lee, S. M., Kim, J. E., Kim, S. H., and Jung, Y. (2017). Effect of Platelet-Rich Plasma with Self-Assembled Peptide on the Rotator Cuff Tear Model in Rat. *J. Tissue Eng. Regen. Med.* 11 (1), 77–85. doi:10.1002/term.1984

Koh, K. H., Kang, K. C., Lim, T. K., Shon, M. S., and Yoo, J. C. (2011). Prospective Randomized Clinical Trial of Single- versus Double-Row Suture Anchor Repair in 2- to 4-cm Rotator Cuff Tears: Clinical and Magnetic Resonance Imaging Results. *Arthrosc. J. Arthrosc. Relat. Surg.* 27 (4), 453–462. doi:10.1016/j.arthro.2010.11.059

Kuo, L. A.-O., Chen, H. M., Yu, P. A., Chen, C. L., Hsu, W. H., Tsai, Y. H., et al. (1932). Depression Increases the Risk of Rotator Cuff Tear and Rotator Cuff Repair Surgery: A Nationwide Population-Based Study. *PLoS One* 14 (11), e0225778–6203. (Electronic)). doi:10.1371/journal.pone.0225778

Kuzel, B. R., Grindel, S., Papandrea, R., and Ziegler, D. (2013). Fatty Infiltration and Rotator Cuff Atrophy. *J. Am. Acad. Orthop. Surg.* 21 (10), 613–623. doi:10.5435/jaaos-21-10-613

Lee, H.-Y., Hwang, C.-H., Kim, H.-E., and Jeong, S.-H. (2018). Enhancement of Bio-Stability and Mechanical Properties of Hyaluronic Acid Hydrogels by Tannic Acid Treatment. *Carbohydr. Polym.* 186, 290–298. doi:10.1016/j.carbpol.2018.01.056

Lenart, B. A., Martens, K. A., Kearns, K. A., Gillespie, R. J., Zoga, A. C., and Williams, G. R. (2015). Treatment of Massive and Recurrent Rotator Cuff Tears Augmented with a Poly-L-Lactide Graft, a Preliminary Study. *J. shoulder Elb. Surg.* 24 (6), 915–921. doi:10.1016/j.jse.2014.09.044

Li, H., Chen, Y., and Chen, S. (2019). Enhancement of Rotator Cuff Tendon-Bone Healing Using Bone Marrow-Stimulating Technique along with Hyaluronic Acid. *J. Orthop. Transl.* 17, 96–102. doi:10.1016/j.jot.2019.01.001

Liang, H., Russell, S. J., Wood, D. J., and Tronci, G. (2018). A Hydroxamic Acid-Methacrylated Collagen Conjugate for the Modulation of Inflammation-Related MMP Upregulation. *J. Mat. Chem. B* 6 (22), 3703–3715. doi:10.1039/c7tb03035e

Liem, D., Lichtenberg, S., Magosch, P., and Habermeyer, P. (2007). Magnetic Resonance Imaging of Arthroscopic Supraspinatus Tendon Repair. *J. Bone Jt. Surgery-American Volume* 89 (8), 1770–1776. doi:10.2106/00004623-200708000-00015

Lin, Y. H., Lee, S. I., Lin, F. H., Wu, G. X., Wu, C. S., and Kuo, S. M. (2021). Enhancement of Rotator Cuff Healing with Farnesol-Impregnated Gellan Gum/Hyaluronic Acid Hydrogel Membranes in a Rabbit Model. *Pharmaceutics* 13 (7). doi:10.3390/pharmaceutics13070944

Liu, Q., Yu, Y., Reisdorf, R. L., Qi, J., Lu, C.-K., Berglund, L. J., et al. (2019). Engineered Tendon-Fibrocartilage-Bone Composite and Bone Marrow-Derived Mesenchymal Stem Cell Sheet Augmentation Promotes Rotator Cuff Healing in a Non-weight-bearing Canine Model. *Biomaterials* 192, 189–198. doi:10.1016/j.biomaterials.2018.10.037

Liu, X., He, J., Zhang, S., Wang, X. M., Liu, H. Y., and Cui, F. Z. (2013). Adipose Stem Cells Controlled by Surface Chemistry. *J. Tissue Eng. Regen. Med.* 7 (2), 112–117. doi:10.1002/term.498

Ma, Y., Lin, M., Huang, G., Li, Y., Wang, S., Bai, G., et al. (2018). 3D Spatiotemporal Mechanical Microenvironment: A Hydrogel-Based Platform for Guiding Stem Cell Fate. *Adv. Mater* 30 (49), e1705911. doi:10.1002/adma.201705911

Marycz, K., Smieszek, A., Trynda, J., Sobierajska, P., Targonska, S., Grosman, L., et al. (2019). Nanocrystalline Hydroxyapatite Loaded with Resveratrol in Colloidal Suspension Improves Viability, Metabolic Activity and Mitochondrial Potential in Human Adipose-Derived Mesenchymal Stromal Stem Cells (hASCs). *Polym. (Basel)* 11 (1). doi:10.3390/polym11010092

Moffat, K. L., Kwei, A. S.-P., Spalazzi, J. P., Doty, S. B., Levine, W. N., and Lu, H. H. (2009). Novel Nanofiber-Based Scaffold for Rotator Cuff Repair and Augmentation. *TISSUE Eng. PART A* 15 (1), 115–126. doi:10.1089/ten.tea.2008.0014

Nho, S. J., Yadav, H., Shindle, M. K., and Macgillivray, J. D. (2008). Rotator Cuff Degeneration. *Am. J. Sports Med.* 36 (5), 987–993. doi:10.1177/0363546508317344

Nichol, J. W., Koshy, S. T., Bae, H., Hwang, C. M., Yamanlar, S., and Khademhosseini, A. (2010). Cell-laden Microengineered Gelatin Methacrylate Hydrogels. *Biomaterials* 31 (21), 5536–5544. doi:10.1016/j.biomaterials.2010.03.064

Oh, J. H., Park, M. S., and Rhee, S. M. (2018). Treatment Strategy for Irreparable Rotator Cuff Tears. *Clin. Orthop. Surg.* 10 (2), 119–134. doi:10.4055/cios.2018.10.2.119

Oliva, N., Conde, J., Wang, K., and Artzi, N. (2017). Designing Hydrogels for On-Demand Therapy. *Acc. Chem. Res.* 50 (4), 669–679. doi:10.1021/acs.accounts.6b00536

Park, H.-J., Jin, Y., Shin, J., Yang, K., Lee, C., Yang, H. S., et al. (2016). Catechol-functionalized Hyaluronic Acid Hydrogels Enhance Angiogenesis and Osteogenesis of Human Adipose-Derived Stem Cells in Critical Tissue Defects. *Biomacromolecules* 17 (6), 1939–1948. doi:10.1021/acs.biomac.5b01670

Patil, S., Nune, K., and Misra, R. (2018). Alginate/poly(amidoamine) Injectable Hybrid Hydrogel for Cell Delivery. *J. Biomater. Appl.* 33 (2), 295–314. doi:10.1177/0885328218790211

Pelham, R. J., and Wang, Y.-L. (1998). Cell Locomotion and Focal Adhesions Are Regulated by Substrate Flexibility. *Proc. Natl. Acad. Sci. U. S. A.* 94 (25), 13661–13665. doi:10.1073/pnas.94.25.13661

Prabhath, A., Vernekar, V. N., Sanchez, E., and Laurencin, C. T. (2018). Growth Factor Delivery Strategies for Rotator Cuff Repair and Regeneration. *Int. J. Pharm.* 544 (2), 358–371. doi:10.1016/j.ijpharm.2018.01.006

Proctor, C. S. (2014). Long-term Successful Arthroscopic Repair of Large and Massive Rotator Cuff Tears with a Functional and Degradable Reinforcement Device. *J. shoulder Elb. Surg.* 23 (10), 1508–1513. doi:10.1016/j.jse.2014.01.010

Rossetti, L., Kuntz, L. A., Kunold, E., Schock, J., Müller, K. W., Grabmayr, H., et al. The Microstructure and Micromechanics of the Tendon-Bone Insertion. *Nat. Mater* 16, 1476–1122. (Print)). doi:10.1038/nmat4863

Rothrauff, B. B., Smith, C. A., Ferrer, G. A., Novaretti, J. V., Pauyo, T., Chao, T., et al. (2019). The Effect of Adipose-Derived Stem Cells on Enthesis Healing after Repair of Acute and Chronic Massive Rotator Cuff Tears in Rats. *J. shoulder Elb. Surg.* 28 (4), 654–664. doi:10.1016/j.jse.2018.08.044

Shi, L., Zhang, Y., and Ossipov, D. (2018). Enzymatic Degradation of Hyaluronan Hydrogels with Different Capacity for *In Situ* Bio-Mineralization. *Biopolymers* 109 (2). doi:10.1002/bip.23090

Shih, C.-A., Wu, K.-C., Shao, C.-J., Chern, T.-C., Su, W.-R., Wu, P.-T., et al. (2018). Synovial Fluid Biomarkers: Association with Chronic Rotator Cuff Tear Severity and Pain. *J. shoulder Elb. Surg.* 27 (3), 545–552. doi:10.1016/j.jse.2017.09.020

Sieminski, A. L., Was, A. S., Kim, G., Gong, H., and Kamm, R. D. (2007). The Stiffness of Three-Dimensional Ionic Self-Assembling Peptide Gels Affects the Extent of Capillary-like Network Formation. *Cell. Biochem. Biophys.* 49 (2), 73–83. doi:10.1007/s12013-007-0046-1

Sugaya, H., Maeda, K., Matsuki, K., and Moriishi, a. J. (2007). Repair Integrity and Functional Outcome after Arthroscopic Double-Row Rotator Cuff Repair. *J. Bone Jt. Surgery-American Volume* 89 (5), 953–960. doi:10.2106/00004623-200705000-00006

Tang, J.-N., Cores, J., Huang, K., Cui, X.-L., Luo, L., Zhang, J.-Y., et al. (2018). Concise Review: Is Cardiac Cell Therapy Dead? Embarrassing Trial Outcomes and New Directions for the Future. *STEM CELLS Transl. Med.* 7 (4), 354–359. doi:10.1002/sctm.17-0196

Tashjian, R. Z., Hollins, A. M., Kim, H.-M., Teefey, S. A., Middleton, W. D., Steger-May, K., et al. (2010). Factors Affecting Healing Rates after Arthroscopic Double-Row Rotator Cuff Repair. *Am. J. Sports Med.* 38 (12), 2435–2442. doi:10.1177/0363546510382835

Teng, C., Fang, Y., Zhu, H., Huang, L., Jin, Y., and Ye, Z. (2021). A Dual-Factor Releasing Hydrogel for Rotator Cuff Injury Repair. *Front. Mater.* 8. doi:10.3389/fmats.2021.754973

Thankam, F. G., Diaz, C., Chandra, I., Link, J., Newton, J., Dilisio, M. F., et al. (2021). Hybrid Interpenetrating Hydrogel Network Favoring the Bidirectional Migration of Tenocytes for Rotator Cuff Tendon Regeneration. *J. Biomed. Mater Res. B Appl. Biomater.* 110 (2), 467–477. doi:10.1002/jbm.b.34924

Thorsness, R., and Romeo, A. (2016). Massive Rotator Cuff Tears: Trends in Surgical Management. *Orthopedics* 39 (3), 145–151. doi:10.3928/01477447-20160503-07

Toda, H., Yamamoto, M., Uyama, H., and Tabata, Y. (2016). Fabrication of Hydrogels with Elasticity Changed by Alkaline Phosphatase for Stem Cell Culture. *Acta biomater.* 29, 215–227. doi:10.1016/j.actbio.2015.10.036

Toh, W. S., Lim, T. C., Kurisawa, M., and Spector, M. (2012). Modulation of Mesenchymal Stem Cell Chondrogenesis in a Tunable Hyaluronic Acid Hydrogel Microenvironment. *Biomaterials* 33 (15), 3835–3845. doi:10.1016/j.biomaterials.2012.01.065

Tokunaga, T., Ide, J., Arimura, H., Nakamura, T., Uehara, Y., Sakamoto, H., et al. (2015). Local Application of Gelatin Hydrogel Sheets Impregnated with Platelet-Derived Growth Factor BB Promotes Tendon-To-Bone Healing after Rotator Cuff Repair in Rats. *Arthrosc. J. Arthrosc. Relat. Surg.* 31 (8), 1482–1491. doi:10.1016/j.arthro.2015.03.008

Tokunaga, T., Karasugi, T., Arimura, H., Yonemitsu, R., Sakamoto, H., Ide, J., et al. (2017). Enhancement of Rotator Cuff Tendon-Bone Healing with Fibroblast Growth Factor 2 Impregnated in Gelatin Hydrogel Sheets in a Rabbit Model. *J. shoulder Elb. Surg.* 26 (10), 1708–1717. doi:10.1016/j.jse.2017.03.020

Tokunaga, T., Shukunami, C., Okamoto, N., Taniwaki, T., Oka, K., Sakamoto, H., et al. (2015). FGF-2 Stimulates the Growth of Tenogenic Progenitor Cells to Facilitate the Generation of Tenomodulin-Positive Tenocytes in a Rat Rotator Cuff Healing Model. *Am. J. Sports Med.* 43 (10), 2411–2422. doi:10.1177/0363546515597488

Toussaint, B., Schnaser, E., Bosley, J., Lefebvre, Y., and Gobezie, R. (2011). Early Structural and Functional Outcomes for Arthroscopic Double-Row Transosseous-Equivalent Rotator Cuff Repair. *Am. J. Sports Med.* 39 (6), 1217–1225. doi:10.1177/0363546510397725

Veronesi, F., Borsari, V., Contartese, D., Xian, J., Baldini, N., and Fini, M. (2020). The Clinical Strategies for Tendon Repair with Biomaterials: A Review on Rotator Cuff and Achilles Tendons. *J. Biomed. Mater Res.* 108 (5), 1826–1843. doi:10.1002/jbm.b.34525

Visser, J., Levett, P. A., te Moller, N. C., Besems, J., Boere, K. W., van Rijen, M. H., et al. (2015). Crosslinkable Hydrogels Derived from Cartilage, Meniscus, and Tendon Tissue. *Tissue Eng. Part A* 21 (7-8), 1195–1206. doi:10.1089/ten.TEA.2014.0362

Wang, J., Xu, J., Wang, X., Sheng, L., Zheng, L., Song, B., et al. (2021). Magnesium-pretreated Periosteum for Promoting Bone-Tendon Healing after Anterior Cruciate Ligament Reconstruction. *Biomaterials* 268, 120576. doi:10.1016/j.biomaterials.2020.120576

Wang, L., Wang, J., Zhou, X., Sun, J., Zhu, B., Duan, C., et al. (2020). A New Self-Healing Hydrogel Containing hucMSC-Derived Exosomes Promotes Bone Regeneration. *Front. Bioeng. Biotechnol.* 8, 564731. doi:10.3389/fbioe.2020.564731

Wen, J. H., Vincent, L. G., Fuhrmann, A., Choi, Y. S., Hribar, K. C., Taylor-Weiner, H., et al. (2014). Interplay of Matrix Stiffness and Protein Tethering in Stem Cell Differentiation. *Nat. Mater* 13 (10), 979–987. doi:10.1038/nmat4051

Wu, G., Xu, P. C., Wu, P., Hu, K., Sun, Y., Cheng, B., et al. (2017). Advances in the Treatment of Rotator Cuff Lesions by Cytokines. *Front. Biosci. (Landmark Ed.* 22, 516–529. doi:10.2741/4499

Xie, J., Li, X., Lipner, J., Manning, C. N., Schwartz, A. G., Thomopoulos, S., et al. (2010). "Aligned-to-random" Nanofiber Scaffolds for Mimicking the Structure of the Tendon-To-Bone Insertion Site. *Nanoscale* 2 (6), 923–926. doi:10.1039/c0nr00192a

Yadav, H., Nho, S., Romeo, A., and MacGillivray, J. D. (2009). Rotator Cuff Tears: Pathology and Repair. *Knee Surg. Sports Traumatol. Arthrosc.* 17 (4), 409–421. doi:10.1007/s00167-008-0686-8

Yang, R., Li, G., Zhuang, C., Yu, P., Ye, T., Zhang, Y., et al. (2021). Gradient Bimetallic Ion-Based Hydrogels for Tissue Microstructure Reconstruction of Tendon-To-Bone Insertion. *Sci. Adv.* 7 (26). doi:10.1126/sciadv.abg3816

Zhang, Z.-Z., Zhou, Y.-F., Li, W.-P., Jiang, C., Chen, Z., Luo, H., et al. (2019). Local Administration of Magnesium Promotes Meniscal Healing through Homing of Endogenous Stem Cells: A Proof-Of-Concept Study. *Am. J. Sports Med.* 47 (4), 954–967. doi:10.1177/0363546518820076

Zhao, D., Yu, Z., Li, Y., Wang, Y., Li, Q., and Han, D. (2020). GelMA Combined with Sustained Release of HUVECs Derived Exosomes for Promoting Cutaneous Wound Healing and Facilitating Skin Regeneration. *J. Mol. Hist.* 51 (3), 251–263. doi:10.1007/s10735-020-09877-6

Zhao, S., Su, W., Shah, V., Hobson, D., Yildirimer, L., Yeung, K. W. K., et al. (2017). Biomaterials Based Strategies for Rotator Cuff Repair. *Colloids Surfaces B Biointerfaces* 157, 407–416. doi:10.1016/j.colsurfb.2017.06.004

Conflict of Interest: The authors declare that the research was conducted in the absence of any commercial or financial relationships that could be construed as a potential conflict of interest.

Publisher's Note: All claims expressed in this article are solely those of the authors and do not necessarily represent those of their affiliated organizations, or those of the publisher, the editors and the reviewers. Any product that may be evaluated in this article, or claim that may be made by its manufacturer, is not guaranteed or endorsed by the publisher.

Copyright © 2022 Xu, Fang, Chen, Zhao, Wei and Teng. This is an open-access article distributed under the terms of the Creative Commons Attribution License (CC BY). The use, distribution or reproduction in other forums is permitted, provided the original author(s) and the copyright owner(s) are credited and that the original publication in this journal is cited, in accordance with accepted academic practice. No use, distribution or reproduction is permitted which does not comply with these terms.

frontiers | Frontiers in Bioengineering and Biotechnology

ORIGINAL RESEARCH
published: 27 June 2022
doi: 10.3389/fbioe.2022.902894

Dual-Action Icariin-Containing Thermosensitive Hydrogel for Wound Macrophage Polarization and Hair-Follicle Neogenesis

Ying-Ying Teng[1†], Ming-Li Zou[2†], Si-Yu Liu[2], Yuan Jia[2], Kai-Wen Zhang[2], Zheng-Dong Yuan[1], Jun-Jie Wu[1], Jun-Xing Ye[1], Shun Yu[1], Xia Li[1], Xiao-Jin Zhou[1] and Feng-Lai Yuan[1,2]**

[1]Institute of Integrated Chinese and Western Medicine, The Hospital Affiliated to Jiangnan University, Wuxi, China, [2]Wuxi Clinical Medicine School of Integrated Chinese and Western Medicine, Nanjing University of Chinese Medicine, Wuxi, China

OPEN ACCESS

Edited by:
Bruce Alan Bunnell,
University of North Texas Health Science Center, United States

Reviewed by:
Sumit Ghosh,
The Research Institute at Nationwide Children's Hospital, United States
Linli Zhou,
University of Cincinnati, United States

***Correspondence:**
Xiao-Jin Zhou
zxjyfb@163.com
Feng-Lai Yuan
bjjq88@jiangnan.edu.cn

†These authors have contributed equally to this work and share first authorship

Specialty section:
This article was submitted to Tissue Engineering and Regenerative Medicine, a section of the journal Frontiers in Bioengineering and Biotechnology

Received: 23 March 2022
Accepted: 03 June 2022
Published: 27 June 2022

Citation:
Teng Y-Y, Zou M-L, Liu S-Y, Jia Y, Zhang K-W, Yuan Z-D, Wu J-J, Ye J-X, Yu S, Li X, Zhou X-J and Yuan F-L (2022) Dual-Action Icariin-Containing Thermosensitive Hydrogel for Wound Macrophage Polarization and Hair-Follicle Neogenesis. Front. Bioeng. Biotechnol. 10:902894. doi: 10.3389/fbioe.2022.902894

Bone morphogenetic protein (BMP) pathway is essential for M2 macrophage polarization and hair-follicle neogenesis. Icariin, a flavonoid derived from *Epimedium*, is a mediator of the BMP pathway. Here, we develop a hydrogel formulation functionalized with icariin for regulation of macrophage polarization to accelerate wound healing and hair-follicle neogenesis. Compared to skin defects without icariin treatment, those treated with icariin+PEG hydrogel healed faster and had new hair follicles. Results *in vivo* showed that icariin+PEG hydrogel induced a higher level of M2 phenotypic transformation of macrophages. Moreover, icariin+PEG hydrogel significantly accelerated wound-repair process by reducing the invasion of inflammation, excessive deposition of collagen, immoderate activation of myofibroblasts, and increasing the regeneration of hair follicles. Furthermore, studies *in vitro* demonstrated that the icariin+PEG hydrogel induced macrophages to polarize to the M2 phenotype and dermal papilla cell to hair follicles. Finally, molecular analysis demonstrated that the icariin+PEG hydrogel increased the expression of BMP4 and Smad1/5 phosphorylation in skin wounds. These results demonstrate the therapeutic potential of icariin-containing thermosensitive hydrogels for inducing M2 macrophage polarization to accelerate wound healing and promote hair-follicle neogenesis by regulating the BMP pathway.

Keywords: icariin, wound repair, bone morphogenetic protein 4, macrophage polarization, hair-follicle regeneration

INTRODUCTION

Skin, the largest organ of the human body, plays a vital role in protecting the body from environmental and microbial invasion (Zhao et al., 2017). However, skin injuries, especially chronic wounds, burns, and infected wounds, when not cared for appropriately, can make the healing process difficult or promote the formation of pathological scars, causing dysfunction of the protective role of the skin and burdening an already overloaded health care system (Zhu et al., 2017; Zhong et al., 2019). Scar tissue comprises cells (mainly fibroblasts) and unorganized collagen and elastic fibers. They lack functional skin accessories (sweat glands, sebaceous glands, and hair follicles). Hypertrophic scar is often symptomatic and causes itching, burning, pain, sensation, and thermoregulation disability (Stoddard et al., 2014). Although most of the drugs and bio-activators, wound dressing, and autologous skin grafting can promote wound healing

well, regenerating the skin with complete appendages remains challenging. Therefore, a new treatment method should be developed for faster wound healing with hair-follicle regeneration.

Wound healing is a complex process. It has three major overlapping phases: inflammation, formation of new tissues, and remodeling (Takeo et al., 2015). The immune response in the early stage of wound healing plays a crucial role in tissue regeneration. Although inflammation at the site of tissue injury is necessary for initiating the healing response, the elimination of inflammation is also essential for promoting the healing process and restoring tissue integrity (Forbes and Rosenthal 2014). Macrophages are one of the most important inflammatory cell types involved in wound healing (Funes et al., 2018). Polarized macrophages can be activated according to their functions (Jiménez-García et al., 2018). M1 macrophages have a proinflammatory role and mainly secrete proinflammatory factors, while M2 macrophages can reduce inflammation and perform tissue-repair functions. Timely transformation of M1 macrophages to M2 macrophages (the anti-inflammatory phenotype) has great applicability in regenerative medicine (Sindrilaru et al., 2011; Miao et al., 2016; Li et al., 2021). If the skin appendages (hair follicles, sweat glands, and sebaceous glands) are completely destroyed, they cannot be fully regenerated, resulting in a scar (Murawala et al., 2012). Many studies have shown that hair follicles possibly regenerate mesenchymal cells during wound healing (Rippa et al., 2019; de Groot et al., 2021). Application of drugs and different drug-delivery systems in the healing process has been investigated. For example, prostaglandin E2 is used to regulate the phenotype of macrophages to reduce inflammation and promote wound healing (Zhang et al., 2018). Parker *et al.* have produced large-scale fibronectin nanofibers to repair the dermal papilla and recruit basal epithelial cells to promote the regeneration of hair follicles (Chantre et al., 2018). However, none of these strategies restore the skin tissue to its original form with a dual synergistic function, i.e., suppression of inflammation and promotion of hair-follicle regeneration during the wound healing process.

Recent studies have revealed that bone morphogenetic protein 4 (BMP4) is a promising option for wound healing because it can regulate cell proliferation and differentiation, macrophage polarization, stem-cell self-renewal, and embryonic development (Tong et al., 2015). Interestingly, a recent study has confirmed that the enhanced BMP signaling in myofibroblasts is related to hair-follicle regeneration and might promote wound healing (Plikus et al., 2017). Moreover, the participation of BMP4 can promote the proliferation and migration of dermal papilla cells and induce hair-shaft differentiation (Daszczuk et al., 2020). Interestingly, in acute lymphoblastic leukemia, BMP4 can upregulate the expression of interleukin (IL)-10 and promote the polarization of M1-like macrophages to the M2 phenotype (Zylbersztejn et al., 2018). Therefore, a material that is easy to source and able to modulate skin wound healing processes may be a potential solution to accelerate this process and reduce scar tissue formation by regulating BMP4 signaling.

Icariin, an extract from the traditional Chinese medicine Herba Epimedii, can increase the expression of BMP4 pathway components, enhance BMP4 signal transduction, and accelerate wound healing (Liu et al., 2018; Mi et al., 2018; Singh et al., 2019; Owen et al., 2020; Xie et al., 2020). Its remarkable pharmacological and biological effects, such as anti-inflammatory, antitumor, and neuroprotective effects, have already been confirmed (Shen and Wang 2018; He et al., 2020). Although Mi Bobin el. studied the effect of icariin on wound healing, they only focused on the role of keratinocytes (Mi et al., 2018), ignored the potential roles of macrophages and hair follicles and their possible mechanisms in skin wounds. Medical biomaterials can control the release of cytokines and drugs in time and space to simulate the dynamic changes of signals during normal tissue regeneration (Sun et al., 2018; Xu et al., 2018). However, the efficacy of icariin with hydrogels for accelerating wound healing and hair-follicle neogenesis by activating the BMP4 signaling pathway has not yet been elucidated. We hypothesized that treatment concepts based on mediation strategies of the BMP4 pathway in wounds could have a therapeutic potential. Herein, we develop a novel thermosensitive hydrogel drug-delivery system by encapsulating icariin with a poly (lactic acid-co-glycolic acid)–poly (ethylene glycol)–poly (lactic acid-co-glycolic acid) (PLGA–PEG–PLGA) triblock copolymer-based hydrogel. We also investigate its effects on macrophage polarization both *in vitro* and *in vivo* as well as on the regeneration of hair follicles. The findings of this study may help improve the wound healing process.

MATERIALS AND METHODS

Hydrogel Preparation

DL-lactide, glycolide, and polyethylene glycol (molar ratio: 2:2:1, Guidechem Chemical, China) were added to a three-necked flask, followed by the addition of 0.5% stannous octoate as a catalyst (Guidechem Chemical, China). The mixture was then repeatedly ventilated with nitrogen and vacuumed to remove trace amounts of moisture and oxygen. Next, under normal pressure, the tube was filled with nitrogen and then heated to 160°C under magnetic stirring for 8 h to obtain the PLGA–PEG–PLGA copolymer. The polymer was dissolved in dichloromethane and precipitated using petroleum ether to obtain a purified product. The polymer was then vacuum-dried to a constant weight. Finally, a 20 wt% solution of the polymer in deionized water was made and used as a temperature-sensitive hydrogel. The thermosensitive hydrogel was placed in a 1.5 ml EP tube, and a specific amount of icariin (489-32-7, Sigma-Aldrich) was dispersed in the thermosensitive hydrogel, which was completely dissolved by shaking in a 4°C refrigerator.

Hydrogel Morphology

The morphology of the hydrogel was observed using a cryo-scanning electron microscope (Cryo-SEM, Quorum,

United Kingdom). The samples were frozen by liquid nitrogen and put onto the cold table of an electron microscope (the temperature of which can reach −185°C) through the freezing transmission system for observation.

Rheological Analysis

Rheological analysis of the hydrogels was performed on a rheometer (Mars 40, Thermo Fisher Scientific, Germany) equipped with a 40 mm diameter parallel plate geometry. The hydrogel precursor solutions were pipetted between the parallel plates with a gap of 0.5 mm. Then the Oscillatory rheological measurements were carried on as the temperature of the plate was heated up from 4 to 37°C at a heating rate of 1°C min-1 and balanced at 37°C for 600 s to measure the storage modulus (G′) and loss modulus (G″). In addition, cycling three times between 1 and 1,000% was conducted to test its self-healing property.

Release of Icariin

After coagulation in a 15-ml centrifuge tube, 1 ml of the icariin+PEG hydrogel was shaken (37 °C, 60 rpm) with phosphate-buffered saline (PBS) (10 ml). Subsequently, 5.0 ml of the released medium was removed after certain time intervals (0.5, 1.5, 3, 5, 8, 12, 16, 20, 24, 32, 40, and 48 h) and replaced with 5.0 ml of fresh buffer. An ultraviolet-visible spectrophotometer (LAMBDA 35, PerkinElmer) set at a wavelength of 283 nm was used to determine the concentration of icariin in the released medium, and quantitative analysis was performed with the standard curve of previously prepared buffer solutions.

Cell Lines and Cell Cultures

The human monocytic cell line THP-1 was used to detect the polarization of macrophages *in vitro*. 5.0 × 104 cells per well were seeded in 6-well plates and treated by 100 ng/ml PMA for 24 h at 37°C. This cultivation method used herein was designed based on previous studies (Borchert et al., 2021). After the cells adhered, the culture medium was replaced with fresh medium, and the effect of the hydrogel on macrophages was observed by adding different treatments (PBS, PEG hydrogel, icariin only, icariin+PEG hydrogel) above the transwell chamber. The morphology of the cells was photographed with a microscope (Olympus Corporation, Tokyo, Japan).

Human hair dermal papilla cells (HDDPCs) (ZQY002, Zhongqiaoxinzhou Biotech, Shanghai, China) were cultured in Mesenchymal stem cell medium with 5% fetal bovine serum (FBS), 1% mesenchymal stem cell growth factor, 100 U/mL penicillin, and 100 μg/ml streptomycin. The cells were cultured at 37°C and 5% CO_2 and were serially passaged at 85–95% confluence.

Cytotoxicity Assay

The biocompatibility and cytotoxicity of the hydrogel were tested by both a cell counting kit-8 (CCK-8) assay and live/dead cell staining (Beyotime, China).

Immunofluorescence Staining

The influence of the hydrogel on the macrophage phenotype and inflammatory response was detected by immunofluorescence staining, according to methods described previously (Feng et al., 2020). The fluorescence images were taken by an inverted fluorescence microscope. Primary antibodies against CD206, tumor necrosis factor-alpha (TNF-α), cytokeratin, CD68, CD31, and Ki67 as well as secondary antibodies for fluorescence staining were purchased from Abcam (Cambridge, United Kingdom). Goat anti-rabbit (H + L) horseradish peroxidase secondary antibody was purchased from Bioworld Technology (St. Louis, MO, United States).

Western Blotting

Western blotting was performed to explore M2 polarization of macrophages and the level of skin fibrosis. The following antibodies were used in the western blotting assays: alpha-smooth muscle actin (α-SMA, 1:100, ab8211, Abcam); IL-10 (1:100, ab34843, Abcam); type I collagen (Col Ⅰ, 1:200, ab260043, Abcam); IL-6 (1:500, ab6672, Abcam); cytokeratin 17 (1:500, ab109725, Abcam); TNF-α (1:1000, ab6671, Abcam); arginase-1 (1:500/1:50, #93668, Cell Signaling Technology); CD206 (1:1000, #PA5-114310, Invitrogen); Smad1/5 (1:500, bs-2973R, Bioss Antibodies); phospho-Smad1/5 (1:1000, bs-3418R, Bioss Antibodies); BMP4 (1:500, bs-1374R, Bioss Antibodies); and GAPDH (1:10000, ab181602, Abcam).

Reverse Transcription–Polymerase Chain Reaction (RT-PCR)

A real-time quantitative RT-PCR system (QuantStudio 3, Thermo, United States) was used to detect changes at the gene level. The sequences of the primers are listed in **Supplementary Table S1**.

Flow Cytometric Analysis

After the treatment, 1×10^6 cells belonging to the control group, icariin group, and IL-4 group were incubated with 2 μL of FTTC anti-human CD206 antibody (321104, Biolegend) and 2 μL of APC anti-human CD68 antibody (333809, Biolegend) diluted in a staining buffer for 30 min on ice in the dark. Next, the cells were washed twice with the staining buffer to remove excess antibodies, followed by their resuspension in 500 μL of the staining buffer. The stained cells were analyzed by flow cytometry (BD FACSCalibur, San Jose, CA, United States). The flow cytometry data was analyzed by FlowGo.

Animal Model for Dermal Wound Healing

Sterile ophthalmic scissors were used to create skin full-thickness wounds of 1-cm diameter in the back of male C57BL/6 mice (8–12 weeks) deep to the fascia. The mice were randomly divided into three groups: those treated with 0.9% saline, those treated with PEG hydrogels, and the rest treated with icariin-loaded PEG hydrogels. The hydrogels were directly injected onto the surface of each wound, which was then covered with a 3M Tegaderm™ film and secured with a medical

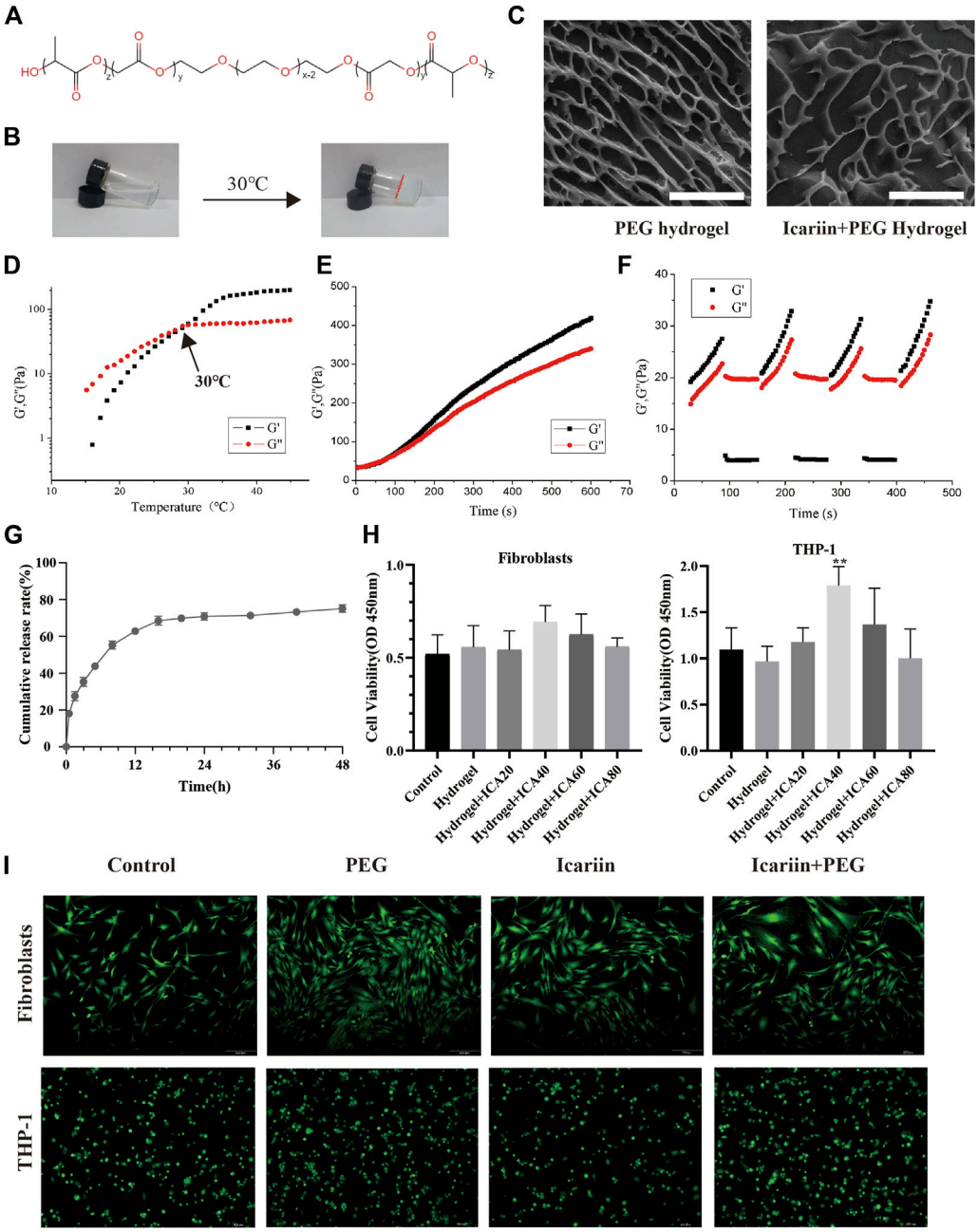

FIGURE 1 | Characterization and biocompatibility of the PEG hydrogel. **(A)** Chemical structure of the PEG hydrogel. **(B)** PEG hydrogel solution gelled at 30°C. **(C)** Cryo-scanning electron microscopy images of PEG and icariin+PEG hydrogels. Scale bar, 30 μm. **(D)** Temperature dependence of the storage modulus (G′) and loss modulus (G″) of the PEG hydrogel. **(E)** Gelation time of the PEG hydrogel at 35°C. **(F)** G′ and G″ of the PEG hydrogel when circulated three times between strain of 1 and 1,000%. **(G)** Release profile of icariin from the icariin+PEG hydrogel by UV spectrophotometry. **(H)** Cell viability on human fibroblast cells and THP-1 macrophages with hydrogel extracts of different compositions for 48 h. ICA20: 20 μg/ml icariin, ICA40: 40 μg/ml icariin, ICA60: 60 μg/ml icariin, ICA80: 80 μg/ml icariin, $^{**}p < 0.01$ *vs*. the control. **(I)** Fluorescence microscopy of fibroblasts and macrophages was performed with live/dead cell staining. Live cells emit green fluorescence, while dead cells emit red fluorescence.

bandage. A digital camera was used to take photos of the wound at 0, 3, 7, 10, and 14 days after the treatment. ImageJ was used to analyze the wound-healing rate. All procedures were approved by the Experimental Animal Committee of Jiangnan University, China.

Histological Analysis

Hematoxylin and eosin staining, Masson's staining, and immunofluorescence staining (Beyotime, China) were performed on the skin tissue slices to analyze the wound condition, including the healing speed, fibrosis, and

regeneration of the skin appendages. The images were analyzed by ImageJ software.

Cell Migration Assay

Cells were plated at a density of 1×10^5/well in 6-well plates. When the transfected cells reached 100% confluence, a sterile micropipette tip was used to create a scratch. The cells were washed with PBS, and minimal medium was added. Cell migration was observed and imaged at 0 h and after incubation for 6 and 12 h at 37°C. Cell migration was analyzed using ImageJ software.

Statistical Analysis

Statistical analysis was performed using GraphPad Prism 8.0.1 software (GraphPad Software Inc., San Diego, CA, United States). Data were expressed as the mean ± standard error of the mean. Statistically significant differences between the groups were assessed by analysis of variance or the two-tailed Student's *t*-test. For all tests, $^{*}p < 0.05$, $^{**}p < 0.01$, and $^{***}p < 0.001$ were considered statistically significant.

RESULTS

Characteristics of icariin+PEG Hydrogel

The hydrogel was fabricated using DL-lactide, glycolide, and polyethylene glycol (**Figure 1A**). The hydrogel was thermosensitive and could be transformed from a liquid state to a hydrogel at 30°C (**Figure 1B**). The microstructure of the hydrogel was observed by cryo-scanning electron microscopy. As shown in **Figure 1C**, both the PEG and icariin+PEG hydrogels presented interconnected three-dimensional networks with a uniform pore size distribution, indicating that icariin was evenly distributed inside the PLGA–PEG–PLGA network, without forming agglomerates. To further verify the performance of the PEG hydrogel upon a temperature change, an oscillating rheological test was conducted. At 15–45°C, the storage modulus (G′) of the hydrogel gradually exceeded the loss modulus (G″), indicating that the sol–gel changes at the critical temperature of 30°C (**Figures 1D,E**). Therefore, the refrigerated icariin+PEG hydrogel can be injected into the wound and cover wounds of any shape and quickly become a colloid when heated to 30°C, which is close to the surface temperature of the human body. The self-healing ability of the hydrogel dressings was also confirmed (**Figure 1F**). After conducting three steps of strain cycles during the rheological analysis, the quick drop in the values of G′ and G″ at high strain (1,000%) and their rapid recovery under low shear strain (1%) indicated that the hydrogel has a good shear-thinning ability and self-healing properties. The hydrogels merged without any visible interface when solutions of two different colors were incubated for 30 min, indicating that the hydrogel has a good self-healing ability (**Supplementary Figure S1B**). The drug-release efficiency of the hydrogel was evaluated by monitoring the concentration of icariin in the supernatant. **Figure 1G** shows that the release curve was relatively stable and gradually increased, reaching a peak at 24 h. The CCK-8 results showed that the drug-loaded gel extract at the optimal concentration of 40 μg/ml could promote the proliferation of macrophages and did not exert any significant effect on the growth of fibroblasts (**Figure 1H**).

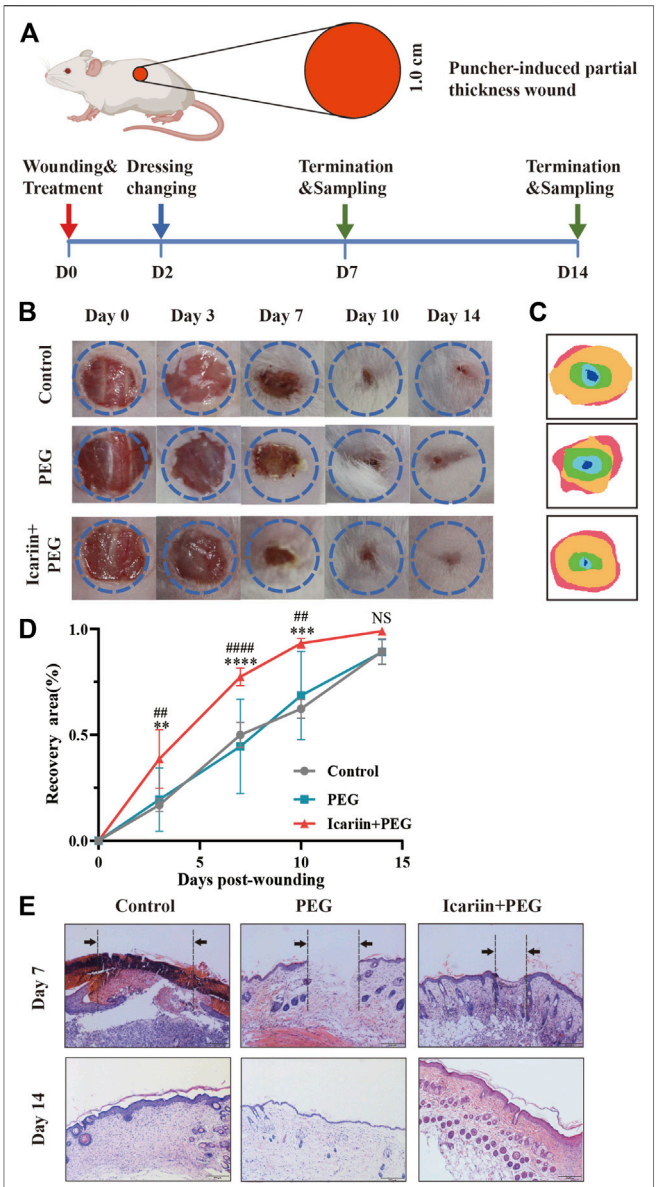

FIGURE 2 | Icariin+PEG hydrogel speeded up skin repair. **(A)** Schematic diagram of the mouse skin full-thickness injury model and experiments *in vivo*. A circular wound of 1-cm diameter was made by using ophthalmic scissors on the back of the mouse. The wounds were observed after application of the hydrogel. On days 7 and 14, the skin tissues were taken for follow-up experiments. **(B)** Representative images and schematic diagrams of wounds with different treatments: PBS, PEG hydrogel, and icariin+PEG hydrogel dressings. **(C)** Schematic diagram of the healing process on day 0, 3, 7, 10, 14 after wounding was measured by ImageJ. **(D)** Wound-recovery rates of different treatment groups (control, PEG, and icariin+PEG) over 14 days. $n \geq 4$. $^{**}p < 0.005$, $^{***}p < 0.0005$, $^{****}p < 0.0001$ *vs*. PBS; $^{\#\#}p < 0.005$, $^{\#\#\#\#}p < 0.0001$ *vs*. PEG. **(E)** HE staining showing the morphological appearance of skin treated with hydrogels on days 7 and 14. The black arrows and broken lines indicate the edge of the wound visible under a microscope. Scale bar: 200 μm.

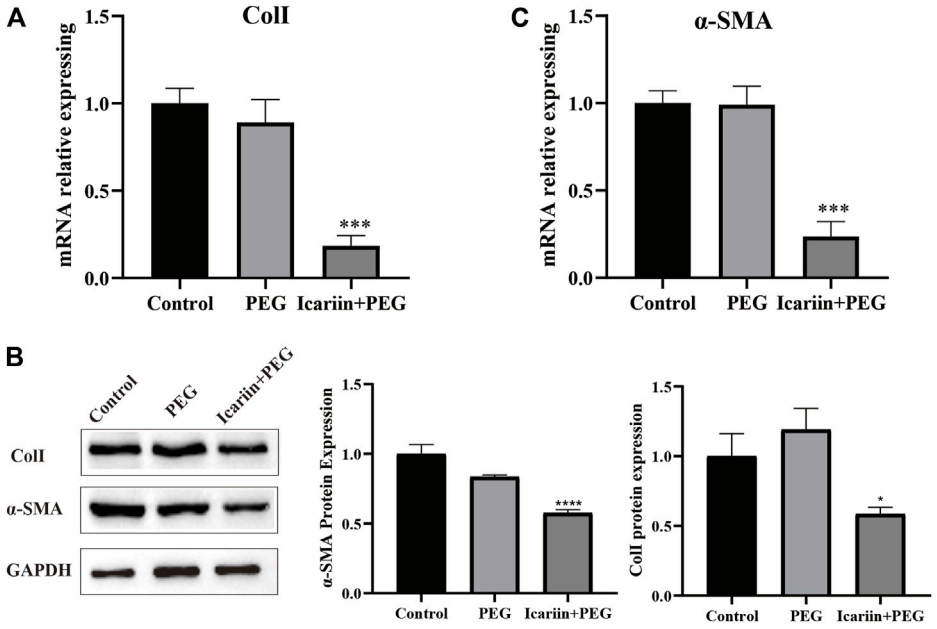

FIGURE 3 | Icariin+PEG hydrogel alleviated skin fibrosis. **(A)** RT-PCR analysis of ColI expression in three groups. **(B)** Protein expression level of Col I and α-SMA as detected by western blotting on day 14 at the injured sites. Quantification of the western blotting bands compared to that of the control group. **(C)** RT-PCR analysis of α-SMA expression in three groups.

To further study the biocompatibility of the hydrogel, transwells were used to co-culture the hydrogel and cells. A representative live/dead cell staining experiment is shown in **Figure 1I**. The cells incubated with PBS, icariin, PEG hydrogel, and icariin+PEG hydrogel showed shining green fluorescence; red fluorescence could scarcely be seen in the images, implying that there was little cell death and a good biocompatibility.

Icariin+PEG Hydrogel Accelerates *in vivo* Wound Repair Process

We used a mouse skin-wound-healing model to evaluate the therapeutic effect of the icariin+PEG hydrogel *in vivo*. The icariin+PEG hydrogel, PEG hydrogel, and PBS were used to treat the injured area, and the wounds at different time points were photographed to investigate the effects of the icariin+PEG hydrogel on the healing rate (**Figures 2A,B**). A comparison of these images showed that the icariin+PEG group speeded up the wound-healing process compared to that achieved with the other groups (PEG and control groups) (**Figure 2B**). The wound areas in all groups were clearly reduced after 7 days of treatment; the icariin+PEG group showed the fastest healing compared to others. The changes in the healing process are shown in a composite figure for clarity (**Figure 2C**). The percentage of the wound area also confirmed the gross observation results (**Figure 2D**). Subsequently, HE staining was performed to observe wound regeneration (**Figure 2E**). The control group and the PEG group had a slower closing rate than that achieved with the icariin+PEG group, which is consistent with the results of visual healing. Thick abundant granulation tissue can be clearly seen in icariin+PEG-treated wounds. In contrast, wounds in the control and PEG groups showed a very small amount of newly formed tissue at day 7. Especially on the last day of observation, the regeneration of the wound in the Icariin+PEG group was almost complete, the edges of the wound were not obvious, the thickness of the epidermis was moderate, and the hair follicles in the center of the wound grew well. Hence, it is clear that the icariin+PEG hydrogel enhanced the healing efficacy of wounds and showed a fairly high level of wound recovery.

Icariin+PEG Hydrogel Suppresses Skin Fibrosis After Wound

Wound healing can lead to skin fibrosis, resulting in scar formation and ultimately in the loss of skin functions. Col I is the primary material involved in the formation of scar tissue. Thick Col I forms large-diameter collagen fibers with horizontal stripes at the wound site, making the scar structure hard and inelastic, which is completely different from the normal skin tissue (Feng et al., 2020; Zhao et al., 2021). On day 14 after treatment, RT-PCR analysis showed that the *Col I* gene expression of the icariin+PEG group was markedly lower than that of the other two groups (**Figure 3A**). In addition, western blot analysis showed that the icariin+PEG dressing dramatically decreased the protein level of Col I (**Figure 3B**).

Myofibroblasts proliferate and differentiate into myofibroblasts expressing α-SMA. Subsequently, myofibroblasts continuously migrate and synthesize a large amount of collagen, resulting in excessive fibrosis. Therefore, we used the α-SMA to calculate the number of myofibroblasts in

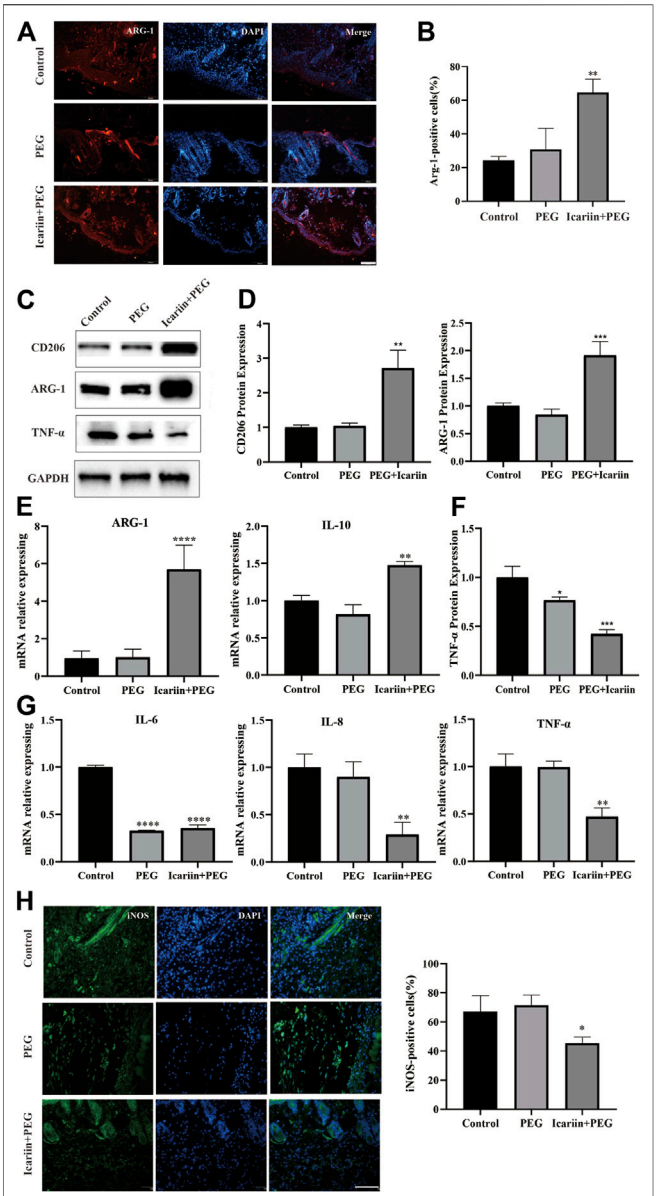

FIGURE 4 | Icariin+PEG hydrogel promoted macrophage M2 polarization and reduced inflammation in the early stage of wound healing *in vivo*. **(A)** Representative immunofluorescence pictures of ARG1 expression on day 7 at the injured sites. Scale bar: 100 μm. **(B)** Quantification of ARG1-positive cells in different groups. **(C,D)** Protein expression level of CD206 and ARG1 as detected by western blotting on day 7 at injured sites. Quantification of the western blotting bands compared to that of the control group. **(E)** Expression levels of M2-related genes *ARG1* and *IL-10* of the three groups by RT-PCR. **(F)** Protein expression level of TNF-α as detected by western blotting on day 7 at the injured sites. Quantification of the western blotting bands compared to that of the control group. **(G)** Expression level of inflammation-related genes IL-6, IL-8, and TNF-α in different groups by RT-PCR. **(H)** Representative immunofluorescence pictures of iNOS expression on day 7 at injured sites. Scale bar: 100 μm. Quantification of iNOS-positive cells in different groups.

the injured tissue (Limandjaja et al., 2021). Clearly, RT-PCR analysis showed that the α-SMA gene expression of the icariin+PEG group was markedly lower than that of the other two groups (**Figure 3C**). The western blotting results were consistent with the gene levels measured by PCR (**Figure 3B**). Taken together, the icariin released from the icariin+PEG hydrogel exerted additional effects by reducing excessive collagen deposition and excess myofibroblast differentiation during skin wound healing, which together promote wound healing.

Icariin+PEG Hydrogel Promotes M2 Polarization of Macrophages and Enhances Anti-Inflammation at Injured Sites

As macrophages are the main inflammatory cell type during the early stage of the healing process, their role in both M1 and M2 phenotypic polarization has been extensively studied. M2 phenotype of macrophages has been proved to promote cutaneous wound healing (Zhang et al., 2010). Therefore, we next analyzed the M2 macrophage markers ARG1 and CD206 to explore the distribution of macrophages at the site of the icariin+PEG hydrogel treatment (Kim et al., 2019). As shown in **Figures 4A,B**, the PEG hydrogel group had fewer ARG1-positive cells; in contrast, their distribution in the icariin+PEG hydrogel group was more widespread under the skin of the wound. This observation indicates that the icariin released by the icariin+PEG hydrogel produced higher levels of M2 macrophages at the wound site (**Figures 4C,D**). Then, CD206 was chosen as another surface marker of M2 macrophages, and CD68 for macrophages of all the subsets. As shown in the representative fluorescent pictures in Figure S, in the subcutaneous layer on the wounds, the icariin+PEG group exhibited a more widely distribution of CD206 positive cells. ARG1-and CD206-specific antibodies were used to further identify the presence of M2 macrophages during the initial state of the injury. RT-PCR analysis showed that the icariin+PEG hydrogel greatly improved the expression of *IL-10* and *ARG1* genes, which are related to M2 macrophages (**Figures 4E,F**). Hence, the icariin+PEG hydrogel promoted the polarization of M2 macrophages at the injury site.

Inflammatory cell infiltration initiates the wound-healing process. It removes necrotic material to prepare the wound bed for the subsequent tissue regeneration (Pratsinis et al., 2019). Thus, we explored various anti-inflammatory effects of the different treatment methods using TNF-α as an indicator of the inflammatory response (Arabpour et al., 2021). The early stage of the inflammatory response is characterized by numerous M1 macrophages, which produce large amounts of proinflammatory cytokines. The western blot and PCR results of TNF-α expression showed that the concentration of proinflammatory cytokines in the wound bed was significantly reduced after treatment with the icariin+PEG hydrogel (**Figures 4G,H**). In addition, the icariin+PEG hydrogel greatly reduced the levels of the local proinflammatory cytokines IL-6 and IL-8 on day 7 after injury (**Figure 4G**). Furthermore, the inflammatory cell infiltration of the mouse skin injury model was monitored by immunofluorescence to evaluate the role of the icariin+PEG hydrogel on inflammation. The icariin+PEG hydrogel treatment slightly reduced the aggregation of inducible nitric

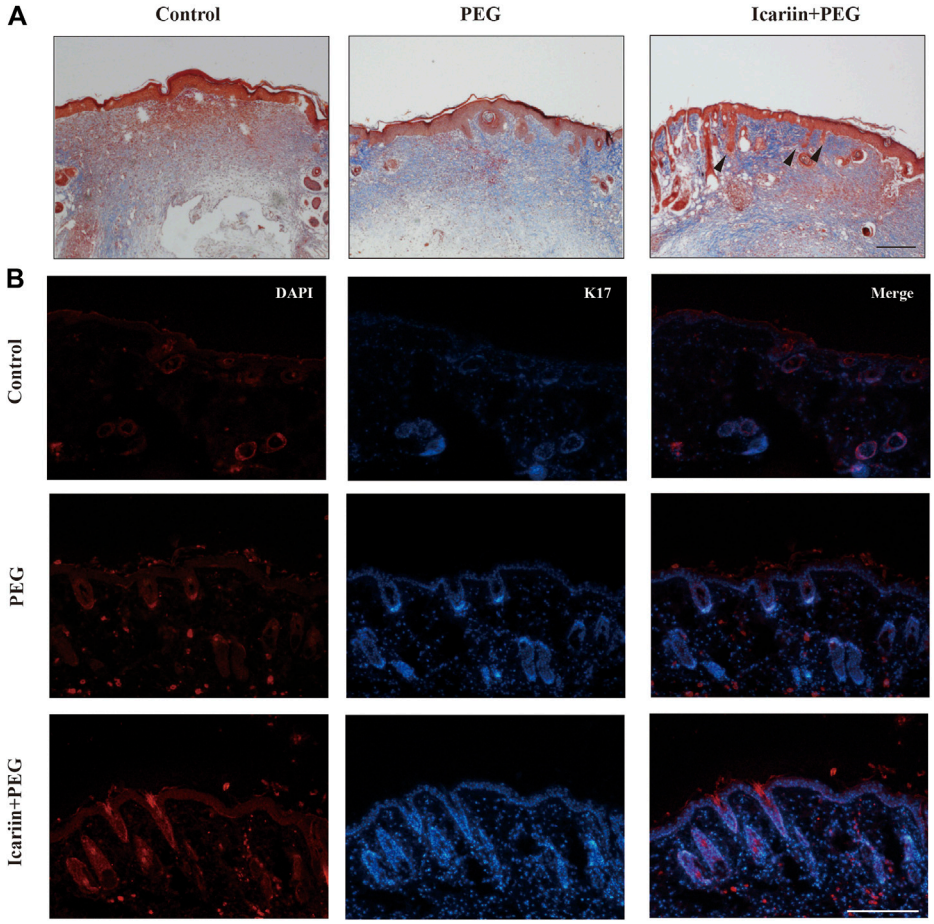

FIGURE 5 | Hair follicles are regenerated with icariin+PEG hydrogel treatment. **(A)** Masson staining of different groups on day 14. Red arrows indicate new hair follicles. Scale bar: 200 μm. **(B)** Representative immunofluorescence images of K17 expression on day 14 at the injured sites. Scale bar: 100 μm.

oxide synthase (iNOS)-positive cells (**Figure 4I**). Hence, the icariin+PEG hydrogel could prevent inflammation at the center of the injury by managing M1 macrophages, thereby reducing the infiltration of inflammatory cells. Therefore, the icariin+PEG hydrogel greatly increased the number of repairing M2 macrophages and improved the quality of wound healing, thus showing important anti-inflammatory effects and repair during the healing process.

Icariin+PEG Hydrogel Promotes the Regeneration of Hair Follicles at Injured Sites

In addition to the excessive deposition of collagen fibers, another major feature of scarring is the loss of skin accessory organs, especially the aplasia of hair follicles at the late stage of wound healing (Zhang et al., 2016). To further investigate this phenomenon, we investigated hair-follicle regeneration in the skin wound of mice. Apart from severe fibrosis and hyperplasia observed at the wound center, the number of hair follicles was also reduced in the groups treated with PBS or the drug-free hydrogel (**Figure 5A**). Next, we investigated whether any epidermal cell type promotes epidermal homeostasis and repair in icariin-treated wounds (Ito et al., 2007; Blanpain and Fuchs 2009). Keratin 17 (K17) marks the outer root sheath of specific hair follicles in epidermal cells (**Figure 5B**). By day 14 after treatment, the tissues treated with the icariin+PEG hydrogel showed an extensive presence of K17 around the epidermis and hair follicles. Although wound contraction may make it difficult to image the complete structure of hair follicles, the presence of epidermal cells in drug-treated tissues is attractive and may increase the possibility of repairing functional hair follicles.

Icariin+PEG Hydrogel Promotes the Polarization of Macrophages to the M2 Phenotype *in vitro*

Insufficient M2 polarization is related to many pathological processes such as the hard healing surface of chronic wounds, as can be seen in diabetic ulcers, which can inhibit the inflammatory response and hinder tissue regeneration (Ferrante and Leibovich 2012). Therefore, we first tested the

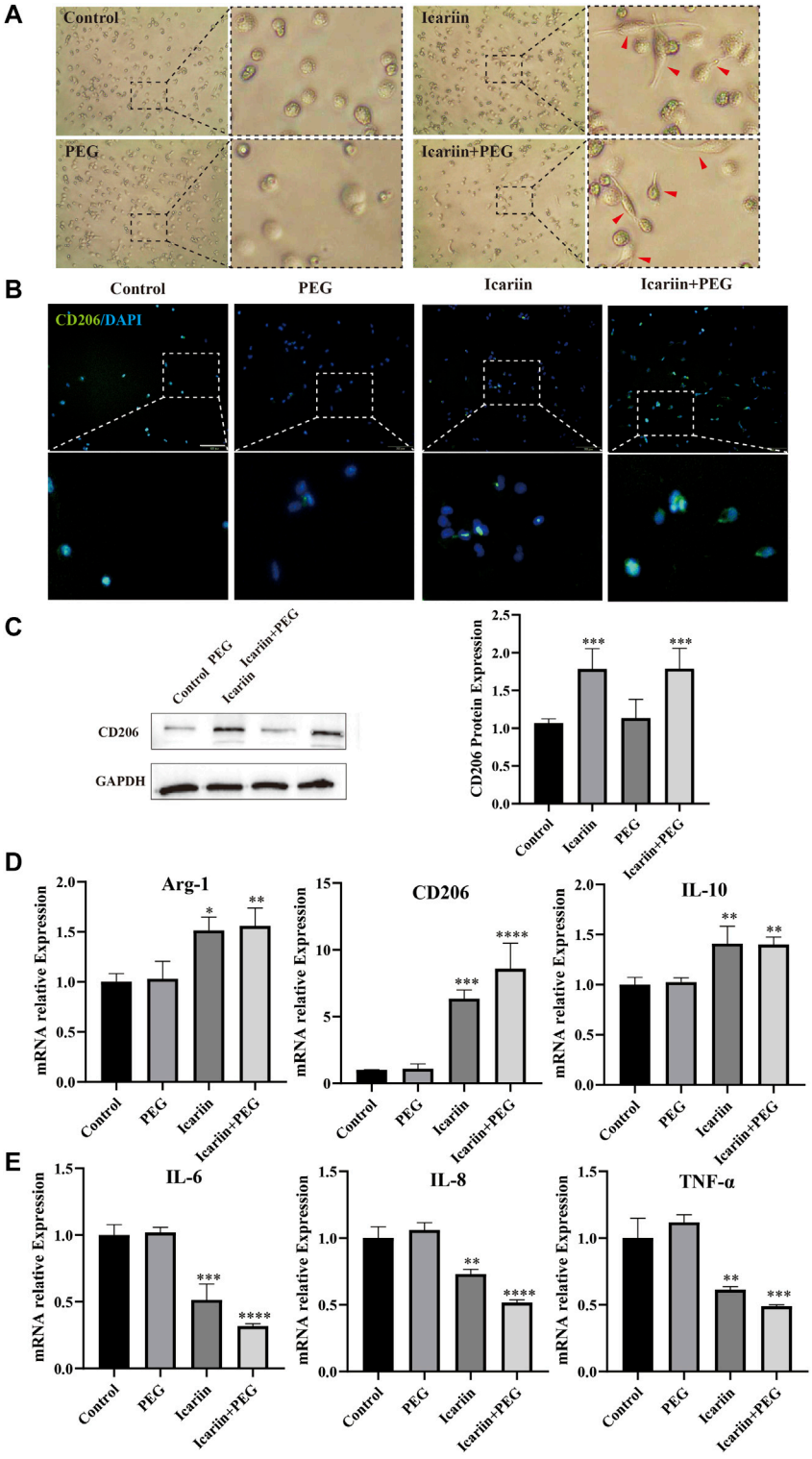

FIGURE 6 | Icariin+PEG hydrogel promoted M2 polarization of macrophages and enhanced anti-inflammatory effects *in vitro*. **(A)** Morphological changes of THP-1 macrophages after icariin treatment for 48 h were observed under an optical microscope. Red arrows indicate elongated macrophages. **(B)** Representative pictures of THP-1 immunofluorescence staining with CD206 antibody after being co-cultured with the hydrogel for 48 h. Scale bar: 100 μm; scale bar of magnified pictures: 25 μm. **(C)** Western blot analysis of the CD206 protein expression level in macrophages treated with different dressings for 48 h. Quantification of the western blotting bands compared to that of the control group. **(D)** RT-PCR analysis of M2-related gene (*ARG1*, *CD206*, and *IL-10*) expression in macrophages. **(E)** RT-PCR analysis of M1-related gene (*IL-6*, *IL-8*, and *TNF-α*) expression in macrophages.

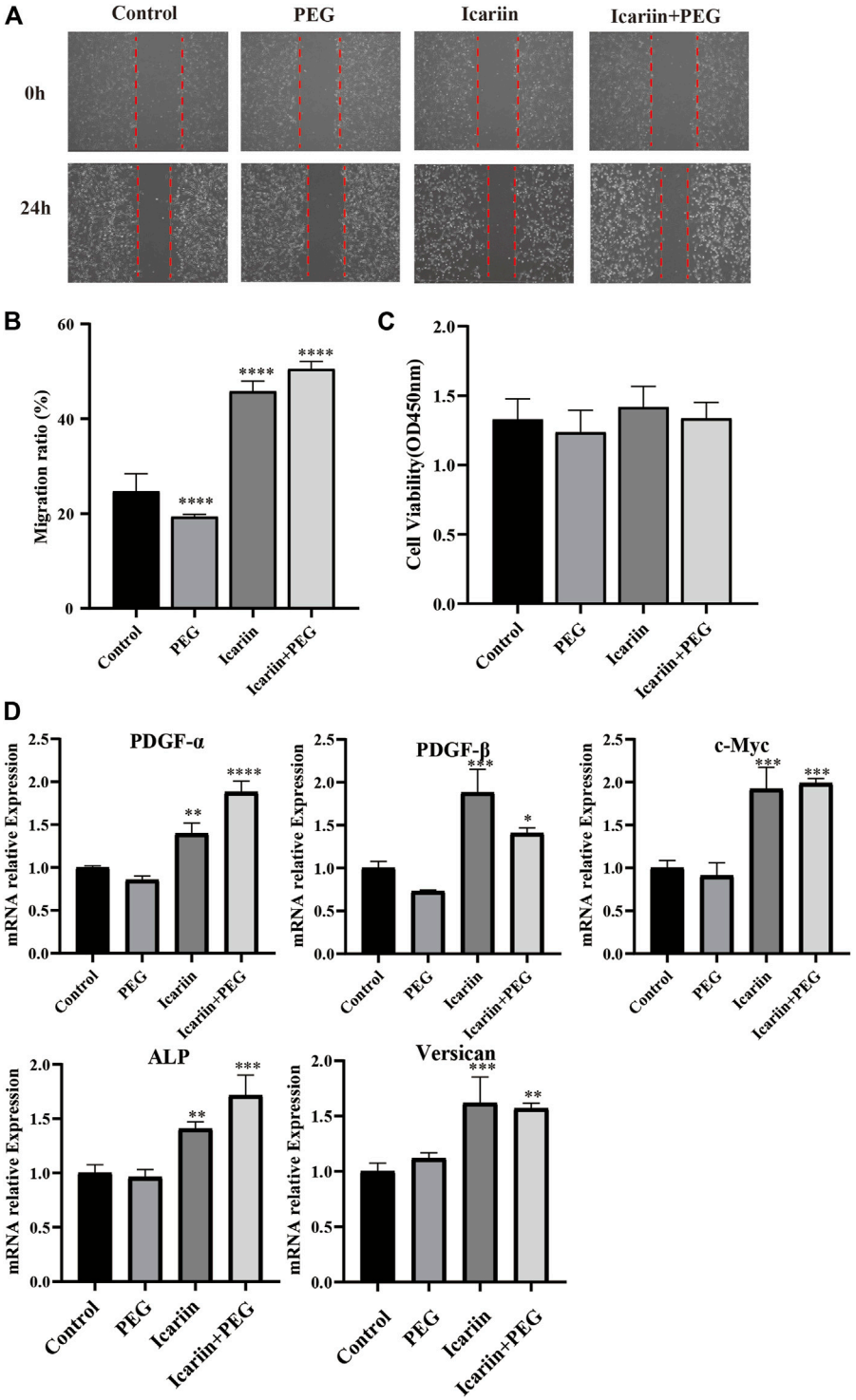

FIGURE 7 | Effect of icariin+PEG hydrogel on the migration, viability, and gene expression of hair follicle dermal papilla cells (HHDPCs). **(A)** Effect of icariin+PEG hydrogel on the migration of HHDPC cells. **(B)** Migration rate of HHDPCs. **(C)** Biocompatibility of different groups. **(D)** RT-PCR analysis of genes that can promote hair-follicle regeneration (*PDGF-α*, *PDGF-β*, c-*Myc, ALP, and Versican*).

biological effects of icariin on the polarization of THP-1 macrophages *in vitro* on the M2 phenotype. After 24 h of treatment with the polymethacrylate (PMA) copolymer, the THP-1 macrophages that adhered to the wall from a suspended state successfully differentiated into M0 macrophages (**Supplementary Figure S3A**). Flow cytometry

experiments revealed an increase in the expression of CD68 induced by PMA, further proving the formation of M0 macrophages (**Supplementary Figure S3B**).

Next, we cultured the newly formed M0 macrophages with PBS, icariin, PEG hydrogel, icariin+PEG hydrogel in the upper chamber of the transwell insert. The macrophages were treated with different dressings for 48 h. **Figure 6A** shows that the macrophages in an environment without icariin are round and aggregated. In contrast, longer spindle-shaped macrophages formed in the presence of icariin. Likewise, the icariin+PEG hydrogel-treated macrophages showed a significantly higher average fluorescence intensity of *CD206* staining, indicating that the M2 polarization state of macrophages had increased considerably (**Figure 6B**). In addition, western blotting showed a higher level of CD206 protein, further confirming the effect of icariin+PEG hydrogel on the polarization of macrophages (**Figure 6C**). These results are consistent with the expression of M2 macrophage-related genes (*IL-10*, *CD206*, and *ARG1*) after treatment with the icariin+PEG hydrogel for 48 h (**Figure 6D**). We further verified the polarization of M2 macrophages after icariin treatment by flow cytometry (**Supplementary Figure S4**). Specifically, compared with the mean fluorescence intensity (MFI) for CD206 staining of the control (0.27), the MFI of the icariin group was significantly increased to 32.4, while that of the positive control group was 41.8. Hence, icariin induced the differentiation of macrophages to the M2 anti-inflammatory type. Additionally, the icariin+PEG hydrogel inhibited the expression of M1 macrophage-related genes (*IL-6*, *TNF-α*, and *IL-8*) after 48 h of treatment (**Figure 6E**). Therefore, the icariin+PEG hydrogel increased the number of M2 anti-inflammatory macrophages even in the inflammatory microenvironment *in vitro*. Furthermore, icariin regulated the polarization of M2 macrophages involved in wound healing.

Icariin+PEG Hydrogel Facilitates the Migration, Viability, and Gene Expression of Hair Follicle Dermal Papilla Cells

Hair dermal papilla is located at the base of the hair follicle and produces hair fibers by inducing epidermal hair-follicle development (Kwack et al., 2018). It plays a crucial role in the hair growth cycle, which is regulated by various molecular pathways, including BMP4 signaling (Liu et al., 2021). To further investigate the effect of icariin+PEG hydrogel, HHDPCs were used to co-culture with separate PEG, separate icariin, and icariin+PEG hydrogel. Icariin alone as well as the icariin+PEG hydrogel effectively promoted HHDPC migration (**Figures 7A,B**). Furthermore, we compared the cell numbers with the results of CCK8 analysis after 48 h (**Figure 7C**). No significant difference was observed between different groups, which proved that our novel material did not harm the vitality and proliferation of HHDPCs. In addition, an obvious effect of the icariin+PEG hydrogel combination in stimulating the expression of some cytokines that can promote hair-follicle regeneration was observed (**Figure 7D**). Significantly, the icariin+PEG hydrogel could stimulate the expression of *PDGF-α*, *PDGF-β*, and *c-Myc* (genes of hair-follicle anagen markers), indicating the stimulation of hair-follicle growth (Kamp et al., 2003; Dong et al., 2017).

BMP4 Signaling Is Required for the Effects of icariin+PEG Hydrogel on Macrophages and HHDPCs

BMP4 plays an important role in embryonic development and tissue homeostasis (Botchkarev and Sharov 2004; Tong et al., 2015; Zylbersztejn et al., 2018). Previous work has shown that icariin is associated with the activation of BMP signaling (Sen et al., 2009; Singh et al., 2019). To determine whether icariin+PEG hydrogel-induced BMP signaling was required for macrophage M2 polarization during the wound healing process, we analyzed western blotting results and noted that BMP4 and the downstream phosphorylated Smad1/5 expression were observably increased after the addition of the icariin+PEG hydrogel (**Figures 8A,B**). Meanwhile, the BMP4 and p-Smad1/5 protein expression of HHDPCs treated with icariin+PEG hydrogel was significantly increased compared to that achieved with the control group (**Figures 8C,D**). Moreover, our immunofluorescence staining of the skin wound revealed that most hair follicles exhibited the activation of Smad1/5 phosphorylation at the dermal papilla, in contrast to the controls (**Supplementary Figure S5**). These results suggest that the icariin+PEG hydrogel can activate BMP4 signaling, which promotes macrophage M2 polarization and hair-follicle regeneration, thus increasing the possibility of wond repair.

DISCUSSION

This study demonstrates for the first time that a thermosensitive hydrogel can adapt to wounds of different shapes and gradually release icariin to further promote wound healing. The study also shows that icariin+PEG hydrogels can polarize macrophages towards an M2 anti-inflammatory phenotype during the wound healing process. In addition, this study shows that the icariin+PEG hydrogel was involved in regulating the formation of new hair follicles and speeding up the process of wound healing. At the molecular level, the icariin+PEG hydrogel promoted wound healing by inducing BMP4 and downstream phosphorylated Smad1/5 activation. A schematic representation of this study is depicted in **Scheme 1**.

The typical treatment for full-thickness skin trauma involves skin transplantation, including autologous transplantation, allogeneic transplantation, xenotransplantation, and skin substitutes (Tavis et al., 1978). Skin substitutes include synthetic scaffolds that can be made with three-dimensional bioprinting using cells (Hosseini and Shafiee 2021). Many bioactive dressings have been developed. In many of these dressings, substances conducive to wound healing can be added, such as drugs, cytokines, and growth factors (Kaushik et al., 2015). A hydrogel is a three-dimensional hydrophilic polymer network, whose structure and function are similar to those of natural extracellular matrix (Sun et al., 2018). In addition, the hydrogel can protect these substances without

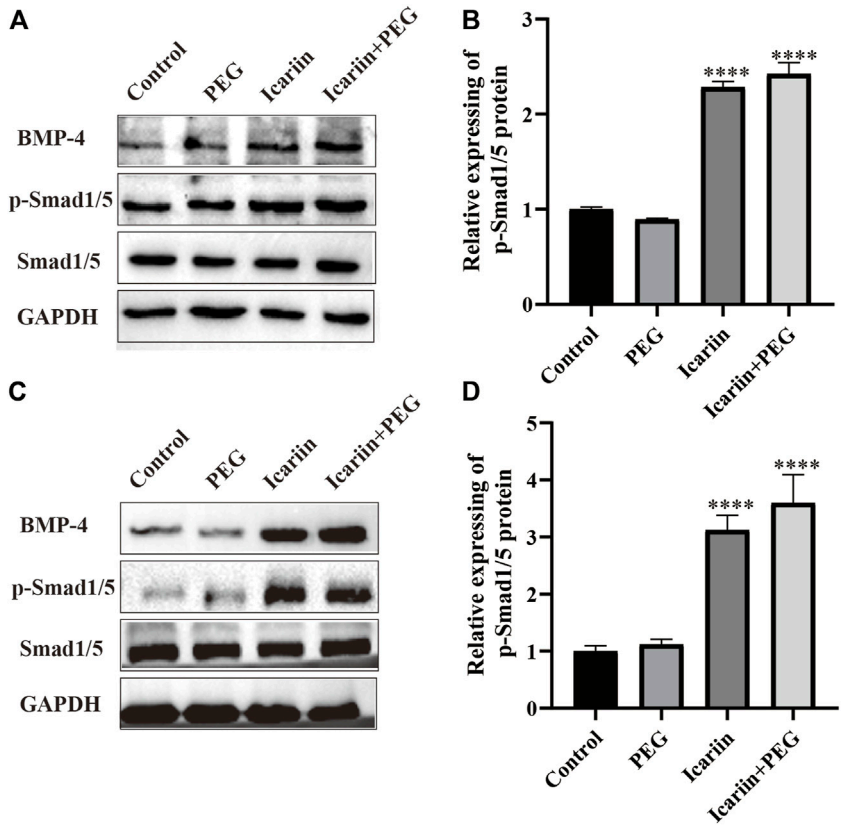

FIGURE 8 | Participation of BMP4 in M2 macrophage polarization and hair-follicle regeneration. **(A)** Protein expression levels of BMP4, p-Smad1/5, and Smad1/5 as detected by western blotting in the macrophages treated with the different dressings for 48 h. **(B)** Quantification of western blotting bands. **(C)** Protein expression levels of BMP4, p-Smad1/5, and Smad1/5 as detected by western blotting in the HHDPCs treated with the different dressings for 48 h. **(D)** Quantification of western blotting bands.

changing their properties, which can then be smoothly delivered to related cells (Xu et al., 2018). PEG-based polymers have a superior biocompatibility; hence, they have been studied as wound-healing scaffolds (Shi et al., 2021). Our team developed a PEG-based temperature-sensitive hydrogel that can be formed *in situ*. The hydrogel had good injection ability and could be injected with a needle to adapt to any irregular shape (**Supplementary Figure S1A**). The time required for turning the liquid hydrogel into a gel could be managed by temperature, which makes the treatment and care of irregular wound more convenient. Rheological tests showed that the hydrogels could fill any irregular wounds before the sol–gel transition process and had excellent self-healing properties. Notably, realization of repair of the complete skin structure mainly depends on the optimum combination of cells, signaling molecules, and scaffolds.

During wound care, any imbalance or defect in the coordinated interaction between multiple cell types, cytokines, and the extracellular matrix can disrupt the balance of related cells and make it difficult to achieve optimum tissue repair, leading to hypertrophic scars that further impair normal tissue function and eventually lead to organ failure and death (Wu et al., 2019). Interestingly, scarless healing can be seen in human fetuses; those with a cleft lip and palate have no obvious scars after undergoing laparoscopic repairs (Mast et al., 1992; Longaker et al., 1994; Bartkowska and Komisarek 2020). Comparison of the wound-healing process in adults and fetuses shows that fetal wounds are characterized by milder inflammation (Lin et al., 1994; Liechty et al., 2000; Walmsley et al., 2015). While the inflammatory response is essential to protect the body from infection and necrosis, preparing the body for the subsequent regeneration is also a major pathogenic factor in scar formation (Childs and Murthy 2017). Fibroblasts, the most important cells involved in repairing damaged tissues, are closely related to inflammation (Landén et al., 2016; McGinty and Siddiqui 2021). When there are excessive inflammatory cells in the early stage of wound healing, fibroblasts are more likely to differentiate into myofibroblasts under the influence of proinflammatory factors like TNF-α and IL-6 (Thulabandu et al., 2018).

Macrophages are widely distributed and one of the most important immune cells in wound healing (Arabpour et al., 2021; Wolf et al., 2021). They are the main phagocytes that perform clearance and secretion functions during the inflammatory phase of wound healing. The phenotype of macrophages and the types of cytokines released can change at different times after trauma and are closely related to the inflammation and remodeling stage of the wound (Zhang and

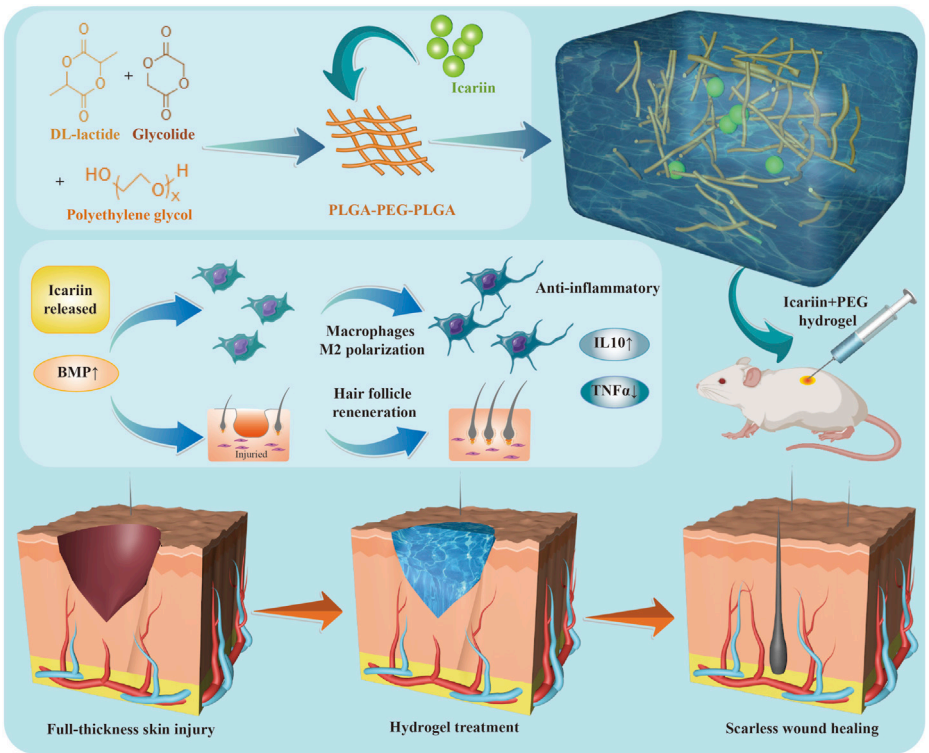

SCHEME 1 | Formation of icariin+PEG hydrogels and mechanism of wound healing.

Mosser 2008; Martinez et al., 2009). They can be stimulated into different types with contrasting functions. Several studies have shown that macrophages undergo morphological changes under the stimulation of different molecular signals (Luu et al., 2015; Jia et al., 2019). In contrast to the M1 type, anti-inflammatory macrophages tend to be elongated (Porcheray et al., 2005; Gao et al., 2019). The morphological changes of macrophages are related to their functional polarization (McWhorter et al., 2015). Elongated macrophages tend to polarize into M2 macrophages and inhibit M1 polarization. We verified that macrophages were induced to polarize to the elongated anti-inflammatory M2 phenotype by icariin released from the hydrogel both *in vivo* and *in vitro*. Furthermore, we showed that the icariin+PEG hydrogel accelerated wound healing and reduced tissue fibrosis. However, it should also be investigated whether persistently inhibiting M1 macrophages will make wounds susceptible to infection and thus difficult to heal, forming chronic wounds. Considering the dual role of macrophages in the wound-healing process, it is necessary to carefully explore the balance between proinflammatory and anti-inflammatory cells.

If the hair follicles are completely destroyed, they cannot be fully regenerated and scar repair occurs (Boyce and Lalley 2018). Several different progenitor cell populations in hair follicles, including bulge, upper bulge, tight junction barrier in hair follicles, and the infundibulum next to sebaceous glands, play an important role in skin regeneration (Hu et al., 2014; Mokos and Mosler 2014; Garcin and Ansell 2017). Genetic tracing of epithelial stem cells expressing K17 in the germ area of the secondary hair of the hair follicle showed that these cells migrated to the epidermis from the full-thickness outer wound surface. This observation showed that after trauma disrupts the epidermal homeostasis, the epithelial stem cells in hair follicles proliferate, supplement epidermal cells, and promote re-epithelialization. Fortunately, our research showed that additional new hair follicles would appear on the skin with this new medicated hydrogel. Hence, it can be speculated that the use of the icariin+PEG hydrogel could exert the expected therapeutic influence. Furthermore, immunofluorescence experiments indicated that most of the hair follicles showed Smad1/5 phosphorylation activation at the dermal papilla, strongly suggesting that the icariin+PEG hydrogel stimulated the formation of hair follicles by activating the BMP4 pathway.

Although BMP signaling has not been directly linked to any stage of wound healing, BMPs are a promising option for skin regeneration because they are related to hair-follicle regeneration and might promote wound healing (Plikus et al., 2017). Interestingly, BMP4 resulting from acute lymphoblastic leukemia can upregulate the expression of interleukin (IL)-10 and promote the polarization of M1-like macrophages to the M2 phenotype (Zylbersztejn et al., 2018). Our results also confirmed that BMP4 signaling is required for the effects of icariin+PEG hydrogel on macrophages and HHDPCs. However, BMP signaling of other cell types in response to injury has not been studied. Previous studies have proved a BMP5 gene regulates the injury element in zebrafish wound models; however, the

mechanisms that lead to the reactivation of BMPs following injury are still unknown (Heller et al., 2022). Therefore, further studies on the therapeutic effects of BMP signaling should be performed to investigate whether it can be targeted therapeutically in skin fibrotic diseases.

CONCLUSION

Our group developed a new thermosensitive *in situ* injectable hydrogel. The precursor hydrogel could be injected into wounds of any shape. It could quickly become a colloid when heated to the temperature of the skin surface, with good mechanical properties and biocompatibility. *In vitro*, the icariin in the hydrogel enhanced the BMP4 signaling pathway and promoted the conversion of macrophages from the M1 phenotype to the M2 phenotype. *In vivo*, the hydrogel reduced inflammation in the early stage of wound healing and significantly increased the number of new hair follicles in the late stage. Overall, the icariin released from the icariin+PEG hydrogel reduced excessive collagen deposition and excess myofibroblast differentiation during skin-wound healing, thereby promoting healing and hair-follicle regeneration. Therefore, it has great potential for practical applications. However, any future successful clinical application of icariin+PEG hydrogels depend on optimizing the release of icariin and precisely regulating the spatiotemporal molecular signals at the injured site during wound healing.

DATA AVAILABILITY STATEMENT

The datasets presented in this study can be found at https://figshare.com/articles/dataset/Date_zip/20138330, DOI:10.6084/m9.figshare.20138330.

ETHICS STATEMENT

The animal study was reviewed and approved by Ethics Committee of The Hospital Affiliated to Jiangnan University.

AUTHOR CONTRIBUTIONS

Y-YT, M-LZ: Conceptualization, Methodology, Formal analysis, Investigation, Writing original draft. S-YL: Resources. YJ: Investigation, Visualization. K-WZ: Resources. Z-DY: Investigation, Resources. J-JW: Visualization. J-XY: Methodology, Formal analysis. SY: Methodology. XL: Writing–review and editing, Funding acquisition. X-JZ: Supervision, Project administration. F-LY: Writing-review and editing, Supervision, Project administration, Funding acquisition.

FUNDING

Funding for this study was provided by the Natural Science Foundation of Jiangsu Province (Grant BK20191141), Top Talent Support Program for young and middle-aged people of Wuxi Health Committee (BJ2020044; BJ2020057; HB2020043), and Fundamental Research Funds of Health and Family Planning Commission of Wuxi (M202024), and special program for translational medicine research of Wuxi translational medicine center (2020DHYB07; 2020DHYB03); Key special project of precision medicine of Wuxi health commission (J202101).

SUPPLEMENTARY MATERIAL

The Supplementary Material for this article can be found online at: https://www.frontiersin.org/articles/10.3389/fbioe.2022.902894/full#supplementary-material

REFERENCES

Arabpour, M., Saghazadeh, A., and Rezaei, N. (2021). Anti-inflammatory and M2 Macrophage Polarization-Promoting Effect of Mesenchymal Stem Cell-Derived Exosomes. *Int. Immunopharmacol.* 97, 107823. doi:10.1016/j.intimp.2021.107823

Bartkowska, P., and Komisarek, O. (2020). Scar Management in Patients after Cleft Lip Repair-Systematic Review Cleft Lip Scar Management. *J. Cosmet. Dermatol* 19 (8), 1866–1876. doi:10.1111/jocd.13511

Blanpain, C., and Fuchs, E. (2009). Epidermal Homeostasis: a Balancing Act of Stem Cells in the Skin. *Nat. Rev. Mol. Cell Biol.* 10 (3), 207–217. doi:10.1038/nrm2636

Borchert, T., Beitar, L., Langer, L. B. N., Polyak, A., Wester, H.-J., Ross, T. L., et al. (2021). Dissecting the Target Leukocyte Subpopulations of Clinically Relevant Inflammation Radiopharmaceuticals. *J. Nucl. Cardiol.* 28 (4), 1636–1645. doi:10.1007/s12350-019-01929-z

Botchkarev, V. A., and Sharov, A. A. (2004). BMP Signaling in the Control of Skin Development and Hair Follicle Growth. *Differentiation* 72 (9-10), 512–526. doi:10.1111/j.1432-0436.2004.07209005.x

Boyce, S. T., and Lalley, A. L. (2018). Tissue Engineering of Skin and Regenerative Medicine for Wound Care. *Burns Trauma* 6, 4. doi:10.1186/s41038-017-0103-y

Chantre, C. O., Campbell, P. H., Golecki, H. M., Buganza, A. T., Capulli, A. K., Deravi, L. F., et al. (2018). Production-scale Fibronectin Nanofibers Promote Wound Closure and Tissue Repair in a Dermal Mouse Model. *Biomaterials* 166, 96–108. doi:10.1016/j.biomaterials.2018.03.006

Childs, D. R., and Murthy, A. S. (2017). Overview of Wound Healing and Management. *Surg. Clin. N. Am.* 97 (1), 189–207. doi:10.1016/j.suc.2016.08.013

Daszczuk, P., Mazurek, P., Pieczonka, T. D., Olczak, A., BoryńŁ, Ł. M., and Kobielak, K. (2020). An Intrinsic Oscillation of Gene Networks inside Hair Follicle Stem Cells: An Additional Layer that Can Modulate Hair Stem Cell Activities. *Front. Cell Dev. Biol.* 8, 595178. doi:10.3389/fcell.2020.595178

de Groot, S. C., Ulrich, M. M. W., Gho, C. G., and Huisman, M. A. (2021). Back to the Future: From Appendage Development toward Future Human Hair Follicle Neogenesis. *Front. Cell Dev. Biol.* 9, 661787. doi:10.3389/fcell.2021.661787

Dong, L., Hao, H., Liu, J., Ti, D., Tong, C., Hou, Q., et al. (2017). A Conditioned Medium of Umbilical Cord Mesenchymal Stem Cells Overexpressing Wnt7a Promotes Wound Repair and Regeneration of Hair Follicles in Mice. *Stem Cells Int.* 2017, 3738071. doi:10.1155/2017/3738071

Feng, Y., Wu, J.-J., Sun, Z.-L., Liu, S.-Y., Zou, M.-L., Yuan, Z.-D., et al. (2020). Targeted Apoptosis of Myofibroblasts by Elesclomol Inhibits Hypertrophic Scar Formation. *EBioMedicine* 54, 102715. doi:10.1016/j.ebiom.2020.102715

Ferrante, C. J., and Leibovich, S. J. (2012). Regulation of Macrophage Polarization and Wound Healing. *Adv. Wound Care (New Rochelle)* 1 (1), 10–16. doi:10.1089/wound.2011.0307

Forbes, S. J., and Rosenthal, N. (2014). Preparing the Ground for Tissue Regeneration: from Mechanism to Therapy. *Nat. Med.* 20 (8), 857–869. doi:10.1038/nm.3653

Funes, S. C., Rios, M., Escobar-Vera, J., and Kalergis, A. M. (2018). Implications of Macrophage Polarization in Autoimmunity. *Immunology* 154 (2), 186–195. doi:10.1111/imm.12910

Gao, S., Wang, Y., Li, D., Guo, Y., Zhu, M., Xu, S., et al. (2019). TanshinoneIIA Alleviates Inflammatory Response and Directs Macrophage Polarization in Lipopolysaccharide-Stimulated RAW264.7 Cells. *Inflammation* 42 (1), 264–275. doi:10.1007/s10753-018-0891-7

Garcin, C. L., and Ansell, D. M. (2017). The Battle of the Bulge: Re-evaluating Hair Follicle Stem Cells in Wound Repair. *Exp. Dermatol* 26 (2), 101–104. doi:10.1111/exd.13184

He, C., Wang, Z., and Shi, J. (2020). Pharmacological Effects of Icariin. *Adv. Pharmacol.* 87, 179–203. doi:10.1016/bs.apha.2019.10.004

Heller, I. S., Guenther, C. A., Meireles, A. M., Talbot, W. S., and Kingsley, D. M. (2022). Characterization of Mouse Bmp5 Regulatory Injury Element in Zebrafish Wound Models. *Bone* 155, 116263. doi:10.1016/j.bone.2021.116263

Hosseini, M., and Shafiee, A. (2021). Engineering Bioactive Scaffolds for Skin Regeneration. *Small*, 17 (41), e2101384. doi:10.1002/smll.202101384

Hu, M. S.-M., Rennert, R. C., McArdle, A., Chung, M. T., Walmsley, G. G., Longaker, M. T., et al. (2014). The Role of Stem Cells during Scarless Skin Wound Healing. *Adv. Wound Care (New Rochelle)* 3 (4), 304–314. doi:10.1089/wound.2013.0471

Ito, M., Yang, Z., Andl, T., Cui, C., Kim, N., Millar, S. E., et al. (2007). Wnt-dependent De Novo Hair Follicle Regeneration in Adult Mouse Skin after Wounding. *Nature* 447 (7142), 316–320. doi:10.1038/nature05766

Jia, Y., Yang, W., Zhang, K., Qiu, S., Xu, J., Wang, C., et al. (2019). Nanofiber Arrangement Regulates Peripheral Nerve Regeneration through Differential Modulation of Macrophage Phenotypes. *Acta Biomater.* 83, 291–301. doi:10.1016/j.actbio.2018.10.040

Jiménez-García, L., Higueras, M. Á., Herranz, S., Hernández-López, M., Luque, A., de Las Heras, B., et al. (2018). A Hispanolone-Derived Diterpenoid Inhibits M2-Macrophage Polarization *In Vitro* via JAK/STAT and Attenuates Chitin Induced Inflammation *In Vivo*. *Biochem. Pharmacol.* 154, 373–383. doi:10.1016/j.bcp.2018.06.002

Kamp, H., Geilen, C. C., Sommer, C., and Blume-Peytavi, U. (2003). Regulation of PDGF and PDGF Receptor in Cultured Dermal Papilla Cells and Follicular Keratinocytes of the Human Hair Follicle. *Exp. Dermatol* 12 (5), 662–672. doi:10.1034/j.1600-0625.2003.00089.x

Kaushik, N., Kaushik, N., Pardeshi, S., Sharma, J., Lee, S., and Choi, E. (2015). Biomedical and Clinical Importance of Mussel-Inspired Polymers and Materials. *Mar. Drugs* 13 (11), 6792–6817. doi:10.3390/md13116792

Kim, I. S., Park, H. C., Quan, H., Kim, Y., Wu, L., and Yang, H. C. (2019). Effects of Triethylene Glycol Dimethacrylate and Hydroxyethyl Methacrylate on Macrophage Polarization. *Int. Endod. J.* 52 (7), 987–998. doi:10.1111/iej.13088

Kwack, M. H., Yang, J. M., Won, G. H., Kim, M. K., Kim, J. C., and Sung, Y. K. (2018). Establishment and Characterization of Five Immortalized Human Scalp Dermal Papilla Cell Lines. *Biochem. Biophysical Res. Commun.* 496 (2), 346–351. doi:10.1016/j.bbrc.2018.01.058

Landén, N. X., Li, D., and Ståhle, M. (2016). Transition from Inflammation to Proliferation: a Critical Step during Wound Healing. *Cell. Mol. Life Sci.* 73 (20), 3861–3885. doi:10.1007/s00018-016-2268-0

Li, M., Hou, Q., Zhong, L., Zhao, Y., and Fu, X. (2021). Macrophage Related Chronic Inflammation in Non-healing Wounds. *Front. Immunol.* 12, 681710. doi:10.3389/fimmu.2021.681710

Liechty, K. W., Adzick, N. S., and Crombleholme, T. M. (2000). Diminished Interleukin 6 (IL-6) Production during Scarless Human Fetal Wound Repair. *Cytokine* 12 (6), 671–676. doi:10.1006/cyto.1999.0598

Limandjaja, G. C., Niessen, F. B., Scheper, R. J., and Gibbs, S. (2021). Hypertrophic Scars and Keloids: Overview of the Evidence and Practical Guide for Differentiating between These Abnormal Scars. *Exp. Dermatol* 30 (1), 146–161. doi:10.1111/exd.14121

Lin, R. Y., Sullivan, K. M., Argenta, P. A., Peter Lorenz, H., and Scott Adzick, N. (1994). Scarless Human Fetal Skin Repair Is Intrinsic to the Fetal Fibroblast and Occurs in the Absence of an Inflammatory Response. *Wound Repair Regen.* 2 (4), 297–305. doi:10.1046/j.1524-475x.1994.20411.x

Liu, J., Mattheos, N., Su, C., Deng, C., Luo, N., Wang, Z., et al. (2018). The Effects of Icariin on Wound Healing of Extraction Sites with Administration of Zoledronic and Dexamethasone: A Rat Model Study. *J. Oral Pathol. Med.* 47 (2), 198–205. doi:10.1111/jop.12659

Liu, G., Cheng, G., Zhang, Y., Gao, S., Sun, H., Bai, L., et al. (2021). Pyridoxine Regulates Hair Follicle Development via the PI3K/Akt, Wnt and Notch Signalling Pathways in Rex Rabbits. *Anim. Nutr.* 7 (4), 1162–1172. doi:10.1016/j.aninu.2021.09.003

Longaker, M. T., Whitby, D. J., Ferguson, M. W. J., Lorenz, H. P., Harrison, M. R., and Adzick, N. S. (1994). Adult Skin Wounds in the Fetal Environment Heal with Scar Formation. *Ann. Surg.* 219 (1), 65–72. doi:10.1097/00000658-199401000-00011

Luu, T. U., Gott, S. C., Woo, B. W. K., Rao, M. P., and Liu, W. F. (2015). Micro- and Nanopatterned Topographical Cues for Regulating Macrophage Cell Shape and Phenotype. *ACS Appl. Mat. Interfaces* 7 (51), 28665–28672. doi:10.1021/acsami.5b10589

Martinez, F. O., Helming, L., and Gordon, S. (2009). Alternative Activation of Macrophages: an Immunologic Functional Perspective. *Annu. Rev. Immunol.* 27, 451–483. doi:10.1146/annurev.immunol.021908.132532

Mast, B. A., Diegelmann, R. F., Krummel, T. M., and Cohen, I. K. (1992). Scarless Wound Healing in the Mammalian Fetus. *Surg. Gynecol. Obstet.* 174 (5), 441–451.

McGinty, S., and Siddiqui, W. J. (2021). *Keloid. StatPearls. Treasure Island (FL), StatPearls Publishing Copyright © 2021*. StatPearls Publishing LLC, Tampa, Florida, United States

McWhorter, F. Y., Davis, C. T., and Liu, W. F. (2015). Physical and Mechanical Regulation of Macrophage Phenotype and Function. *Cell. Mol. Life Sci.* 72 (7), 1303–1316. doi:10.1007/s00018-014-1796-8

Mi, B., Liu, J., Liu, G., Zhou, W., Liu, Y., Hu, L., et al. (2018). Icariin Promotes Wound Healing by Enhancing the Migration and Proliferation of Keratinocytes via the AKT and ERK Signaling Pathway. *Int. J. Mol. Med.* 42 (2), 831–838. doi:10.3892/ijmm.2018.3676

Miao, L., Shen, X., Whiteman, M., Xin, H., Shen, Y., Xin, X., et al. (2016). Hydrogen Sulfide Mitigates Myocardial Infarction via Promotion of Mitochondrial Biogenesis-dependent M2 Polarization of Macrophages. *Antioxidants Redox Signal.* 25 (5), 268–281. doi:10.1089/ars.2015.6577

Mokos, Z. B., and Mosler, E. L. (2014). Advances in a Rapidly Emerging Field of Hair Follicle Stem Cell Research. *Coll. Antropol.* 38 (1), 373–378.

Murawala, P., Tanaka, E. M., and Currie, J. D. (2012). Regeneration: the Ultimate Example of Wound Healing. *Seminars Cell & Dev. Biol.* 23 (9), 954–962. doi:10.1016/j.semcdb.2012.09.013

Owen, R., Bahmaee, H., Claeyssens, F., and Reilly, G. C. (2020). Comparison of the Anabolic Effects of Reported Osteogenic Compounds on Human Mesenchymal Progenitor-Derived Osteoblasts. *Bioeng. (Basel)* 7 (1). doi:10.3390/bioengineering7010012

Plikus, M. V., Guerrero-Juarez, C. F., Ito, M., Li, Y. R., Dedhia, P. H., Zheng, Y., et al. (2017). Regeneration of Fat Cells from Myofibroblasts during Wound Healing. *Science* 355 (6326), 748–752. doi:10.1126/science.aai8792

Porcheray, F., Viaud, S., Rimaniol, A.-C., Léone, C., Samah, B., Dereuddre-Bosquet, N., et al. (2005). Macrophage Activation Switching: an Asset for the Resolution of Inflammation. *Clin. Exp. Immunol.* 142 (3), 481–489. doi:10.1111/j.1365-2249.2005.02934.x

Pratsinis, H., Mavrogonatou, E., and Kletsas, D. (2019). Scarless Wound Healing: From Development to Senescence. *Adv. Drug Deliv. Rev.* 146, 325–343. doi:10.1016/j.addr.2018.04.011

Rippa, A. L., Kalabusheva, E. P., and Vorotelyak, E. A. (2019). Regeneration of Dermis: Scarring and Cells Involved. *Cells* 8 (6). 607. doi:10.3390/cells8060607

Sen, C. K., Gordillo, G. M., Roy, S., Kirsner, R., Lambert, L., Hunt, T. K., et al. (2009). Human Skin Wounds: a Major and Snowballing Threat to Public Health and the Economy. *Wound Repair Regen.* 17 (6), 763–771. doi:10.1111/j.1524-475x.2009.00543.x

Shen, R., and Wang, J. H. (2018). The Effect of Icariin on Immunity and its Potential Application. *Am. J. Clin. Exp. Immunol.* 7 (3), 50–56.

Shi, J., Yu, L., and Ding, J. (2021). PEG-based Thermosensitive and Biodegradable Hydrogels. *Acta Biomater.* 128, 42–59. doi:10.1016/j.actbio.2021.04.009

Sindrilaru, A., Peters, T., Wieschalka, S., Baican, C., Baican, A., Peter, H., et al. (2011). An Unrestrained Proinflammatory M1 Macrophage Population

Induced by Iron Impairs Wound Healing in Humans and Mice. *J. Clin. Invest.* 121 (3), 985–997. doi:10.1172/jci44490

Singh, W. R., Devi, H. S., Kumawat, S., Sadam, A., Appukuttan, A. V., Patel, M. R., et al. (2019). Angiogenic and MMPs Modulatory Effects of Icariin Improved Cutaneous Wound Healing in Rats. *Eur. J. Pharmacol.* 858, 172466. doi:10.1016/j.ejphar.2019.172466

Stoddard, F. J., Jr., Ryan, C. M., and Schneider, J. C. (2014). Physical and Psychiatric Recovery from Burns. *Surg. Clin. N. Am.* 94 (4), 863–878. doi:10.1016/j.suc.2014.05.007

Sun, G., Shen, Y. I., and Harmon, J. W. (2018). Engineering Pro-regenerative Hydrogels for Scarless Wound Healing. *Adv. Healthc. Mater* 7 (14), e1800016. doi:10.1002/adhm.201800016

Takeo, M., Lee, W., and Ito, M. (2015). Wound Healing and Skin Regeneration. *Cold Spring Harb. Perspect. Med.* 5 (1), a023267. doi:10.1101/cshperspect.a023267

Tavis, M. J., Thornton, J., Danet, R., and Bartlett, R. H. (1978). Current Status of Skin Substitutes. *Surg. Clin. N. Am.* 58 (6), 1233–1248. doi:10.1016/s0039-6109(16)41688-9

Thulabandu, V., Chen, D., and Atit, R. P. (2018). Dermal Fibroblast in Cutaneous Development and Healing. *Wiley Interdiscip. Rev. Dev. Biol.* 7 (2). 1. doi:10.1002/wdev.307

Tong, K. K., Ma, T. C., and Kwan, K. M. (2015). BMP/Smad Signaling and Embryonic Cerebellum Development: Stem Cell Specification and Heterogeneity of Anterior Rhombic Lip. *Dev. Growth Differ.* 57 (2), 121–134. doi:10.1111/dgd.12198

Walmsley, G. G., Maan, Z. N., Wong, V. W., Duscher, D., Hu, M. S., Zielins, E. R., et al. (2015). Scarless Wound Healing: Chasing the Holy Grail. *Plastic Reconstr. Surg.* 135 (3), 907–917. doi:10.1097/prs.0000000000000972

Wolf, S. J., Melvin, W. J., and Gallagher, K. (2021). Macrophage-mediated Inflammation in Diabetic Wound Repair. *Semin. Cell Dev. Biol.* 119, 111-118. doi:10.1016/j.semcdb.2021.06.013

Wu, J., Chen, A., Zhou, Y., Zheng, S., Yang, Y., An, Y., et al. (2019). Novel H2S-Releasing Hydrogel for Wound Repair via *In Situ* Polarization of M2 Macrophages. *Biomaterials* 222, 119398. doi:10.1016/j.biomaterials.2019.119398

Xie, L., Liu, N., Xiao, Y., Liu, Y., Yan, C., Wang, G., et al. (2020). *In Vitro* and *In Vivo* Osteogenesis Induced by Icariin and Bone Morphogenetic Protein-2: A Dynamic Observation. *Front. Pharmacol.* 11, 1058. doi:10.3389/fphar.2020.01058

Xu, Q., Guo, L., Sigen, A., Gao, Y., Zhou, D., Greiser, U., et al. (2018). Injectable Hyperbranched Poly(β-Amino Ester) Hydrogels with On-Demand Degradation Profiles to Match Wound Healing Processes. *Chem. Sci.* 9 (8), 2179–2187. doi:10.1039/c7sc03913a

Zhang, X., and Mosser, D. (2008). Macrophage Activation by Endogenous Danger Signals. *J. Pathol.* 214 (2), 161–178. doi:10.1002/path.2284

Zhang, Q.-Z., Su, W.-R., Shi, S.-H., Wilder-Smith, P., Xiang, A. P., Wong, A., et al. (2010). Human Gingiva-Derived Mesenchymal Stem Cells Elicit Polarization of M2 Macrophages and Enhance Cutaneous Wound Healing. *Stem Cells* 28 (10), 1856–1868. doi:10.1002/stem.503

Zhang, B., Tsai, P.-C., Gonzalez-Celeiro, M., Chung, O., Boumard, B., Perdigoto, C. N., et al. (2016). Hair Follicles' Transit-Amplifying Cells Govern Concurrent Dermal Adipocyte Production through Sonic Hedgehog. *Genes Dev.* 30 (20), 2325–2338. doi:10.1101/gad.285429.116

Zhang, S., Liu, Y., Zhang, X., Zhu, D., Qi, X., Cao, X., et al. (2018). Prostaglandin E2 Hydrogel Improves Cutaneous Wound Healing via M2 Macrophages Polarization. *Theranostics* 8 (19), 5348–5361. doi:10.7150/thno.27385

Zhao, X., Wu, H., Guo, B., Dong, R., Qiu, Y., and Ma, P. X. (2017). Antibacterial Anti-oxidant Electroactive Injectable Hydrogel as Self-Healing Wound Dressing with Hemostasis and Adhesiveness for Cutaneous Wound Healing. *Biomaterials* 122, 34–47. doi:10.1016/j.biomaterials.2017.01.011

Zhao, Q. N., Zhou, Y. M., Ma, Y. Y., and Han, H. H. (2021). Research Advances on the Effect of Early Intervention on Post-traumatic Scar Formation. *Zhonghua Shao Shang Za Zhi* 37 (7), 697–701. doi:10.3760/cma.j.cn501120-20200315-00169

Zhong, Y., Wang, J., Yuan, Z., Wang, Y., Xi, Z., Li, L., et al. (2019). A Mussel-Inspired Carboxymethyl Cellulose Hydrogel with Enhanced Adhesiveness through Enzymatic Crosslinking. *Colloids Surfaces B Biointerfaces* 179, 462–469. doi:10.1016/j.colsurfb.2019.03.044

Zhu, Y., Zhang, J., Song, J., Yang, J., Xu, T., Pan, C., et al. (2017). One-step Synthesis of an Antibacterial and Pro-healing Wound Dressing that Can Treat Wound Infections. *J. Mat. Chem. B* 5 (43), 8451–8458. doi:10.1039/c7tb02477k

Zylbersztejn, F., Flores-Violante, M., Voeltzel, T., Nicolini, F.-E., Lefort, S., and Maguer-Satta, V. (2018). The BMP Pathway: A Unique Tool to Decode the Origin and Progression of Leukemia. *Exp. Hematol.* 61, 36–44. doi:10.1016/j.exphem.2018.02.005

Conflict of Interest: The authors declare that the research was conducted in the absence of any commercial or financial relationships that could be construed as a potential conflict of interest.

Publisher's Note: All claims expressed in this article are solely those of the authors and do not necessarily represent those of their affiliated organizations, or those of the publisher, the editors and the reviewers. Any product that may be evaluated in this article, or claim that may be made by its manufacturer, is not guaranteed or endorsed by the publisher.

Copyright © 2022 Teng, Zou, Liu, Jia, Zhang, Yuan, Wu, Ye, Yu, Li, Zhou and Yuan. This is an open-access article distributed under the terms of the Creative Commons Attribution License (CC BY). The use, distribution or reproduction in other forums is permitted, provided the original author(s) and the copyright owner(s) are credited and that the original publication in this journal is cited, in accordance with accepted academic practice. No use, distribution or reproduction is permitted which does not comply with these terms.

frontiers | Frontiers in Bioengineering and Biotechnology

ORIGINAL RESEARCH
published: 05 July 2022
doi: 10.3389/fbioe.2022.831007

Poloxamer 407 and Hyaluronic Acid Thermosensitive Hydrogel-Encapsulated Ginsenoside Rg3 to Promote Skin Wound Healing

Xiaojuan Peng[1†], Chuanbo Ding[2†], Yingchun Zhao[1], Mingqian Hao[1], Wencong Liu[1], Min Yang[2]*, Fengyan Xiao[2] and Yinan Zheng[1]*

[1]College of Chinese Medicinal Materials, Jilin Agricultural University, Changchun, China, [2]Jilin Agricultural Science and Technology University, Jilin, China

OPEN ACCESS

Edited by:
Bruce Alan Bunnell, University of North Texas Health Science Center, United States

Reviewed by:
Linli Zhou, University of Cincinnati, United States
Ahmed El-Fiqi, Dankook University, South Korea
Giovanni Vozzi, University of Pisa, Italy
Jochen Salber, Ruhr-University Bochum, Germany

***Correspondence:**
Wencong Liu
liuwencong@jlau.edu.cn
Min Yang
15356067@qq.com

[†]These authors have contributed equally to this work

Specialty section:
This article was submitted to Tissue Engineering and Regenerative Medicine, a section of the journal Frontiers in Bioengineering and Biotechnology

Received: *07 December 2021*
Accepted: *23 May 2022*
Published: *05 July 2022*

Citation:
Peng X, Ding C, Zhao Y, Hao M, Liu W, Yang M, Xiao F and Zheng Y (2022) Poloxamer 407 and Hyaluronic Acid Thermosensitive Hydrogel-Encapsulated Ginsenoside Rg3 to Promote Skin Wound Healing. Front. Bioeng. Biotechnol. 10:831007. doi: 10.3389/fbioe.2022.831007

Ginsenoside Rg3 has shown beneficial effects in various skin diseases. The current interest in designing and developing hydrogels for biomedical applications continues to grow, inspiring the further development of drug-loaded hydrogels for tissue repair and localized drug delivery. The aim of the present study was to develop an effective and safe hydrogel (Rg3-Gel), using ginsenoside Rg3, and we evaluated the wound-healing potential and therapeutic mechanism of Rg3-Gel. The results indicated that the optimized Rg3-Gel underwent discontinuous phase transition at low and high temperatures. Rg3-Gel also exhibited good network structures, swelling water retention capacity, sustainable release performance, and excellent biocompatibility. Subsequently, the good antibacterial and antioxidant properties of Rg3-Gel were confirmed by *in vitro* tests. In full-thickness skin defect wounded models, Rg3-Gel significantly accelerated the wound contraction, promoted epithelial and tissue regeneration, and promoted collagen deposition and angiogenesis. In addition, Rg3-Gel increased the expression of autophagy proteins by inhibiting the MAPK and NF-KB pathways *in vivo*. It simultaneously regulated host immunity by increasing the abundance of beneficial bacteria and the diversity of the wound surface flora. From these preliminary evaluations, it is possible to conclude that Rg3-Gel has excellent application potential in wound-healing drug delivery systems.

Keywords: ginsenoside Rg3, hydrogel, wound healing, autophagy, microbiota

1 INTRODUCTION

The skin is the largest and most extensive organ in the human body. The skin acts as a wall between the organism and the exterior milieu to protect the underlying organs, perform physiological functions necessary for survival, and resist external pathogens given its constant exposure to potential injury in daily life (Proksch et al., 2008; Takeo et al., 2015). Wounds are among the most common skin conditions, representing a discontinuity and loss function of the epithelial integrity. High morbidity of cutaneous injuries imposes a significant burden on both the individual patient's physical and healthcare economy, even requiring long-term painstaking treatment with the potential for cosmetic damage or death.

Wound healing, a complex coordinated process subjected to many intrinsic and exogenous imbalances, is an evolved dynamic biological process essential for species' survival. Wound healing

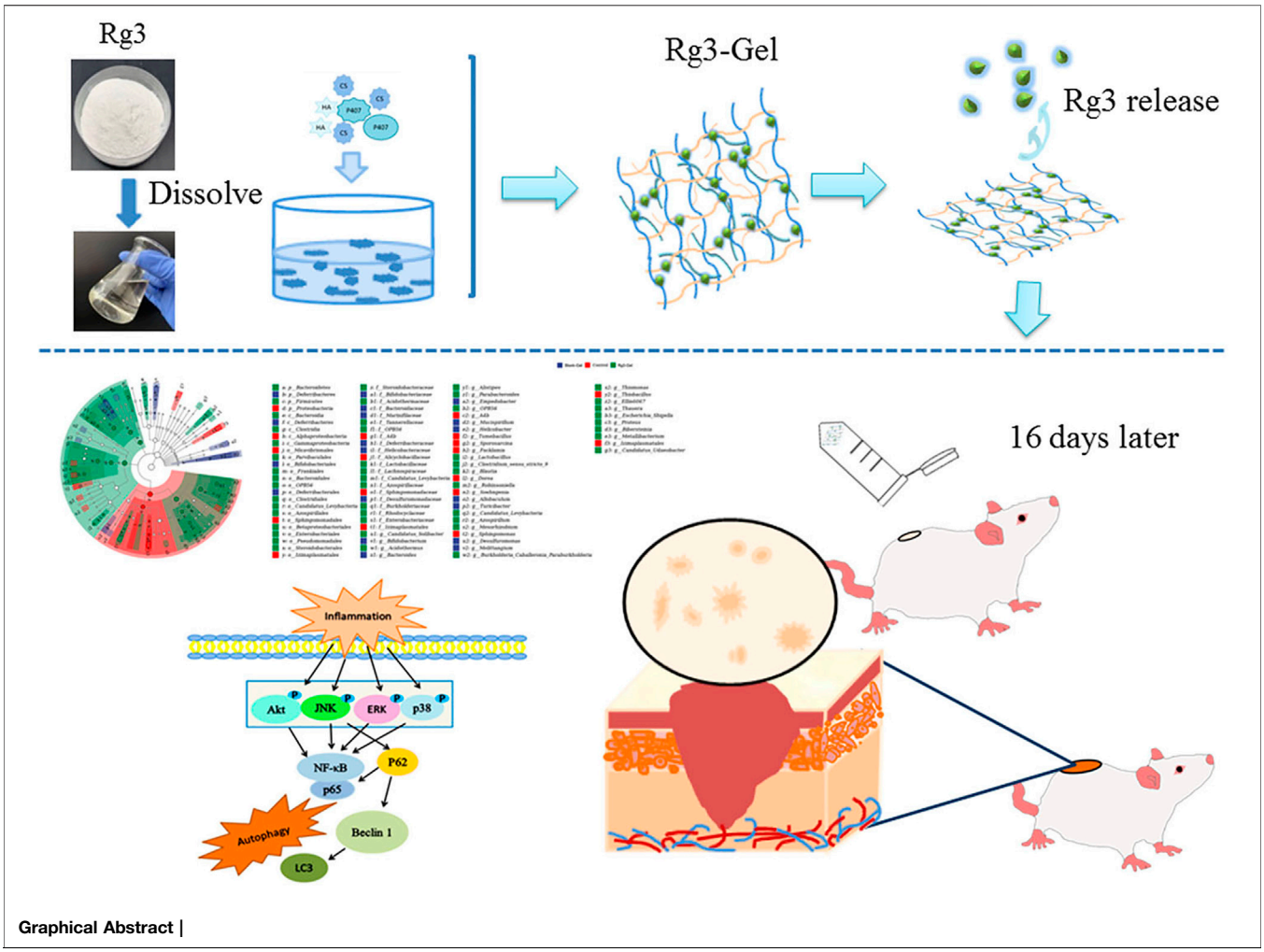

Graphical Abstract |

involves tightly controlled biochemical and cellular events, such as inflammation, proliferation, and remodeling, which occur sequentially in a continuous and sometimes overlapping fashion (Wang P.-H. et al., 2018; Oryan et al., 2019; Singer, 2022). The main goal of tissue regeneration in wound healing is the speed and quality of healing to effectively regenerate new healthy *epidermis* and lead to better cosmetic results. Wound management preparations should actively modulate the three phases of wound healing. A key concomitant activity in the proliferative phase of many healing wounds is the induced presence of vessel growth, a process known as angiogenesis (Veith et al., 2019). Epithelialization is another essential component of wound healing. Re-epithelialization begins with the migration of keratinocytes and participates in the cellular and molecular processes that initiate, maintain, and complete epithelialization, which in turn control wound closure and repair events (Pastar et al., 2014). During the proliferation and remodeling phases, various types of cells are extensively activated to induce the production of growth factors, following which, the wound surface recovers through re-epithelialization, collagen synthesis, matrix deposition, and vessel reconstruction (Reinke and Sorg, 2012; Pastar et al., 2014).

Emerging evidence has linked autophagy to skin wound healing. Recently, numerous studies have shown that autophagy is a process of cell catabolism to degrade and recover cytoplasmic components in eukaryotes (Sil et al., 2018; Ren et al., 2022). In addition to promoting the activation of inflammatory cells and enhancing their anti-inflammatory and anti-infective activities, autophagy is also beneficial to cell survival, migration, and proliferation associated with healing, thereby playing an important role in maintaining cell homeostasis under physiological and pathophysiological conditions. The impact of skin microbiome host interactions on wound-healing outcomes is another field of exciting research. The exact role of the microbiome in wound healing remains unclear, let alone the mechanisms of healing using therapeutics. Human skin harbors one billion microorganisms/cm2, collectively termed the microbiota, which can promote innate and adaptive immune responses to promote normal skin homeostasis and provide pathogen defense when the skin is intact (Pistone et al., 2021). Current studies suggest that many of these dimensions change, especially when wounds are formed, including microbial diversity, microbial load, and abundance of potential pathogens (Xu and Hsia, 2018). If the wound is not

rapidly healed, the accumulation of inflammatory exudates can cause damage to the wound microenvironment and cell damage, following which, the skin microbes can multiply into sterile tissues, leading to bacterial overgrowth and infection, which thereby delay and complicate wound healing.

With an increased understanding of previously unknown cellular and molecular pathways involved in wound-healing processes, a broad range of further development is also underway based on new biomaterials and material fabrication techniques. So far, researchers are not only committed to rapidly expanding the range of research on wound dressings, such as sponges, foams, electrospun nanofibers, membranes, and hydrogels but also pay close attention to excavating their functions to exert advantage of their use in treatment (Dong and Guo, 2021). Hydrogels are generally synthesized from natural or synthetic crosslinked polymers and defined as highly hydrated three-dimensional (3D) linked network structures that have excellent ability to swell and bind several-fold more water or biological fluids, which enable them to be used as vehicles for the delivery of small and large drug molecules, providing them with versatile applications in biomedical areas (Tavakoli and Klar, 2020). Hydrogel networks can be cast into various sizes and shapes that are ideal to meet the demands of effective target drug delivery and rapid wound closure due to their unique properties. In particular, thermosensitive hydrogels are considered promising candidates for partial application of local therapy, which rapidly and reversibly undergo sol–gel transition behavior depending on ambient temperature changes, endowing the drug delivery capacity with controllable local spatial and temporal effects, as well as with moldability, biocompatibility, biodegradability, and tissue similarity to improve the bioavailability of drugs.

Ginsenoside Rg3 (Rg3) is one of the most important components from the traditional Chinese medicine Panax ginseng and has emerged as an effective anti-oxidative, anti-inflammatory, anticancer, antifatiguing, and cardioprotective medicine with evident effects (Kao et al., 2020). Recently, the use of Rg3 in the skin has started gaining considerable research attention, and Rg3 is considered to have therapeutic benefits in malignant melanoma, atopic dermatitis, skin senescence, and skin healing (Shan et al., 2014; Lee et al., 2018, 2019). Moreover, several studies have suggested that Rg3 serves as an early intervention for treating patients with hypertrophic scars (HS) by promoting wound healing in the early stage and inhibiting scar hyperplasia in the late stage (Cheng et al., 2013; Sun et al., 2014; Xu et al., 2019). Previous studies on the pharmacological effects of Rg3 can provide a theoretical basis for its application in skin treatment. However, Rg3 is a crystalline drug that is almost insoluble in water and dissolves only slightly in the mixed solvent of chloroform and methanol and dimethyl sulfoxide (DMSO) and other organic solvents; this greatly limits the bioavailability and formulation development of Rg3 (Yu et al., 2015). Therefore, the preparation of an effective drug delivery for Rg3 is critical to increase Rg3 solubility and improve absorption. In recent years, Rg3 has been tested in various formulations, including electrospun membranes, microparticles, microspheres, liposomes, and nanoparticles (Wang X. et al., 2018; Cheng et al., 2020). Some of the previous studies proposed the use of a nano-in-micro electrospun fiber membrane to fully exploit the potential of Rg3 as a skin repair drug delivery system (Cheng et al., 2020). However, to the best of our knowledge, no previous study has reported on the use of ginsenoside Rg3-loaded hydrogel wound dressings.

2 MATERIALS AND METHODS

2.1 Materials

2.1.1 Chemicals

Ginsenoside Rg3 was produced in the laboratory (the purified Rg3, having two configurations >95% total composition); P407 was supplied by BASF (Ludwigshafen, Germany); low-molecular-weight chitosan obtained from shrimp shells (*Pandalus borealis*) was purchased from Sigma-Aldrich (Shanghai) Trading Co., Ltd (the deacetylation degree of chitosan was 95.8%); sodium hyaluronate (15–25 MDa) was purchased from Shanghai Yuanye Bio-Technology Co., Ltd; SDS was purchased from Beijing Solarbio Science Technology Co., Ltd.; HPLC-grade acetonitrile (LiChrosolv®, CAS-No: 67-56-1) was purchased from Merck (Darmstadt, Germany); RIPA lysis buffer and BCA protein assay kit (BCA) were purchased from Beyotime Institute of Biotechnology (Jiangsu, China); the antibodies against p-ERK, p-JNK, and p-p38 were obtained from Cell Signaling Technology (Beverly, United States); antibodies against β-actin, GAPDH, and the goat antirabbit secondary antibody, NF-κB p65, Akt, ERK, JNK, p38, LC3, and Beclin-1 were obtained from the Proteintech (Santa Cruz, CA, United States); and antibodies against p-Akt and p62 were obtained from Arigo Biolaboratories Corp.

2.1.2 Animal and Cell Lineages

Male ICR mice weighing 20–30 g were obtained from YiSi Experimental Animal Co., Ltd. (Chang Chun, China). The human immortalized keratinocytes (HaCat) cell line was purchased from Guangzhou Cellcook Biotech Co., Ltd.

DMEM medium, penicillin–streptomycin antibiotics (PS), fetal bovine serum albumin (FBS), and phosphate buffer saline (PBS) were purchased from Thermo Fisher Biochemical Products Co., Ltd. Moreover, 3-(4,5-Dimethyl-2-thiazolyl)-2,5-diphenyl-2H-tetrazolium bromide (MTT) was obtained from Aladdin Industrial Corporation (Shanghai, China).

2.2 Preparation of Rg3-Gel

The preparation of our hydrogel is partly based on the method explained by Soriano-Ruiza and colleagues (Soriano-Ruiz et al., 2020). In accordance with their published work, the required amounts of chitosan (CS) were prepared by adding the weight quantity in acetic acid solution (0.5% w/v) with continuous stirring until completely dissolved, and the required amounts of P407 were subsequently used for inclusion of Cs solutions using the cold method. HA 5% (w/v) solutions were prepared by adding hyaluronic acid (HA) to distilled water under continuous stirring for 1 h at room temperature and then utilized for inclusion of before adding Poloxamer 407(P407) and CS using

the cold method. The precipitates of these polymer contents were then removed to get completely clear solutions obtained *in situ* forming hydrogels. Next, 10 mg Rg3 were pre-dissolved in 1 ml of SDS aqueous solution (0.4%, w/v) and then mixed with 9 ml of P407/Cs/HA in drug-loaded hydrogels using an AB mixing tube.

2.3 Characterization of Rg3-Gel

Fourier transform infrared spectroscopy (FT-IR) of the hydrogel was performed to confirm the chemical compositions of the prepared Rg3:P407:Cs:HA (Rg3-Gel) hydrogels. Both freeze-dried Rg3-Gel and Blank-Gel were mixed with KBr and compressed into a flake, the samples were scanned and recorded by FT-IR, and the spectroscopy was performed on a Thermo (United States) Nicolet iS50 in the wavelength range of 500–4,000 cm^{-1}.

The X-ray diffraction (XRD) curves of the freeze-dried hydrogels and raw Rg3, P407, Cs, and HA were recorded using an X-ray diffractometer (JDX-3532 JEOL Japan), with the angle of diffraction (2θ) and the counts. The diffraction angle ranged from 10° to 80° at 45 kV and 40 mA.

The surface morphological structure of the prepared Rg3-Gel was examined by using a scanning electron micro-scope (SEM, BX-51; Olympus; Tokyo, Japan), and photographs were taken using a lens at ×800 and ×4000 magnification power. Before the observation, all the samples were freeze-dried and sputter-coated with gold.

2.4 Properties of Rg3-Gel

2.4.1 Swelling Behavior

The swelling ratio of the Blank-Gel and Rg3-Gel were studied by the gravimetric method. The oven-dried samples of the hydrogels were weighed (Wd) and recorded before being immersed in phosphate-buffered saline (PBS) at 37°C. At regular intervals, the swollen samples were removed and the weight (Ww) was measured after carefully wiping off the surface moisture. The measurements were continued until the equilibrium swelling state was achieved.

The swelling ratio was calculated according to the following equation:

$$\textbf{Swelling ratio}\,(\%) = (\mathbf{Ww} - \mathbf{Wd})/\,\mathbf{Wd},$$

where Ww and Wd represent the weight of the hydrogel after swelling and the weight of the hydrogel after freeze-drying, respectively.

2.4.2 *In Vitro* Drug Release

The *in vitro* drug release experiment of Rg3-Gel was performed with slight modification according to a previously described method (Song et al., 2019). Briefly, hydrogel samples with PBS buffer solution (pH 7.4, 0.01 M) were placed into a 10-ml centrifuge tube at 37°C. Equal amounts of samples were collected at predetermined time intervals and added to the volume of fresh PBS buffer solution medium in order to maintain a simulated release condition. Then, the concentration of Rg3 was determined by using high performance liquid chromatography (HPLC) analysis (Waters 2,695). The mobile phase consisted of acetonitrile (solvent A), water (solvent B), and acetonitrile at a flow rate of 1.0 ml/min. The column used was an Ultimate SHISEIDO PAK C18 ACR (4.6 mm × 250 mm, 5 μm), and the detector wavelength was set to 203 nm. The samples were performed in triplicate for each experiment. The cumulative release mass and percentage at the intervals of each time point was calculated.

Additional information and details regarding the *in vitro* activity studies are available in the Materials and Methods section in the Supporting Information.

2.5 *In Vivo* Wound Healing Studies

2.5.1 Animal Experimental Protocol

All animal experiments were conducted in accordance with the relevant laws and institutional guidelines, and were approved by the Animal Ethics Committee of Jilin Agricultural University. Thirty-six healthy male ICR mice weighing 20–30 g were used in this study. The animals were divided into clean cages under a temperature-controlled condition of 23 ± 2°C. After being reared adaptively for 1 week, the mice were anesthetized *via* intraperitoneal injection of chloral hydrate (0.3 mg/kg body weight). Subsequently, the dorsal hair on their backs was shaved using an electric razor, before being depilated up to the depth of loose subcutaneous tissue and disinfected with 70% alcohol. Next, 10 mm diameter circular full-thickness wounds were created on the back of each mouse under aseptic conditions. These wound mice were randomly distributed to three groups ($n = 12$ mice per group): mice in group I did not receive any treatment (naked injury–Control), group II mice were treated with Blank-Gel, while mice in group III were once daily treated with Rg3-Gel, the total amount of each administration was 200 ml. The wound area of the lesions was photographed and measured (ImageJ software) at days 0, 4, 8, 12, and 16.

The degree of wound healing was expressed as the wound contraction ratio (WCR) to assess the wound-healing property. The WCR was calculated by the following equation:

$$\textit{Percentage of wound contraction}\ (\%) = (\boldsymbol{A0} - \boldsymbol{At})/\boldsymbol{A0}\times 100\%,$$

where A0 and At represent the initial wound area and the wound area at certain times, respectively.

2.5.2 Histopathological Evaluation

Histology was performed to evaluate the degree of healthy skin dermal organization, keratin staining, collagen staining, extracellular matrix composition and organization, and the structural integrity of cellularized constructs. Briefly, each mouse was euthanized at the experimental endpoint of 16 days. Wound lesion tissues were harvested and immediately cleaned with PBS, before fixing in 4% paraformaldehyde buffer for 48 h. The fixed samples were dehydrated in graded ethanol, cleaned with xylene, and embedded in paraffin blocks. Both the center and edge portions of the tissue were subsequently sliced into 5 μm sections and stained using hematoxylin–eosin (H&E) and Masson's trichrome staining kits, respectively, according to the manufacturer's guidelines. The slides were then imaged by light microscopy.

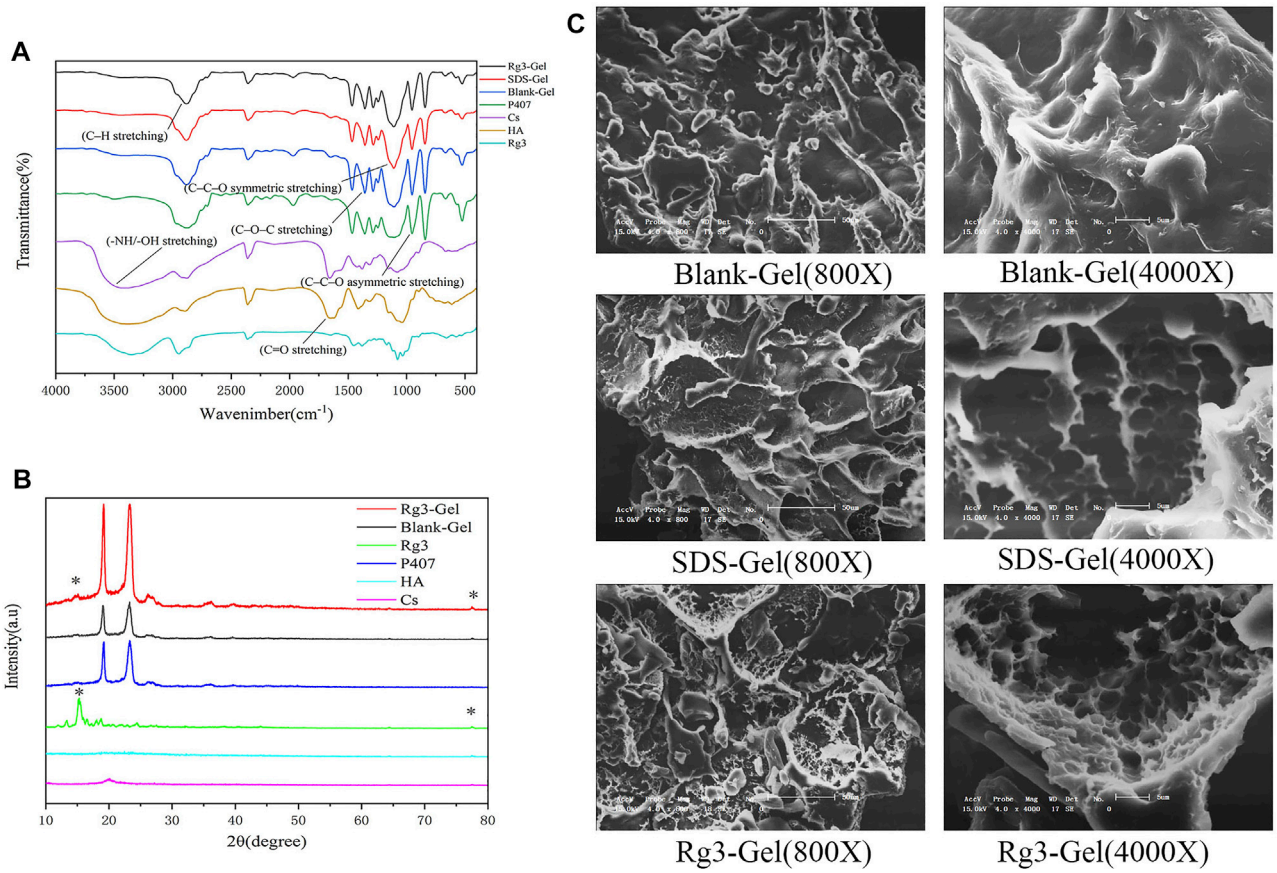

FIGURE 1 | Structural characteristics of the Rg3-Gel. **(A)** Fourier transform infrared spectra of Rg3, neat P407, Cs, HA, Blank-Gel, SDS-Gel, and Rg3-Gel. **(B)** XRD pattern of Rg3, neat P407, Cs, HA, Blank-Gel, and Rg3-Gel. **(C)** SEM images of freeze-dried Blank-Gel, SDS-Gel, and Rg3-Gel samples (X800 & X4000).

2.5.3 Immunofluorescence Analysis

Using the same method described in the H&E staining section, the immunofluorescence of the wound section on the 16th day after surgery was conducted on sections with a thickness of 5 μm. After that, the tissue samples were deparaffinized with xylene, dehydrated with ethanol solutions (100, 95, and 80%), and blocked with PBS solution with 10% goat serum. The sections were further incubated with the primary antibody pan-keratin and then with specific secondary antibodies and DAPI. The stained sections were observed using a fluorescence microscope (Olympus IX71 Corporation, Tokyo, Japan), and the structures positive stained with pan-keratin (green) and DAPI nuclear staining (blue) were identified and photographed.

2.6 Western Blotting

Western blotting was conducted as described previously (Kim et al., 2018). The cell extracts were prepared using RIPA protein lysate (Beyotime, P0013) and measured by a Bio-Rad protein assay. The proteins were separated on 10% sodium dodecyl sulfate polyacrylamide gel electrophoresis (SDS-PAGE), blotted onto PVDF membranes, and the membranes were immediately blocked with 5% skim milk/bovine serum albumin (BSA) in tris-buffered saline and Tween 20 (TBST) for 1 h at room temperature, followed by incubation with primary antibodies at 4°C overnight. Following incubation, the blots were incubated with the corresponding horseradish peroxidase secondary antibody. The target proteins were visualized with an enhanced chemiluminescence system using ECL Advance Western Blotting Detection Reagents (GE Healthcare, Buckinghamshire, United Kingdom). Densitometric analysis for the quantification of the band intensities was performed using ImageJ software.

2.7 Analysis of Bacterial Inactivation in Wounds by DNA Sequencing

On day 16, bacterial samples from the wounds were collected by gently wiping the wounds of mice in the Control and Rg3-Gel groups back-and-forth with wet cotton swabs. Then, the swab tip was broken off and loaded into a provided sterile sample collection tube. The bacterial samples were shipped to Shanghai Personal Biotechnology Co., Ltd (Shanghai, China) for high-throughput sequencing. The paired-end raw sequencing data of the skin microbiota were de-multiplexed, joined, filtered, analyzed, and visualized using the Quantitative Insights into Microbial Ecology (QIIME2) pipeline. The obtained sequence information was used for flora composition analysis to

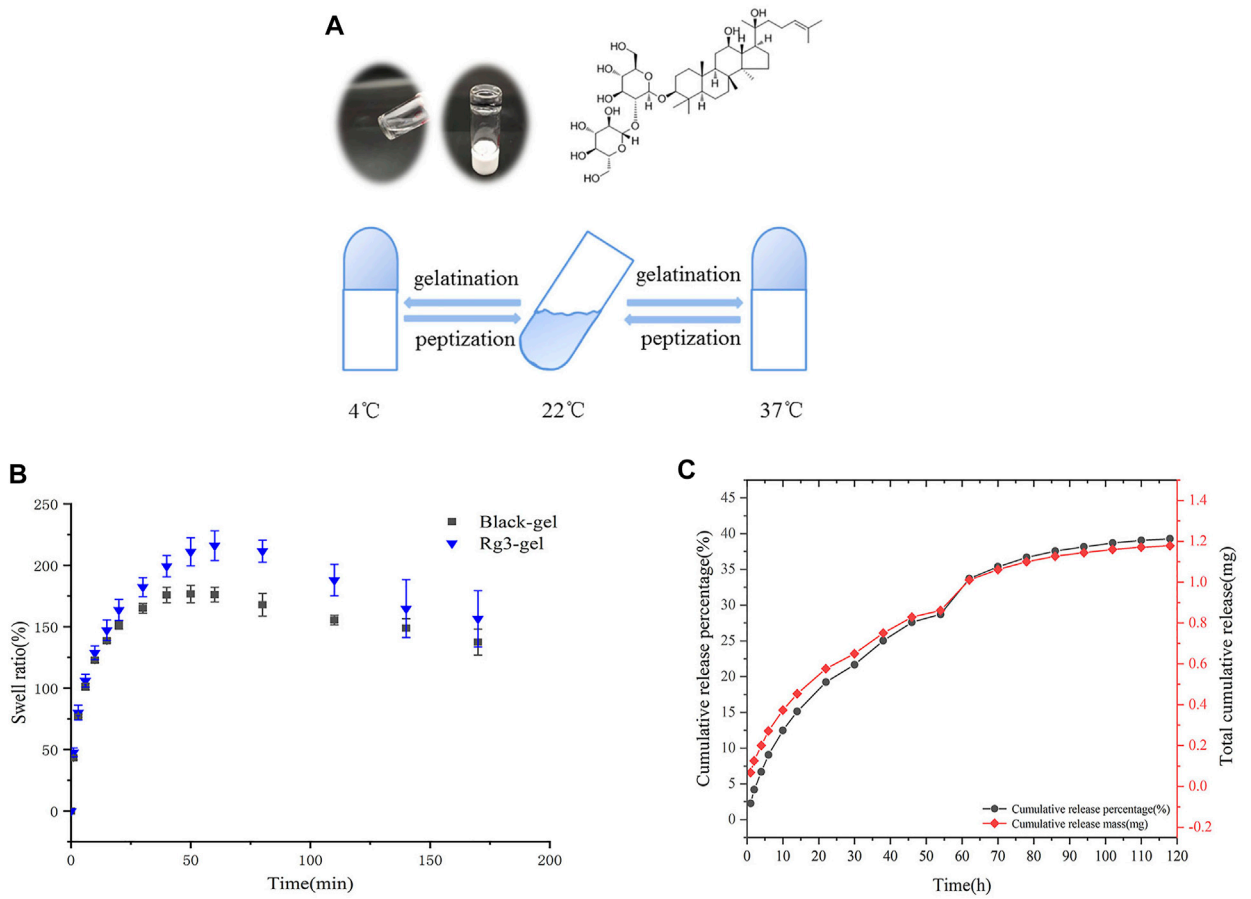

FIGURE 2 | Excellent properties of Rg3-Gel. **(A)** Schematic and tube inversion images of Rg3-Gel with temperature (sol–gel transition). **(B)** Swelling characteristics of Blank-Gel and Rg3-Gel dry samples; data represent average of triplicate experiments ±SD (n = 3). **(C)** Cumulative release profile of Rg3 from the hydrogel sample at 37°C in 0.1 (M) PBS buffer by HPLC; data represent average of triplicate release experiments ±SD (n = 3). Antioxidant, antibacterial ability, and cytotoxicity of Rg3-Gel.

systematically explore whether and how Rg3-Gel treatment affects the type and relative abundance of bacteria in the wound and to allow assessment of bacterial involvement in the wound after Rg3 treatment.

2.8 Statistical Analysis

Data are presented as the mean value ±standard deviation (SD). Graphs and statistical analyzes were performed by using GraphPad Prism 8 (GraphPad, United States) and SPSS 17.0 (IBM Corporation, United States). The differences among groups were measured by one-way ANOVA with Tukey's HSD test *post hoc* comparisons. Statistical significance was defined as p-values < 0.05.

3 RESULTS AND DISCUSSION

3.1 Synthesis and Characterization of Rg3-Gel

At present, together with the functional hydrogel, the utility of other active pharmaceutical ingredients (such as cells, antibacterial agents, growth factors, drugs, or proteins) produce extremely effective hydrogel dressings for use in wound healing (Cheng et al., 2020). Notably, a recent study exhibited a microsphere/hydrogel composite constructed from ciprofloxacin (Cip)-loaded poly (lactic-co-glycolic acid) (PLGA) microspheres and ginsenoside Rh2 showed excellent potential applications in topical treatment of skin infection (Sun et al., 2020). Furthermore, to prevail the limitations related to ginsenosides delivery, a therapeutic delivery system based on microemulsion composite hydrogel has been designed to improve the low water solubility of ginsenosides (Kim et al., 2018). Inspired by this, we presented polymeric materials and anionic surfactants based composite thermo-sensitive hydrogel system for delivery of Rg3 as a drug release vehicle (Rg3-Gel) in this work.

The characteristic chemical bonding peak of Rg3-Gel is observed in **Figure 1A**. The hydrogel samples in the freeze-dried form showed (C–H stretching) and (C=O stretching) at 2,875 and 1,645 cm^{-1}, respectively, and these peaks also included 1,282 cm^{-1} (C–O–C stretching), 1,110 cm^{-1} (C–C–O symmetric stretching), and 964 cm^{-1} (C–C–O asymmetric

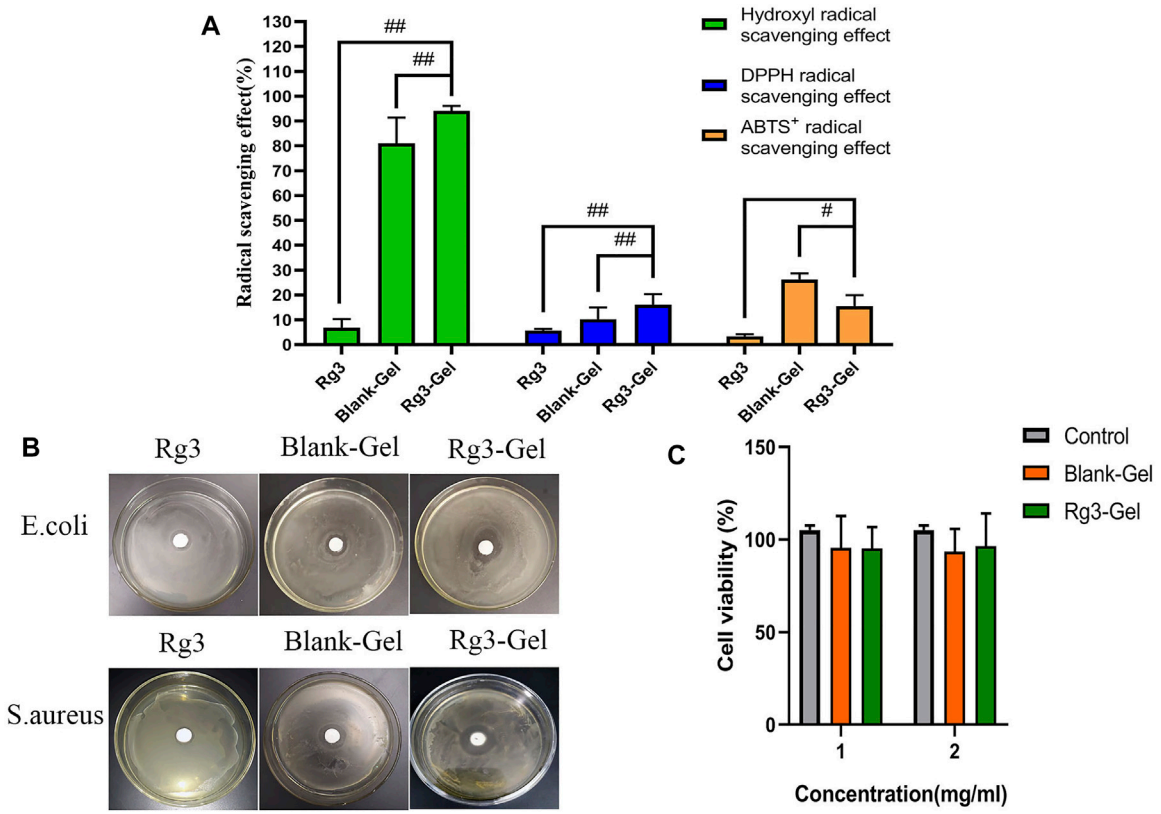

FIGURE 3 | Antioxidant, antibacterial ability, and cytotoxicity of Rg3-Gel. **(A)** Each radical scavenging property of the Rg3, Blank-Gel, and Rg3-Gel ($^{\#}p < 0.05$, $^{\#\#}p < 0.01$, and $n = 3$). **(B)** Antibacterial inhibition zones of the Rg3, Blank-Gel, and Rg3-Gel for *S. aureus* and *E. coli*, respectively ($n = 3$). **(C)** Cell viability of human HaCaT keratinocytes (MTT assay) treated with Rg3-loaded Rg3-Gel and Rg3-unloaded Blank-Gel samples; data represent average of five experiments ±SD ($^{\#}p < 0.05$, $^{\#\#}p < 0.01$, and $n = 5$).

stretching). It was found that the chemical structure of Rg3 hydrogel was not only nearly consistent with that of the *in situ* hydrogel but also matched that of P407. All samples showed the disappearance of broad characteristic peaks at 3,200–3,600 cm^{-1} of the hydroxyl group (O-H or N-H stretching) vibration of the loaded drug compound. There is almost no chemical change in the combined spectrum of the Rg3 hydrogel compared to the blank hydrogel and P407, which is consistent with that reported previously for P407 as the main matrix (Soriano-Ruiz et al., 2020).

This result also appeared in the XRD pattern (**Figure 1B**), in which characteristic P407 diffraction peaks were clearly observed at 19.05° and 23.25°. The diffractogram of the drug encapsulated hydrogel and blank hydrogel also showed large diffraction peak patterns corresponding to their crystalline regions, as well as higher intensities. The diffraction sharp narrow peaks of the hydrogel encapsulated with Rg3 at 15.2° and 77.4° was due to the highly crystalline Rg3 structure. However, no change in the crystal phase due to chitosan doping was observed in the XRD spectra. This may be because the added chitosan is so small that it was below the XRD detection limit. The diffraction pattern may also indicate that Rg3 existed in the intrinsic crystal form in Rg3-Gel.

Simultaneously, the SEM of our hydrogel illustrated a significant difference structure in different hydrogel formulations (**Figure 1C**). The hydrogel formed after the addition of SDS showed a typical 3D porous morphology and appears looser and more porous in nature than the blank hydrogel. In addition, the Rg3 content did not significantly affect the pore structure. These SEM images indicated that the 3D structures of the hydrogel may contribute to the encapsulated and controlled release of drugs, as well as maintain a physiologically moist microenvironment and provide channels for gas exchange at the wound site to promote healing.

3.2 Properties of Rg3-Gel

The relationship between the classical anionic surfactant sodium lauryl sulfate (SDS) with stable hydrogels was studied many years ago (Wu et al., 2012, 2017). Similarly, another report recommends that fibroin aggregation and gelation can be accelerated by SDS in a matter of minutes, based on hydrophobic interactions and electrostatic effects. The SDS-treated hydrogels are further reported to possess excellent cytocompatibility *in vitro* (Kao et al., 2020). The Rg3-Gel outlined in this study is transparent in appearance, and the diagram is shown in **Figure 2A**. Interestingly, we used the

TABLE 1 | Bacterial inhibition zone of the different samples.

Sample name	Inhibition zone (mm)	
	E. coli	*S. aureus*
Rg3	15.2 ± 0.8	12.4 ± 0.7
Blank-Gel	14.2 ± 0.8	18.2 ± 0.9
Rg3-Gel	20.3 ± 1.2	25.0 ± 1.1

Diameter of inhibition zone of different samples. Data represent average of three experiments ±SD.

tube inversion method to record the gelation of the hydrogel, and found that the gelation formulation of the Rg3-Gel not only exhibited a phase transition at physiological temperature with the addition of SDS, but the hydrogel also solidified into semisolids (gels) at low temperature, which attests to it has bidirectional temperature sensitivity. Although the cause of its gelation process remains unknown, early studies reported that in addition to chemical reactions, physical interactions, such as hydrogen bonds, hydrophobic bonds, and electrostatic interactions, may occur during the gelation process (Wang X. et al., 2018).

Figure 2B shows the swelling properties of poloxamer-based Blank-Gel and Rg3-Gel to analyze the water uptake capacity of the hydrogels. Both hydrogels swelled rapidly within the first 25 min of immersion in PBS, and within 50 min of immersion, the swelling equilibrium was reached. However, Blank-Gel was equilibrated slower compared to the Rg3-Gel, probably due to the three-dimensional (3D) structure of the Rg3-Gel, which is looser and more porous. All of the results suggest that all hydrogels have abundant pores to take up large amounts of water; therefore, it can prevent the accumulation of exudates at the wound bed, making them suitable for wound dressing.

A good drug carrier can also enhance drug stability. HPLC chromatography was used to obtain the controlled Rg3 release process from the Rg3 hydrogel. The bioactive Rg3 was effectively encapsulated in the hydrogel and exhibited a representative long-term temperature-sensitive sustained release behavior. The Rg3 release profile is shown in **Figure 2C**. The Rg3 released from the Rg3 hydrogel showed a rapid burst release of approximately 9% over 6 h, and approximately 28.7% over 54 h. The sustained and controlled release of Rg3 could be observed, while the formation of a burst of Rg3 from the loose part of the hydrogel surface can promote early liberation. The drug cumulative release profile was consistent with its cumulative release percentage, and we detected a cumulative release of 1.18 mg of Rg3 over 120 h from 3 ml hydrogel. These Rg3 release behaviors of the hydrogels demonstrated their potential use as drug release carriers.

3.3 Antioxidant, Antibacterial Ability, and Cytotoxicity of Rg3-Gel

Free radicals are present at high levels in the wound site, and this results in oxidative stress and chronic inflammation, degeneration, and cell death, all of which compromise the wound-healing process. Rg3 has been reported to have excellent antioxidant properties and can scavenge free radicals (Kang et al., 2006). Here, the antioxidant activities of Rg3-Gel and pure Rg3 solution were evaluated by testing the removal efficiency of hydroxyl, DPPH, and ABTS oxide radicals. The results revealed a more obvious radical scavenging efficiency of the blank hydrogel combination (**Figure 3A**). The blank hydrogel combination showed 81.0, 10.3, and 26.27% scavenging of hydroxyl, DPPH, and ABTS, respectively, which were higher than single Rg3. The pure Rg3 solution showed no obvious scavenging efficiency at the same concentrations, while the hydrogel showed increased antioxidant capacity with the addition of Rg3 (except for the ABTS free radical scavenging efficiency). Taking the hydroxyl radical scavenging efficiency as an example, after adding Rg3 hydrogel, the hydroxyl absorption peak intensity was significantly reduced, indicating that these hydrogels have good antioxidant ability. These results indicate that the strong hydroxyl radical scavenging property blank hydrogel of the biopolymer combination could effectively combine with Rg3 to improve the antioxidant activity. Overall, Rg3-Gel has good antioxidant capacity and shows great potential as a wound-dressing material.

Bacterial infection is not only one of the main causes of wound infection but also one of the main factors inhibiting the wound-healing process. Thus, the desired wound dressing should have a good antibacterial activity to inhibit the propagation of microorganisms at the wound site and prevent the wound from being invaded by external bacteria (Chen et al., 2018; Song et al., 2019). In this regard, **Figure 3B** illustrates the antimicrobial activity of the hydrogel-loaded Rg3 compared to the hydrogel alone as the control sample. As has been observed, the prepared hydrogel, irrespective of whether or not it contained Rg3-loaded hydrogel, showed the effectiveness of inhibiting the growth of both bacterial species of *S. aureus* and *E. coli*. Furthermore, the mean diameters of the zone of inhibition recorded for Rg3-loaded hydrogel against *E. coli* and *S. aureus* were 20.3 ± 1.2 and 25.0 ± 1.1 mm, respectively, which were higher than those of Rg3 ($p < 0.01$) and the blank hydrogel ($p < 0.01$), revealing that Rg3-loaded hydrogels have greater antimicrobial potential. Similarly, the antibacterial activity of pure Rg3 was investigated against *S. aureus* and *E. coli*, the result of which is shown in **Table 1**. Statistical analyses revealed that pure Rg3 could combat those common pathogens associated with acute wounds. In addition, according to previous studies, chitosan exhibits good antibacterial toward bacteria (Gram-positive and Gram-negative), suggesting that the strong antibacterial activity of Rg3-Gel may be due to the synergistic effect of Rg3 and chitosan. Therefore, based on the aforementioned results, Rg3-Gel showed sufficient inhibition of bacterial growth to protect wounds.

Excellent cytocompatibility is one of the most important properties of materials in biomedical applications. The cytotoxicity level of materials is generally divided into four level grades, where relative survival rates >70% (Grade 1) can be considered non-toxic (Zhang et al., 2021). **Figure 3C** shows the results of cell viability, following treatment with Blank-Gel and Rg3-Gel. The cell viability of two treatment groups was statistically significant ($p < 0.05$) compared to the controls. The relative cell survival rates of the two hydrogels at different

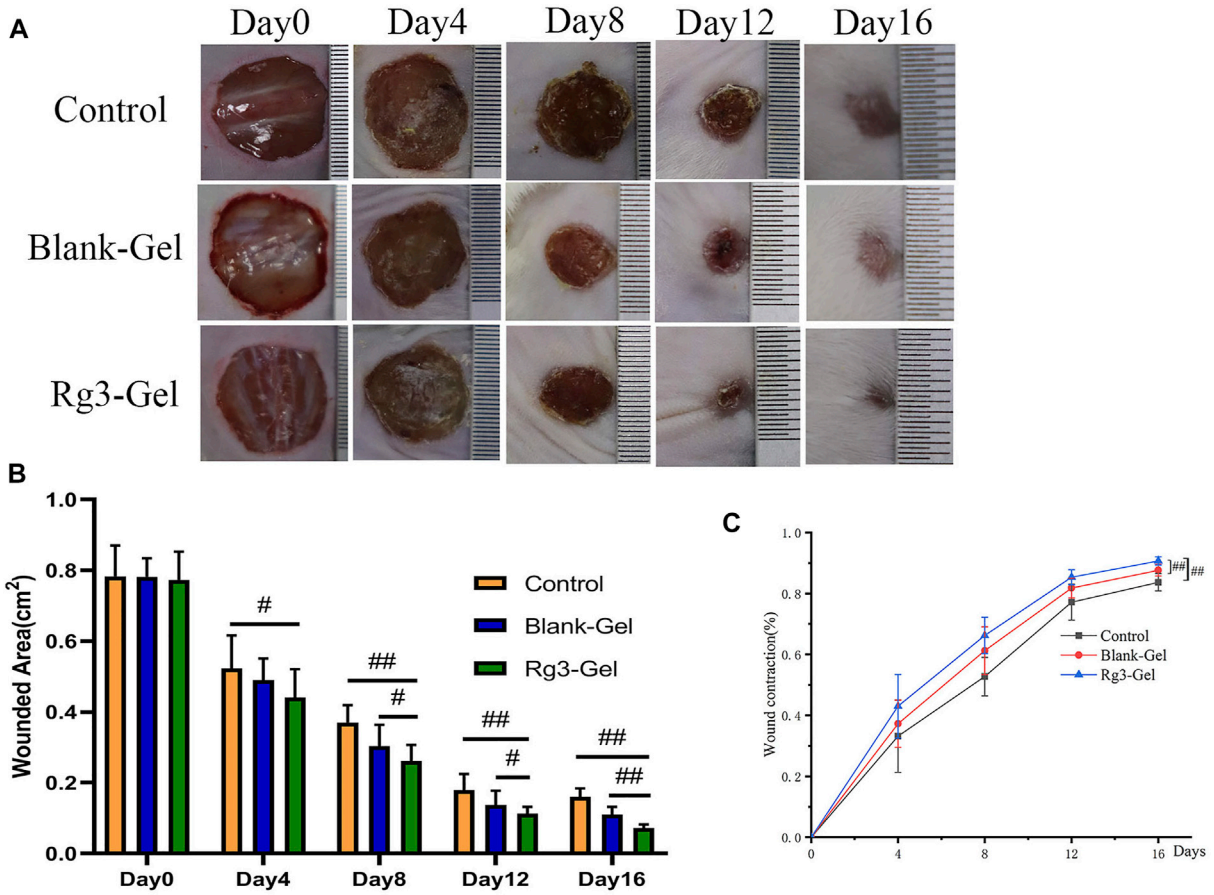

FIGURE 4 | *In vivo* wound healing effect of Rg3-loaded Rg3-Gel on full-thickness excision wound model. **(A)** Wounds photographs at 0, 4, 8, 12, and 16 days post-injury in Control, Blank-Gel, and Rg3-Gel group. The scale bar indicates 10 mm. **(B)** Quantification analysis of wound areas at 0, 4, 8, 12, and 16 days post-injury in each group (#$p < 0.05$, ##$p < 0.01$, and $n = 12$). **(C)** Wound closure represented as the percentage of reduction of the initial area in each group during post-injury 14 days. Control, Blank-Gel, and Rg3-Gel represent the Control group, the blank hydrogel group, and the Rg3 hydrogel group, respectively (#$p < 0.05$, ##$p < 0.01$, and n = 12).

concentrations were >70% after 24 h. The results prove that Rg3-Gel had no toxicity toward the treated samples, indicating that Rg3-Gel can provide an ideal environment for cell culture and may facilitate the rapid repair of skin cells.

3.4 Evaluation of Wound Healing

The faster the wound closes, the more effective the treatment. A full-thickness skin wound on the back of the mice was created and treated with Blank-Gel and Rg3-Gel. Representative images of the change in size of the wound areas from four groups on post-surgery days 0, 4, 8, 12, and 16 are exhibited (**Figure 4A**). On day 4 post treatment, reduction in wound size was observed in the animals to some extent, while Rg3-Gel exhibited the smallest wound area on days 8, 12, and 16 ($p < 0.05$ and $p < 0.01$). Moreover, the mice in the Rg3-Gel group showed a much higher reduction in the wound area as compared to the Blank-Gel ($p < 0.05$ and $p < 0.01$) (**Figure 4B**). Consistent with the gross observation, the Rg3-Gel group exhibited faster healing rates than those observed in the other groups during the whole healing process, with 90.68 ± 1.3% closure rates on day 16, while the wound-healing rates of the *in situ* hydrogel and the Control group were 87.63 and 83.67%, respectively (**Figure 4C**). This finding indicates that the hydrogel supports Rg3 sustained release and biological activity.

3.5 Histological and Angiogenesis Analyses

Collagen participates in the healing process through its role in cell migration and new tissue development. By Masson staining, collagens are stained blue and keratins are stained red. Masson trichrome staining revealed that all groups showed more collagen deposition compared to the Control group (**Figure 5A**). ImageJ software was used to calculate the collagen content of the wound dermis, represented by the average optical density (**Figure 5B**). As a result, the highest collagen deposition and a better collagen array were found in the Blank-Gel group, which increased in the mean area (%) of collagen deposition compared to other groups. These findings indicate that Blank-Gel accelerated the healing process by promoting ECM deposition at the wound site. Although the increased collagen content was weaker in the Rg3-Gel group than that in the Blank-Gel group, the collagen-

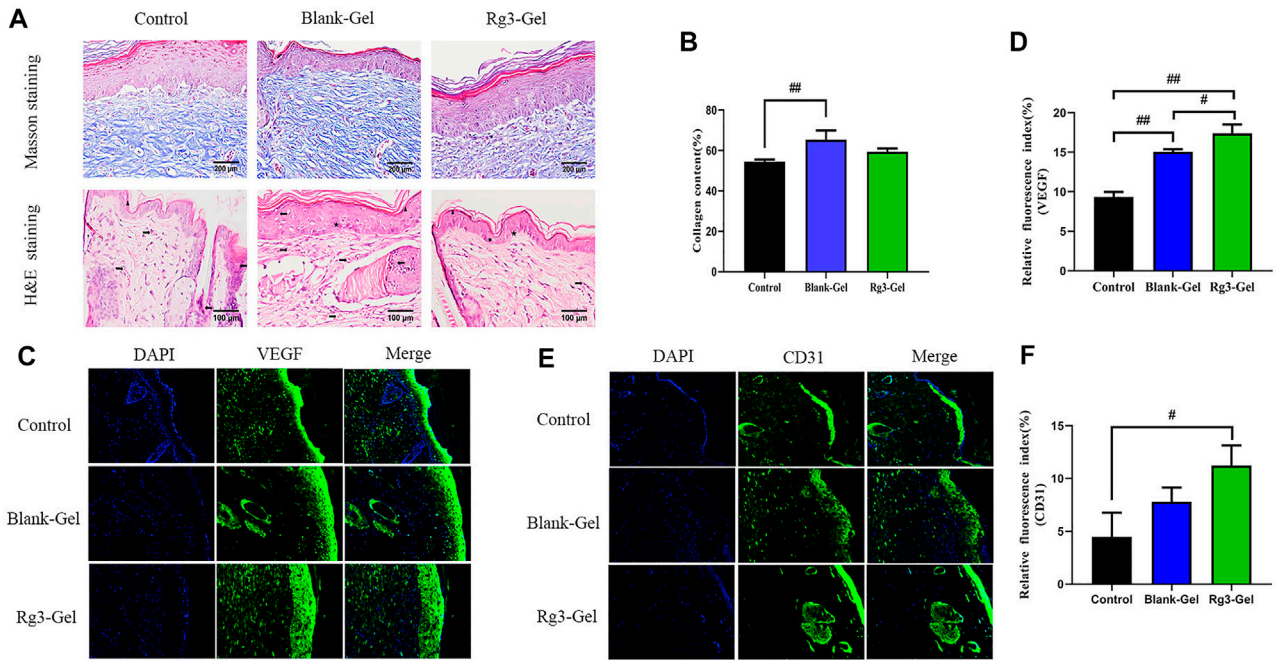

FIGURE 5 | Histological and vascularization assessment after different treatments. **(A)** Masson trichrome staining and H&E histological staining of wounded skin tissue sections in different groups at 16 days post-wounding (×400 magnification and scale bar 200,100 μm). The right arrow represents capillary vessels, while the left arrows represent inflammatory cells. The triangle, star, and circle represent *epidermis*, hair follicles and glands, respectively. **(B)** Proportion of collagen fibers in the regenerative tissues (n = 3). **(C,D)** VEGF immunofluorescence staining images and quantitative analysis in wound areas of different groups. **(E,F)** CD31 immunofluorescence staining images and quantitative analysis in wound areas of different groups (n = 3).

based protein quantification results indicated that collagen I and III expressions under the wound increased significantly in the Rg3-Gel group compared to the Blank-Gel group (**Figure 6A**, $p < 0.01$ and $p < 0.05$). Collagen has been reported to stimulate the adhesion, proliferation, migration, and epidermal differentiation of human keratinocytes, as well as to promote skin regeneration and wound healing in rats (Kim et al., 2014; Chen et al., 2019). The altered collagen content in the Rg3-Gel–treated wounds could be attributed to the introduction of Rg3 into the hydrogel system to a large extent, which may promote collagen deposition and accelerate wound healing.

H&E staining confirmed the superiority of the Rg3-Gel group in terms of histopathological repair. The normal skin of mice is mainly composed of three layers: the *epidermis*, dermis, and hypodermis. According to the H&E staining results, the dermal layer was still collapsed in the Control group, while the Blank-Gel–treated wound showed the basic structure of the epithelial layer and an intact dermis layer, with no obvious edema, and a few hair follicles and glands (**Figure 5C**). However, the skin epithelium and appendage arrangement were not as regular as those in the wounds treated by Rg3-Gel. Our data showed that slightly fewer inflammatory cells and many skin appendages were observed in the Rg3-Gel group. The infiltration of inflammatory cells into the wound site occurs when the wound is infected by bacteria. Relative hypoxia is another characteristic feature of tissue growth or following tissue injury and impaired blood flow, and stimulating angiogenesis and restoring the vascular network can provide the required nutrients and oxygen for the wound repair process (Ahluwalia and Tarnawski, 2012; Feng et al., 2021). Indeed, it has long been known that angiogenesis plays an important role in multiple stages of the wound-healing process. In the current staining plot, the effect of Rg3-Gel on angiogenesis at the wound site is unclear.

The lack of nutrients and oxygen is the principal factor that stimulates angiogenesis. Angiogenesis is also the result of endothelial cell proliferation and the production of various growth factors and cytokines, which provide the necessary cellular and molecular signals for a normal healing process. Among them, vascular endothelial growth factor (VEGF) is the most important mediator in promoting angiogenesis (Ferrara et al., 2003; Li et al., 2003). To further explore the potential regulatory effect of Rg3-Gel on angiogenesis, we verified the formation of blood vessels by immunofluorescence staining with the angiogenesis markers platelet endothelial cell adhesion molecule-1 (CD31) and VEGF (**Figures 5C–F**). The results showed that Rg3-Gel significantly enhanced the expression of VEGF and CD31 in mouse skin wounds compared with the Control group, thereby promoting angiogenesis ($p < 0.01$ and $p < 0.05$). In addition, the VEGF protein detected by western blotting was highly expressed in the wounds of the Rg3-Gel group (**Figure 6B**, $p < 0.01$). We also noted that the hypoxia-inducible factor (HIF)-1α (HIF-1α) protein level were significantly increased in the Rg3-Gel group compared to the Control group (**Figure 6B**, $p < 0.05$). HIF-1α is a major transcription factor, which participates in VEGF-mediated angiogenesis under hypoxic conditions, as well as induces the expression of multiple critical molecules for wound

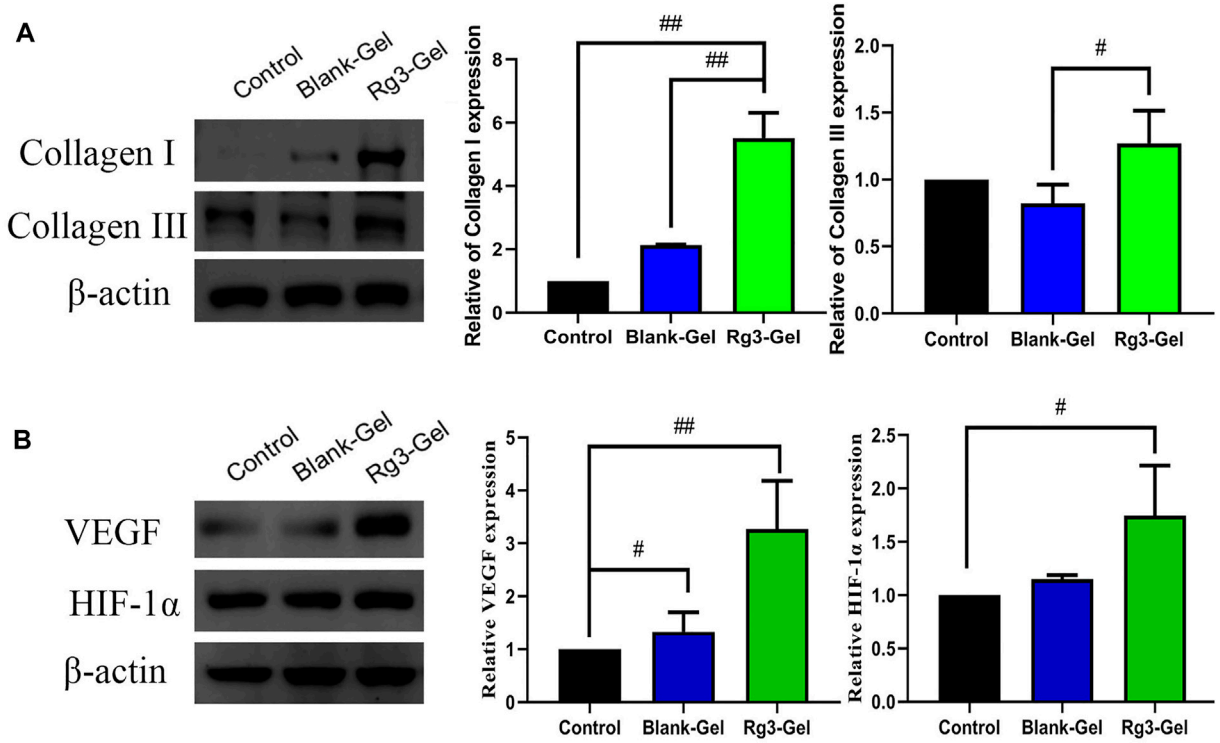

FIGURE 6 | Effects of Rg3-Gel on collagen and angiogenesis at wound-healing sites. **(A)** Representative western blots and their quantitative analysis of Collagen I and Collagen III proteins in skin tissue of three groups. **(B)** Representative western blots and their quantitative analysis of VEGF and HIF-1α proteins in skin tissue of three groups (#$p < 0.05$, ##$p < 0.01$, and $n = 3$)

healing (Rey and Semenza, 2010). The quality and quantity of neovascularization determine the quality of wound healing. Previous studies have reported the use of 20(S)-protopanaxadiol (PPD) in wound-healing therapy by stimulating angiogenesis through HIF-1α-mediated VEGF expression. Micromolar concentrations of Rg3 have been shown to increase nitric oxide (NO) production in the vascular endothelium, promote human endothelial cell proliferation, migration, and tube formation *in vitro*, and promote as *ex vivo* endothelial sprouting (Chen et al., 2010; Hien et al., 2010; Kwok et al., 2012). Taken together, these findings provide solid evidence that Rg3-Gel promotes angiogenesis. These results are consistent with our previous collagen expression results, suggesting that Rg3-Gel may enhance wound healing by promoting angiogenesis.

3.6 Immunofluorescence Analysis of Pan-Keratin

Keratins (KRT) are the largest subfamily of intermediate filaments (IFs) and the most abundant cellular proteins in simple epithelial cells. KRTs represent the main component of the epithelial cytoskeleton, which not only provides structural support to epithelial cells but also contributes to cell-type-specific functions, such as regulating cell proliferation, migration, adhesion, metabolism, and inflammatory features of keratinocytes (Zhang et al., 2019). Pan-keratin is a marker of re-epithelialization of the extracellular matrix. Previous studies on these Rg3 compounds have focused on their anticancer effects, with few reporting their effects on keratin (Sun et al., 2017). More recently, keratin has been reported in the use of novel biocompatible materials, such as membranes and hydrogels, in tissue engineering scaffolds, wound dressings, and surgical interventions, among others (Volkov and Cavaco-Paulo, 2016). Normal expression of keratin proteins is responsible for maintaining the structural stability and integrity of keratinocytes, and its mutation or abnormal expression is related to various skin diseases. In this study, immunofluorescence imaging of pan-keratin was conducted to assess the formation of a new KRT network. As demonstrated in **Figures 7A**,**B**, the expression of pan-keratin in the Rg3-gel group was significantly higher than that in the other groups, especially the Control group ($p < 0.01$). This result concluded that the enhancement of hydrogel system-mediated wound healing by Rg3 may occur through stimulation of pan-keratin.

3.7 Analysis of the MAPK/NF-κB Signaling Pathway and Expression of Autophagy-related 496 Proteins

The canonical transcription factor NF-κB is an accepted upstream trigger of the pro-inflammatory signal, which is activated by reactive oxygen species (ROS) and drives the expression of numerous genes, including those of pro-

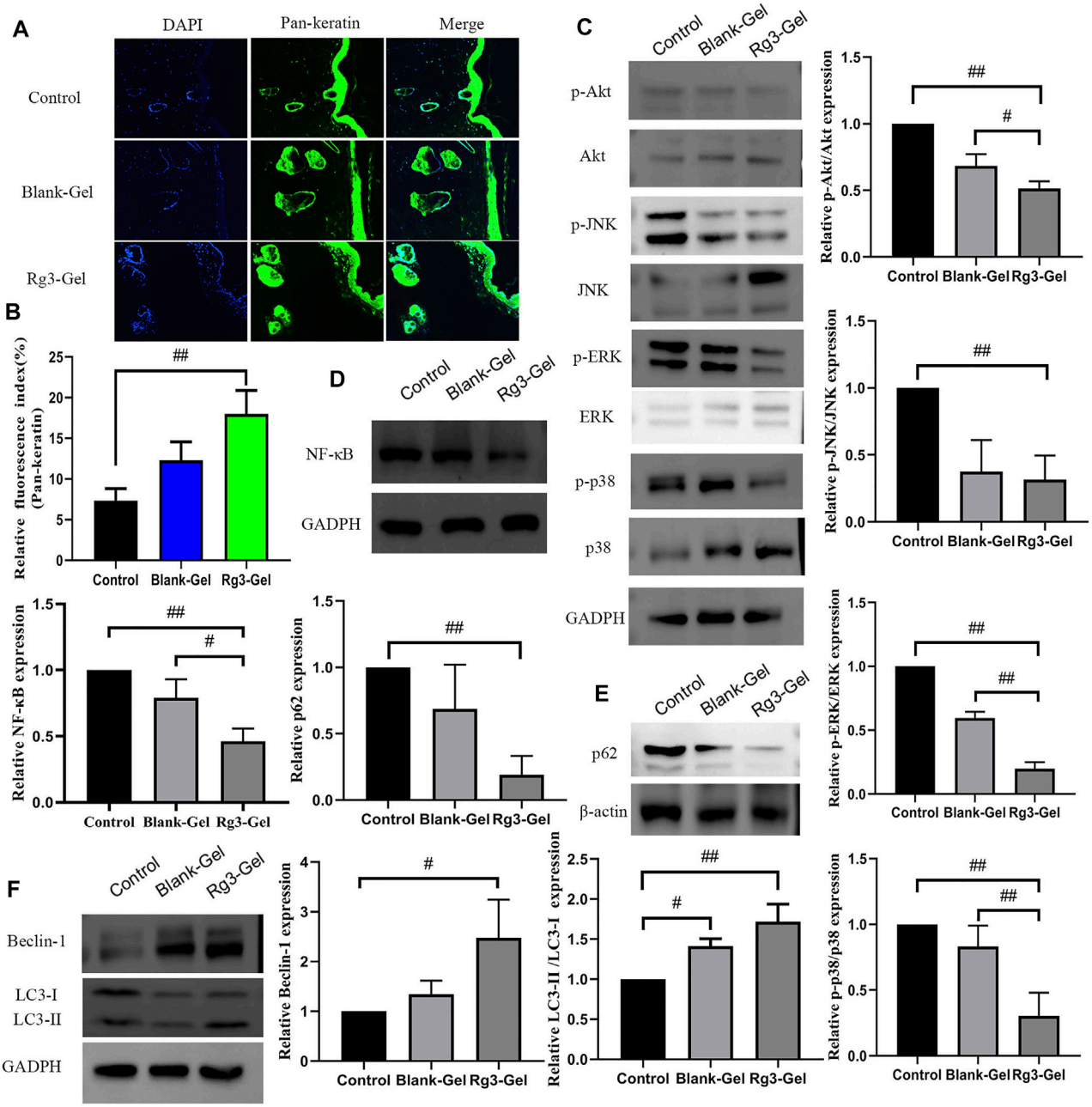

FIGURE 7 | Effect of Rg3-Gel on the expression of various proteins in wound tissues. **(A)** Representative images of pan-keratin immunofluorescence staining on day 16 post surgery. **(B)** Expression of pan-keratin protein affected through the Rg3-Gel treatment in skin tissue in mouse (#$p < 0.05$, ##$p < 0.01$, and $n = 3$). **(C)** Representative western blotting of Akt, JNK, ERK, p38, and their phosphorylated proteins in skin tissue of three groups. **(D)** Effects of different treatment on the protein expressions of NF-κB, **(E)** p62, **(F)** Beclin-1, and LC3 (#$p < 0.05$, ##$p < 0.01$, and $n = 3$). Analysis of the MAPK/NF-κB signaling pathway and expression of autophagy-related proteins.

inflammatory cytokines, chemokines, adhesion molecules, and enzymes (Best et al., 2019). P65 is one of the important heterodimer members of the NF-κB family, the expression of which has been shown to be inhibited by Rg3 (Ma et al., 2020). Following activation by ROS, NF-κB can activate signaling pathways, including MAPKs and PI3K/Akt, which are crucial to regulating inflammation and producing inflammatory factors. The MAPKs regulate cell growth and differentiation as well as in the control of the cellular responses to cytokines and various stresses (Kwon et al., 2018; Best et al., 2019). To confirm the anti-inflammatory *in vivo* results, the effects of Rg3-Gel on the activation of MAPK family members, including p38 MAPK, JNK, ERK, and AKT (all of which are involved in the early stage of autophagy), were determined by western blotting. ROS

are necessary participants in mitogen-activated protein kinase (MAPK) pathways, activated p38 and ERK signaling proteins are involved in the main signaling pathways for migration and proliferation of endothelial cells, and the MAPK signaling pathway is also responsible for the activation of nuclear factor-kB (NF-κB). Moreover, JNK is principally activated by ROS, but can also be activated by many other stimuli, including cytokines, hormones, cell stress, toxins, drugs, and metabolic changes (Shen et al., 2015; Niu et al., 2020). Inflammation occurs following wound formation as an adaptive response ubiquitous to both acute and chronic wounds. This inflammation induces and stimulates NF-κB and its upstream major translocation regulator, mitogen-activated protein kinases (MAPKs), including p38, ERK1/2, and JNK (**Figure 7C**). Of note, a substantial decrease in the ratio of phospho-Akt/Akt was detected following the treatment with Blank-Gel and Rg3-Gel ($p < 0.01$). Similar alterations in the ratio of phospho-JNK/JNK were also detected ($p < 0.01$), while treatment with specific inhibitors of ERK decreased the phosphorylation ($p < 0.01$). We detected low levels of p38 MAPK phosphorylation, an inhibitor of NF-kB, in the skin tissue of hydrogel-treated wounds ($p < 0.01$), while NF-κB was decreased to a similar level ($p < 0.01$, **Figure 7D**). Taken together, these findings show that the hydrogel loaded with Rg3 is apparently involved in inhibition of the inflammatory response in wound healing. This indicates that the use of hydrogel treatment in the wound can inhibit the activation of NF-κB and reduce inflammation, at least partially, by inhibiting the MAPK and NF-κB signaling pathways.

Autophagy is an essential homeostatic cellular process, which degrades damaged and dysfunctional organelles and proteins under highly conservative conditions (Sil et al., 2018). Several studies have proved that the NF-κB-p62 mitophagy pathway specifically inhibits pro-inflammatory processes to help restore homeostasis. The activation of autophagy significantly reduced the accumulation of p62, the expression of cathelicidin/LL-37, and the production of inflammatory cytokines. In short, NF-κB exerts an anti-inflammatory effect by delaying accumulation of the autophagy receptor p62/SQSTM1 (Lee et al., 2011). Further research indicates that autophagy is also related to the AMPK pathway, in which phosphorylated AMPK deactivates mTOR, which in turn activates the expression of LC3 and induces autophagy (Lu et al., 2021).

P62, one of several primary regulators of skin inflammation, was previously shown to have roles in the control of epidermal processes (Sukseree et al., 2021). P62 can modulate the degradation of ubiquitinated proteins during autophagy and acts independently as an adapter protein in autophagy. P62 not only induces cellular proliferation by activating the NF-κB pathway but also plays an important role in cell signaling crossroads, such as cellular apoptosis, inflammation, and autophagy (Usategui-Martín et al., 2020). To further elucidate the role of Rg3-Gel associated with the induction of autophagy *in vivo* under wound-healing conditions, the protein levels of downstream autophagy-related markers in the healed skin wounds were evaluated. We found an inverse correlation between p62 and Beclin-1 levels in skin tissue at wound healing sites of mice, whereas the highest p62 expression was present in the Control group ($p < 0.01$, **Figure 7E**). Several studies have proved that the JNK/Beclin-1 pathway plays a crucial role in mediating autophagic cell death. The downstream targets of JNK include the transcription factor c-Jun, which translocates to the nucleus after JNK-mediated phosphorylation. Other reports showed that the association between JNK and c-Jun not only activates c-Jun but also stabilizes c-Jun. When activated, the JNK-mediated phosphorylation of both Ser63 and Ser73 at the c-Jun N-terminal activates c-Jun and potentiates its transcriptional activity, thereby enhancing the transcriptional activity of Beclin-1. This process is important for the formation of autophagosomes and mediates the localization of other autophagy proteins on the autophagy precursor membrane (Sheng et al., 2021). The literature suggests that autophagy is impaired in the diabetic skin model due to the decreased expression of beclin-1 and LC3-II (Chowdhury et al., 2019). In line with this observation, as shown in **Figure 7F**, expression levels of Beclin-1 protein were lowest in Control group mice and highest in Rg3 hydrogel mice ($p < 0.05$). Similarly, low levels of Beclin-1 expression were found to be inversely correlated with p62 and positively correlated with LC3 in this study. Compared to the Control group, Rg3-Gel intervention significantly upregulated the expression of LC3 proteins ($p < 0.01$). The protein levels of these markers were upregulated by hydrogel treatment, and this effect was more pronounced with Rg3-Gel than Blank-Gel treatment, although no statistical differences existed between the Control and treated groups. From these findings, we concluded that Rg3-Gel stimulates autophagy *via* Beclin-1 and LC3 to significantly accelerate wound healing.

3.8 Analysis of Wound Bacterial Effect by DNA Sequencing

Microbiota induces a form of adaptive immunity that couples antimicrobial function with tissue repair. The purpose of microbiota manipulation in skin wound healing is to prevent pathogen infection and increase the proportion of beneficial microbiota. Numerous studies have investigated the microbial differences between healthy skin and diseased skin to find a cure to restore health. It is unclear what alterations in the microbiome are caused by the Rg3 hydrogel or whether it will improve the imbalance of the microbiota and contribute to skin wound healing. Generally, there exist four prevailing skin-associated taxonomic units on the skin: Actinobacteria, Proteobacteria, Firmicutes, and Bacteroidetes, all of which are actively involved in the infection and repair of skin wounds. It has been reported that certain skin bacteria can convert aromatic amino acids (AAA) into trace amines (TA), which accelerate wound healing, further confirming the significance of the epidermal microorganisms for wound healing (Luqman et al., 2020). Metagenomics is a novel method to detect species, population structure, diversity, and evolutionary relationships of microbiomes by high-throughput sequencing technology. In this study, metagenomics technology was used to detect the wounds of mice treated with hydrogel and to explore the microbial changes in the wounds after the introduction of Rg3. These models are displayed in **Figure 8**.

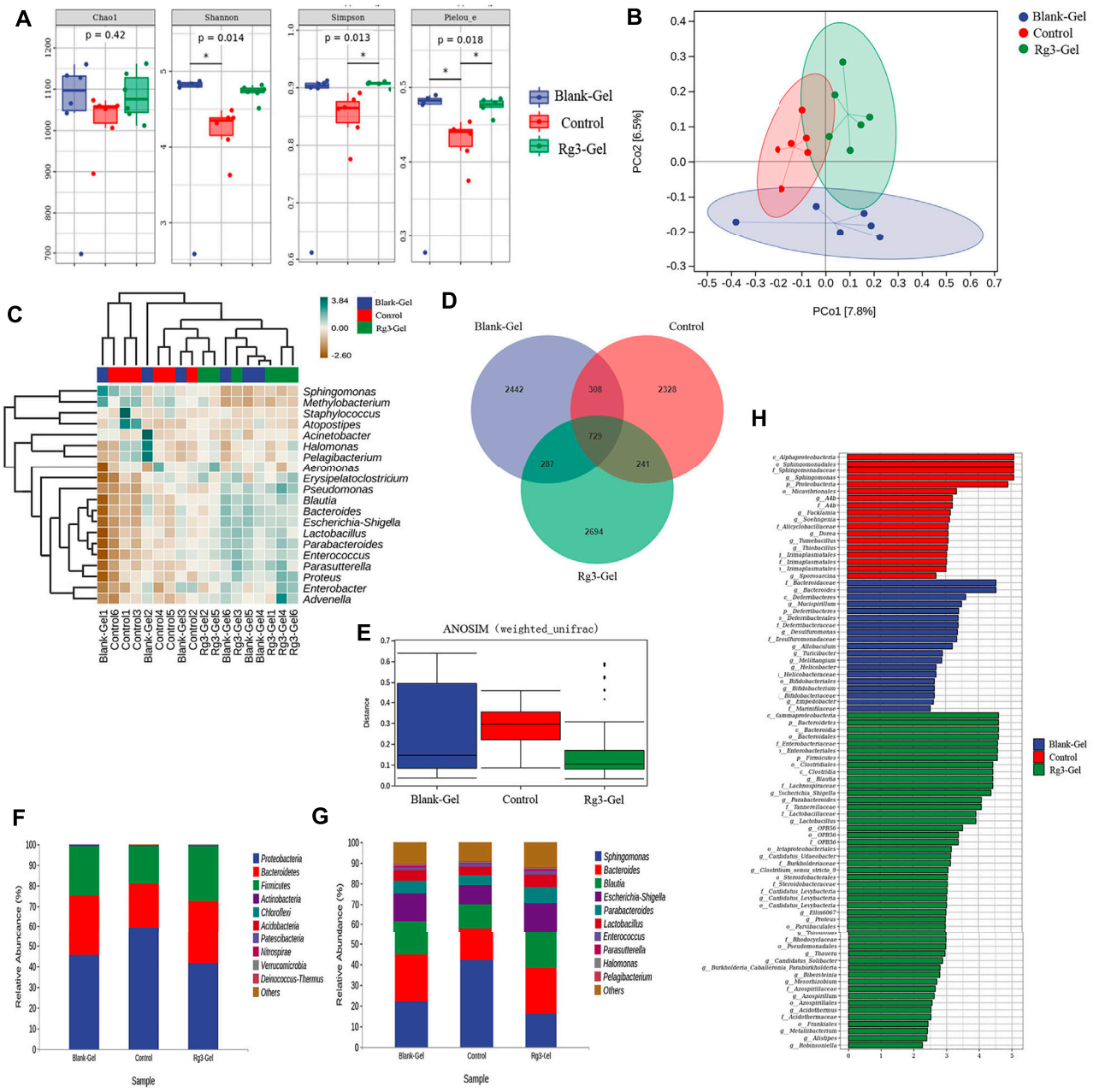

FIGURE 8 | Effects of different treatments on wound flora. **(A)** Box plots of four different alpha diversity measures. **(B)** Multivariate analysis of beta-diversity: PCoA results based on weighted UniFrac (consider sequencing amounts when analyzing) across the three different sample groups. Blue, red, and green colors represent samples from Blank-Gel, Control, and Rg3-Gel individuals, respectively. **(C)** Correlation heatmap between three groups important differential wound microbes and the top 20 genera in abundance. **(D)** Venn diagram of shared and unique bacterial genera in the skin wound microbiome. **(E)** One way ANOSIM analysis (test statistic R > 0). **(F) (G)** Histogram of species distribution was used to compare the differences of relative abundance in phylum and genus levels between different groups. **(H)** LDA chart. The score was obtained by LDA analysis (linear regression analysis) (n = 6).

We analyzed the microbial communities on the wound surface of each group of mice using 16S rRNA Illumina high-throughput sequencing. The Wayne diagram in **Figure 8D** shows that the Blank-Gel, Control, and Rg3-Gel groups contained 3,766, 3,606, and 3,951 bacterial operational taxonomic units (OTU), respectively. The Rg3-Gel group had the most abundant microbes and the control the least, which indicates that the microbial diversity of untreated in wound is reduced compared to that of the Rg3 hydrogel treatment. Moreover, there was a trend toward increased species abundance and diversity of the two hydrogels compared to those observed in the Control group, as calculated by the alpha diversity metrics (**Figure 8A**). The differences within the sample groups were statistically significant (p < 0.05) for all diversity indices,

FIGURE 9 | LEfSe cladograms analysis of wound surface taxa at genus levels among the different groups.

including the Shannon, Simpson, and Pieloue indices. The Shannon diversity index is a measure of both species richness and the evenness of each species. A low index indicates low diversity, which is usually present in infections because a single microorganism dominates the balance and leads to disease, while a high index indicates greater diversity and is usually observed in normal, stable, and healthy communities (Kim et al., 2019). Evidence suggests that the imbalance of the microbial flora without any invading pathogens is an underlying cause of skin diseases. Therefore, simply eliminating all microorganisms is not a reasonable method to promote healing (Pang et al., 2020). The maintenance of skin health not only requires the inhibition of pathogenic bacteria but also to promote the growth of symbiotic bacteria (Grice et al., 2009). The bacterial diversity in the Rg3 hydrogel treatment group was significantly higher than that of the Control and blank hydrogel treatment groups; that is, mice that appeared to be more beneficial to assist wound healing by using Rg3-Gel to control microbial diversity. One-way ANOSIM analysis (test statistic $R > 0$) revealed significant differences between the three groups (Blank-Gel, Control, and Rg3-Gel) in terms of wound healing (**Figure 8E**), and the microbiota similarity of the samples can be observed by the clustering in the principal coordinate analysis plots (PCoA) (**Figure 8B**). Beta diversity analysis using the Jaccard similarity index and PCoA generation revealed a clear distinction in wound microbiota composition among the three groups, and the differences between the three groups of our study have statistical significance. According to reports, a continuous change of microbial diversity and community may indicate a tendency for wound tends to heal, while stabilizing in low diversity suggests that the wound may be chronic or not conducive to healing (Pang et al., 2020). Rg3-Gel treatments are consistent with the previously reported samples of normal skin, indicating a stable microbiota that returns to a "normal" state, following Rg3-Gel treatment during the wound-healing process.

In addition, phylum- and genus-level taxonomic classifications of the wound microbiome revealed a variation in representative organism abundances between the two hydrogel treatment groups versus the Control group mice. In the current study, Proteobacteria, Bacteroidetes, Firmicutes, and Actinobacteria were observed as the four dominant microorganisms in the wound samples (**Figure 8F**). The relative frequency of *Proteobacteria* in the Rg3-Gel treatment group was reduced compared to that in the Control group, whereas *Bacteroidetes* and *Firmicutes* were increased. At the genus level, the six predominant groups identified were *Sphingomonas*, *Bacteroides*, *Blautia*, *Escherichia-Shigella*, *Parabacteroides*, and *Lactobacillus* (**Figure 8G**). The relative frequency of *Sphingomonas* was reduced in the two hydrogel treatment groups, while the other genera were increased. Moreover, the microbial community composition of these genera of the Rg3-Gel-treated mice varied more than that of the blank hydrogel. The heatmaps simultaneously illustrated *Sphingomonas*, *Methylobacterium*, *Staphylococcus*, *Atopostipes*, *Acinetobacter*, *Halomonas*, *Pelagibacterium*, and *Aeromonas* were the most prominent genera (**Figure 8C**). Moreover, *Bacteroides* normally function as friendly commensal bacteria in the host, and in rats with atopic dermatitis (AD) induction, the same treatments significantly decreased the relative abundance of the phylum *Bacteroidetes* and the genus *Bacteroides*. The intestinal microbiota seems to affect the health of the skin. Indeed, *Escherichia/Shigella* or *Veillonella* are found to be more prominent in the stools of patients with AD (Łoś-Rycharska et al., 2021). We observed a recovery in the level of *Lactobacillus* of skin microbiomes compared to the Control group mice skin, which showed that Rg3 hydrogel could regulate the skin microbiota at the genus level, similar to the findings of a previous study of diabetic skin (Jiao et al., 2020). *Sphingomonas*, a member of the phylum *Proteobacteria*, is an abundant genus that is identified on allergic skin. Many authors have indicated that the wound microbiome species, such as *Streptotrophomonas*, *Brachyrhizobium*, *Sphingomonas*, and *Phyllobacterium*, have a negative impact on wound healing, while *Leuconostoc*, *Enterococcus*, and *Bacillus* are beneficial to wounds (Mei et al., 2020). LEfSe (Linear discriminant analysis Effect Size) analysis showed the evolutionary relationship of different flora among groups (**Figure 9**). The dominant bacteria of the Control group

were from *Proteobacteria*, while the representative bacteria of the Rg3-Gel groups expanded to *Bacteroidetes* and *Firmicutes*. Based on the results of linear discriminant analysis (LDA) (**Figure 8H**), Blank-Gel mice were characterized by a higher relative abundance of *Bacteroides*, *Mucispirillum*, *Desulfuromonas*, *Allobaculum*, *Turicibacter*, *Melittangium*, *Helicobacter*, *Bifidobacterium*, and *Empedobacter*, but lower amounts of *Sphingomonas*, A4b, *Facklamia*, *Soehngenia*, *Dorea*, *Tumebacillus*, and *Thiobacillus* than the Control group. In the Rg3-Gel treatment group, the main taxa with high LDA scores included *Blautia*, *Escherichia–Shigella*, *Parabacteroides*, *Lactobacillus*, *Clotridium_sensu_stricto*, and *Alistipes*. Culture-based studies of skin microbiota suggest that skin microbes can affect skin properties, immune responses, pathogen growth, and wound healing. Studies in recent decades have found that skin damage results in colonization by microorganisms, thereby increasing the risk of inflammation, which is reported to make damaged skin more susceptible to infection and ultimately affect wound healing. Overall, a shift in the microbiota composition by Rg3-Gel had a positive effect on wound healing. However, more studies must address the causal relationship between natural active ingredients and their influence on the composition of skin wound microbiota.

4 CONCLUSION

In this work, a new method for producing a temperature-sensitive injectable hydrogel containing Rg3 was developed using SDS as the gelling agent. Considering both safety and system simplicity, the hydrogels based on the chemical structure and temperature-sensitive properties of poloxamer were selected to use hyaluronic acid and chitosan along with Rg3 to accelerate the wound-healing process. The hydrogels, which show a unique porous morphology, promising biocompatibility, controlled Rg3 release, and good antioxidant and antibacterial activities, are ideal for use in wound healing. The experimental *in vivo* wound closure data show that the temperature-sensitive hydrogels with Rg3 could enhance wound contraction, re-epithelialization, collagen deposition, and angiogenesis, all of which accelerated the wound-healing process. The increase in autophagy protein expression suggests that hydrogels with Rg3 could enhance autophagy in wounds to promote healing. High-throughput data analysis showed that the biomimetic hydrogel with Rg3 increased the microbial diversity on the skin wound surface and reduced the abundance of harmful bacteria. Overall, the temperature-sensitive injectable hydrogels with Rg3 hold great promise for use in wound-healing applications.

DATA AVAILABILITY STATEMENT

The original contributions presented in the study are included in the article/**Supplementary Material**; further inquiries can be directed to the corresponding authors.

ETHICS STATEMENT

The studies involving human participants were reviewed and approved by Animal Ethics Committee of Jilin Agricultural University. The patients/participants provided their written informed consent to participate in this study. The animal study was reviewed and approved by Animal Ethics Committee of Jilin Agricultural University.

AUTHOR CONTRIBUTIONS

XP performed the experiments and writing-original draft. CD performed terminology, methodology, and formal analysis. YZ (3rd author) performed the experiments with software. MH performed the visualization and investigation. WL was responsible for conceptualizing, writing–review and editing, supervision, and resources. MY and FX performed the funding acquisition, and resources. YZ (8th author) performed the project administration.

FUNDING

This study was supported by the Natural Science Foundation of Jilin Province (20210101219JC); Innovation Capacity Building Project of Jilin Provincial Development and Reform Commission (2021C041-3).

ACKNOWLEDGMENTS

This is a short text to acknowledge the contributions of specific colleagues, institutions, or agencies that aided the efforts of the authors.

SUPPLEMENTARY MATERIAL

The Supplementary Material for this article can be found online at: https://www.frontiersin.org/articles/10.3389/fbioe.2022.831007/full#supplementary-material

REFERENCES

Ahluwalia, A., and Tarnawski, A. S. (2012). Critical Role of Hypoxia Sensor - HIF-1α in VEGF Gene Activation. Implications for Angiogenesis and Tissue Injury Healing. *Curr. Med. Chem.* 19, 90–97. doi:10.2174/092986712803413944

Best, K. T., Lee, F. K., Knapp, E., Awad, H. A., and Loiselle, A. E. (2019). Deletion of NFKB1 Enhances Canonical NF-κB Signaling and Increases Macrophage and Myofibroblast Content during Tendon Healing. *Sci. Rep.* 9, 10926. doi:10.1038/s41598-019-47461-5

Chen, Q.-J., Zhang, M.-Z., and Wang, L.-X. (2010). Gensenoside Rg3 Inhibits Hypoxia-Induced VEGF Expression in Human Cancer Cells. *Cell Physiol. Biochem.* 26, 849–858. doi:10.1159/000323994

Chen, H., Cheng, J., Ran, L., Yu, K., Lu, B., Lan, G., et al. (2018). An Injectable Self-Healing Hydrogel with Adhesive and Antibacterial Properties Effectively Promotes Wound Healing. *Carbohydr. Polym.* 201, 522–531. doi:10.1016/j.carbpol.2018.08.090

Chen, J., Gao, K., Liu, S., Wang, S., Elango, J., Bao, B., et al. (2019). Fish Collagen Surgical Compress Repairing Characteristics on Wound Healing Process *In Vivo*. *Mar. Drugs* 17, 33. doi:10.3390/md17010033

Cheng, L., Sun, X., Li, B., Hu, C., Yang, H., Zhang, Y., et al. (2013). Electrospun Ginsenoside Rg3/poly(lactic-Co-Glycolic Acid) Fibers Coated with Hyaluronic Acid for Repairing and Inhibiting Hypertrophic Scars. *J. Mat. Chem. B* 1, 4428–4437. doi:10.1039/c3tb20441c

Cheng, L., Sun, X., Chen, L., Zhang, L., Wang, F., Zhang, Y., et al. (2020). Nano-in-micro Electronspun Membrane: Merging Nanocarriers and Microfibrous Scaffold for Long-Term Scar Inhibition. *Chem. Eng. J.* 397, 125405. doi:10.1016/j.cej.2020.125405

Chowdhury, S., Ghosh, S., Das, A. K., and Sil, P. C. (2019). Ferulic Acid Protects Hyperglycemia-Induced Kidney Damage by Regulating Oxidative Insult, Inflammation and Autophagy. *Front. Pharmacol.* 10, 27. doi:10.3389/fphar.2019.00027

Dong, R., and Guo, B. (2021). Smart Wound Dressings for Wound Healing. *Nano Today* 41, 101290. doi:10.1016/j.nantod.2021.101290

Feng, P., Qiu, H., Luo, Y., Hu, J., Cao, Y., Pang, Q., et al. (2021). Development of Poloxamer Hydrogels Containing Antibacterial Guanidine-Based Polymers for Healing of Full-Thickness Skin Wound. *ACS Biomater. Sci. Eng.* 7, 4557–4568. doi:10.1021/acsbiomaterials.1c00600

Ferrara, N., Gerber, H.-P., and LeCouter, J. (2003). The Biology of VEGF and its Receptors. *Nat. Med.* 9, 669–676. doi:10.1038/nm0603-669

Grice, E. A., Kong, H. H., Conlan, S., Deming, C. B., Davis, J., Young, A. C., et al. (2009). Topographical and Temporal Diversity of the Human Skin Microbiome. *Science* 324, 1190–1192. doi:10.1126/science.1171700

Hien, T. T., Kim, N. D., Pokharel, Y. R., Oh, S. J., Lee, M. Y., and Kang, K. W. (2010). Ginsenoside Rg3 Increases Nitric Oxide Production via Increases in Phosphorylation and Expression of Endothelial Nitric Oxide Synthase: Essential Roles of Estrogen Receptor-dependent PI3-Kinase and AMP-Activated Protein Kinase. *Toxicol. Appl. Pharmacol.* 246, 171–183. doi:10.1016/j.taap.2010.05.008

Jiao, C., Xie, Y., Yun, H., Liang, H., He, C., Jiang, A., et al. (2020). The Effect of Ganoderma Lucidum Spore Oil in Early Skin Wound Healing: Interactions of Skin Microbiota and Inflammation. *Aging* 12, 14125–14140. doi:10.18632/aging.103412

Kang, K. S., Kim, H. Y., Yamabe, N., and Yokozawa, T. (2006). Stereospecificity in Hydroxyl Radical Scavenging Activities of Four Ginsenosides Produced by Heat Processing. *Bioorg. Med. Chem. Lett.* 16, 5028–5031. doi:10.1016/j.bmcl.2006.07.071

Kao, C.-Y., Nguyen, H.-Q. -D., and Weng, Y.-C. (2020). Characterization of Porcine Urinary Bladder Matrix Hydrogels from Sodium Dodecyl Sulfate Decellularization Method. *Polymers* 12, 3007. doi:10.3390/polym12123007

Kim, K.-O., Lee, Y., Hwang, J.-W., Kim, H., Kim, S. M., Chang, S. W., et al. (2014). Wound Healing Properties of a 3-D Scaffold Comprising Soluble Silkworm Gland Hydrolysate and Human Collagen. *Colloids Surfaces B Biointerfaces* 116, 318–326. doi:10.1016/j.colsurfb.2013.12.004

Kim, K.-T., Kim, M.-H., Park, J.-H., Lee, J.-Y., Cho, H.-J., Yoon, I.-S., et al. (2018). Microemulsion-based Hydrogels for Enhancing Epidermal/dermal Deposition of Topically Administered 20(S)-Protopanaxadiol: *In Vitro* and *In Vivo* Evaluation Studies. *J. Ginseng Res.* 42, 512–523. doi:10.1016/j.jgr.2017.07.005

Kim, J. H., Yang, B., Tedesco, A., Lebig, E. G. D., Ruegger, P. M., Xu, K., et al. (2019). High Levels of Oxidative Stress and Skin Microbiome Are Critical for Initiation and Development of Chronic Wounds in Diabetic Mice. *Sci. Rep.* 9, 19318. doi:10.1038/s41598-019-55644-3

Kwok, H.-H., Guo, G.-L., Lau, J. K.-C., Cheng, Y.-K., Wang, J.-R., Jiang, Z.-H., et al. (2012). Stereoisomers ginsenosides-20(S)-Rg3 and -20(R)-Rg3 Differentially Induce Angiogenesis through Peroxisome Proliferator-Activated Receptor-Gamma. *Biochem. Pharmacol.* 83, 893–902. doi:10.1016/j.bcp.2011.12.039

Kwon, D., Cha, H.-J., Choi, E., Leem, S.-H., Kim, G.-Y., Moon, S.-K., et al. (2018). Schisandrin A Suppresses Lipopolysaccharide-Induced Inflammation and Oxidative Stress in RAW 264.7 Macrophages by Suppressing the NF-κB, MAPKs and PI3K/Akt Pathways and Activating Nrf2/HO-1 Signaling. *Int. J. Mol. Med.* 41, 264–274. doi:10.3892/ijmm.2017.3209

Lee, H.-M., Shin, D.-M., Yuk, J.-M., Shi, G., Choi, D.-K., Lee, S.-H., et al. (2011). Autophagy Negatively Regulates Keratinocyte Inflammatory Responses via Scaffolding Protein p62/SQSTM1. *J. Immunol.* 186, 1248–1258. doi:10.4049/jimmunol.1001954

Lee, W.-J., Kim, Y.-S., and Shim, W.-S. (2018). Korean Red Ginseng Extract and Ginsenoside Rg3 Have Anti-pruritic Effects on Chloroquine-Induced Itch by Inhibition of MrgprA3/TRPA1-Mediated Pathway. *J. Ginseng Res.* 42, 470–475. doi:10.1016/j.jgr.2017.05.004

Lee, H., Hong, Y., Tran, Q., Cho, H., Kim, M., Kim, C., et al. (2019). A New Role for the Ginsenoside RG3 in Antiaging via Mitochondria Function in Ultraviolet-Irradiated Human Dermal Fibroblasts. *J. Ginseng Res.* 43, 431–441. doi:10.1016/j.jgr.2018.07.003

Li, J., Zhang, Y.-P., and Kirsner, R. S. (2003). Angiogenesis in Wound Repair: Angiogenic Growth Factors and the Extracellular Matrix. *Microsc. Res. Tech.* 60, 107–114. doi:10.1002/jemt.10249

Łoś-Rycharska, E., Gołębiewski, M., Sikora, M., Grzybowski, T., Gorzkiewicz, M., Popielarz, M., et al. (2021). A Combined Analysis of Gut and Skin Microbiota in Infants with Food Allergy and Atopic Dermatitis: A Pilot Study. *Nutrients* 13, 1682. doi:10.3390/nu13051682

Lu, Q., Shu, Y., Wang, L., Li, G., Zhang, S., Gu, W., et al. (2021). The Protective Effect of Veronica Ciliata Fisch. Extracts on Relieving Oxidative Stress-Induced Liver Injury via Activating AMPK/p62/Nrf2 Pathway. *J. Ethnopharmacol.* 270, 113775. doi:10.1016/j.jep.2021.113775

Luqman, A., Muttaqin, M. Z., Yulaipi, S., Ebner, P., Matsuo, M., Zabel, S., et al. (2020). Trace Amines Produced by Skin Bacteria Accelerate Wound Healing in Mice. *Commun. Biol.* 3, 277. doi:10.1038/s42003-020-1000-7

Ma, L., Li, L. Y., and Zhao, T. L. (2020). Anti-inflammatory Effects of Ginsenoside Rg3 on the Hypertrophic Scar Formation via the NF-κB/IκB Signaling Pathway in Rabbit Ears. *Pharmazie* 75, 102–106. doi:10.1691/ph.2020.9852

Mei, F., Liu, J., Wu, J., Duan, Z., Chen, M., Meng, K., et al. (2020). Collagen Peptides Isolated from *Salmo salar* and Tilapia Nilotica Skin Accelerate Wound Healing by Altering Cutaneous Microbiome Colonization via Upregulated NOD2 and BD14. *J. Agric. Food Chem.* 68, 1621–1633. doi:10.1021/acs.jafc.9b08002

Niu, T., Tian, Y., Wang, G., Guo, G., Tong, Y., and Shi, Y. (2020). Inhibition of ROS-NF-κB-dependent Autophagy Enhances Hypocrellin A United LED Red Light-Induced Apoptosis in Squamous Carcinoma A431 Cells. *Cell. Signal.* 69, 109550. doi:10.1016/j.cellsig.2020.109550

Oryan, A., Alemzadeh, E., and Moshiri, A. (2019). Role of Sugar-Based Compounds on Cutaneous Wound Healing: what Is the Evidence? *J. Wound Care* 28, s13–s24. doi:10.12968/jowc.2019.28.Sup3b.S13

Pang, M., Yao, Z., Chen, C., Lei, X., and Cheng, B. (2020). Human-microorganism Mutualism Theory: Possible Mechanisms for the Delayed Chronic Wound Healing Process. *Med. Hypotheses* 141, 109720. doi:10.1016/j.mehy.2020.109720

Pastar, I., Stojadinovic, O., Yin, N. C., Ramirez, H., Nusbaum, A. G., Sawaya, A., et al. (2014). Epithelialization in Wound Healing: A Comprehensive Review. *Adv. Wound Care* 3, 445–464. doi:10.1089/wound.2013.0473

Pistone, D., Meroni, G., Panelli, S., D'Auria, E., Acunzo, M., Pasala, A. R., et al. (2021). A Journey on the Skin Microbiome: Pitfalls and Opportunities. *Int. J. Mol. Sci.* 22, 9846. doi:10.3390/ijms22189846

Proksch, E., Brandner, J. M., and Jensen, J.-M. (2008). The Skin: an Indispensable Barrier. *Exp. Dermatol.* 17, 1063–1072. doi:10.1111/j.1600-0625.2008.00786.x

Reinke, J. M., and Sorg, H. (2012). Wound Repair and Regeneration. *Eur. Surg. Res.* 49, 35–43. doi:10.1159/000339613

Ren, H., Zhao, F., Zhang, Q., Huang, X., and Wang, Z. (2022). Autophagy and Skin Wound Healing. *Burns Trauma* 10, tkac003. doi:10.1093/burnst/tkac003

Rey, S., and Semenza, G. L. (2010). Hypoxia-inducible Factor-1-Dependent Mechanisms of Vascularization and Vascular Remodelling. *Cardiovasc. Res.* 86, 236–242. doi:10.1093/cvr/cvq045

Shan, X., Fu, Y.-S., Aziz, F., Wang, X.-Q., Yan, Q., and Liu, J.-W. (2014). Ginsenoside Rg3 Inhibits Melanoma Cell Proliferation through Down-Regulation of Histone Deacetylase 3 (HDAC3) and Increase of P53 Acetylation. *PLoS One* 9, e115401. doi:10.1371/journal.pone.0115401

Shen, Y., Yang, J., Zhao, J., Xiao, C., Xu, C., and Xiang, Y. (2015). The Switch from ER Stress-Induced Apoptosis to Autophagy via ROS-Mediated JNK/p62 Signals: A Survival Mechanism in Methotrexate-Resistant Choriocarcinoma Cells. *Exp. Cell Res.* 334, 207–218. doi:10.1016/j.yexcr.2015.04.010

Sheng, J.-Q., Wang, M.-R., Fang, D., Liu, L., Huang, W.-J., Tian, D.-A., et al. (2021). LncRNA NBR2 Inhibits Tumorigenesis by Regulating Autophagy in Hepatocellular Carcinoma. *Biomed. Pharmacother.* 133, 111023. doi:10.1016/j.biopha.2020.111023

Sil, P., Wong, S.-W., and Martinez, J. (2018). More Than Skin Deep: Autophagy Is Vital for Skin Barrier Function. *Front. Immunol.* 9, 1376. doi:10.3389/fimmu.2018.01376

Singer, A. J. (2022). Healing Mechanisms in Cutaneous Wounds: Tipping the Balance. *Tissue Eng. Part B Rev.* doi:10.1089/ten.teb.2021.01141

Song, R., Zheng, J., Liu, Y., Tan, Y., Yang, Z., Song, X., et al. (2019). A Natural Cordycepin/chitosan Complex Hydrogel with Outstanding Self-Healable and Wound Healing Properties. *Int. J. Biol. Macromol.* 134, 91–99. doi:10.1016/j.ijbiomac.2019.04.195

Soriano-Ruiz, J. L., Calpena-Campmany, A. C., Silva-Abreu, M., Halbout-Bellowa, L., Bozal-de Febrer, N., Rodríguez-Lagunas, M. J., et al. (2020). Design and Evaluation of a Multifunctional Thermosensitive Poloxamer-Chitosan-Hyaluronic Acid Gel for the Treatment of Skin Burns. *Int. J. Biol. Macromol.* 142, 412–422. doi:10.1016/j.ijbiomac.2019.09.113

Sukseree, S., Bakiri, L., Palomo-Irigoyen, M., Uluçkan, Ö., Petzelbauer, P., and Wagner, E. F. (2021). Sequestosome 1/p62 Enhances Chronic Skin Inflammation. *J. Allergy Clin. Immunol.* 147, 2386–2393.e4. doi:10.1016/j.jaci.2021.02.028

Sun, X., Cheng, L., Zhu, W., Hu, C., Jin, R., Sun, B., et al. (2014). Use of Ginsenoside Rg3-Loaded Electrospun PLGA Fibrous Membranes as Wound Cover Induces Healing and Inhibits Hypertrophic Scar Formation of the Skin. *Colloids Surfaces B Biointerfaces* 115, 61–70. doi:10.1016/j.colsurfb.2013.11.030

Sun, M., Ye, Y., Xiao, L., Duan, X., Zhang, Y., and Zhang, H. (2017). Anticancer Effects of Ginsenoside Rg3 (Review). *Int. J. Mol. Med.* 39, 507–518. doi:10.3892/ijmm.2017.2857

Sun, M., Zhu, C., Long, J., Lu, C., Pan, X., and Wu, C. (2020). PLGA Microsphere-Based Composite Hydrogel for Dual Delivery of Ciprofloxacin and Ginsenoside Rh2 to Treat Staphylococcus Aureus-Induced Skin Infections. *Drug Deliv.* 27, 632–641. doi:10.1080/10717544.2020.1756985

Takeo, M., Lee, W., and Ito, M. (2015). Wound Healing and Skin Regeneration. *Cold Spring Harb. Perspect. Med.* 5, a023267. doi:10.1101/cshperspect.a023267

Tavakoli, S., and Klar, A. S. (2020). Advanced Hydrogels as Wound Dressings. *Biomolecules* 10, 1169. doi:10.3390/biom10081169

Usategui-Martín, R., Gestoso-Uzal, N., Calero-Paniagua, I., De Pereda, J. M., del Pino-Montes, J., and González-Sarmiento, R. (2020). A Mutation in P62 Protein (P. R321C), Associated to Paget's Disease of Bone, Causes a Blockade of Autophagy and an Activation of NF-kB Pathway. *Bone* 133, 115265. doi:10.1016/j.bone.2020.115265

Veith, A. P., Henderson, K., Spencer, A., Sligar, A. D., and Baker, A. B. (2019). Therapeutic Strategies for Enhancing Angiogenesis in Wound Healing. *Adv. Drug Deliv. Rev.* 146, 97–125. doi:10.1016/j.addr.2018.09.010

Volkov, V., and Cavaco-Paulo, A. (2016). Enzymatic Phosphorylation of Hair Keratin Enhances Fast Adsorption of Cationic Moieties. *Int. J. Biol. Macromol.* 85, 476–486. doi:10.1016/j.ijbiomac.2015.12.082

Wang, P.-H., Huang, B.-S., Horng, H.-C., Yeh, C.-C., and Chen, Y.-J. (2018a). Wound Healing. *J. Chin. Med. Assoc.* 81, 94–101. doi:10.1016/j.jcma.2017.11.002

Wang, X., Zhang, X., Fan, L., He, H., Zhang, X., Zhang, Y., et al. (2018b). Influence of Polymeric Carrier on the Disposition and Retention of 20(R)-ginsenoside-rg3-loaded Swellable Microparticles in the Lung. *Drug Deliv. Transl. Res.* 8, 252–265. doi:10.1007/s13346-017-0456-6

Wu, X., Hou, J., Li, M., Wang, J., Kaplan, D. L., and Lu, S. (2012). Sodium Dodecyl Sulfate-Induced Rapid Gelation of Silk Fibroin. *Acta Biomater.* 8, 2185–2192. doi:10.1016/j.actbio.2012.03.007

Wu, Y., Li, H., Rao, Z., Li, H., Wu, Y., Zhao, J., et al. (2017). Controlled Protein Adsorption and Delivery of Thermosensitive poly(N-Isopropylacrylamide) Nanogels. *J. Mat. Chem. B* 5, 7974–7984. doi:10.1039/c7tb01824j

Xu, Z., and Hsia, H. C. (2018). The Impact of Microbial Communities on Wound Healing: A Review. *Ann. Plastic Surg.* 81, 113–123. doi:10.1097/SAP.0000000000001450

Xu, T., Yang, R., Ma, X., Chen, W., Liu, S., Liu, X., et al. (2019). Bionic Poly(γ-Glutamic Acid) Electrospun Fibrous Scaffolds for Preventing Hypertrophic Scars. *Adv. Healthc. Mat.* 8, e1900123. doi:10.1002/adhm.201900123

Yu, X., Xu, H., Hu, M., Luan, X., Wang, K., Fu, Y., et al. (2015). Ginsenoside Rg3 Bile Salt-Phosphatidylcholine-Based Mixed Micelles: Design, Characterization, and Evaluation. *Chem. Pharm. Bull.* 63, 361–368. doi:10.1248/cpb.c15-00045

Zhang, X., Yin, M., and Zhang, L.-J. (2019). Keratin 6, 16 and 17-Critical Barrier Alarmin Molecules in Skin Wounds and Psoriasis. *Cells* 8, 807. doi:10.3390/cells8080807

Zhang, D., Ouyang, Q., Hu, Z., Lu, S., Quan, W., Li, P., et al. (2021). Catechol Functionalized Chitosan/active Peptide Microsphere Hydrogel for Skin Wound Healing. *Int. J. Biol. Macromol.* 173, 591–606. doi:10.1016/j.ijbiomac.2021.01.157

Conflict of Interest: The authors declare that the research was conducted in the absence of any commercial or financial relationships that could be construed as a potential conflict of interest.

Publisher's Note: All claims expressed in this article are solely those of the authors and do not necessarily represent those of their affiliated organizations, or those of the publisher, the editors, and the reviewers. Any product that may be evaluated in this article, or claim that may be made by its manufacturer, is not guaranteed or endorsed by the publisher.

Copyright © 2022 Peng, Ding, Zhao, Hao, Liu, Yang, Xiao and Zheng. This is an open-access article distributed under the terms of the Creative Commons Attribution License (CC BY). The use, distribution or reproduction in other forums is permitted, provided the original author(s) and the copyright owner(s) are credited and that the original publication in this journal is cited, in accordance with accepted academic practice. No use, distribution or reproduction is permitted which does not comply with these terms.

frontiers | Frontiers in Bioengineering and Biotechnology

TYPE Original Research
PUBLISHED 17 August 2022
DOI 10.3389/fbioe.2022.973886

Check for updates

OPEN ACCESS

EDITED BY
Bruce Alan Bunnell,
University of North Texas Health Science Center, United States

REVIEWED BY
Shiv Dutt Purohit,
Yeungnam University, South Korea
Dejian Li,
Fudan University Pudong Medical Center, China

*CORRESPONDENCE
Shuyu Sun,
sunshuy1095@126.com
Qianzhou Jiang,
jqianzhou@126.com

†These authors have contributed equally to this work

SPECIALTY SECTION
This article was submitted to Tissue Engineering and Regenerative Medicine, a section of the journal Frontiers in Bioengineering and Biotechnology

RECEIVED 20 June 2022
ACCEPTED 14 July 2022
PUBLISHED 17 August 2022

CITATION
Tan G, Chen R, Tu X, Guo L, Guo L, Xu J, Zhang C, Zou T, Sun S and Jiang Q (2022), Research on the osteogenesis and biosafety of ECM–Loaded 3D–Printed Gel/SA/58sBG scaffolds. *Front. Bioeng. Biotechnol.* 10:973886. doi: 10.3389/fbioe.2022.973886

COPYRIGHT
© 2022 Tan, Chen, Tu, Guo, Guo, Xu, Zhang, Zou, Sun and Jiang. This is an open-access article distributed under the terms of the Creative Commons Attribution License (CC BY). The use, distribution or reproduction in other forums is permitted, provided the original author(s) and the copyright owner(s) are credited and that the original publication in this journal is cited, in accordance with accepted academic practice. No use, distribution or reproduction is permitted which does not comply with these terms.

Research on the osteogenesis and biosafety of ECM–Loaded 3D–Printed Gel/SA/58sBG scaffolds

Guozhong Tan[1,2†], Rongfeng Chen[1†], Xinran Tu[1], Liyang Guo[1], Lvhua Guo[1], Jingyi Xu[1], Chengfei Zhang[3], Ting Zou[3], Shuyu Sun[4*] and Qianzhou Jiang[1*]

[1]Department of Endodontics, Affiliated Stomatology Hospital of Guangzhou Medical University, Guangdong Engineering Research Center of Oral Restoration and Reconstruction, Guangzhou Key Laboratory of Basic and Applied Research of Oral Regenerative Medicine, Guangzhou, China, [2]Department of Oral and Maxillofacial Surgery, Affiliated Stomatology Hospital of Guangzhou Medical University, Guangdong Engineering Research Center of Oral Restoration and Reconstruction, Guangzhou Key Laboratory of Basic and Applied Research of Oral Regenerative Medicine, Guangzhou, China, [3]Endodontology, Restorative Dental Sciences, Faculty of Dentistry, The University of Hong Kong, Hong Kong, China, [4]Department of Endodontics, Stomatological Hospital, Southern Medical University, Guangzhou, China

Employing scaffolds containing cell–derived extracellular matrix (ECM) as an alternative strategy for the regeneration of bone defects has shown prominent advantages. Here, gelatin (Gel), sodium alginate (SA) and 58s bioactive glass (58sBG) were incorporated into deionized water to form ink, which was further fabricated into composite scaffolds by the 3D printing technique. Then, rat aortic endothelial cells (RAOECs) or rat bone mesenchymal stem cells (RBMSCs) were seeded on the scaffolds. After decellularization, two kinds of ECM–loaded scaffolds (RAOECs–ECM scaffold and RBMSCs–ECM scaffold) were obtained. The morphological characteristics of the scaffolds were assessed meticulously by scanning electron microscopy (SEM). In addition, the effects of scaffolds on the proliferation, adhesion, and osteogenic and angiogenic differentiation of RBMSCs were evaluated by Calcein AM staining and reverse transcription polymerase chain reaction (RT–PCR). *In vivo*, full–thickness bone defects with a diameter of 5 mm were made in the mandibles of Sprague–Dawley (SD) rats to assess the bone regeneration ability and biosafety of the scaffolds at 4, 8 and 16 weeks. The osteogenic and angiogenic potential of the scaffolds were investigated by microcomputed tomography (Micro–CT) and histological analysis. The biosafety of the scaffolds was evaluated by blood biochemical indices and histological staining of the liver, kidney and cerebrum. The results showed that the ECM–loaded scaffolds were successfully prepared, exhibiting interconnected pores and a gel–like ECM distributed on their surfaces. Consistently, *in vitro* experiments demonstrated that the scaffolds displayed favourable cytocompatibility. *In vitro* osteogenic differentiation studies showed that scaffolds coated with ECM could significantly increase the expression of osteogenic and angiogenic genes. In addition, the results from mandibular defect repair *in vivo* revealed that the ECM–loaded scaffolds effectively promoted the healing of bone defects when compared to the pure scaffold. Overall, these findings demonstrate that both RAOECs–ECM scaffold and

RBMSCs–ECM scaffold can greatly enhance bone formation with good biocompatibility and thus have potential for clinical application in bone regeneration.

KEYWORDS

3D printing, ECM, scaffolds, bone defects, biosafety, bone regeneration

1 Introduction

Bone defects of the oral and maxillofacial areas derived from congenital defects, trauma, infection or surgical removal usually need surgical external intervention to enhance regeneration. Autografts are considered the gold standard in bone repair but can cause donor site morbidity, and the sources are limited (Agarwal and García Andrés, 2015). Allografts and xenografts can also have osteoconductive and osteoinductive properties but suffer from the risks of immune rejection and pathogen transmission (Lee et al., 2019; Zhu et al., 2020). As a result, synthetic bone substitutes have been the focus of attention and not only can be produced on a large scale but also possess osteogenic properties. In our previous study, gelatin (Gel), sodium alginate (SA) and bioactive glass (BG) were deemed to have promising prospects for fabricating composite scaffolds by 3D printing technology, which showed that the prepared scaffolds have good osteogenic induction performance (Wu J. et al., 2019).

To improve the osteogenic potential of engineering scaffolds, bioactive factors with osteoinductive activity are integrated into the scaffolds to provide guidance for cell differentiation or tissue regeneration. The extracellular matrix (ECM), a complex network with a noncellular component, is composed of various structural and functional molecules secreted by cells, such as collagen, fibronectin, laminin, glycosaminoglycans, and proteoglycans (Carvalho Marta et al., 2019). The functional molecules of the ECM can produce a native microenvironment to improve cell proliferation, adhesion and differentiation. Several studies have attempted to imitate the ECM microenvironment by integrating supporting molecules into synthetic biomaterials, but they provide limited components that present specific functional receptors for cell attachment or proliferation and cannot satisfy the entire function of native ECM (Wu Y.-H. A. et al., 2019b). Natural ECM, with its complex structure and composition, is difficult to synthesize artificially. Moreover, it is hard to realize application by using a single ECM as the mechanical properties of ECM are poor; therefore, the combined application of scaffolds and ECM is currently a popular approach. Studies are aimed at incorporating natural ECM from specific tissue or cultured cells into scaffolds, which produces cell–or tissue–specific cues to enhance osteogenesis and has been receiving growing research attention. In particularly, cell–derived ECM can be easily obtained through cell culture, proliferation and differentiation, followed by decellularization, which can be combined with scaffolds to enhance the osteogenic ability and has been reported by numerous studies (Pati et al., 2015; Kim et al., 2018).

Inspired by this, we attempted to ornament the Gel/SA/58sBG scaffolds with cell–derived ECM to induce angiogenesis and accelerate bone repair. Adequate blood supply is also crucial for bone regeneration of scaffolds after implantation, which involves the interaction of a series of precursor cells, growth factors and angiogenic factors. The lack of vasculature in tissue engineered scaffolds could result in inadequate oxygen and nutrition supply and waste removal, eventually leading to hypoxia and cell death. To our knowledge, one of the most effective strategies to improve the angiogenic and osteogenic potential of scaffolds is to combine endothelial progenitor cells (EPCs)–derived ECM (Peng et al., 2019; Lin et al., 2021). EPCs are the precursor of endothelial cells, and transplanted EPCs reportedly stimulate angiogenesis by differentiating into mature endothelial cells or triggering angiogenic events by secreting various trophic factors (Ishikawa and Asahara, 2004; Critser and Yoder, 2010; Kim et al., 2010; Ackermann et al., 2014). Rat aortic endothelial cells (RAOECs) are types of endothelial cells that are commonly used for research on cardiovascular diseases. Recently, RAOECs have also been used to study fracture healing and bone tissue engineering (Pekozer Gorke et al., 2016). Considering that the extracellular matrix plays a vital role in angiogenesis, we hypothesize that RAOECs–derived ECM combined with scaffolds may produce an effective way to induce angiogenesis. Bone marrow mesenchymal stem cells (BMSCs) with superior osteoconductive potential are a primary choice in bone tissue engineering applications, as they promote vascularization through paracrine action and differentiate into osteoblasts and are thus beneficial for bone regeneration and angiogenesis (Chen et al., 2018; Ying et al., 2020). Several studies have investigated the abilities of BMSCs–derived ECM to induce bone tissue regeneration (Wei et al., 2015; Gao et al., 2018; Sun et al., 2018; Chi et al., 2020). For our research, 3D–printed Gel/SA/58sBG scaffolds exhibit several advantages, including porous structure and good mechanical characteristics, which also contribute to oxygenation up-take, waste excretion and effective support. With the appropriate pore size and porosity, the cell–derived ECM can enter and adhere to the scaffolds to promote angiogenesis and osteogenesis. An appealing option is to combine RBMSCs–or RAOECs–derived ECM with scaffolds to simulate the natural osteogenic bone microenvironment for bone repairing. Therefore, we seeded

RBMSCs or RAOECs on Gel/SA/58sBG scaffolds to obtain two kinds of cell–derived ECM scaffolds by decellularized treatment, which meet all the characteristics of functional scaffolds, including simulating the complex composition of the cell–derived ECM and the interactions among various macromolecules *in vitro* and *vivo*. The aim of this study was to investigate the osteogenic potential and biosafety of the two kinds of cell–derived ECM scaffolds.

In this research, Gel, SA and 58sBG were mixed according to a certain proportion to form ink, and scaffolds were fabricated by 3D printing. The scaffolds were cultured with RAOECs or RBMSCs and loaded with ECM after decellularization. *In vitro*, we assessed the surface morphology, cytocompatibility and osteogenic differentiation of the scaffolds. The bone regeneration capability and biosafety of the scaffolds *in vivo* were evaluated after implantation into mandibular bone defects of rats. Ultimately, both kinds of ECM–loaded scaffolds were proven to be more suitable for bone regeneration with favourable cytocompatibility, osteogenic activity and biosafety.

2 Materials and methods

2.1 Fabrication of 3D–printed Gel/SA/58s BG scaffolds

58sBG with a composition of TEOS (6.6 ml), TEP (0.86 ml) and $Ca(NO_3)_2$ $4H_2O$ (4.25 g) was prepared by an evaporation–induced self–assembly (EISA) method as previously reported (Tsigkou et al., 2014). The ink was first prepared before printing. A total of 1.05 g 58sBG, 1.5 g Gel and 0.6 g of SA were added to 10 ml of deionized water at 55°C in a constant temperature system. Then, magnetic and mechanical stirring were used to mix the materials. The obtained ink was transferred to the barrel of a 3D bioprinter (Regenovo, Hangzhou, China). The experimental parameters of the printing process were set as follows: the needle diameter was 0.4 mm, the extrusion pressure was 0.38 MPa, the printing speed was 15 mm/s, the adjacent filaments were 1.2 mm, and the extrusion temperature was 28°C. According to the needs, two different shapes of scaffolds were printed (10 mm × 10 mm × 1.5 mm cubic scaffold for *in vitro* study, 5 mm diameter and 1.5 mm high cylindrical scaffold for *in vivo* study). Next, the obtained scaffolds were soaked in 10% $CaCl_2$ solution and cross–linked for 10 min. Further cross–linking in 0.25% glutaraldehyde solution for 30 min was carried out. After that, scaffolds were washed with distilled water 5 times and soaked in distilled water for 8 h. Finally, scaffolds were frozen at 80°C and dried for 24 h in a freeze dryer (CHRIST, Germany) for further use.

2.2 Cell culture

RAOECs, RBMSCs (Procell, Wuhan, China), and L929 (iCell Bioscience Inc., Shanghai, China) cells were cultured with Dulbecco's modified Eagle's medium (DMEM) supplemented with 10% foetal bovine serum (Gibco, Thermo Fisher Scientific, Inc., United States). The cells were maintained at 37°C in a humidified atmosphere with 5% CO_2. These cells were then subcultured and frozen for storage for later use.

2.3 Preparation of ECM loaded–3D–printed Gel/SA/58s BG scaffolds

Before seeding, all cells were expanded in standard culture medium in a monolayer until they reached 80%–90% confluence. RAOECs or RBMSCs were seeded on scaffolds, which were placed in 6–well plates at passages 3–5 with a density of 2×10^5 cells per scaffold. The medium was changed every 2 days. After 14 days of cultivation and proliferation, the scaffolds were transferred to new well plates to remove nonadherent cells. Based on previously reported methods (Kang et al., 2012; Gong et al., 2017), the cell–scaffold composites were immersed in 0.1% ammonium hydroxide (NH_4OH) + 0.5% Triton X–100 (Sigma–Aldrich, St. Louis, MO) solution for 30 min and then washed with PBS 3 times. All vital cells were removed for decellularization, and RAOECs–ECM scaffold and RBMSCs–ECM scaffold were obtained. Finally, the ECM–loaded scaffolds were frozen for further use.

2.4 Cell attachment and morphology

To detect the cell viability and attachment of the RBMSCs seeded on the pure scaffold, RAOECs–ECM scaffold or RBMSCs–ECM scaffold. RBMSCs (4×10^5 cells/scaffold) were seeded onto the scaffolds and incubated at 37°C. After 1, 3 and 7 days, the medium was removed, and the scaffolds were washed with PBS three times and then treated with Calcein AM (Bestbio, Shanghai, China). The live cells on the scaffolds were observed under a fluorescence microscope. To observe the attachment and morphology of cells grown on the scaffolds, the cell–scaffold composites were collected at Day 3, washed twice with PBS and chemically fixed using 2.5% glutaraldehyde solution. The specimens were subsequently dehydrated twice with a series of graded ethanol (30%, 50%, 70%, 80%, 90%, and 100%). After dehydration, the scaffolds were immersed in hexamethyl–disilazane for 2 min and vacuum–dried overnight. Finally, the scaffolds were sputter–coated for 60 s at 10 mA with gold, and the gold–coated scaffolds were observed via SEM.

2.5 Gene expression by real–time polymerase chain reaction

After RBMSCs were seeded on the scaffolds for 7 and 14 days, the scaffolds were removed from the medium and washed twice

TABLE 1 RT–PCR primers.

Gene/primer target	Forward primer (5′–>3′)	Reverse primer (5′–>3′)
GAPDH	TCTCTGCTCCTCCCTGTTC	ACACCGACCTTCACCATCT
RUNX2	GAAATGCCTCTGCTGTTATGA	AAGTGAAACTCTTGCCTCGTC
BMP2	GAGAAAAGCGTCAAGCCAAAC	GTCATTCCACCCCACATCACT
CD31	AGAATCCGCCCTGGAGTGTT	ACGGCAGCAGAGCAGAAAGC
VEGF	CCACGACAGAAGGGGAGCA	ACACCGCATTAGGGGCACA

with PBS. Total RNA from each group was extracted using an RNA extraction kit (AG21017, Accurate Biology, China) and quantified by a spectrophotometer (NanoDrop 2000; Thermo Fisher Scientific, Waltham, MA, United States). The obtained RNA was used to synthesize complementary DNA (cDNA) *via* an RT–PCR Kit (AG11706, Accurate Biology, China). Finally, RT–PCR was performed using SYBR® Premix Ex TaqTM II (RR820A, Takara, Japan) in a CFX96 Real–time PCR machine (Bio–Rad, Hercules, CA, United States). The relative gene expression was calculated using $2^{-\Delta\Delta Ct}$. GAPDH was used as the housekeeping gene, and the genes examined were RUNX2, BMP2, CD31 and VEGF. The primer sequences are detailed in Table 1.

2.6 Preparation of mandibular bone defect

A total of 108 male SD rats weighing 280–320 g were purchased from the experimental animal centre of Guangzhou University of Chinese Medicine (licence number: SCXK (Guangdong) 2018–0034) and divided into four groups (n = 9 each group at each time point): 1) control group; 2) scaffold group; 3) RAOECs–ECM scaffold group; and 4) RBMSCs–ECM scaffold group. Briefly, general anaesthesia was achieved by intraperitoneally injecting pentobarbital (40 mg/kg), and a 15 mm longitudinal incision was made 2 mm above the lower edge of the mandible body to expose the bone surface when adequacy of the anaesthesia had been confirmed. Then, 5 mm full–thickness critical defects were created on the right side of the mandibular ramus of the rats by using a 5 mm trephine bur. Physiological saline irrigation was maintained throughout the drilling procedure to prevent heat damage. The fillings of the defects were randomly assigned. Defects were filled with pure scaffold, RAOECs–ECM scaffold or RBMSCs–ECM scaffold, respectively. The control group was not filled with any material. The wounds were closed with sutures in layers, and penicillin sodium (160,000 IU/ml) was intramuscularly injected in the first 3 days after surgery. Rats were euthanized via carbon dioxide asphyxiation at 4, 8 and 16 weeks postsurgery. The mandibles were harvested and soaked in 4% paraformaldehyde for further analysis.

2.7 Microcomputed tomography (Micro–CT) test

To analyse the newly formed bone tissue in the defect area, five mandibles of each group were scanned by a Micro–CT scanner (SkyScan 1,174 Compact Micro CT, Kontich, Belgium) with a resolution of 10 μm at each time point. Mandibles were dried with a paper towel to remove the residual paraformaldehyde solution and perpendicularly stabilized in the exact centre of the 4 cm diameter cylindrical moulds. After that, Micro–CT scans were performed, and transverse sections were acquired from the raw data processed by NRecon software. The obtained sections were transferred to CTan software for quantitative analysis, which included the parameters of total volume (TV, mm^3), bone volume (BV, mm^3), percent of bone volume (BV/TV, %) and bone mineral density (BMD, mg/cm^3).

2.8 Microfil perfusion

After full anaesthesia, four rats from each group at each time point were supine on the operating table and cut from the sternal notch to the midline of the abdomen. Then, the thorax and pericardium were cut open with scissors to expose the heart. The left ventricle was inserted with a blunt 18–size needle, and 300 ml of heparin normal saline and 4% paraformaldehyde were injected successively. Then, 18 ml of Microfil (Microfil MV–120, Flow Tech) was perfused. When the blood vessel was infused with the contrast agent, staining of the tongue and the coronary artery was visible. The mandibular bones of the carcasses were removed and stored overnight in a refrigerator at 4°C, kept in 4% paraformaldehyde for 24 h, and fully decalcified in 10% ethylene diamine tetraacetic acid (EDTA) solution for approximately 2 months. Micro–CT was used to scan the mandibular defects after decalcification, and neovascularization was detected by 3D reconstruction imaging. The area of local blood vessels in bone defects was evaluated by CTvox software.

2.9 Histological and immunohistological analyses

After incubation in 4% paraformaldehyde for 24 h and decalcification in 10% EDTA for 2 months, the obtained samples were dehydrated with alcohol gradients and embedded in paraffin. Then, the samples were cut longitudinally along the axial plane to make 4–μm–thick sections. The sections from each sample were subjected to haematoxylin–eosin (H&E) and Masson's trichrome (MT) staining. Histologic observations and images were acquired by light microscopy under ×10 and ×200 magnification. To evaluate the osteogenesis and angiogenesis of the defects, immunohistochemical (IHC) staining of RUNX2, OCN, CD31 and VEGF was performed. Rabbit anti–RUNX2 (1:50, Abcam, United Kingdom), rabbit anti–OCN antibody (1:200, Bioss, United States), rabbit anti–CD31 antibody (1:1,000, Abcam, United Kingdom) and rabbit anti–VEGF antibody (1: 200, Bioss, United States) were used as the primary antibodies. After dewaxing and rehydration, antigen retrieval was performed in a pressure cooker for 10 min. Subsequently, 3% hydrogen peroxide (Boster, China) and 10% bovine serum albumin (Solarbio, China) were used to eliminate endogenous peroxidase activity and block nonspecific antibody binding sites, respectively. The sections were then incubated with the primary antibodies overnight at 4°C. Next, the sections were incubated with the secondary antibodies (Beyotime Biotechnology, China) against rabbit IgG, and diaminobenzidine (DAB) (Cell Signaling Technology, United States) was used to show the positive staining. Finally, the sections were counterstained with haematoxylin, and images were captured with a light microscope (Leica, Germany). For quantitative analysis, the percentage of the new bone area in H&E staining was calculated with the new bone area/tissue area × 100%. For IHC analysis, the average optical density (AOD) was quantitatively measured by ImageJ.

2.10 Histopathological and biochemical analyses

At each time point after surgery, 5 rats from each group were fixed in a metabolism cage for blood collection. In brief, a 2 ml blood sample from each rat was drawn at each time point via the caudal vein, which was used to analyse the levels of albumin (ALB), total protein (TP), aspartate aminotransferase (AST), alanine transaminase (ALT), creatinine (Cr) and blood urea nitrogen (BUN) in the Guangzhou Key Laboratory of Basic and Applied Research of Oral Regenerative Medicine. After that, animals were sacrificed via carbon dioxide asphyxiation. The liver, kidney and cerebrum were collected from rats, which were fixed with 4% paraformaldehyde for 24 h, embedded in paraffin, and stained with haematoxylin–eosin (H&E) at a 4 μm thickness to reveal if pathological changes had occurred.

2.11 Statistical analysis

All data are presented as the mean ± standard deviation for $n \geq 3$. SPSS (IBM SPSS Inc., United States) demonstrated that all data were in accordance with a normal distribution. Statistical significance between groups was tested using one–way analysis of variance (ANOVA) followed by Tukey's post–hoc test. $p < 0.05$ was considered statistically significant.

3 Results

3.1 Morphology and characterization of scaffolds

The general morphology and surface characterization of the scaffolds are shown in Figure 1 **(A)** The general morphology of the scaffolds was observed. **(B)** The surface morphologies and internal structures of the freeze–dried scaffolds were evaluated by SEM. According to different needs, we prepared scaffolds with cylindrical shapes (diameter: 5 mm, height: 5 mm), which were applied for the experiments *in vivo*. All the scaffolds showed a complete macrostructure with multiple pores, rough walls and connected apertures, which is conducive to cell recruitment, adhesion and differentiation. The addition of ECM indicated that the scaffold surface was covered with a biological layer, generating a more homogenous porous structure, which further increased cellular infiltration.

3.2 Cell adhesion, proliferation and RT–PCR assay

As shown in Figure 2A, Calcein AM staining confirmed the occurrence of viable cells on the porous structures of scaffolds, and the homogeneous distribution of viable cells was more evident at ECM–loaded scaffolds, which demonstrated that ECM provides an appropriate microenvironment and a biocompatible surface for RBMSCs adhesion. (Figure 2B) SEM showed that RBMSCs adhered to the surface of porous scaffolds. After 7 days of incubation, the cells showed an irregular shape in the pure scaffold group, while in the ECM–loaded scaffold group, cells on the scaffold surface became long and spindle–shaped with extended filopodia. (Figure 2C) The expression levels of osteogenic (RUNX2, BMP2) and vascularized genes (CD31, VEGF) were detected by RT–PCR at Day 0, 7 and 14. The results showed that the mRNA expression levels of a series of genes in RBMSCs were upregulated in the ECM–loaded scaffold groups. In particular, the gene expression levels in the

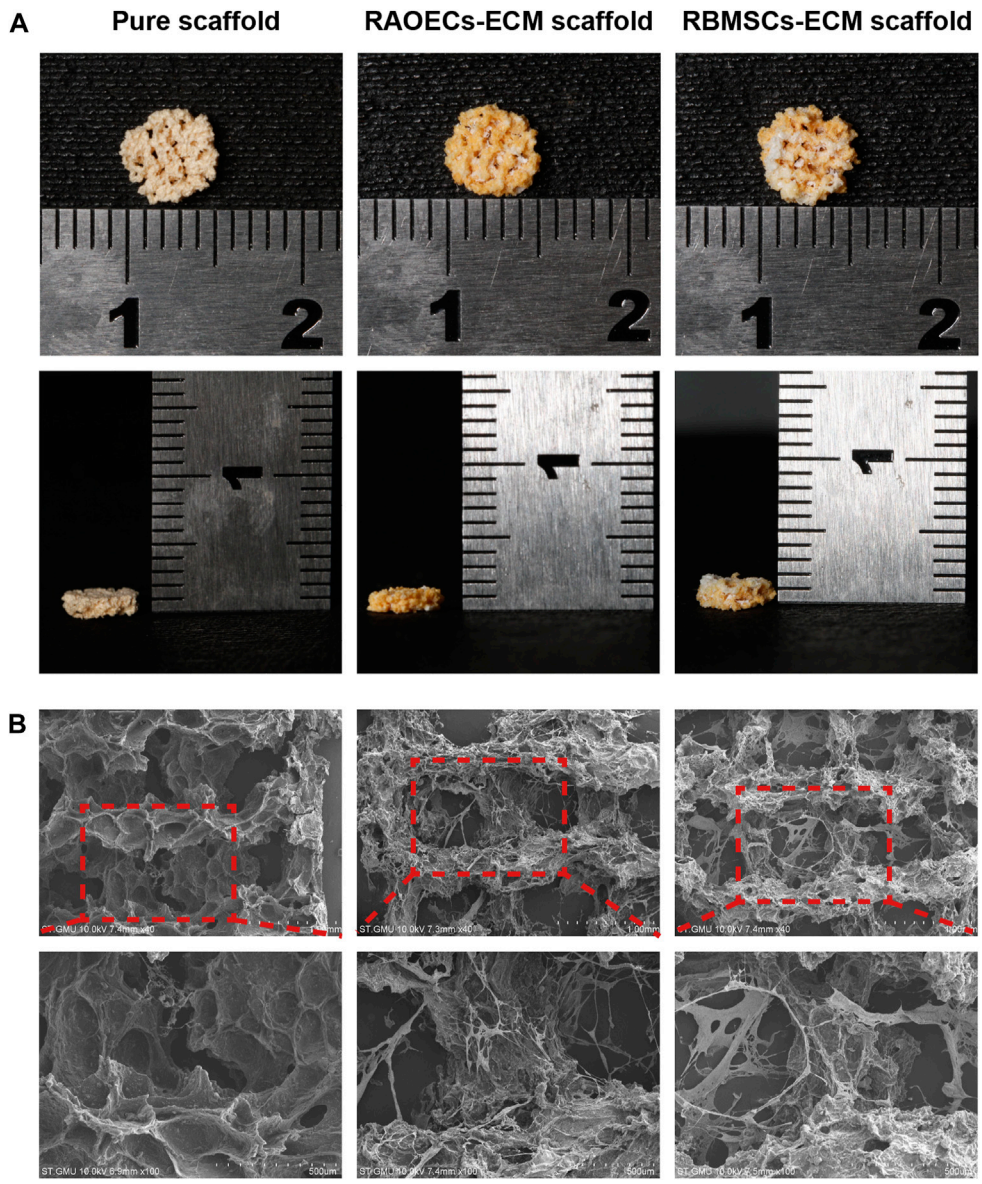

FIGURE 1
Morphological characteristics of the pure scaffold, RAOECs–ECM scaffold and RBMSCs–ECM scaffold. **(A)** Optical images of fabricated scaffolds with cylindrical shapes were observed from the top view and side view. **(B)** SEM images at various magnifications showed the surface morphology and microstructure of the scaffolds.

RAOEC–ECM scaffold group were significantly increased compared to those in the other groups ($p < 0.05$).

3.3 Images of the surgical procedure and results

As shown in Figure 3, during the surgical process, the prepared scaffolds fit the defects well and were easy to handle. After 4, 8 and 16 weeks, mandibular samples were harvested to characterize the status of defect closure. In the blank control group, a large amount of fibrous connective tissue was observed in the defect area, while in the scaffold–implanted groups, the scaffold materials were stably combined with the defects, and the material surface was covered by new fibrous connective tissue. The scaffold materials in the scaffold–implanted groups were partially degraded but still existed at 16 weeks after surgery. All defects healed uneventfully, with no evidence of wound dehiscence during healing, and no infection or necrosis was observed at the buccal and lingual sites.

10.3389/fbioe.2022.973886

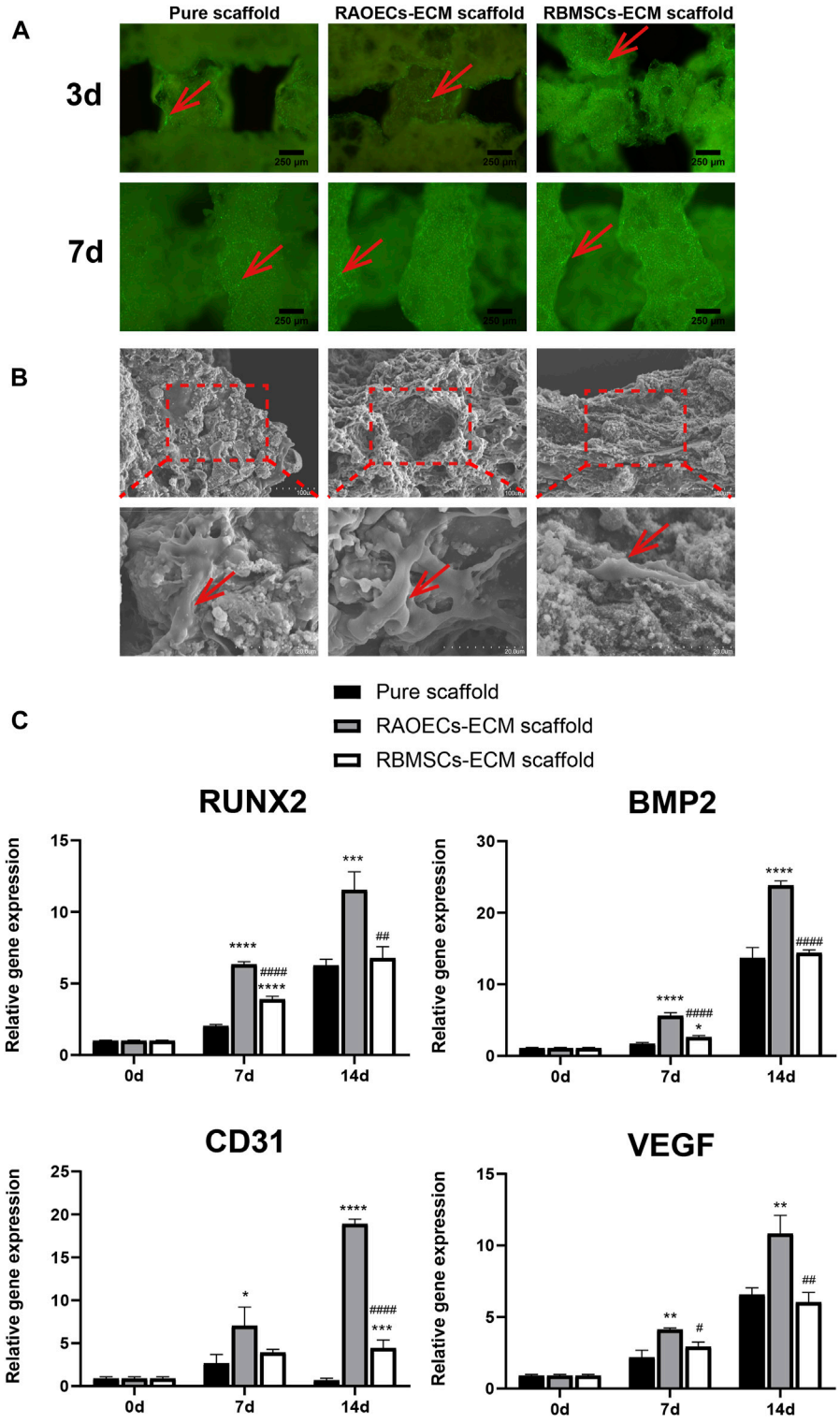

FIGURE 2
Cell adhesion, proliferation and RT–PCR assessment. **(A)** Fluorescence microscopy images of RBMSCs–seeded scaffolds after Calcein AM staining. **(B)** Scanning electron micrographs of RBMSCs (arrows) adhering to the surfaces of scaffolds at various magnifications. **(C)** The expression levels of osteogenic and vascularization–related genes after 0, 7 and 14 d of induction. (Significant effect compared to pure scaffold: $*p < 0.05$, $**p < 0.01$, $***p < 0.001$, $****p < 0.0001$. Significant effect compared to the RAOECs–ECM scaffold: $\#p < 0.05$, $\#\#p < 0.01$, $\#\#\#\#p < 0.0001$, $n = 3$.)

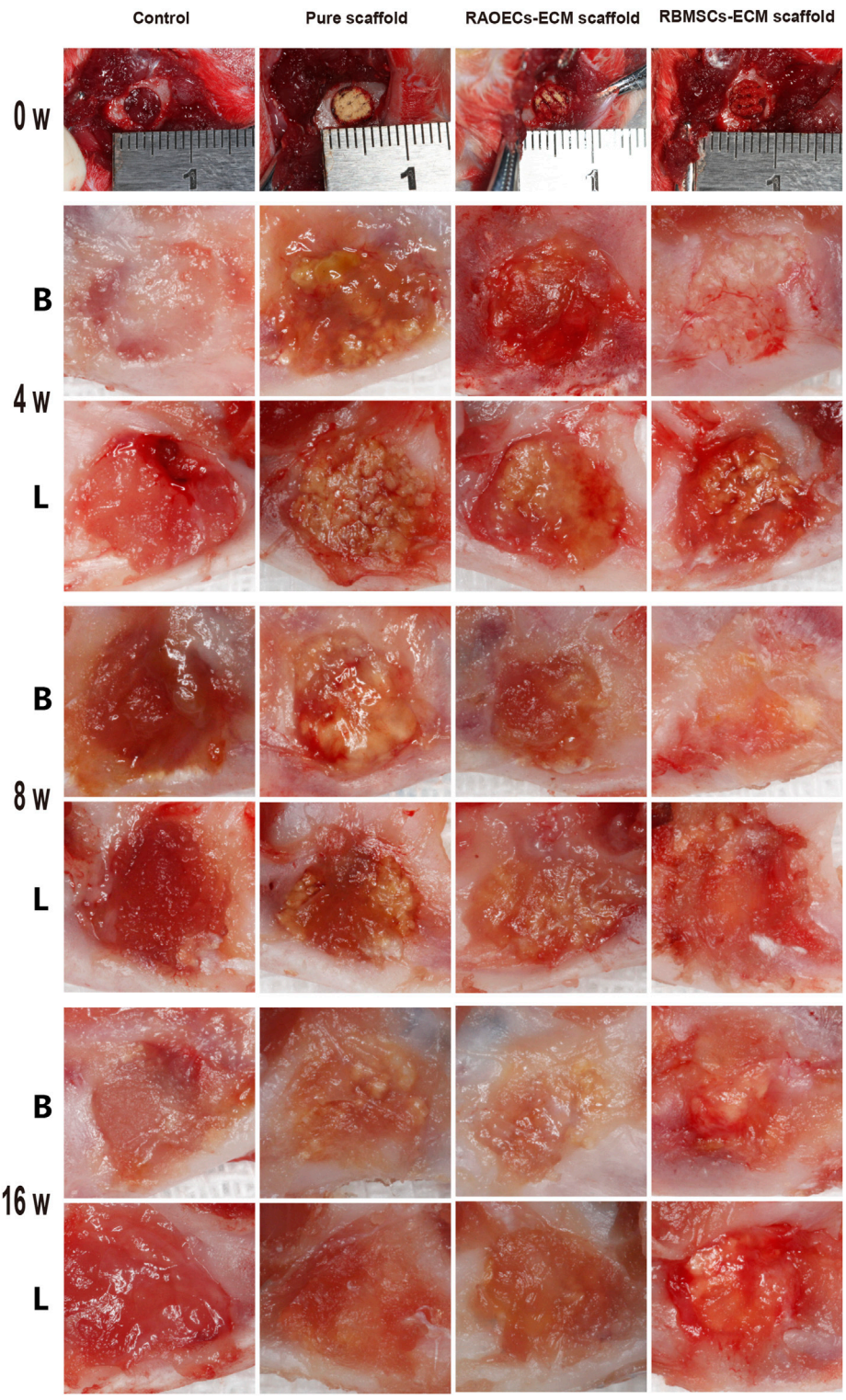

FIGURE 3
Photographs of the surgical procedure and postoperative healing. The structural integrity of all the scaffolds was maintained during surgery. At 4, 8 and 16 weeks after surgery, the defect sites of each group were observed from buccal (B) and lingual (L) angles.

3.4 Micro–CT analyses

Micro–CT analyses were used to verify postoperative new bone formation and residual bone defect areas at different weeks (Figure 4). Representative 3D reconstruction images are shown in Figure 4A. New bone and scaffold materials are presented in white and red, respectively. At 4 weeks, new bone was identified around the defect margins in all groups. Scaffolds treated with ECM showed more newly formed bone tissues than the control and pure scaffold group. At 8 weeks, more new bone tissues grew into defects in all groups. Newly formed bone tissues surrounded the residual materials and narrowed the defect areas in the scaffold–implanted groups. In the control group, new bone tissues mainly appeared at the borderline of the bone defect, which was significantly lower than that in the scaffold–implanted groups. At 16 weeks, new bone tissues filling the defect areas were more significant in the ECM–loaded scaffold groups than in the other groups. Moreover, the materials of the scaffold groups loaded with ECM were partially degraded but still remained. Accordingly, quantitative analysis of the newly regenerated bone in the defects was detected by calculating BV/TV and BMD (Figure 4B). The pure scaffolds showed higher values than the control group. Moreover, the two kinds of ECM–loaded scaffolds had significantly higher values than the pure scaffold at all different time points ($p < 0.05$). In particular, there was no significant difference in either ECM–loaded scaffolds ($p > 0.05$). All of these results suggested that Gel/SA/58sBG scaffolds had a positive effect on promoting new bone regeneration during the defect repair period, and this effect could be strengthened when they were loaded with ECM from RAOECs or RBMSCs.

3.5 Analyses of neovascular formation

The blood vessel formation effect of each group was studied by Microfil perfusion and Micro–CT imaging after implantation (Figure 5). Images of microangiography revealed newly formed blood vessels distributed in the defect areas. Compared with the control group, the scaffold–implanted groups had more neovascularization, and the vascular network was denser. This phenomenon was more obvious with increasing time. Moreover, the vascular networks in both ECM–loaded scaffolds were abundant, and the newly formed blood vessels extended along the defect areas at 16 weeks. Both ECM–loaded scaffolds displayed more new blood vessels than the pure scaffold at each time point. Quantitative analyses of neovascular formation corresponded to the above results, which showed that both ECM–loaded scaffold groups had significantly higher new vessel volumes than the other groups ($p < 0.05$). These results indicated that ECM–loaded scaffolds could effectively promote neovascularization in the process of repairing defective bones.

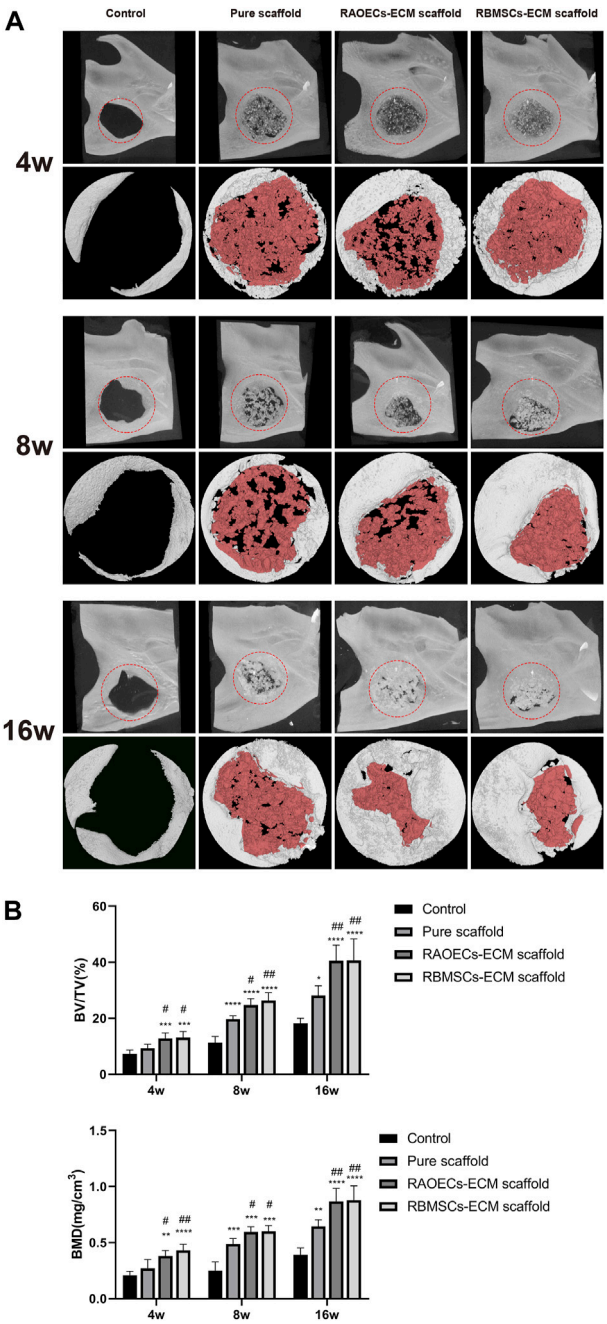

FIGURE 4
Micro–CT analysis of the control, pure scaffold, RAOECs–ECM scaffold and RBMSCs–ECM scaffold groups at 4, 8 and 16 weeks. **(A)** Three–dimensional images (top) and reconstruction images (bottom) are shown; white indicates new bone, and red represents residual scaffold materials. **(B)** Bone regeneration analysis of the ratio of the bone volume/tissue volume (BV/TV%) and bone mineral density (BMD, mg/cm^3). (Significant effect compared to the control group: $*p < 0.05$, $**p < 0.01$, $***p < 0.001$, $****p < 0.0001$. Significant effect compared to pure scaffold: $\#p < 0.05$, $\#\#p < 0.01$, $n = 5$.)

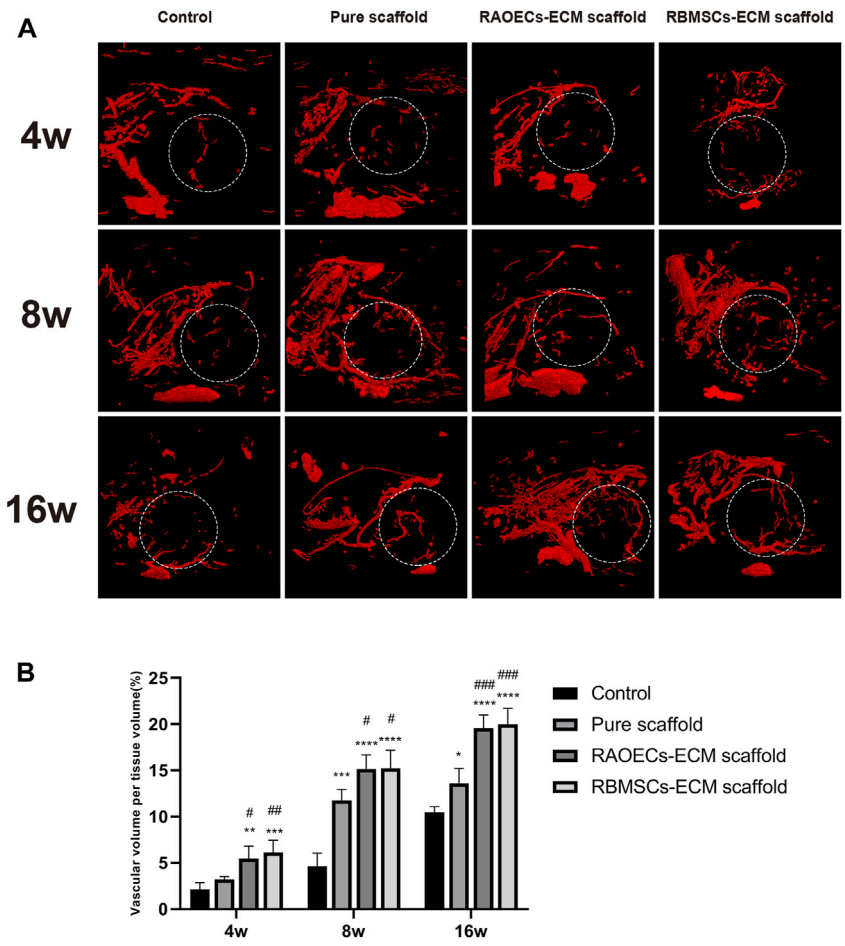

FIGURE 5
The vascular volume at different mandible defects was examined by Micro–CT at 4, 8, and 16 weeks after the operation. **(A)** 3D–reconstructed blood vessel images. **(B)** Quantitative analysis of vascular volume in the bone defect areas. (Significant effect compared to control group: $*p < 0.05$, $**p < 0.01$, $***p < 0.001$, $****p < 0.0001$. Significant effect compared to pure scaffold: $\#p < 0.05$, $\#\#p < 0.05$, $\#\#\#p < 0.001$, $n = 4$.)

3.6 Histological assessment

Histologic analysis performed with H&E and MT staining further revealed the condition of the bone defect at different time points. As shown in Figure 6, in the H&E staining, the newly formed bone sprouted from the margin of the defects in all groups at different weeks, as confirmed by the typical structure of sparse osteocytes embedded in lacunas and osteoblasts lining the outer edge of the bone tissue. In the control group, large amounts of loose fibrous tissues (black arrows) in the defect areas were observed at each time point, indicating poor bone regeneration capacity. In contrast, the groups implanted with scaffolds exhibited relatively reduced infiltrative growth of fibrous tissues and increased formation of dense bone tissue at the defect sites. Additionally, a significantly larger amount of new bone (green arrows) was observed in the ECM–loaded groups than in the pure scaffold group. Moreover, residual materials (yellow arrows) were also observed in the scaffold–implanted groups at 16 weeks, which were infiltrated by vast collagen tissues. Following MT staining, collagenous tissue and new bone were stained blue, while muscular tissues and mature lamellar bone were stained red. In the control group, limited new collagen and new bone formation were observed in the defect area at each time point, which was predominantly filled with loose fibrous tissue. However, the newly formed collagenous and bone tissue were more obvious in the scaffold–implanted groups. Especially at 16 weeks, mature lamellar bone and bridging trabeculae were generally most evident in ECM–loaded scaffolds, which was similar to the H&E staining results. Immunohistochemical staining of decalcified mandibles was performed to test the osteogenic markers RUNX2 and OCN and the angiogenic markers CD31 and VEGF. Positive staining in tissue slicing was dyed brown. The staining results showed a smaller positive area in the control group. The scaffold–implanted groups showed obvious positive areas for

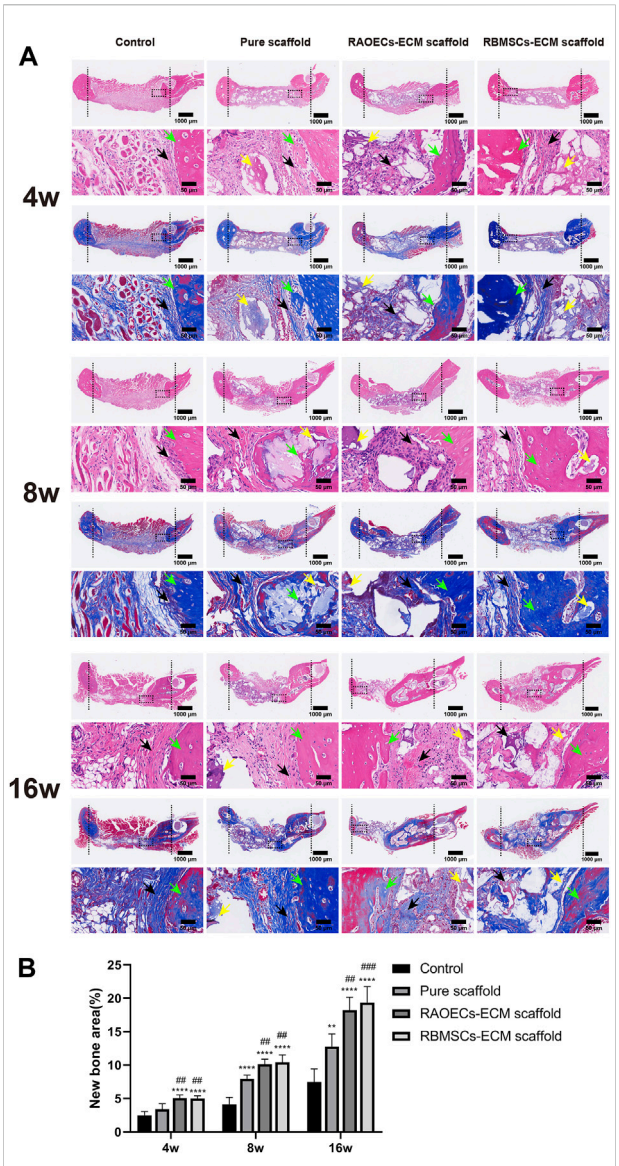

FIGURE 6
(A) H&E and MT staining of the cross–sections showed the histological morphology in the mandibular bone defects at 4, 8 and 16 weeks (black arrows: fibrous tissues, green arrows: new bone, yellow arrows: residual materials). **(B)** Quantitative histomorphometric analyses of new bone area. (Significant effect compared to control group: $^{**}p < 0.01$, $^{****}p < 0.0001$. Significant effect compared to pure scaffold: $^{\#\#}p < 0.01$, $^{\#\#\#}p < 0.001$, $n = 5$.)

RUNX2 and OCN. Positive staining of RUNX2 and OCN accumulated in the tip of the newly formed collagen and bone tissue. Notably, both ECM–loaded scaffolds had significantly higher expression levels of RUNX2 and OCN than the pure scaffold group. Additionally, the most pronounced positive staining of CD31 and VEGF was also observed in the ECM–loaded scaffold groups (Figure 7A). The percentage of positive staining area of osteogenic and angiogenic markers suggested that the ECM–loaded scaffold groups were more significant than the other groups (Figure 7B). These results showed that ECM–loaded scaffolds can effectively promote the expression of osteogenic and angiogenic markers in the bone defect area, and the effect was better than those of the pure scaffold group and control group.

3.7 Biosafety assessment

Blood biochemical analysis data are shown in Table 2. Compared to the control group, no statistically significant changes were revealed in any parameters in the scaffold–implanted groups. Histopathologic examinations of the liver, kidney and cerebrum revealed normal architecture and indicated a lack of morphologic disturbances in all experimental animals (Figure 8).

4 Discussion

To date, one of the essential challenges in bone defect repair is the development of safe bone substitutes with good biological properties for the treatment of larger defects with complex shapes. For the application of bone tissue engineering, scaffolds display unique advantages, with pore structure providing transport channels for nutrients and metabolites for cell growth, facilitating cell proliferation and thus promoting bone regeneration. Recently, the development of 3D printing techniques has shown bright prospects, as this technology can be used to fabricate scaffolds with customized shapes and pore sizes as required (Lai et al., 2021). Hence, we prepared porous Gel/SA/58sBG scaffolds by 3D printing technology. Meanwhile, to modify the scaffolds, ECM was added to them to achieve rapid and sufficient angiogenesis and osteogenesis. ECM is an ideal alternative for regenerative medicine because most cells are strongly associated with the neighbouring ECM environment that supplies biophysical and biochemical signals for cell adhesion, migration, and differentiation (Lu et al., 2011; Choi et al., 2014). In bone tissue engineering research, synthetic scaffolds ornamented with native ECM may offer a cell microenvironment to improve the biological properties of scaffolds (Kim et al., 2018). In fact, decellularization of cells or tissue to generate ECM has been widely reported in tissue engineering. Among that, cell–derived ECM obtained by *in vitro* culturing has been identified as a feasible method for bone tissue engineering scaffold settings. Several approaches have been proposed to combine cells or other growth factors with scaffolds to achieve sufficient angiogenesis (Kanczler and Oreffo, 2008; Grellier et al., 2009; Kirkpatrick et al., 2011). Thus, in this study, prevascularization of Gel/SA/58sBG scaffolds was prepared by coating RAOECs–or RBMSCs–derived ECM, and RAOECs–ECM scaffold and RBMSCs–ECM scaffold

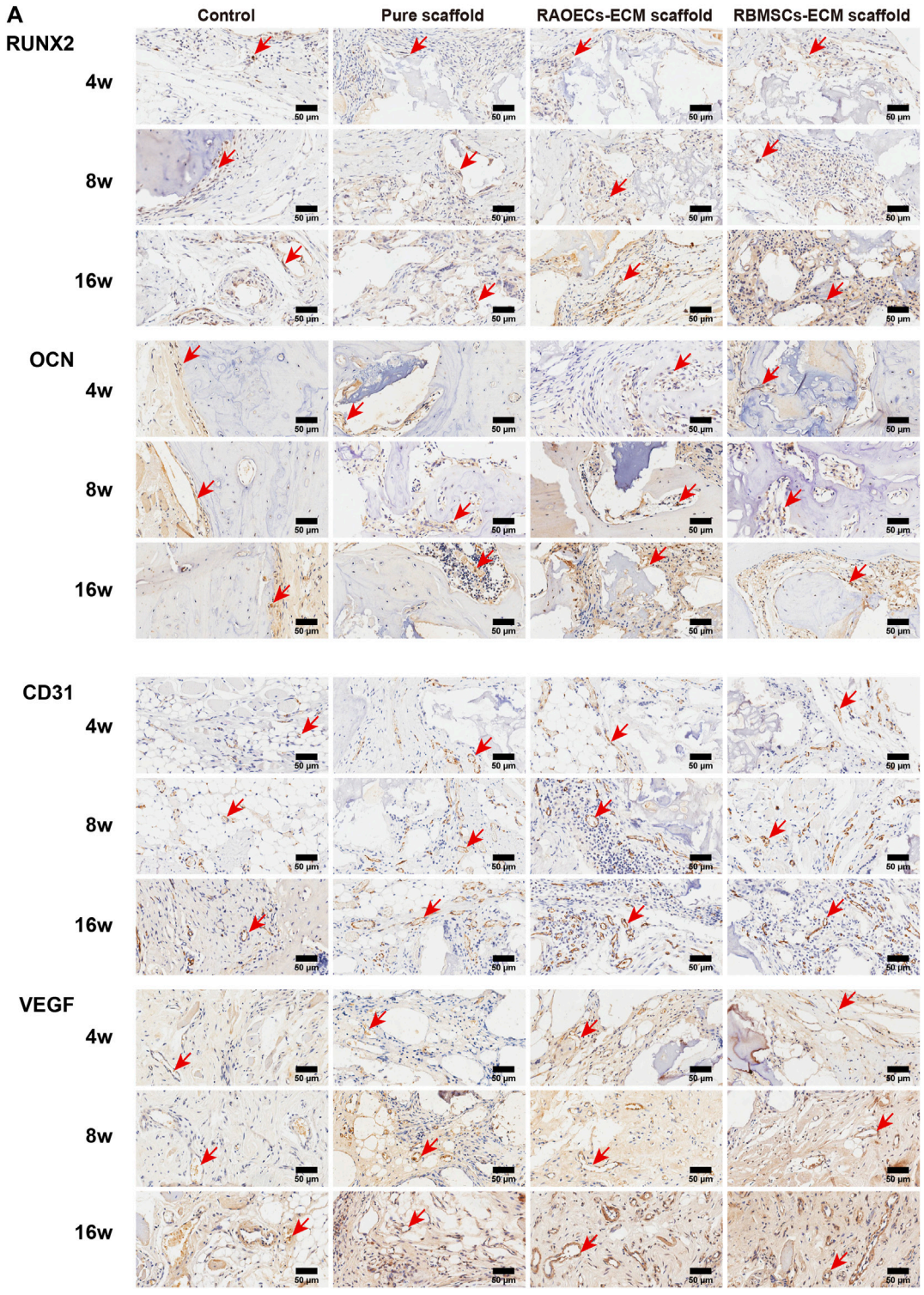

FIGURE 7
(Continued). **(A)** Images of immunohistochemical staining of RUNX2, OCN, CD31 and VEGF in bone defects. Bone regeneration activity was defined aspositive staining for RUNX2 and OCN. Blood vessel formation was indicated by positive staining for CD31 and VEGF. Positive staining for RUNX2, OCN, CD31 and VEGF was obvious in RAOECs and RBMSCs–ECM–loaded scaffolds, which had significant hyperchromatism compared with theother groups. **(B)** Quantitative analyses of the positive staining area. (Significant effect compared to control group: *$p < 0.05$, **$p < 0.01$, ***$p < 0.001$, ****$p < 0.0001$. Significant effect compared to pure scaffold: #$p < 0.05$, ##$p < 0.01$, ###$p < 0.001$, $n = 4$).

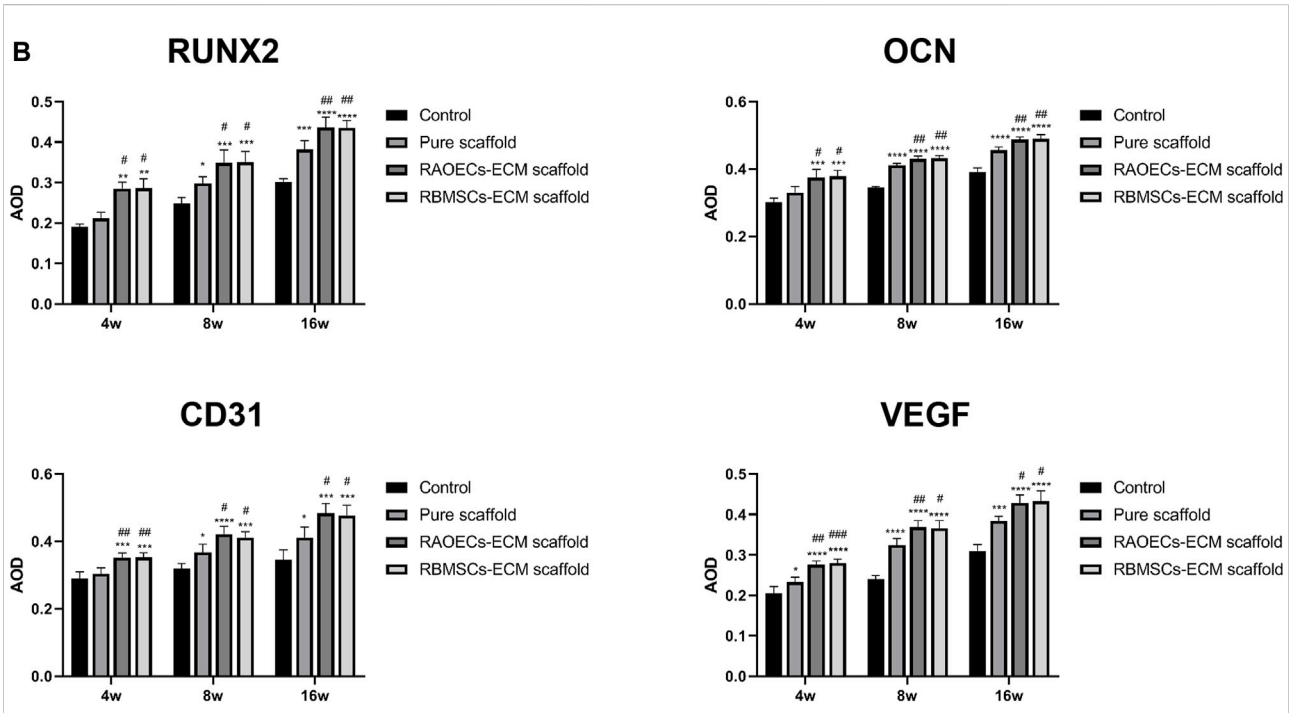

FIGURE 7
(Continued). (A) Images of immunohistochemical staining of RUNX2, OCN, CD31 and VEGF in bone defects. Bone regeneration activity was defined aspositive staining for RUNX2 and OCN. Blood vessel formation was indicated by positive staining for CD31 and VEGF. Positive staining for RUNX2, OCN, CD31 and VEGF was obvious in RAOECs and RBMSCs–ECM–loaded scaffolds, which had significant hyperchromatism compared with theother groups. (B) Quantitative analyses of the positive staining area. (Significant effect compared to control group: pp < 0.05, ppp < 0.01, pppp <0.001, ppppp < 0.001. Significant effect compared to pure scaffold: #p < 0.05, ##p < 0.01, ###p < 0.001, n = 4).

were obtained. The prepared scaffolds with precisely controlled shapes are shown in Figure 1. All the scaffolds exhibited a rough surface with a microporous structure. The interconnected pores of scaffolds were potentially suitable for cell growth and nutrient delivery. ECM was homogeneously distributed in ECM–loaded scaffolds and showed fully loose granules. Many micropores could be seen on the surfaces of all scaffolds by SEM, with irregular filaments on the surfaces of ECM–loaded scaffolds.

Cell adhesion takes place in the early stage of tissue regeneration, which is essential to establish layers of cells for matrix maturation (Fragal et al., 2019). Proper cell adhesion is the premise of subsequent biological functions, such as cell migration and differentiation (Wu et al., 2020). As shown in Figure 2A, the Calcein AM staining results indicated that live RBMSCs seeded on the ECM–loaded scaffolds were more obvious than those in the control group, which may be attributed to the natural ECM coating, which provides a better niche and more binding sites for the cell interaction. Moreover, cells with long spindle shapes and extended filopodia could be seen on the surfaces of ECM–loaded scaffolds from the SEM view (Figure 2B). Most notably, RBMSCs were surrounded by some mineralized matter and spread out in ECM–loaded scaffold groups. For the pure scaffold, cells on the surface of the scaffold had a short spindle shape. This result indicated that scaffolds coated with ECM provide a rougher surface and a suitable environment for cell attachment and migration.

The osteogenic and angiogenic capacities of the ECM–loaded scaffolds were further verified *in vitro*. The eluates of the different scaffolds were collected after RBMSCs culture and subjected to RT–PCR (Figure 2C). The mRNA expression levels of osteogenic genes in ECM–loaded scaffolds, including RUNX2 and BMP2, were significantly upregulated compared with those in the pure scaffold and were regarded as the most representative markers for osteogenic differentiation and further contributed to bone regeneration *in vivo*. Moreover, bone tissue regeneration *in vivo* also derives directly from the differentiation of osteogenic stem or progenitor cells (Xu et al., 2021). In particular, among the three groups of scaffolds, RAOECs–ECM scaffold showed the highest expression of osteogenic genes *in vitro*. We inferred that the extracellular matrix of RAOECs has a significant influence on the differentiation of RBMSCs (Lozito Thomas et al., 2009; Saleh Fatima et al., 2011).

The increased expression levels of angiogenic genes in RT–PCR demonstrated that scaffolds loaded with RAOECs–derived ECM presented excellent angiogenic differentiation ability, followed by RBMSCs–ECM scaffold. Moreover, both CD31 and VEGF were evidently expressed at the center of the defects in both kinds of ECM–loaded scaffolds, which further proved that scaffolds decorated with RAOECs–or RBMSCs–derived ECM significantly facilitated angiogenesis. Moreover, 3D reconstruction images of the Microfil (contrast

TABLE 2 Differences in some biochemical indices among groups of rats implanted with ECM–loaded scaffolds, pure scaffold and control at different times after implantation.

A

Parameter	Control	Pure scaffold	RAOECs–ECM scaffold	RBMSCs–ECM scaffold
TP (g/L)	76.24 ± 5.42	80.52 ± 6.47	71.80 ± 5.31	70.64 ± 8.52
ALB (g/L)	40.24 ± 1.97	41.94 ± 1.20	39.12 ± 1.29	40.98 ± 1.89
ALT (U/L)	79.78 ± 38.12	76.76 ± 23.87	78.90 ± 43.34	70.54 ± 15.83
AST (U/L)	308.74 ± 76.43	297.04 ± 18.53	228.82 ± 14.91	249.20 ± 66.47
Cr (μmol/L)	47.80 ± 7.85	57.40 ± 11.41	56.00 ± 10.56	64.20 ± 15.66
BUN (mmol/L)	6.76 ± 0.60	8.78 ± 1.51	8.16 ± 2.40	6.90 ± 1.66

B

Parameter	Control	Pure scaffold	RAOECs–ECM scaffold	RBMSCs–ECM scaffold
TP (g/L)	70.26 ± 2.93	73.20 ± 3.23	71.32 ± 2.24	70.42 ± 4.54
ALB (g/L)	37.08 ± 3.20	38.68 ± 1.58	38.46 ± 0.68	36.62 ± 1.79
ALT (U/L)	59.64 ± 29.16	58.88 ± 20.36	59.40 ± 12.05	72.02 ± 13.71
AST (U/L)	221.02 ± 87.58	231.16 ± 56.50	166.02 ± 22.98	197.36 ± 55.01
Cr (μmol/L)	57.80 ± 14.75	63.20 ± 25.64	72.40 ± 22.82	65.80 ± 9.91
BUN (mmol/L)	8.02 ± 3.24	7.68 ± 0.89	9.80 ± 3.00	6.92 ± 0.54

C

Parameter	Control	Pure scaffold	RAOECs–ECM scaffold	RBMSCs–ECM scaffold
TP (g/L)	71.80 ± 2.30	72.56 ± 5.80	69.60 ± 3.57	67.14 ± 5.06
ALB (g/L)	37.90 ± 1.80	38.66 ± 2.53	36.98 ± 3.01	36.84 ± 2.46
ALT (U/L)	74.04 ± 37.18	67.24 ± 29.93	68.12 ± 24.10	64.98 ± 23.71
AST (U/L)	235.12 ± 50.10	188.28 ± 39.22	199.96 ± 40.65	181.06 ± 23.29
Cr (μmol/L)	51.60 ± 21.82	81.80 ± 25.57	94.00 ± 24.32	63.00 ± 29.72
BUN (mmol/L)	7.46 ± 0.69	8.62 ± 2.03	9.26 ± 1.93	7.94 ± 2.15

Values expressed as the mean ± SD., Statistical analysis: One–way ANOVA, followed by Tukey's multiple comparison test. A, B and C represent 4, 8 and 16 weeks after surgery, respectively. The indices of all groups showed no significant differences compared with those of the other groups at each time point ($p > 0.05$, $n = 5$).

medium)–based angiographic technique for evaluating vascular morphology in Figure 5 also showed more vessel formation in both ECM–loaded scaffold groups. Cumulative evidence demonstrated that loading RAOECs–or RBMSCs–derived ECM in scaffolds can accelerate the formation of blood vessels, which facilitated new bone regeneration and, eventually, mature bone formation in the defect sites.

To test the osteogenic effect of implanted materials *in vivo*, it is usually necessary to set up a bone defect model, which must satisfy the requirement that the defect area be large enough to avoid complete self–healing without any treatment and thus prevent overestimation of spontaneous healing in a surgically created defect. The ideal state is to form new bone when only the bone repair material is present to verify the bone repair effect of the materials. A critical size defect (CSD) is the smallest bone defect that cannot completely heal itself in laboratory animals under natural conditions. At present, when the material is used to repair the mandibular defect in rats, a 5–mm–diameter perforating bone defect is usually created in the mandibular ascending ramus, which is considered the critical bone defect of the rat mandible (Zhang et al., 2016; Yu et al., 2018; Zhang et al., 2018). Therefore, the ECM–loaded scaffolds were implanted into critical–sized defects of the mandibles of rats to detect the bone repair potential in this study. After 4, 8 and 16 weeks of implantation, new bone ingrowth was detected and analysed by Micro–CT (Figure 4). The quantitative CT results illustrated that the repaired defects with ECM–loaded scaffolds had the following characteristics: higher bone volume fraction and bone density compared to both the pure scaffold and the blank control group. Histological analysis was used to provide a more detailed analysis of the bone response to the scaffolds with or without ECM, the results of which are shown in Figure 6. In the control and scaffold groups, H&E images showed that defects were filled with fibrous connective tissue with sparse new bone formation at the edge of the host bone. In contrast, in the ECM–loaded scaffold groups, residual materials surrounded by fibrous connective tissue could be observed in the defects, with a large amount of new bone formation at the edge. Moreover, RUNX2 expression was increased, and OCN staining was obviously deposited in the newly generated tissue in both

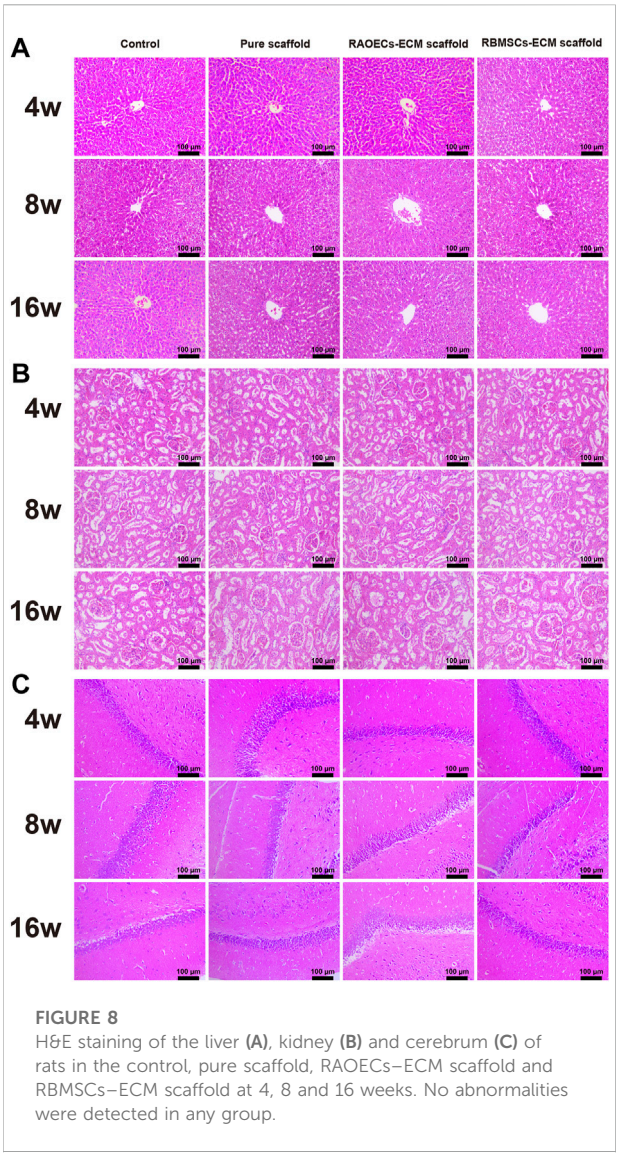

FIGURE 8
H&E staining of the liver **(A)**, kidney **(B)** and cerebrum **(C)** of rats in the control, pure scaffold, RAOECs–ECM scaffold and RBMSCs–ECM scaffold at 4, 8 and 16 weeks. No abnormalities were detected in any group.

ECM–loaded scaffold groups (Figure 7). RUNX2, an early osteogenic marker activating the development of stem cells into preosteoblasts, is the main regulator of osteoblast differentiation and acts as the determinant of bone remodelling and skeletal integrity (Ngo et al., 2020; Yang et al., 2021). OCN secreted by mature osteoblasts is a key marker in later–phase osteogenic differentiation (Quan et al., 2019). The obvious expression of RUNX2 and OCN also suggests that scaffolds combined with RAOECs–or RBMSCs–derived ECM can accelerate bone formation in the early and later stages of bone defect healing. In Masson's trichrome staining, blue staining is indicative of collagen fibrous tissue and osteoid. This staining could serve as a good indication for bone tissue formation because of the enrichment of collagen in the bone matrix (Zhao et al., 2018). In the control and pure scaffold groups, limited collagen and new bone deposition were observed in the defect area compared to the other groups at each time point. Notably, a large amount of collagen and new bone components were detected in the defect sites implanted with the ECM–loaded scaffolds, indicating the improved osteogenic ability of the ECM. These results indicated that the presence of ECM–loaded scaffolds provides a bone–like environment for bone mineralization with the contribution of functional ECM molecules.

The results *in vitro* and *vivo* show that ECM–loaded scaffolds have better bone regeneration effect than the pure one. Possible reasons are as follows: 1) RAOECs–or RBMSCs–ECM contains several kinds of bioactive growth factors and various functional proteins that contribute to cell recruitment, which is the first step for cells and materials interaction, and the better cell recruitment is more beneficial to subsequent cell proliferation and tissue regeneration. 2) In addition, when RAOECs–or RBMSCs–ECM loaded on scaffolds, microporosity of the ECM provided some advantages, such as more binding sites for protein combination, which is an effective approach to improve tissue repair and regeneration. At the meantime, the surface and interior of scaffolds are coated by ECM, which imitate the biological macro and microenvironment to promote cell migration and invasion into the scaffolds to realize self-assembly of cells. 3) ECM could regulate cell differentiation by concerning mechanical and biochemical signals, which provide cellular support to modulate the biological and physical cues and further achieve bone regeneration.

The biosafety of a material should be considered when it is directly implanted into the body. Biosafety assessments generally refer to a series of evaluation standards for medical biomaterials and devices. When the scaffolds are implanted in the defects, they can wear out and separate free particles in the process of mandible movement, which may cause embolism or inflammation (Koff Matthew et al., 2019; Qiu et al., 2020). Normal physiological activities can be affected by this phenomenon. Therefore, postimplantation local reactions and systemic toxicity tests were employed in our study. The application of the local reaction test after implantation in the bone defect model is mainly achieved by means of gross observation and histological staining of the implanted area. Based on our observations, all the experimental animals could eat on their own within 3 days after surgery, the defect areas healed well in the scaffold–implanted groups after surgery, and no adverse response related to inflammation in the defect areas was aggravated. This response is regarded as the bioglass of scaffolds exhibiting chemotactic activity for inflammatory cells (Zhang et al., 2020). The biosafety performance of the scaffolds was investigated in the mandibular defects of rats over 3 months. The scaffold–implanted areas showed no infection or necrosis at either site (Figure 3). In addition to observing the biocompatibility of the material with surrounding tissues, *in vivo* toxicity tests are also needed to identify any toxic damage caused by the material itself or its degradation products to vital organs. Lai et al. (2019) evaluated the biosafety of materials *in vivo* by detecting changes in related

indicators of liver and kidney function after the implantation of materials into bone defects. Jia et al. (2021) evaluated the toxicity of implant materials for bone defects *in vivo* by detecting pathological changes in the liver, kidney and other important organs. In this study, the blood biochemical indices of the scaffold–implanted groups showed no significant differences compared to the control group (Table 2). The H&E staining of vital organs in the scaffold groups showed no obvious abnormalities (Figure 8). All of the *in vitro* and *in vivo* results demonstrated that the 3D–printed scaffolds presented admirable biosafety, indicating that the implanted scaffolds circumvented the side effect of movement of the mandible and could still perform certain functions under specific size defects in place of the defective bone. This also indicates that the scaffolds were qualified for treating the mandibular defects caused by clinical diseases.

In summary, although these ECM–loaded scaffolds showed acceptable osteogenic effects, targeted improvements of scaffolds for repairing large animal models to reveal craniomaxillofacial bone healing more accurately could be our next work, which would include combining the different ECMs in various proportions to enhance the osteogenic effect.

5 Conclusion

The results of our study show that individualized scaffolds are easily fabricated using 3D printing technology and that RAOECs–or RBMSCs–derived ECM is an ideal factor for accelerating osteogenesis and angiogenesis. *In situ* bone defect repair with of RBMSCs–ECM scaffold or RAOECs–ECM scaffold clearly promoted bone regeneration and neovascularization. Moreover, the scaffolds showed good biosafety *in vitro* and *in vivo*. Thus, the combination of Gel/SA/58sBG scaffolds with RAOECs–or RBMSCs–derived ECM may provide an effective strategy for treating bone defects. However, due to the complexity of the RAOECs–derived ECM and RBMSCs–derived ECM components and functions, it is hard to identify the specific mechanism of the osteogenesis. In addition, is there a synergistic osteogenesis effect when RAOECs–derived ECM and RBMSCs–derived ECM are mixed in a certain proportion? These two still needed further research in the future.

Data availability statement

The datasets presented in this study can be found in online repositories. The names of the repository/repositories and accession number(s) can be found in the article/supplementary material.

Ethics statement

The animal study was reviewed and approved by The Animal Care and Use Committee of Guangzhou University of Chinese Medicine.

Author contributions

All authors listed have made a substantial, direct, and intellectual contribution to the work and approved it for publication.

Funding

This study was supported by the Guangdong Provincial Science and Technology Project, China (No. 2018B050502012), the Natural Science Foundation of Guangdong Province (No. 2021A1515010870) and the Key Research and Development Program of Scientific Research Institutions in Guangdong Province (No. 2020B1111490004).

Acknowledgments

The authors would also like to thank Dr. Zhang Yang's team at Guangzhou ZhongDa Medical Equipment Company Limited.

Conflict of interest

The authors declare that the research was conducted in the absence of any commercial or financial relationships that could be construed as a potential conflict of interest.

Publisher's note

All claims expressed in this article are solely those of the authors and do not necessarily represent those of their affiliated organizations, or those of the publisher, the editors and the reviewers. Any product that may be evaluated in this article, or claim that may be made by its manufacturer, is not guaranteed or endorsed by the publisher.

References

Ackermann, M., Pabst, A. M., Houdek, J. P., Ziebart, T., and Konerding, M. A. (2014). Priming with proangiogenic growth factors and endothelial progenitor cells improves revascularization in linear diabetic wounds[J]. *Int. J. Mol. Med.* 33, 833–839. doi:10.3892/ijmm.2014.1630

Agarwal, R., and García Andrés, J. (2015). Biomaterial strategies for engineering implants for enhanced osseointegration and bone repair. *Adv. Drug Deliv. Rev.* 94, 53–62. doi:10.1016/j.addr.2015.03.013

Carvalho Marta, S., Silva João, C., Cabral Joaquim, M. S., Silva, C. L., and Vashishth, D. (2019). Cultured cell-derived extracellular matrices to enhance the osteogenic differentiation and angiogenic properties of human mesenchymal stem/stromal cells. *J. Tissue Eng. Regen. Med.* 13, 1544–1558. doi:10.1002/term.2907

Chen, W., Liu, X., Chen, Q., Bao, C., Zhao, L., Zhu, Z., et al. (2018). Angiogenic and osteogenic regeneration in rats via calcium phosphate scaffold and endothelial cell co-culture with human bone marrow mesenchymal stem cells (MSCs), human umbilical cord MSCs, human induced pluripotent stem cell-derived MSCs and human embry. *J. Tissue Eng. Regen. Med.* 12, 191–203. doi:10.1002/term.2395

Chi, H., Chen, G., He, Y., Chen, G., Tu, H., Liu, X., et al. (2020). 3D–HA scaffold functionalized by extracellular matrix of stem cells promotes bone repair[J]. *Int. J. Nanomedicine* 15, 5825–5838. doi:10.2147/IJN.S259678

Choi, D. H., Suhaeri, M., Hwang, M. P., Kim, I. H., Han, D. K., and Park, K. (2014). Multi-lineage differentiation of human mesenchymal stromal cells on the biophysical microenvironment of cell-derived matrix. *Cell. Tissue Res.* 357 (3), 781–792. doi:10.1007/s00441-014-1898-5

Critser, P. J., and Yoder, M. C. (2010). Endothelial colony-forming cell role in neoangiogenesis and tissue repair. *Curr. Opin. Organ Transpl.* 15, 68–72. doi:10.1097/mot.0b013e32833454b5

Fragal, E. H., Cellet, T. S. P., Fragal, V. H., Witt, M. A., Companhoni, M. V., Ueda-Nakamura, T., et al. (2019). Biomimetic nanocomposite based on hydroxyapatite mineralization over chemically modified cellulose nanowhiskers: An active platform for osteoblast proliferationfied cellulose nanowhiskers: An active platform for osteoblast proliferation[J]. *Int. J. Biol. Macromol.* 125, 133–142. doi:10.1016/j.ijbiomac.2018.12.004

Gao, C.-Y., Huang, Z-H., Jing, W., Wei, P. F., Jin, L., Zhang, X. H., et al. (2018). Directing osteogenic differentiation of BMSCs by cell-secreted decellularized extracellular matrixes from different cell types. *J. Mat. Chem. B* 6, 7471–7485. doi:10.1039/c8tb01785a

Gong, T., Heng, B. C., Xu, J., Zhu, S., Yuan, C., Lo, E. C. M., et al. (2017). Decellularized extracellular matrix of human umbilical vein endothelial cells promotes endothelial differentiation of stem cells from exfoliated deciduous teeth. *J. Biomed. Mat. Res. A* 105, 1083–1093. doi:10.1002/jbm.a.36003

Grellier, M., Bordenave, L., and Amédée, J. (2009). Cell-to-cell communication between osteogenic and endothelial lineages: Implications for tissue engineering. *Trends Biotechnol.* 27 (10), 562–571. doi:10.1016/j.tibtech.2009.07.001

Ishikawa, M., and Asahara, T. (2004). Endothelial progenitor cell culture for vascular regeneration. *Stem Cells Dev.* 13, 344–349. doi:10.1089/scd.2004.13.344

Jia, B., Yang, H., Zhang, Z., Qu, X., Jia, X., Wu, Q., et al. (2021). Biodegradable Zn–Sr alloy for bone regeneration in rat femoral condyle defect model: *In vitro* and *in vivo* studies[J]. *Bioact. Mat.* 6, 1588–1604. doi:10.1016/j.bioactmat.2020.11.007

Kamali, A., Oryan, A., Hosseini, S., Ghanian, M. H., Alizadeh, M., Baghaban Eslaminejad, M., et al. (2019). Cannabidiol–loaded microspheres incorporated into osteoconductive scaffold enhance mesenchymal stem cell recruitment and regeneration of critical–sized bone defects. *Mater. Sci. Eng. C* 101, 64–75. doi:10.1016/j.msec.2019.03.070

Kanczler, J. M., and Oreffo, R. O. C. (2008). Osteogenesis and angiogenesis: The potential for engineering bone. *Eur. Cell. Mat.* 15, 100–114. doi:10.22203/ecm.v015a08

Kang, Y., Kim, S., Bishop, J., Khademhosseini, A., and Yang, Y. (2012). The osteogenic differentiation of human bone marrow MSCs on huvec–derived ECM andB–TCP scaffold. *Biomaterials* 33, 6998–7007. doi:10.1016/j.biomaterials.2012.06.061

Kim, B., Ventura, R., and Lee, B.-T. (2018). Functionalization of porous BCP scaffold by generating cell–derived extracellular matrix from rat bone marrow stem cells culture for bone tissue engineering. *J. Tissue Eng. Regen. Med.* 12, e1256–e1267. doi:10.1002/term.2529

Kim, J. Y., Song, S. H., Kim, K. L., Ko, J. J., Im, J. E., Yie, S. W., et al. (2010). Human cord blood-derived endothelial progenitor cells and their conditioned media exhibit therapeutic equivalence for diabetic wound healing. *Cell. Transpl.* 19, 1635–1644. doi:10.3727/096368910x516637

Kirkpatrick, C. J., Fuchs, S., and Unger Ronald, E. (2011). Co–culture systems for vascularization––learning from nature[J]. *Adv. Drug Deliv. Rev.* 63, 291–299. doi:10.1016/j.addr.2011.01.009

Koff Matthew, F., Christina, E., Shah, P., Miranda, M., Baral, E., Fields, K., et al. (2019). MRI of tha correlates with implant wear and tissue reactions: A cross–sectional study. *Clin. Orthop. Relat. Res.* 477, 159–174. doi:10.1097/corr.0000000000000535

Lai, W-Y., Chen, Y-J., Lee Alvin, K-X., Lin, Y. H., Liu, Y. W., and Shie, M. Y. (2021). Therapeutic effects of the addition of fibroblast growth factor-2 to biodegradable gelatin/magnesium-doped calcium silicate hybrid 3D-printed scaffold with enhanced osteogenic capabilities for critical bone defect restoration. *Biomedicines* 9 (7), 712. doi:10.3390/biomedicines9070712

Lai, Y., Li, Y., Cao, H., Long, J., Wang, X., Li, L., et al. (2019). Osteogenic magnesium incorporated into PLGA/TCP porous scaffold by 3D printing for repairing challenging bone defect. *Biomaterials* 197, 207–219. doi:10.1016/j.biomaterials.2019.01.013

Lee, Y., Chan, Y., Hsieh, S., Lew, W. Z., and Feng, S. W. (2019). Comparing the osteogenic potentials and bone regeneration capacities of bone marrow and dental pulp mesenchymal stem cells in a rabbit calvarial bone defect model. *Int. J. Mol. Sci.* 20 (20), 5015. doi:10.3390/ijms20205015

Lin, S., He, X., and He, Y. (2021). Co-culture of ASCs/EPCs and dermal extracellular matrix hydrogel enhances the repair of full-thickness skin wound by promoting angiogenesis. *Stem Cell. Res. Ther.* 12, 129. doi:10.1186/s13287-021-02203-1

Lozito Thomas, P., Kuo Catherine, K., Taboas Juan, M., and Tuan, R. S. (2009). Human mesenchymal stem cells express vascular cell phenotypes upon interaction with endothelial cell matrix. *J. Cell. Biochem.* 107, 714–722. doi:10.1002/jcb.22167

Lu, H., Hoshiba, T., Kawazoe, N., Koda, I., Song, M., and Chen, G. (2011). Cultured cell-derived extracellular matrix scaffolds for tissue engineering. *Biomaterials* 32 (36), 9658–9666. doi:10.1016/j.biomaterials.2011.08.091

Ngo, H. X., Dong, Q. N., Bai, Y., Sha, J., Ishizuka, S., Okui, T., et al. (2020). Bone regeneration capacity of newly developed uncalcined/unsintered hydroxyapatite and poly–l–lactide–co–glycolide sheet in maxillofacial surgery: An *in vivo* study. *Nanomater. (Basel).* 11 (1), 22. doi:10.3390/nano11010022

Pati, F., Song, T., Rijal, G., Jang, J., Kim, S. W., and Cho, D. W. (2015). Ornamenting 3D printed scaffolds with cell-laid extracellular matrix for bone tissue regeneration. *Biomaterials* 37, 230–241. doi:10.1016/j.biomaterials.2014.10.012

Pekozer Gorke, G., Kose Gamze, T., and Vasif, H. (2016). Influence of co-culture on osteogenesis and angiogenesis of bone marrow mesenchymal stem cells and aortic endothelial cells[J]. *Microvasc. Res.* 108, 1–9. doi:10.1016/j.mvr.2016.06.005

Peng, J., Chen, L., Peng, K., Chen, X., Wu, J., He, Z., et al. (2019). Bone marrow mesenchymal stem cells and endothelial progenitor cells Co-culture enhances large segment bone defect repair. *J. Biomed. Nanotechnol.* 15, 742–755. doi:10.1166/jbn.2019.2735

Qiu, J., Peng, P., Xin, M., Wen, Z., Chen, Z., Lin, S., et al. (2020). ZBTB20-mediated titanium particle-induced peri-implant osteolysis by promoting macrophage inflammatory responses. *Biomater. Sci.* 8 (11), 3147–3163. doi:10.1039/d0bm00147c

Quan, C., Zhang, Z., Liang, P., Zheng, J., Wang, J., Hou, Y., et al. (2019). Bioactive gel self-assembled from phosphorylate biomimetic peptide: A potential scaffold for enhanced osteogenesis. *Int. J. Biol. Macromol.* 121, 1054–1060. doi:10.1016/j.ijbiomac.2018.10.148

Saleh Fatima, A., Muna, W., Peter, A., and Genever, P. G. (2011). Regulation of mesenchymal stem cell activity by endothelial cells. *Stem Cells Dev.* 20, 391–403. doi:10.1089/scd.2010.0168

Sun, T., Yao, S., Liu, M., Yang, Y., Ji, Y., Cui, W., et al. (2018). Composite scaffolds of mineralized natural extracellular matrix on true bone ceramic induce bone regeneration through smad1/5/8 and ERK1/2 pathways. *Tissue Eng. Part A* 24, 502–515. doi:10.1089/ten.tea.2017.0179

Tsigkou, O., Labbaf, S., Stevens, M. M., Porter, A. E., and Jones, J. R. (2014). Monodispersed bioactive glass submicron particles and their effect on bone marrow and adipose tissue–derived stem cells[J]. *Adv. Healthc. Mater* 3, 115–125. doi:10.1002/adhm.201300126

Wei, B., Guo, Y., Xu, Y., Mao, F., Yao, Q., Jin, C., et al. (2015). Composite scaffolds composed of bone marrow mesenchymal stem cell–derived extracellular matrix and marrow clots promote marrow cell retention and proliferation[J]. *J. Biomed. Mater Res. A* 103, 2374–2382. doi:10.1002/jbm.a.35373

Wu, J., Miao, G., Zheng, Z., Li, Z., Ren, W., Wu, C., et al. (2019). 3D printing mesoporous bioactive glass/sodium alginate/gelatin sustained release scaffolds for bone repair. *J. Biomater. Appl.* 33, 755–765. doi:10.1177/0885328218810269

Wu, M., Wu, P., Xiao, L., Zhao, Y., Yan, F., Liu, X., et al. (2020). Biomimetic mineralization of novel hydroxyethyl cellulose/soy protein isolate scaffolds promote bone regeneration *in vitro* and *in vivo*[J]. *Int. J. Biol. Macromol.* 162, 1627–1641. doi:10.1016/j.ijbiomac.2020.08.029

Wu, Y.-H. A., Cheng, C. Y., Lin, Y-H., Ho, C-C., Shie, M.-Y., and Chen, Y.-W. (2019). 3D-Printed bioactive calcium silicate/poly–ε–caprolactone bioscaffolds modified with biomimetic extracellular matrices for bone regeneration[J]. *Int. J. Mol. Sci.* 20 (4), 942. doi:10.3390/ijms20040942

Xu, H., Wang, C., Liu, C., Li, J., Peng, Z., Guo, J., et al. (2021). Stem cell–seeded 3D–printed scaffolds combined with self–assembling peptides for bone defect repair[J]. *Tissue Eng. Part A* 28 (3-4), 111–124. undefined: undefined. doi:10.1089/ten.TEA.2021.0055

Yang, G., Liu, H., Cui, Y., Li, J., Zhou, X., Wang, N., et al. (2021). Bioinspired membrane provides periosteum-mimetic microenvironment for accelerating vascularized bone regeneration. *Biomaterials* 268, 120561. doi:10.1016/j.biomaterials.2020.120561

Ying, C., Wang, R., Wang, Z., Tao, J., Yin, W., Zhang, J., et al. (2020). BMSC-exosomes carry mutant HIF-1α for improving angiogenesis and osteogenesis in critical-sized calvarial defects. *Front. Bioeng. Biotechnol.* 8, 565561. doi:10.3389/fbioe.2020.565561

Yu, L., Wu, Y., Liu, J., Li, B., Ma, B., Li, Y., et al. (2018). 3D culture of bone marrow-derived mesenchymal stem cells (BMSCs) could improve bone regeneration in 3D-printed porous Ti6Al4V scaffolds. *Stem Cells Int.* 2018, 2074021. doi:10.1155/2018/2074021

Zhang, J., Feng, Z., Wei, J., Yu, Y., Luo, J., Zhou, J., et al. (2018). Repair of critical-sized mandible defects in aged rat using hypoxia preconditioned BMSCs with up-regulation of hif-1α. *Int. J. Biol. Sci.* 14, 449–460. doi:10.7150/ijbs.24158

Zhang, P., Kang, Y., Zhou, Z., Zhu, X., Li, W., Cao, C., et al. (2020). Customized borosilicate bioglass scaffolds with excellent biodegradation and osteogenesis for mandible reconstruction. *Front. Bioeng. Biotechnol.* 8, 610284. doi:10.3389/fbioe.2020.610284

Zhang, W., Zhang, Z., Chen, S., Macri, L., Kohn, J., and Yelick, P. C. (2016). Mandibular jaw bone regeneration using human dental cell-seeded tyrosine-derived polycarbonate scaffolds. *Tissue Eng. Part A* 22, 985–993. doi:10.1089/ten.tea.2016.0166

Zhao, X., Zhou, L., Li, Q., Zou, Q., and Du, C. (2018). Biomimetic mineralization of carboxymethyl chitosan nanofibers with improved osteogenic activity *in vitro* and *in vivo*[J]. *Carbohydr. Polym.* 195, 225–234. doi:10.1016/j.carbpol.2018.04.090

Zhu, T., Cui, Y., Zhang, M., Zhao, D., Liu, G., and Ding, J. (2020). Engineered three-dimensional scaffolds for enhanced bone regeneration in osteonecrosis. *Bioact. Mat.* 5, 584–601. doi:10.1016/j.bioactmat.2020.04.008

frontiers | Frontiers in Bioengineering and Biotechnology

TYPE Brief Research Report
PUBLISHED 23 August 2022
DOI 10.3389/fbioe.2022.908250

Check for updates

OPEN ACCESS

EDITED BY
Bruce Alan Bunnell,
University of North Texas Health Science Center, United States

REVIEWED BY
Jochen Salber,
Ruhr-University Bochum, Germany
Ying Zhao,
Zhejiang University, China

*CORRESPONDENCE
Mónica Santos González,
monica.santos.gonzalez@juntadeandalucia.es

†These authors share first authorship

SPECIALTY SECTION
This article was submitted to Tissue Engineering and Regenerative Medicine, a section of the journal Frontiers in Bioengineering and Biotechnology

RECEIVED 30 March 2022
ACCEPTED 26 July 2022
PUBLISHED 23 August 2022

CITATION
Rosell-Valle C, Martín-López M, Campos F, Chato-Astrain J, Campos-Cuerva R, Alaminos M and Santos González M (2022), Inactivation of human plasma alters the structure and biomechanical properties of engineered tissues.
Front. Bioeng. Biotechnol. 10:908250.
doi: 10.3389/fbioe.2022.908250

COPYRIGHT
© 2022 Rosell-Valle, Martín-López, Campos, Chato-Astrain, Campos-Cuerva, Alaminos and Santos González. This is an open-access article distributed under the terms of the Creative Commons Attribution License (CC BY). The use, distribution or reproduction in other forums is permitted, provided the original author(s) and the copyright owner(s) are credited and that the original publication in this journal is cited, in accordance with accepted academic practice. No use, distribution or reproduction is permitted which does not comply with these terms.

Inactivation of human plasma alters the structure and biomechanical properties of engineered tissues

Cristina Rosell-Valle[1†], María Martín-López[1,2†], Fernando Campos[3,4], Jesús Chato-Astrain[3,4], Rafael Campos-Cuerva[1,5], Miguel Alaminos[3,4] and Mónica Santos González[1,5*]

[1]Unidad de Producción y Reprogramación Celular de Sevilla (UPRC), Red Andaluza de Diseño y Traslación de Terapias Avanzadas (RADyTTA), Seville, Spain, [2]Escuela Internacional de Doctorado Universidad de Sevilla, Seville, Spain, [3]Tissue Engineering Group, Department of Histology, Universidad de Granada, Granada, Spain, [4]Instituto de Investigación Biosanitaria ibs. Granada, Granada, Spain, [5]Centro de Transfusiones, Tejidos y Células de Sevilla (CTTS), Fundación Pública Andaluza para la Gestión de la Investigación en Salud en Sevilla (FISEVI), Seville, Spain

Fibrin is widely used for tissue engineering applications. The use of blood derivatives, however, carries a high risk of transmission of infectious agents, necessitating the application of pathogen reduction technology (PRT). The impact of this process on the structural and biomechanical properties of the final products is unknown. We used normal plasma (PLc) and plasma inactivated by riboflavin and ultraviolet light exposure (PLi) to manufacture nanostructured cellularized fibrin-agarose hydrogels (NFAHs), and then compared their structural and biomechanical properties. We also measured functional protein C, prothrombin time (PT), activated partial thromboplastin time (APTT), thrombin time (TT) and coagulation factors [fibrinogen, Factor (F) V, FVIII, FX, FXI, FXIII] in plasma samples before and after inactivation. The use of PLi to manufacture cellularized NFAHs increased the interfibrillar spacing and modified their biomechanical properties as compared with cellularized NFAH manufactured with PLc. PLi was also associated with a significant reduction in functional protein C, FV, FX, and FXI, and an increase in the international normalized ratio (derived from the PT), APTT, and TT. Our findings demonstrate that the use of PRT for fibrin-agarose bioartificial tissue manufacturing does not adequately preserve the structural and biomechanical properties of the product. Further investigations into PRT-induced changes are warranted to determine the applications of NFAH manufactured with inactivated plasma as a medicinal product.

Abbreviations: AB plasma, plasma group AB; APTT, activated partial thromboplastin time; DMEM, Dulbecco's modified Eagle's medium; INR, international normalized ratio; NFAH, nanostructured fibrin-agarose hydrogel; PLc, non-inactivated human plasma; PLi, inactivated human plasma; PRT, Pathogen reduction technology; PT, prothrombin time; RT, Room temperature; TE, Tissue engineering; TT, thrombin time; UVA, ultraviolet A.

KEYWORDS

fibrin-agarose hydrogel, tissue engineering, pathogen reduction method, biomechanical properties, bioartificial skin

Introduction

Tissue engineering is an emerging technology in regenerative medicine that combines cells, biomaterials and biochemical and physicochemical factors to restore tissue and organ function (Bakhshandeh et al., 2018; Kwon et al., 2018). Several types of scaffolds and nanoparticles have been developed based on the extracellular matrix of human tissues, to improve their biological, chemical and mechanical properties (Hinderer et al., 2016; Hasan et al., 2018). Numerous synthetic and natural polymers are currently available to produce biomaterials, which are defined as substances engineered to functionally interact with biological systems. A good example of this is the biopolymer fibrin, which is widely used for tissue engineering applications as both a medical device and a biomaterial itself (García Delgado et al., 2019; de Melo et al., 2020; Arai et al., 2021). Fibrin is generated from fibrinogen and is involved in essential biological functions such as wound repair by providing a temporary matrix to support cell growth, invasion, attachment and biochemical activity (Kearney et al., 2021). The US Food and Drug Administration has approved several fibrin-based products as hemostatic sealants and adhesives (Spotnitz, 2014). Fibrin can be combined with agarose in the fabrication of bioartificial tissues, since this combination of fibrin and agarose demonstrated to provide the tissue with adequate biomechanical properties, including the Young modulus, stress at fracture and traction deformation, and permits its use as scaffolds (Ionescu et al., 2020). Several preclinical studies have successfully demonstrated the application of fibrin-agarose hydrogels in the repair of damaged human organs such as the cornea (Alaminos et al., 2006), skin (Carriel et al., 2012), nerves (Chato-Astrain et al., 2018), oral mucosa (Fernández-Valadés-Gámez et al., 2016) and cartilage (García-Martínez et al., 2017). These positive results have paved the way for the clinical translation of two bioartificial tissues, which are currently used for severe skin burns (Egea-Guerrero et al., 2019) and corneal ulcers (Rico-Sánchez et al., 2019).

Human fibrin is a component of blood plasma. While blood components have had a positive impact on the manufacture of advanced therapy medicinal products (Allain et al., 2005), the use of these raw materials carries a risk of pathogen transmission to patients (Klein et al., 2007; Lanteri et al., 2016; Motta et al., 2016). For this reason, regulatory agencies have issued guidelines to prevent and control the transmission of infectious agents [European Pharmacopoeia, 2013; European Directorate for the Quality of Medicines & HealthCare (EDQM), 2017]. In recent years, a number of pathogen reduction technology (PRT) systems have been developed to minimize pathogens in plasma and platelets (Reikvam et al., 2010; Kaiser-Guignard et al., 2014; Viau et al., 2017). The most commonly used PRT is the Mirasol™ (PRT) System (Marschner and Goodrich, 2011; Kwon et al., 2014), which is based on photochemical principles to cross-link the nucleic acids of pathogens. The method uses riboflavin (vitamin B2), which binds to nucleic acids after ultraviolet A (UVA) light exposure, causing the oxidation of proteins and irreversible damage by blocking replication of pathogen DNA (Kumar et al., 2004). Although PRT is desirable and beneficial, whether riboflavin and UVA exposure affects blood derivatives used to manufacture bioartificial tissues has not been tested. Various studies report that PRT can alter the metabolic (pH, sugars, nucleosides) and physiological parameters of platelets (Janetzko et al., 2005; Kerkhoffs et al., 2010; Stivala et al., 2017) and lead to direct modifications of fibrinogen (Hubbard et al., 2016).

Here, we used human non-inactivated plasma (PLc) or plasma inactivated with riboflavin/UVA light exposure (PLi) to fabricate bioartificial tissues based on fibrin-agarose hydrogels. To better understand the effect of PLi on the generation of the hydrogels, we analyzed their structure and biomechanical properties. In addition, we evaluated the effect of riboflavin/UVA exposure on the levels of natural anticoagulants and coagulation factors present in plasma and questioned whether this contributed to modify the essential properties of bioartificial tissues.

Material and methods

Pathogen reduction method

Three plasmapheresis units obtained from AB blood-type donors were treated in the Mirasol™ (PRT) System (Terumo BCT, Zaventem, Belgium), as described (Larrea et al., 2009; Smith and Rock, 2010) (Figure 1A). Group AB plasma was used to prevent potential problems with antigens and isoagglutinins Briefly, 273 ml of plasma was transferred to an illumination bag containing 35 ± 5 ml of a sterile riboflavin solution (500 μM) (Terumo BCT). The bag was placed in the illuminator for UVA light exposure, with a linear agitation of 120 cpm at room temperature (RT). The PLi was then transferred to a storage bag and frozen simultaneously (−80°C) with its matched control (PLc) product.

Generation of cellularized nanostructured fibrin-agarose hydrogels

Nanostructured fibrin-agarose hydrogels (NFAHs) cellularized with human dermal fibroblasts were generated

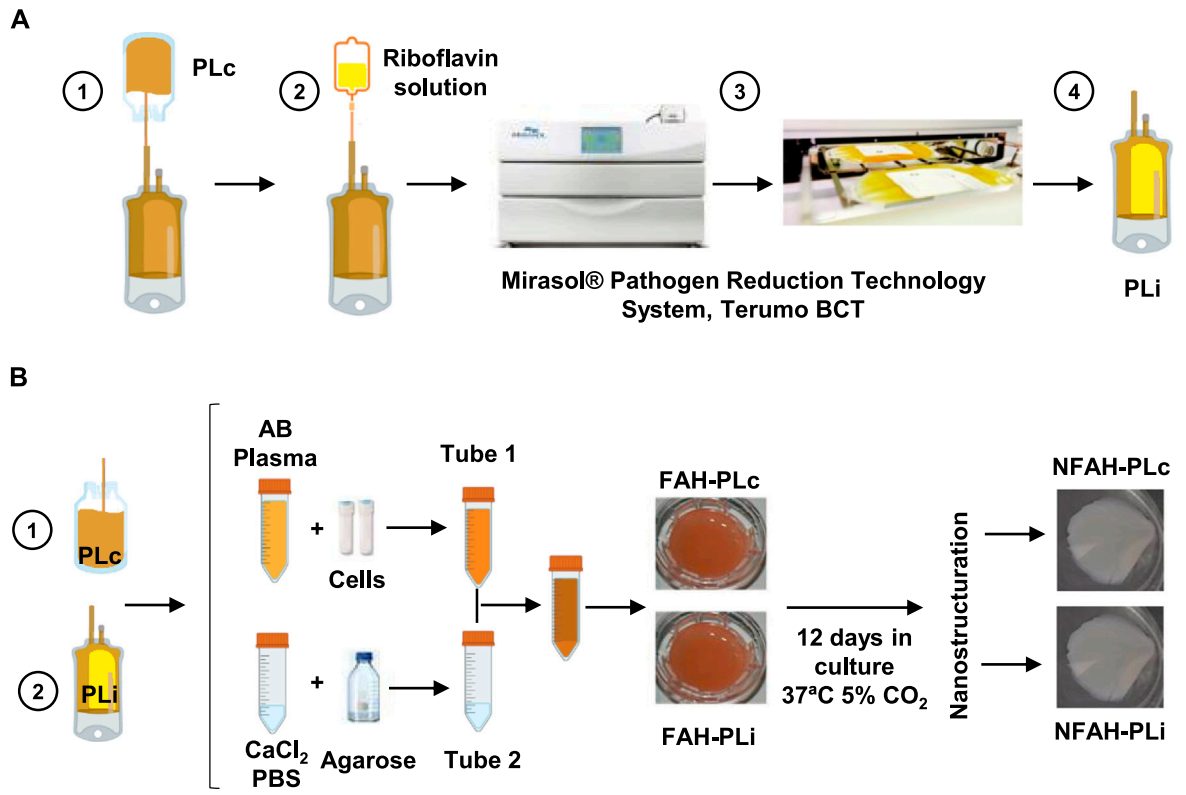

FIGURE 1
Inactivation of human plasma and generation of the cellularized nanostructured fibrin-agarose hydrogel. **(A)** Schematic representation of human plasma treated with the Mirasol® Pathogen Reduction Technology System. **(B)** Experimental design of the generation of nanostructured fibrin-agarose hydrogel with embedded allogeneic dermal fibroblasts with PLc and PLi. PLc, non-inactivated plasma; PLi, inactivated plasma; $CaCl_2$, calcium chloride; PBS, phosphate buffered saline; FAH, fibrin-agarose hydrogel; NFAH, nanostructured fibrin-agarose hydrogel.

with PLc (NFAH PLc) or PLi (NFAH PLi) (Figure 1B) by described protocols (Fernández-Valadés-Gámez et al., 2016; García-Martínez et al., 2017; Ionescu et al., 2020). In brief, 25 ml of AB-type human plasma (PLi or PLc) was mixed in one tube (Tube 1) with Dulbecco's modified Eagle's medium (DMEM) supplemented with 10% fetal bovine serum and 0.5 ml of tranexamic acid (Rottapharm, Milan, Italy) and containing dermal fibroblasts (150,000 cells/mL). The mixture was combined with 1.8 ml of 10% calcium chloride (B. Braun, Melsungen, Germany) and 1.5 ml of liquid 2.2% type VII agarose diluted in phosphate buffered saline (PBS; Sigma-Aldrich, St. Louis, MO, United States), previously prepared in a second tube (Tube 2). The mixture was rapidly aliquoted into a T6 multi-well plate (Corning Gosselin S.A.S. Life Sciences, Hazebrouk Cedex France) and allowed to solidify at 37°C. Six samples of each type (NFAH PLc and NFAH PLi) were generated. The hydrogels were then covered with DMEM containing 1% non-essential amino acids (100×) (Sigma-Aldrich), 20 µg/ml gentamycin (Normon, Madrid, Spain), 1% GlutaMax™ (Life Technologies, Madrid, Spain), 5% human platelet lysate solution (Fernández Muñoz et al., 2021), and stored for 12 days at 37°C/5% CO_2 prior to the nanostructuring process (Campos-Cuerva et al., 2019).

Cell viability analysis in cellularized nanostructured fibrin-agarose hydrogels

Cell viability was determined with the LIVE/DEAD® Viability/Cytotoxicity Kit for mammalian cells (Molecular Probes/Invitrogen, Thermo Fisher Scientific, Waltham, MA, United States) immediately after the nanostructuring process. NFAH samples were washed three times with PBS. The samples were then incubated with the staining solution for 30 min at RT and washed three times with PBS. The number of live and dead cells was determined by fluorescence microscopy, and the cell viability (percentage) was calculated for each study group. Three counts were made for each group of manufactured NFAH.

Structural analysis in cellularized nanostructured fibrin-agarose hydrogels

NFAH samples were fixed in 3.7% buffered formaldehyde at RT, then dehydrated and embedded in paraffin following a standard tissue-processing protocol. NFAH sections were stained with hematoxylin and eosin and examined using a Nikon Eclipse 90i light microscope (Serrato et al., 2009). The porosity of each type of NFAH was determined by quantifying the interfibrillar spaces in the fibrin-agarose fibrillary mesh using ImageJ software (Schneider et al., 2012). Six analyses were made for each group of manufactured NFAH.

Biomechanical analysis of cellularized nanostructured fibrin-agarose hydrogels

The biomechanical properties of the samples (cellularized NFAH PLc and NFAH PLi) were evaluated immediately after nanostructuring (Ionescu et al., 2020). All samples were subjected to tensile testing using an electromechanical material testing instrument (Instron, Model 3345-K3327). Samples were first sectioned to a regular rectangular shape, oriented with their major length along the direction of tension, and clamped at each end. A constant distance of 1 cm between the clamps and the sample was maintained. Analyses were run at a constant strain rate of 5 mm per min at RT to assess the following parameters: Young's modulus (calculated as the tangent modulus of the initial, linear portion of the stress–strain curve of each experimental run), stress at fracture break, and traction deformation. A 50-N Instron load cell was used to obtain the data for the stress–strain curves.

Protein C, prothrombin time, activated partial thromboplastin time and thrombin time assays

Functional protein C, prothrombin time (PT), activated partial thromboplastin time (APTT) and thrombin time (TT) were measured by clotting assays (STA NeoPTimal, STA Cephascreen and STA Thrombin kits, respectively; Diagnostica Stago S.A.S., Asnières sur Seine, France). The international normalized ratio (INR) was derived from the PT and was calculated as the ratio of the PT of the PLi sample to a control PLc PT using the following formula: INR = PLi PT/PLc PT (Shikdar et al., 2021). Samples were analyzed at Echevarne Laboratories, Seville, Spain.

Factor V, VIII, X, XI, XIII and fibrinogen analysis

Factor (F) V, FVIII, FX, FXI, FXIII and fibrinogen were measured by clotting assays (STA Deficient V, STA InmunoDef VIII, STA C.K.Prest, STA InmunoDef XI, K-Assay Factor XIII and STA Liquid Fib Kits Diagnostica Stago S.A.S., respectively). Measurements detect factor activity, excepting factor XIII and fibrinogen assays, which detect factor levels. Samples were analyzed at Echevarne Laboratories, Seville, Spain.

Statistical analysis

Results are presented as mean ± standard error of the mean (SEM). The Shapiro–Wilk test was used to assess normal distribution of data. A two-tailed unpaired Student's t-test was used to compare the structural and biomechanical properties. To identify statistical differences between samples corresponding to NFAH PLc and NFAH PLi, we performed a paired Student's t-test. Correlation analysis was performed using the Pearson correlation coefficient (value ranges from -1 to +1). p-values lower than or equal to 0.05 were considered as statistically significant. All statistical analyses were performed with GraphPad Prism, version 8.0. (GraphPad Software Inc., San Diego, CA).

Results

Structural and biomechanical properties of bioartificial tissues manufactured with PLi or PLc

We first questioned whether NFAHs manufactured with PLi exhibited alterations in cell viability, porosity degree and biomechanical properties. No significant differences were observed between NFAH PLi and NFAH PLc in cell viability ($p > 0.05$; Figures 2A,B). By contrast, PLi negatively affected the structure of NFAH, as shown by a significantly higher interfibrillar spacing (porosity) in NFAH PLi than in NFAH PLc ($t_{10} = 5.087$, $p < 0.001$; Figures 2C,D), suggesting that the application of PRT resulted in a loss of some essential properties of the resulting bioartificial tissues.

Analysis of the biomechanical properties of both hydrogels revealed other significant differences. Specifically, we found significantly lower values for Young's modulus and stress at fracture break in NFAH PLi as compared with NFAH PLc ($t_{10} = 3.599$, $p < 0.05$; $t_{10} = 2.418$, $p < 0.05$, respectively, Figures 2E,F). No significant differences were found between NFAH PLi and NFAH PLc for the traction deformation tests ($p > 0.05$; Figure 2G).

Implications of pathogen reduction technology for human plasma quality

We next comparatively analyzed several factors present in human plasma to determine the putative effects of PRT on

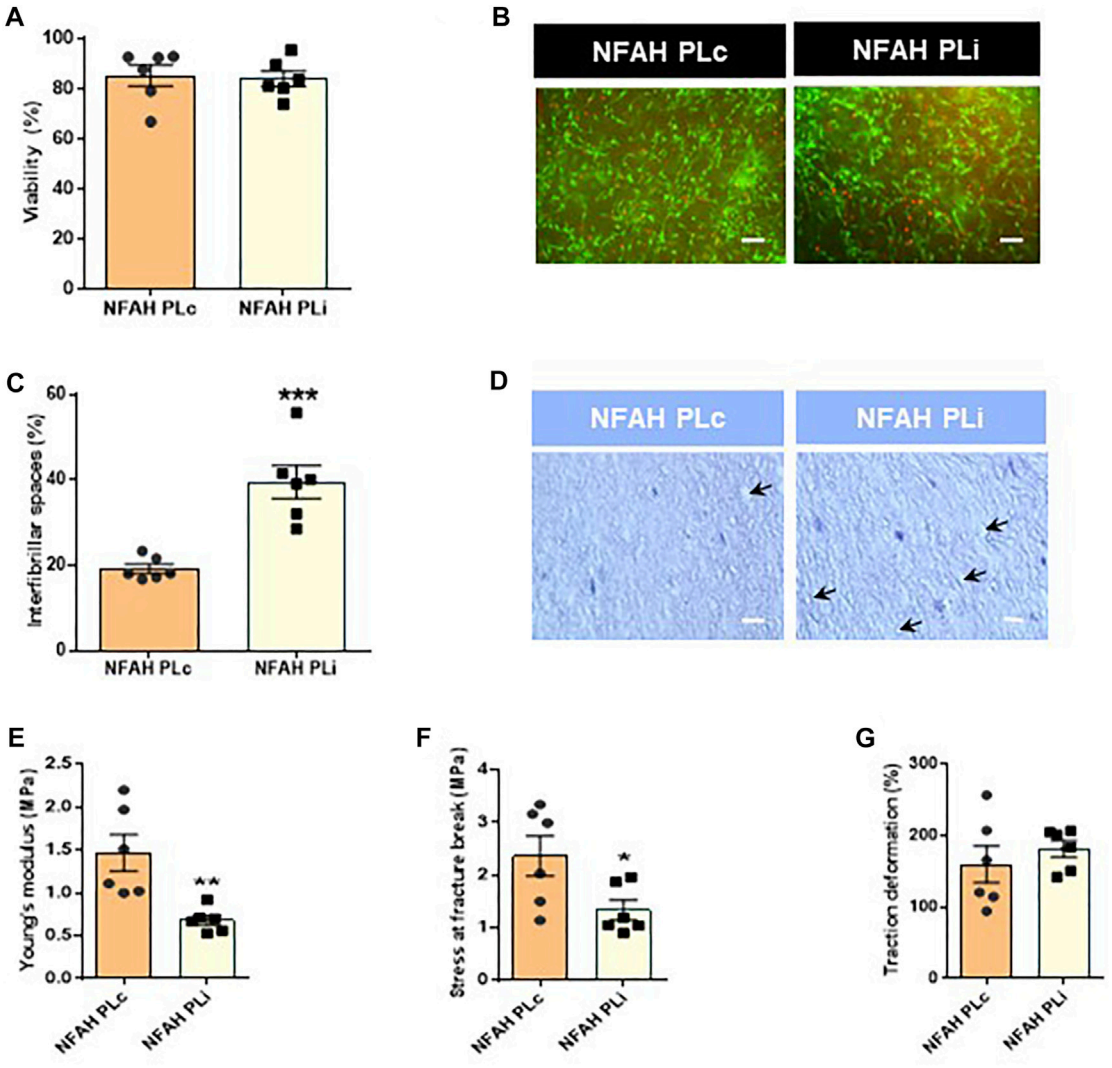

FIGURE 2
Structural and biomechanical characterization of nanostructured fibrin-agarose hydrogels. Bar graph representation of **(A)** percentage of cell viability and **(B)** LIVE/DEAD® Assay staining of cellular NFAH (scale bar: 100 μm). **(C)** Interfibrillar spacing immediately after the nanostructuring process. **(D)** Representative hematoxylin/eosin staining of tissue sections of cellular NFAHs (scale bar: 100 μm). Biomechanical analysis: Bar graph representation of **(E)** Young's modulus, **(F)** stress at fracture-break, and **(G)** traction deformation. Data are shown as mean ± SEM. Arrows indicate interfibrillar spacing. Six independent samples per group were analyzed. Two-tailed unpaired Student's *t*-test: $*p < 0.05$; $***p < 0.0001$.

hydrogels based on human plasma. We focused on measuring factors VIII, XI and fibrinogen because they are the most affected by plasma inactivation (Larrea et al., 2009). Besides, we chose factors V, VIII, X and fibrinogen that form part of the common pathway together with factor II, prothrombin (Chaudhry and Babiker, 2018). For the later, we measured prothrombin time, PT. This test measures, as a whole, the activity of factors II, V, VII, X and fibrinogen. Similarly, we measured thromboplastin time, APTT, which explores coagulation factors XII, XI, X, VIII, X, II and fibrinogen. Additionally, we measured factor XIII, considering it as crucial for our product since it promotes fibrin crosslinking (Beckman et al., 2018).

As shown in Figure 3, we found a significant decrease in the percentage of functional protein C ($t_2 = 6.651$, $p < 0.05$; Figure 3A), and an increase in INR ($t_2 = 18.38$, $p < 0.05$; Figure 3B), APTT ($t_2 = 18.38$, $p < 0.05$; Figure 3C) and TT ($t_2 = 6.08$, $p < 0.001$; Figure 3D) in PLi as compared with PLc. In addition, the percentage of the coagulation factors FV ($t_2 = 7.666$, $p < 0.05$), FX ($t_2 = 6.656$, $p < 0.05$), and FXI ($t_2 = 5.812$, $p < 0.05$) was significantly lower in PLi than in PLc (Figures 3E–G, respectively). PLi samples also showed a slight decrease in the levels of FVIII, FXIII and fibrinogen compared with PLc samples, but the differences were not significant ($p > 0.05$, Figures 3H–J, respectively).

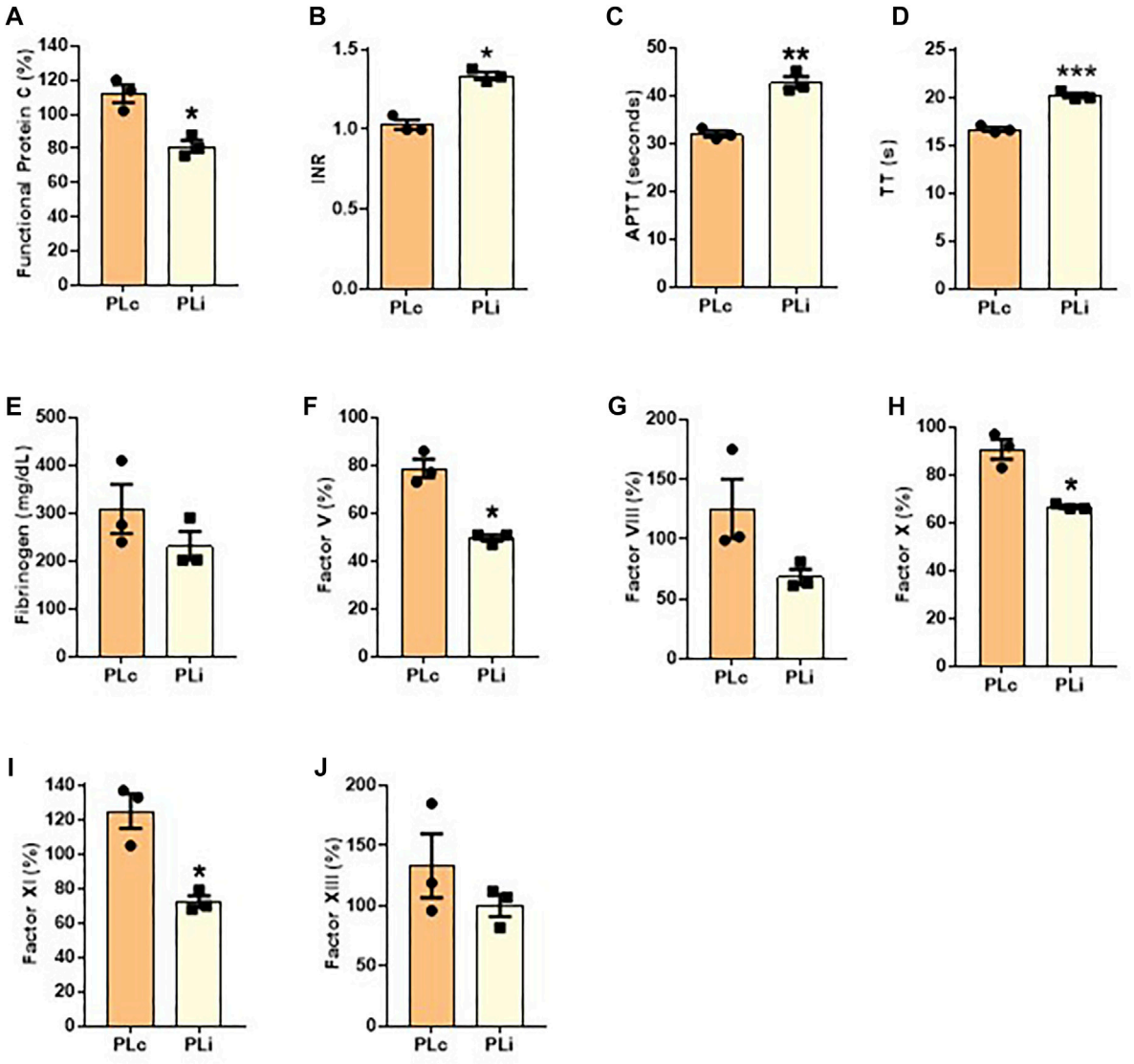

FIGURE 3
Coagulation profile of human plasma after pathogen reduction. The following measurement were performed: **(A)** functional protein C, **(B)** international normalized ratio (INR), **(C)** activated partial thromboplastin time (APTT), **(D)** thrombin time (TT), coagulation factor **(E)** V, **(F)** X, **(G)** XI, **(H)** VIII, and **(I)** XIII and **(J)** fibrinogen. Data are shown as mean ± SEM. Three independent samples per group were analyzed. Student's paired *t*-test: $*p < 0.05$; $**p < 0.01$; $***p < 0.001$.

Correlation between the structural and biomechanical properties of bioartificial tissues and coagulation factor levels

To determine whether there was a relationship between the main changes found in the structural and biomechanical properties and changes in coagulation factors after the application of PRT, we performed correlation analyses (Table 1). Results of these analyses showed that the interfibrillar spacing (porosity) of the NFAH negatively correlated with FV ($r = -0.87$, $p < 0.05$), FX ($r = -0.87$, $p < 0.05$) and FXI ($r = -0.85$, $p < 0.05$). Regarding the biomechanical properties, we found that Young's modulus positively correlated with FV ($r = 0.84$, $p < 0.05$) and FX ($r = 0.79$, $p < 0.05$), whereas the stress at fracture break positively correlated with FV ($r = 0.83$, $p < 0.05$), FVIII ($r = 0.83$, $p < 0.05$), FX ($r = 0.82$, $p < 0.05$) and FXI ($r = 0.82$, $p < 0.05$). No correlation was found with fibrinogen level.

Discussion

Fibrin-agarose hydrogels are scaffold-based tissue engineering products that are gaining widespread interest in

TABLE 1 Correlation matrix between structural and biomechanical properties and coagulation factors.

	Interfibrillar spaces	Young's modulus	Stress at fracture break
Fibrinogen	−0.49	0.42	0.61
p	0.32	0.17	0.20
Factor V	**−0.87**	**0.84**	**0.83**
p	**0.02**	**0.03**	**0.04**
Factor VIII	**−0.87**	0.65	**0.83**
p	**0.02**	0.16	**0.04**
Factor X	**−0.87**	**0.79**	**0.82**
p	**0.02**	**0.05**	**0.05**
Factor XI	**−0.85**	0.77	**0.82**
p	**0.03**	0.07	**0.05**
Factor XIII	−0.47	0.36	0.21
p	0.34	0.48	0.68

Pearson's r coefficient. Significant correlation coefficients and the corresponding significance level (p) are given in bold.

regenerative medicine for the treatment of tissue (Campos et al., 2020). This biomaterial must comply with the basic properties of organs and tissues to which it is applied, and provide structural support for cells and mimic the mechanical properties of native tissue. Our results show that PRT modifies the porosity degree of the final product by increasing the interfibrillar spacing of the fibrin-agarose scaffold. The three-dimensional structure of NFAH PLi was compatible with a loss of integrity when compared with NFAH PLc. The pore size of biomaterials is a critical factor affecting cell attachment and cell physiology (Vu et al., 2015), and maintaining this parameter is very important for bioartificial tissues to be functional. Interestingly, the pore size modification in NFAH PLi was not associated with a decrease in cell viability. While it has been suggested that increased interfibrillar spacing may reduce the strength and flexibility of bioartificial tissues and impair their clinical use (Shahmirzadi et al., 2013), our finding that cell viability was preserved might suggest that the pore size found in both NFAH PLi and NFAH PLc could be within a physiological range.

The biomechanical properties of the manufactured NFAH PLc were similar to those previously determined for fibrin-agarose hydrogels, whereas the properties of NFAH PLi were inferior (Campos et al., 2020; Ionescu et al., 2020). Generally, maintaining the biomechanical properties of an artificial tissue is a prerequisite for tissue-engineered products for clinical use. Whether or not this difference in NFAH PLi has a clinical effect should be determined in future studies in laboratory models. However, we hypothesize that the biomechanical modifications generated by the PRT System compromises the biological function of these artificial tissues. That being said, the structural and biochemical properties are not the only key criteria to be considered for the application of artificial tissues (Linares-Gonzalez et al., 2021). Whether the positive effects of the PRT treatment––in terms of biosafety––outweigh the negative effects of the treatment should be determined on a case-by-case basis, as some applications may not require a bioartificial tissue with strong biomechanical properties.

Because fibrin is mainly obtained from donors' human plasma, PRT is required to lessen the risk of transmission of infectious agents [Klein et al., 2007; European Pharmacopoeia, 2013; Lanteri et al., 2016; Motta et al., 2016; European Directorate for the Quality of Medicines & HealthCare (EDQM), 2017]. Nonetheless, PRT may have adverse effects on the coagulation system, which could change the functionality of the treated plasma and impair clinical applications. In this regard, several authors have analyzed the effects of PRT on plasma components, specifically on coagulation factor levels, finding a decrease in coagulation factor activity after riboflavin/UVA exposure when compared with fresh frozen plasma (Hornsey et al., 2009; Larrea et al., 2009; Smith and Rock, 2010; Marschner and Goodrich, 2011). Nevertheless, these reports concluded that it is unlikely that this decrease has any clinical impact. By contrast, Klompas and colleagues recently demonstrated that the loss of coagulation factor activity in pathogen-reduced COVID-19 convalescent plasma had a clinical impact associated with the pathogen reduction process (Klompas et al., 2022). Moreover, in agreement with our results, they demonstrated an increase in APTT and TT, suggesting that a slight prolongation of coagulation times may occur due to the combined loss of activity of several coagulation factors (Hornsey et al., 2009; Klompas et al., 2022). In line with these studies, we also found a significant reduction of functional protein C and FV, FX, and FXI levels, and a slight decrease in FVIII, FXIII and fibrinogen after inactivation. These results might partly explain the structural and biomechanical changes evident in samples generated with PRT-treated human plasma.

Considering that riboflavin/UVA treatment can act as a cross-linking system able to improve the biomechanical

rigidity of decellularized scaffolds (Xiang et al., 2017) and corneas (Aslanides et al., 2016), it might also have a positive effect on fibrin-agarose scaffolds. However, the correlation analysis revealed the opposite behavior, showing that riboflavin/UVA exposure on plasma did not preserve coagulation factor levels.

Factor V is a component of the prothrombin complex, which interacts with other coagulation proteins, including activated FX and prothrombin to increase the production of thrombin. Thrombin mediates the cleavage of fibrinogen to fibrin monomers that, upon polymerization, form a fibrin clot (Kalafatis and Mann, 1997; Göbel et al., 2018). In addition, FXI also contributes to the generation of thrombin and thus, is involved in the formation of fibrin (Meijers et al., 2000). Undoubtedly, these coagulation proteins are needed to stabilize the fibrin-agarose scaffold and to maintain the fibrillar pattern of hydrogels. The observed relatedness between coagulation factors and the structure of the NFAH also suggests that the loss of their activity could affect biomechanical properties. In this regard, Young's modulus is associated with FV and FX, whereas the stress at fracture break is related to FVIII. Overall, these findings suggest that the loss of key coagulation factors in NFAH produced with PLi is associated with the generation of a less compact fibrillary mesh, which could impact its clinical usefulness. A balance should be reached between PRT and its applicability on artificial tissues to achieve safer and more effective tissue engineered products. Given that the PRT protocol cannot be modified, the balance would rely on the supplementation with coagulation factors that aided fibrin formation prior to NFAH jellification, for example, FV or FX, which resulted significantly affected by inactivation. FX, together with FV (cofactor) convert prothrombin into thrombin, which would further activate fibrin formation and at the same time enhance the intrinsic pathway of the coagulation cascade. Other possibilities could contemplate the addition of biomaterials that reinforced the structure of the hydrogel by reducing interfibrillar spaces. Our group has explored the addition of biomaterials like genipin, which used in concentrations of 0.1%–0.5%, improved structural and biomechanical properties of NFAH (Campos et al., 2018). A different approach could be the addition of 0.7 mg/ml chitosan-silica which has been shown to improve the mechanical stability of fibrin hydrogels with low risks of cytotoxicity (Becerra et al., 2021). Nevertheless, "*in vivo*" studies are still needed to check efficacy and security of either option.

Limitations

Our data indicate that the application of inactivation methods based on riboflavin and UV light alters the coagulation system in plasma. This disruption leads to a loss of coagulation factor activity that may affect the structure of NFAH and consequently, its biomechanical properties. Although our data are robust, we detect some limitations that should be taken into account in future studies.

It is unknown whether the application of other pathogen inactivation methods in plasma samples can mitigate the decrease in coagulation factors activity and consequently, reduce the adverse impact on the structure and biomechanical properties of these hydrogels. Therefore, others PRTs should be tested.

Another consideration could be the incubation period of cellularized fibrin-agarose hydrogels. Fibrin scaffolds accelerate fibroblast growth and remodeling of extracellular matrix (San Matin et al., 2011) thus, if a suitable structure has not formed due to reduced coagulation factors, inter-fibrillar spaces may increase with culture time. In this regard, decreasing the culture time could better preserve the structure and biomechanical properties of cellularized NFAH. In addition, it might be appropriate to explore other alternatives to reinforce the structure and functionality of cellularized NFAH such as the application of genipin (Campos et al., 2018) or the fibrin combination with polymer materials such as polycaprolactone (PCL), that promote smaller aperture and larger fiber diameter in fibrin scaffolds (Lei et al., 2020).

Regarding the effects caused by PRT, these could be compensated by coagulation factors supplementation during hydrogels manufacture, although this step may increase manufacturing costs.

Conclusion

No studies had analyzed the impact of PLi use on bioartificial tissue manufacturing. Considering that blood derivatives must be treated with a pathogen reduction method to prevent the transmission of infectious agents, our results show that the use of riboflavin/UVA-based PLi for the fabrication of NFAH significantly affects the structural, biochemical and biological properties of the fibrin-agarose matrix, possibly due to changes in the level/activity of several coagulation factors. Future studies should evaluate the advantages and disadvantages of PLi used in the manufacturing process of this type of bioartificial tissues and the specific applications in which these changes could be acceptable for clinical use.

Data availability statement

The raw data supporting the conclusion of this article will be made available by the authors, without undue reservation.

Author contributions

CR-V and MM: conception and design, collection and assembly of data, data analysis and interpretation, manuscript

writing. FC, JC-A, RC-C, and MA: collection of data, data analysis and interpretation. MS: conception and design, interpretation and manuscript writing. All authors: revision and final approval of manuscript.

Funding

This research was funded by the Spanish Plan Nacional de Investigación Científica, Desarrollo e Innovación Tecnológica (I+D+i) from Ministerio de Ciencia, Innovación y Universidades (Instituto de Salud Carlos III), grants FIS PI17/0391, RTC-2017-6658-1, PI20/0317 and ICI19/00024 (BIOCLEFT), co-financed by Fondo Europeo de Desarrollo Regional ERDF-FEDER, European Union and PE-0395-2019 from Consejería de Salud y Familias, Junta de Andalucía, Spain.

Acknowledgments

The authors are grateful to Echevarne Laboratories for the coagulation experiments and to Gloria Carmona and Rosario Sánchez Pernaute as well as all members of the Unidad de Producción y Reprogramación Celular (UPRC) for technical help and support. All figures were created through BioRender.com accessed on 1 September 2021.

Conflict of interest

The authors declare that the research was conducted in the absence of any commercial or financial relationships that could be construed as a potential conflict of interest.

Publisher's note

All claims expressed in this article are solely those of the authors and do not necessarily represent those of their affiliated organizations, or those of the publisher, the editors and the reviewers. Any product that may be evaluated in this article, or claim that may be made by its manufacturer, is not guaranteed or endorsed by the publisher.

References

Alaminos, M., Del Carmen Sánchez-Quevedo, M., Muñoz-Avila, J. I., Serrano, D., Medialdea, S., Carreras, I., et al. (2006). Construction of a complete rabbit cornea substitute using a fibrin-agarose scaffold. *Invest. Ophthalmol. Vis. Sci.* 47, 3311–3317. doi:10.1167/iovs.05-1647

Allain, J. P., Bianco, C., Blajchman, M. A., Brecher, M. E., Busch, M., Leiby, D., et al. (2005). Protecting the blood supply from emerging pathogens: The role of pathogen inactivation. *Transfus. Med. Rev.* 19, 110–126. doi:10.1016/J.TMRV.2004.11.005

Arai, K., Kitsuka, T., and Nakayama, K. (2021). Scaffold-based and scaffold-free cardiac constructs for drug testing. *Biofabrication* 13, 042001. doi:10.1088/1758-5090/ac1257

Aslanides, I. M., Dessi, C., Georgoudis, P., Charalambidis, G., Vlassopoulos, D., Coutsolelos, A. G., et al. (2016). Assessment of UVA-riboflavin corneal cross-linking using small amplitude oscillatory shear measurements. *Invest. Ophthalmol. Vis. Sci.* 57, 2240–2245. doi:10.1167/IOVS.15-17956

Bakhshandeh, B., Zarrintaj, P., Oftadeh, M. O., Keramati, F., Fouladiha, H., Sohrabi-jahromi, S., et al. (2018). Tissue engineering; strategies, tissues, and biomaterials. *Biotechnol. Genet. Eng. Rev.* 33. 144–172. doi:10.1080/02648725.2018.1430464

Becerra, N. Y., Restrepo, L. M., Galeano, Y., Tobón, A. C., Tobón, T., Turizo, L. F., et al. (2021). Improving fibrin hydrogels' mechanical properties, through addition of silica or chitosan-silica materials, for potential application as wound dressings. doi:10.1155/2021/9933331

Beckman, J. D., Holle, L. A., and Wolberg, A. S. (2018). Factor XIII cotreatment with hemostatic agents in hemophilia A increases fibrin α-chain crosslinking. *J. Thromb. Haemost.* 16, 131–141. doi:10.1111/JTH.13887

Campos, F., Bonhome-Espinosa, A. B., Chato-Astrain, J., Sánchez-Porras, D., García-García, Ó. D., Carmona, R., et al. (2020). Evaluation of fibrin-agarose tissue-like hydrogels biocompatibility for tissue engineering applications. *Front. Bioeng. Biotechnol.* 0, 596. doi:10.3389/FBIOE.2020.00596

Campos, F., Bonhome-Espinosa, A. B., Vizcaino, G., Rodriguez, I. A., Durand-Herrera, D., López-López, M. T., et al. (2018). Generation of genipin cross-linked fibrin-agarose hydrogel tissue-like models for tissue engineering applications. *Biomed. Mat.* 13, 025021. doi:10.1088/1748-605X/aa9ad2

Campos-Cuerva, R., Fernández-Muñoz, B., Farfán López, F., Pereira Arenas, S., Santos-González, M., Lopez-Navas, L., et al. (2019). Nanostructured fibrin agarose hydrogel as a novel haemostatic agent. *J. Tissue Eng. Regen. Med.* 13, 664–673. doi:10.1002/term.2831

Carriel, V., Garzón, I., Jiménez, J. M., Oliveira, A. C. X., Arias-Santiago, S., Campos, A., et al. (2012). Epithelial and stromal developmental patterns in a novel substitute of the human skin generated with fibrin-agarose biomaterials. *Cells Tissues Organs* 196, 1–12. doi:10.1159/000330682

Chato-Astrain, J., Campos, F., Roda, O., Miralles, E., Durand-Herrera, D., Sáez-Moreno, J. A., et al. (2018). *In vivo* evaluation of nanostructured fibrin-agarose hydrogels with mesenchymal stem cells for peripheral nerve repair. *Front. Cell. Neurosci.* 12, 501. doi:10.3389/fncel.2018.00501

Chaudhry, R., and Babiker, H. M. (2018). Physiology, coagulation pathways. StatPearls Publishing Available at: https://www.ncbi.nlm.nih.gov/books/NBK482253/.

de Melo, B. A. G., Jodat, Y. A., Cruz, E. M., Benincasa, J. C., Shin, S. R., and Porcionatto, M. A. (2020). Strategies to use fibrinogen as bioink for 3D bioprinting fibrin-based soft and hard tissues. *Acta Biomater.* 117, 60–76. doi:10.1016/J.ACTBIO.2020.09.024

Egea-Guerrero, J. J., Carmona, G., Correa, E., Mata, R., Arias-Santiago, S., Alaminos, M., et al. (2019). Transplant of tissue-engineered artificial autologous human skin in andalusia: An example of coordination and institutional collaboration. *Transpl. Proc.* 51, 3047–3050. doi:10.1016/J.TRANSPROCEED.2019.08.014

European Directorate for the Quality of Medicines & HealthCare (EDQM) (2017). *Guide to the preparation, use and quality assurance of blood components.* 19th edition. doi:10.1111/j.1423-0410.2007.00965.x

European Pharmacopoeia (2013). *European directorate for the quality of medicines (EDQM) 5.2.12. Raw materials of biological origin for the production of cell-based and gene therapy medicinal products.* 10th Edn. Strasbourg, France: EDQM, ISBN 978-92-871-8921-9.

Fernández Muñoz, B., Lopez-Navas, L., Gonzalez Bermejo, M., Lomas Romero, I. M., Montiel Aguilera, M. Á., Campos Cuerva, R., et al. (2021). A proprietary gmp human platelet lysate for the expansion of dermal fibroblasts for clinical applications. *Platelets* 1–12, 98–109. doi:10.1080/09537104.2020.1856356

Fernández-Valadés-Gámez, R., Garzón, I., Liceras-Liceras, E., España-López, A., Carriel, V., Martin-Piedra, M. Á., et al. (2016). Usefulness of a bioengineered oral mucosa model for preventing palate bone alterations in rabbits with a

mucoperiostial defect. *Biomed. Mat.* 11, 015015. doi:10.1088/1748-6041/11/1/015015

García Delgado, A. B., De La Cerda, B., Alba Amador, J., Valdés Sánchez, M. L., Fernández-Muñoz, B., Relimpio López, I., et al. (2019). Subretinal transplant of induced pluripotent stem cell-derived retinal pigment epithelium on nanostructured fibrin-agarose. *Tissue Eng. Part A* 25, 799–808. doi:10.1089/ten.tea.2019.0007

García-Martínez, L., Campos, F., Godoy-Guzmán, C., del Carmen Sánchez-Quevedo, M., Garzón, I., Alaminos, M., et al. (2017). Encapsulation of human elastic cartilage-derived chondrocytes in nanostructured fibrin-agarose hydrogels. *Histochem. Cell Biol.* 147, 83–95. doi:10.1007/S00418-016-1485-9

Göbel, K., Eichler, S., Wiendl, H., Chavakis, T., Kleinschnitz, C., and Meuth, S. G. (2018). The coagulation factors fibrinogen, thrombin, and factor XII in inflammatory disorders-a systematic review. *Front. Immunol.* 9, 1731. doi:10.3389/fimmu.2018.01731

Hasan, A., Morshed, M., Memic, A., Hassan, S., Webster, T. J., and Marei, H. E. S. (2018). Nanoparticles in tissue engineering: Applications, challenges and prospects. *Int. J. Nanomedicine* 13, 5637–5655. doi:10.2147/IJN.S153758

Hinderer, S., Layland, S. L., and Schenke-Layland, K. (2016). ECM and ECM-like materials - biomaterials for applications in regenerative medicine and cancer therapy. *Adv. Drug Deliv. Rev.* 97, 260–269. doi:10.1016/J.ADDR.2015.11.019

Hornsey, V. S., Drummond, O., Morrison, A., McMillan, L., MacGregor, I. R., and Prowse, C. V. (2009). Pathogen reduction of fresh plasma using riboflavin and ultraviolet light: Effects on plasma coagulation proteins. *Transfusion* 49, 2167–2172. doi:10.1111/J.1537-2995.2009.02272.X

Hubbard, T., Backholer, L., Wiltshire, M., Cardigan, R., and Ariëns, R. A. S. (2016). Effects of riboflavin and amotosalen photoactivation systems for pathogen inactivation of fresh-frozen plasma on fibrin clot structure. *Transfusion* 56, 41–48. doi:10.1111/TRF.13261

Ionescu, A. M., Chato-Astrain, J., Cardona, J. de la C., Campos, F., Pérez, M. M., Alaminos, M., et al. (2020). Evaluation of the optical and biomechanical properties of bioengineered human skin generated with fibrin-agarose biomaterials. *J. Biomed. Opt.* 25, 1. doi:10.1117/1.jbo.25.5.055002

Janetzko, K., Cazenave, J. P., Klüter, H., Kientz, D., Michel, M., Beris, P., et al. (2005). Therapeutic efficacy and safety of photochemically treated apheresis platelets processed with an optimized integrated set. *Transfusion* 45, 1443–1452. doi:10.1111/J.1537-2995.2005.00550.X

Kaiser-Guignard, J., Canellini, G., Lion, N., Abonnenc, M., Osselaer, J. C., and Tissot, J. D. (2014). The clinical and biological impact of new pathogen inactivation technologies on platelet concentrates. *Blood Rev.* 28, 235–241. doi:10.1016/j.blre.2014.07.005

Kalafatis, M., and Mann, K. G. (1997). Factor VLeiden and thrombophilia. *Arterioscler. Thromb. Vasc. Biol.* 17, 620–627. doi:10.1161/01.ATV.17.4.620

Kearney, K. J., Ariëns, R. A. S., and Macrae, F. L. (2021). The role of fibrin(ogen) in wound healing and infection control. *Semin. Thromb. Hemost.* 48, 174–187. doi:10.1055/s-0041-1732467

Kerkhoffs, J. L. H., Van Putten, W. L. J., Novotny, V. M. J., Te Boekhorst, P. A. W., Schipperus, M. R., Zwaginga, J. J., et al. (2010). Clinical effectiveness of leucoreduced, pooled donor platelet concentrates, stored in plasma or additive solution with and without pathogen reduction. *Br. J. Haematol.* 150, 209–217. doi:10.1111/J.1365-2141.2010.08227.X

Klein, H. G., Anderson, D., Bernardi, M. J., Cable, R., Carey, W., Hoch, J. S., et al. (2007). Pathogen inactivation: Making decisions about new technologies. Report of a consensus conference. *Transfusion* 47, 2338–2347. doi:10.1111/J.1537-2995.2007.01512.X

Klompas, A. M., van Helmond, N., Juskewitch, J. E., Pruthi, R. K., Sexton, M. A., Soto, J. C. D., et al. (2022). Coagulation profile of human COVID-19 convalescent plasma. *Sci. Rep.* 121 12, 637–7. doi:10.1038/s41598-021-04670-1

Kumar, V., Lockerbie, O., Keil, S. D., Ruane, P. H., Platz, M. S., Martin, C. B., et al. (2004). Riboflavin and UV-light based pathogen reduction: Extent and consequence of DNA damage at the molecular level. *Photochem. Photobiol.* 80, 15. doi:10.1562/2003-12-23-RA-036.1

Kwon, S. G., Kwon, Y. W., Lee, T. W., Park, G. T., and Kim, J. H. (2018). Recent advances in stem cell therapeutics and tissue engineering strategies. *Biomater. Res.* 22, 36–38. doi:10.1186/s40824-018-0148-4

Kwon, S. Y., Kim, I. S., Bae, J. E., Kang, J. W., Cho, Y. J., Cho, N. S., et al. (2014). Pathogen inactivation efficacy of Mirasol PRT System and Intercept Blood System for non-leucoreduced platelet-rich plasma-derived platelets suspended in plasma. *Vox Sang.* 107, 254–260. doi:10.1111/VOX.12158

Lanteri, M. C., Kleinman, S. H., Glynn, S. A., Musso, D., Keith Hoots, W., Custer, B. S., et al. (2016). Zika virus: A new threat to the safety of the blood supply with worldwide impact and implications. *Transfusion* 56, 1907–1914. doi:10.1111/TRF.13677

Larrea, L., Calabuig, M., Roldán, V., Rivera, J., Tsai, H.-M., Vicente, V., et al. (2009). The influence of riboflavin photochemistry on plasma coagulation factors. *Transfus. Apher. Sci.* 41, 199–204. doi:10.1016/J.TRANSCI.2009.09.006

Lei, Y., Xiafei, L., Dongmei, W., Songfeng, M., Wenhao, L., YongweiH., et al. (2020). *Improved mechanical properties by modifying fibrin scaffold with PCL and its biocompatibility evaluation. Journal of Biomaterials Science*. doi:10.1080/09205063.2019.1710370*Polym. Ed.*

Linares-Gonzalez, L., Rodenas-Herranz, T., Campos, F., Ruiz-Villaverde, R., and Carriel, V. (2021). *Basic Quality Controls Used in Skin Tissue Engineering*, 11. doi:10.3390/LIFE11101033*Life (Basel, Switz.*

Marschner, S., and Goodrich, R. (2011). Pathogen reduction technology treatment of platelets, plasma and whole blood using riboflavin and UV light. *Transfus. Med. Hemother.* 38, 8–18. doi:10.1159/000324160

Meijers, J. C. M., Tekelenburg, W. L. H., Bouma, B. N., Bertina, R. M., and Rosendaal, F. R. (2000). High levels of coagulation factor XI as a risk factor for venous thrombosis. *N. Engl. J. Med.* 342, 696–701. doi:10.1056/nejm200003093421004

Motta, I. J. F., Spencer, B. R., Cordeiro da Silva, S. G., Arruda, M. B., Dobbin, J. A., Gonzaga, Y. B. M., et al. (2016). Evidence for transmission of zika virus by platelet transfusion. *N. Engl. J. Med.* 375, 1101–1103. doi:10.1056/NEJMC1607262

Reikvam, H., Marschner, S., Apelseth, T. O., Goodrich, R., and Hervig, T. (2010). The Mirasol® Pathogen Reduction Technology system and quality of platelets stored in platelet additive solution. *Blood Transfus.* 8, 186–192. doi:10.2450/2010.0141-09

Rico-Sánchez, L., Garzón, I., González-Andrades, M., Ruíz-García, A., Punzano, M., Lizana-Moreno, A., et al. (2019). Successful development and clinical translation of a novel anterior lamellar artificial cornea. *J. Tissue Eng. Regen. Med.* 13, 2142–2154. doi:10.1002/TERM.2951

San Martin, S., Alaminos, M., Zorn, T. M. T. M., Sánchez-Quevedo, C., Garzón, I., Rodriguez, A., et al. (2011). The effects of fibrin and fibrin-agarose on the extracellular matrix profile of bioengineered oral mucosa. *Tissue Eng. Regen. Med.* doi:10.1002/term.490

Schneider, C. A., Rasband, W. S., and Eliceiri, K. W. (2012). NIH image to ImageJ: 25 years of image analysis. *Nat. Methods* 9, 671–675. doi:10.1038/nmeth.2089

Serrato, D., Nieto-Aguilar, R., Garzón, I., Roda, O., Campos, A., and Alaminos, M. (2009). Comparison of the effect of cryopreservation protocols on the histology of bioengineered tissues. *Histol. Histopathol.* 24, 1531–1540. doi:10.14670/HH-24.1531

Shahmirzadi, D., Bruck, H. A., and Hsieh, A. H. (2013). Quantifying the interfibrillar spacing and fibrillar orientation of the aortic extracellular matrix using histology image processing: Toward multiscale modeling. *IEEE Trans. Biomed. Eng.* 60, 1171–1180. doi:10.1109/TBME.2012.2229708

Shikdar, S., Vashisht, R., and Bhattacharya, P. T. (2021). StatPearls.International normalized ratio (INR).

Smith, J., and Rock, G. (2010). Protein quality in Mirasol pathogen reduction technology-treated, apheresis-derived fresh-frozen plasma. *Transfusion* 50, 926–931. doi:10.1111/j.1537-2995.2009.02517.x

Spotnitz, W. D. (2014). Fibrin sealant: The only approved hemostat, sealant, and adhesive—A laboratory and clinical perspective. *ISRN Surg.*, 1–28. doi:10.1155/2014/203943

Stivala, S., Gobbato, S., Infanti, L., Reiner, M. F., Bonetti, N., Meyer, S. C., et al. (2017). Amotosalen/ultraviolet A pathogen inactivation technology reduces platelet activatability, induces apoptosis and accelerates clearance. *Haematologica* 102, 1650–1660. doi:10.3324/HAEMATOL.2017.164137

Viau, S., Chabrand, L., Eap, S., Lorant, J., Rouger, K., Goudaliez, F., et al. (2017). Pathogen reduction through additive-free short-wave UV light irradiation retains the optimal efficacy of human platelet lysate for the expansion of human bone marrow mesenchymal stem cells. *PLoS One* 12, e0181406–23. doi:10.1371/journal.pone.0181406

Vu, L. T., Jain, G., Veres, B. D., and Rajagopalan, P. (2015). Cell migration on planar and three-dimensional matrices: A hydrogel-based perspective. *Tissue Eng. Part B Rev.* 21, 67–74. doi:10.1089/TEN.TEB.2013.0782

Xiang, J., Liu, P., Zheng, X., Dong, D., Fan, S., Dong, J., et al. (2017). The effect of riboflavin/UVA cross-linking on anti-degeneration and promoting angiogenic capability of decellularized liver matrix. *J. Biomed. Mat. Res. A* 105, 2662–2669. doi:10.1002/JBM.A.36126

frontiers | Frontiers in Bioengineering and Biotechnology

TYPE Original Research
PUBLISHED 13 September 2022
DOI 10.3389/fbioe.2022.994816

Check for updates

OPEN ACCESS

EDITED BY
Bruce Alan Bunnell,
University of North Texas Health Science Center, United States

REVIEWED BY
Bo Zhu,
Guangxi Medical University, China
Jay Trivedi,
Rhode Island Hospital, United States

*CORRESPONDENCE
Baishan Song,
sbssxszl@163.com
Zhigang Qian,
13675868673@163.com

SPECIALTY SECTION
This article was submitted to Tissue Engineering and Regenerative Medicine, a section of the journal Frontiers in Bioengineering and Biotechnology

RECEIVED 15 July 2022
ACCEPTED 23 August 2022
PUBLISHED 13 September 2022

CITATION
Sun Q, Yin W, Ru X, Liu C, Song B and Qian Z (2022), Dual role of injectable curcumin-loaded microgels for efficient repair of osteoarthritic cartilage injury. *Front. Bioeng. Biotechnol.* 10:994816. doi: 10.3389/fbioe.2022.994816

COPYRIGHT
© 2022 Sun, Yin, Ru, Liu, Song and Qian. This is an open-access article distributed under the terms of the Creative Commons Attribution License (CC BY). The use, distribution or reproduction in other forums is permitted, provided the original author(s) and the copyright owner(s) are credited and that the original publication in this journal is cited, in accordance with accepted academic practice. No use, distribution or reproduction is permitted which does not comply with these terms.

Dual role of injectable curcumin-loaded microgels for efficient repair of osteoarthritic cartilage injury

Qicai Sun[1], Wei Yin[2], Xuanliang Ru[1], Chun Liu[1], Baishan Song[1]* and Zhigang Qian[1]*

[1]Department of Orthopaedic Surgery, Zhejiang Hospital, Zhejiang University School of Medicine, Hangzhou, Zhejiang, China, [2]Zhejiang University School of Medicine, Hangzhou, Zhejiang, China

Curcumin has been widely used for the treatment of age-associated diseases, and showed chondroprotective potential for post-traumatic osteoarthritis (OA). However, due to the irregular-shaped and large-sized defects on joint cartilage in degenerated OA, the *in vivo* delivery and therapeutic effect of curcumin for effective repair remain challenging. In this study, we first present a PEG-GelMA [Poly(Ethylene Glycol) Dimethacrylate-Gelatin Methacrylate, PGMs] hydrogel microgel-based curcumin delivery system for both improved anti-inflammatory and pro-regenerative effects in treatment for cartilage defects. The curcumin-loaded PGMs were produced by a microfluidic system based on light-induced gelation of gelatin methacrylate (GelMA). This PGMs embedding curcumin at a relative low dosage were demonstrated to promote the proliferation and chondrogenic differentiation of mesenchymal stem cells *in vitro*. More importantly, the PGMs were shown to attenuate the inflammatory response of chondrocytes under IL-1β stimulation. Lastly, the *in vivo* application of the injectable PGMs significantly promoted the repair of large-sized cartilage injury. These results confirmed that curcumin-loaded PGMs can not only enhance the chondroprotective efficacy under inflammatory conditions but also induce efficient cartilage regeneration. This study provides an advanced strategy with anti-inflammatory and pro-regenerative dual-role therapeutic for treatment of extensive cartilage injuries.

KEYWORDS

Osteoarthritis, PEG-GelMA hydrogel microgel (PGMs), Chondrogenic differentiation, Inflammatory response, Cartilage regeneration

Introduction

Osteoarthritis (OA), which is defined by articular cartilage injuries with varying degrees, is one of the most common joint diseases worldwide (Gross et al., 2011; Chubinskaya et al., 2015). Currently, there is a lack of effective treatments for OA in clinic, and the regeneration of articular cartilage is still challenging. For patients with mild degeneration in the early stage, conservative treatments with non-steroid anti-inflammatory drugs, hyaluronic acid, and platelet-rich plasma

are commonly used (Belk et al., 2021). These approaches alleviated local pathological symptoms, but cannot prevent the persistent degeneration of articular cartilage. For those irreversible degeneration and extensive destruction of articular cartilage, total joint replacement is mainly used to achieve joint structure and function restoration. However, the commonly used artificial joints based on metals and ceramics are not only with limited biological functions, but also can easily lead to infection and foreign body rejection (Veiseh and Vegas, 2019). Risks such as long-term wear and tear, and prosthesis loosening often end up with secondary surgery (Munuera Martinez, 2010).

The structural and functional reconstruction of articular cartilage based on tissue engineering technologies have shown promising future for the treatment of osteoarthritic cartilage injury. Stem cell transplantation, autologous chondrocyte transplantation, microfracture and mosaic surgery provide options for the repair of cartilage defects (Makris et al., 2015). Microfracture surgery mainly relies on bone marrow mesenchymal stem cells derived from subchondral bone to regenerate fibrocartilage-like tissue, but it is limited to small cartilage defects, and the long-term effect is not satisfactory. Autologous chondrocyte transplantation or mosaic surgery could cause additional trauma to the donor area. With a limited tissue source, the tissue integration of the transplanted cartilage and the surrounding normal tissue is poor (Kwon et al., 2019). For the patients with large cartilage defects in the moderate or late stages, there are still obvious gaps and difficulties between effective interventions and severe cartilage injuries. More importantly, in late stage OA, the chronic inflammation caused by inflammatory factors and mediators increases the extracellular matrix (ECM) degradation and impedes the further cartilage repair (Shu et al., 2020).

Curcumin, which is a natural polyphenolic compound that extracted from the turmeric, shows multiple of pharmacological activities (Alok et al., 2015). Curcumin is known for the anti-inflammation efficacy, and recently was extensively studied for the treatment of rheumatoid arthritis (Zheng et al., 2015), post-traumatic osteoarthritis (Zhang et al., 2016a), and other chronic inflammation (He et al., 2015). Therefore, these studies together suggest a promising anti-inflammatory drug for the treatment of osteoarthritic cartilage injuries. However, owing to its poor systemic bioavailability as a result of low solubility in aqueous solution, the therapeutic efficacy and translational applications of curcumin are largely impeded (Lopresti, 2018). Although nano-emulsions or nanoparticles for curcumin delivery have been developed to increase oral bioavailability, metabolic preservation (Young et al., 2014a; Dende et al., 2017), and sustained local-release (Zhang et al., 2016a), the *in vivo* pharmacokinetic and toxicology are still needed to be investigated.

Due to the irregular-shaped and large-sized defects on joint cartilage surface in late-stage of OA (Zhang et al., 2016b; Shi et al., 2017), the injury-site targeted delivery of curcumin for effective repair is still challenging. Besides, the severe degenerative microenvironments are along with a sharp decrease in endogenous reserves of stem cell numbers (Ambrosi et al., 2021) and bioactive factors (Zhang et al., 2022) for efficient cartilage repair and subchondral bone formation. While several studies suggest the implantation of scaffold materials to guide matrix synthesis or combined with growth factors to promote cartilage regeneration (Makris et al., 2015; Liu et al., 2021), high risks of infection and poor tissue integration remained to be elucidated. Novel strategies using growth factor- or cell-loaded microgel (Li et al., 2017; Lei et al., 2021) were shown as effective treatments for osteoarthritic cartilage damage through enhanced recruitment of endogenous stem cells, as well as increased nutrient, metabolite exchange, and more dynamic cell-cell and cell-material interactions (Nguyen et al., 2021). Thus, the above studies suggest that hydrogel microsphere or microgel served as a bioactive drug delivery system shows promising therapeutic approach for cartilage tissue engineering (Castro et al., 2020). Nevertheless, the treatment for OA is still challenge by the co-existence of chronic inflammation and cartilage degeneration.

In this study, we aim to determine the dual role of injectable curcumin-embedded PEG-GelMA hydrogel microgels (PGMs) on the chondroprotective efficacy under inflammatory conditions in OA progression and efficient cartilage regeneration for late-stage degeneration. Our findings showed that the curcumin-loaded PGMs at a relative low dosage was demonstrated to promote chondrogenic differentiation of mesenchymal stem cells, as well as the attenuation for inflammatory response of chondrocytes under IL-1β stimulation. In addition, the *in vivo* application of the injectable PGMs significantly enhanced the repair of large-sized cartilage injury.

Results

Microfluidic polymerization produces the curcumin-embedded PEG-GelMA microgels

The curcumin-loaded PEG-GelMA microgels (PGMs) were fabricated by microfluidic technology and exhibited a mean diameter of 218 ± 5.25 μm (Figure 1A). From the microscopic images, we can find that the spheroids-like PGMs are highly uniform in size (Figure 1B). Previous studies have shown that the addition of GelMA to PEG increased the compressive modulus of composite hydrogels as compared to PEG alone (Hutson et al., 2011; Gao et al., 2015). In this study, the encapsulation of curcumin did not significantly affect the compressive modulus of the hydrogel microgels, as the modulus of PGMs and curcumin-loaded PGMs is about 33.396 ± 2.468 kPa and 35.513 ± 2.033 kPa, respectively (Figure 1C). These data confirmed that the compressive modulus of pure PEG hydrogels were elevated after the addition of GelMA. In addition, the PEG-

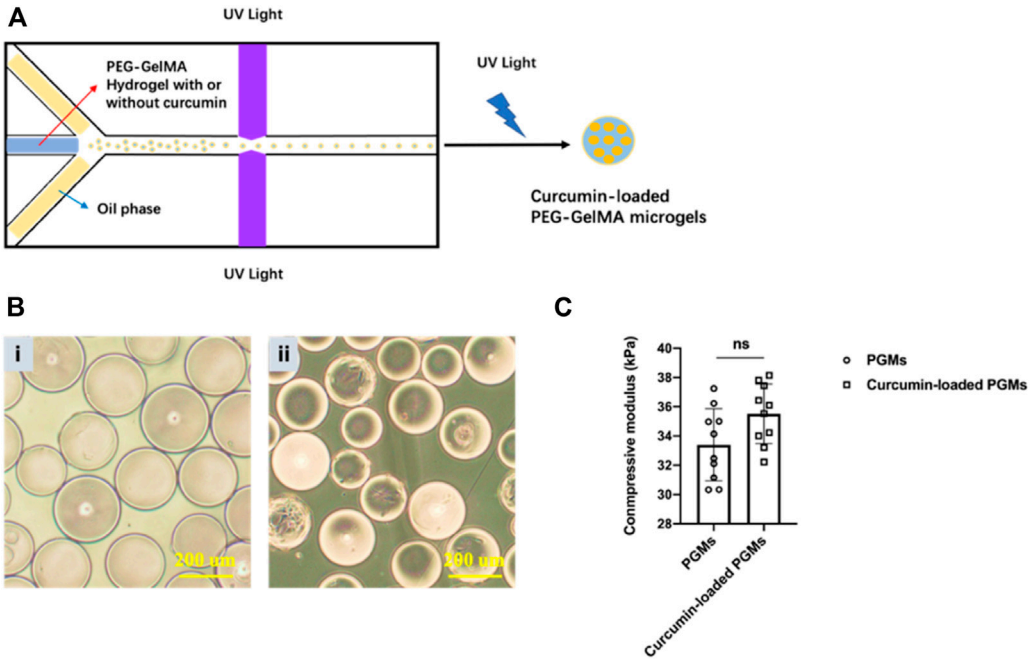

FIGURE 1
Curcumin-loaded PEG-GelMA microgel (PGMs) synthesis and characterization. **(A)** Schematic illustration of PEG-GelMA microgel fabrication by microfluidic technology. **(B)** The microscopic images at bright field of PGMs (i) and curcumin-loaded PGMs (ii), Scale bar = 200 μm. **(C)** The compressive modulus of PGMs and curcumin-loaded PGMs, respectively. *N* = 10 PGMs.

GelMA microgel itself provides a comparable elastic modulus as the native articular cartilage (Beck et al., 2016).

Curcumin-loaded PEG-GelMA hydrogel microgels enhanced the cell proliferation and chondrogenic differentiation potential of stem cells *in vitro*

To evaluate the cell biocompatibility of curcumin-loaded PGMs, ADSCs (Adipose-derived Mesenchymal Stem Cells) were seeded on the surface of these well-prepared PGMs for the *in vitro* culture (Figure 2A). After 1, 3, 5, and 7 days of cell expansion, live/dead staining was performed to analysis the live cell proportion across the varied time points. While dead cells were hardly detected during the culture time for 7 days, the live cells (green color-labelled) showed stable and gradually increased cell numbers (Figure 2B). To further investigate the differences on cell viability and proliferation between PGMs and the curcumin-loaded PGMs, CCK-8 assay was carried out to compare the two groups. Results of the OD values during the 7 days' culture showed that there is no significant difference on cell proliferation at day 1 and day 3 after cell seeding, when a mild decrease of cell proliferation was found at later time points, including day 5 and day 7 (Figure 2C). These results indicate that the curcumin-loaded PGMs are available for the *in vitro* culture and normal cell proliferation, and curcumin encapsulation by PGMSs itself help maintain the cell viability.

We next characterized the effect of curcumin-loaded PGMs on the chondrogenic potential of mesenchymal stem cells. Human adipose-derived mesenchymal stem cells (ADSCs) were cultured either on the PGMs or curcumin-loaded PGMs system for pre-expansion for 1 week, and the differentiation capability was further tested and analyzed by tri-lineage differentiation assays (Figure 3A). After another 21 days of lineage-specific induction, various staining assays were performed for the estimation of osteogenesis, chondrogenesis, and adipogenesis, respectively. Results showed that the osteo- and chondral-lineage differentiation was improved in the curcumin-loaded PGMs group compared with the PGMs only group, while the adipogenesis didn't show any significant difference between the two groups (Figure 3B). Besides, the immunostaining of collagen II expression, a chondrogenic marker, exhibited a much higher ratio of positive expression cells in the curcumin-loaded PGMs compared with pure PGMs (Figure 3C). Consistent with the immunostaining results, the relative mRNA expression of chondrogenic marker genes (COL2A1, SOX9, Aggrecan) was also shown greatly improved by the curcumin (Figure 3D). Collectively, the curcumin-loaded PGMs showed a good biocompatibility and cell viability, and favorable effects on promoting the chondrogenic differentiation. The above results indicated that the curcumin-loaded PGMs as bioactive microcarriers for enhanced stem cell

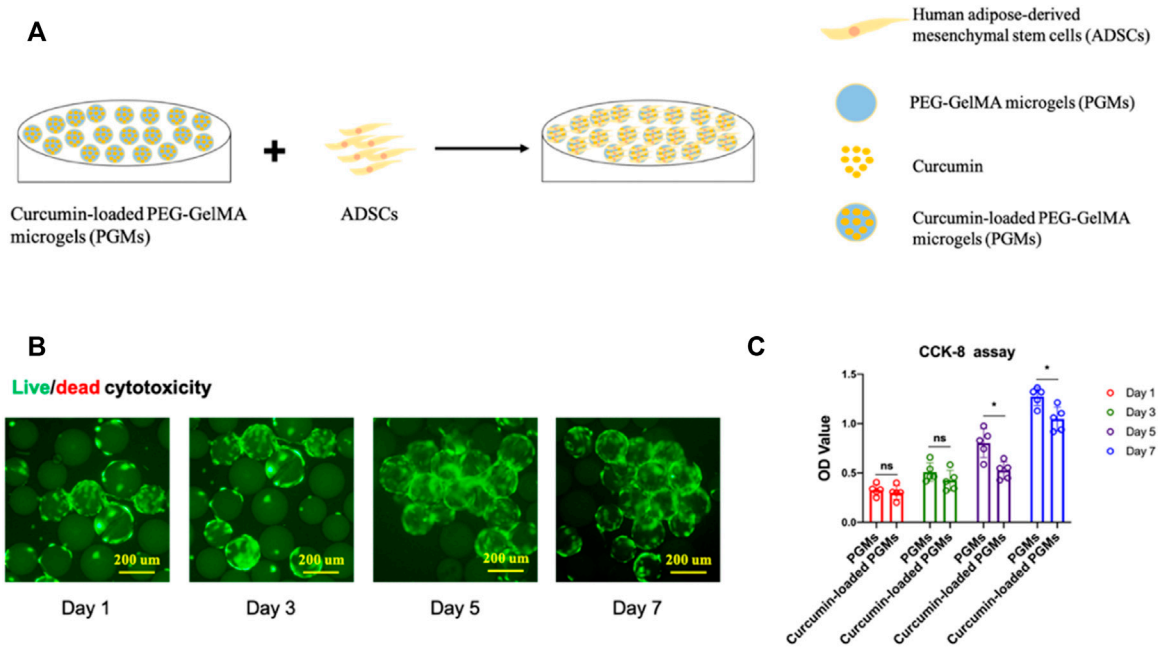

FIGURE 2
Cyto-biocompatibility and cell viability of curcumin-loaded PEG-GelMA microgel (PGMs). **(A)** Schematic of ADSCs seeding on the curcumin-loaded PEG-GelMA microgel (PGMs) for *in vitro* culture. **(B)** The Live/dead staining of ADSCs cultured on the curcumin (5 uM)-loaded PGMs, Scale bar = 200 μm. **(C)** Quantification of cell viability of ADSCs cultured on the PGMs and curcumin-loaded PGMs, respectively. Biological replicates $n = 5$.

growth hold great potential for efficient *in vivo* cartilage injury regeneration by promoting chondrogenic differentiation of joint-resident stem cells.

Curcumin-loaded PEG-GelMA hydrogel microgels alleviate the inflammatory effects of chondrocytes

To better explore the potential of curcumin-loaded PGMs against the chronic microenvironment during the osteoarthritis progression, we thus tested the anti-inflammatory effects of the curcumin-loaded PGMs on the *in vitro* cultured chondrocytes (Figure 4A). After 72 h of culture on the curcumin-loaded PGMs, the chondrocytes were subsequently treated with IL-1β for another 48 h. Interestingly, chondrocytes that cultured on the curcumin-loaded PGMs system showed apparent cell-cell contact as well as significantly fewer black spots, indicating that the loaded curcumin alleviated the cell apoptosis in respond to the IL-1β stimulation (Figure 4B).

The gene expression levels of chondrocyte phenotypic markers and inflammatory factors of chondrocytes were then detected by qRT-PCR assays. The results showed that the relative expression level of chondrocyte marker genes COL2A1, SOX9, and Aggrecan was significantly maintained in the curcumin-loaded PGMs group (Figure 4C), while the inflammation-related genes MMP13 and ADAMTS5 were significantly decreased (Figure 4D). At protein level, the Collagen II expression of chondrocytes was also found greatly increased after IL-1β stimulation in the curcumin-loaded PGMs culture system (Figure 4E). Taken together, the injectable curcumin-loaded PGMs system could not only maintain chondrocyte phenotype, but also ameliorate the local inflammatory state and matrix degeneration of the injured cartilage.

In vivo application of Curcumin-loaded PEG-GelMA hydrogel microgels promoted the regeneration of large-sized cartilage defects

To investigate the dual role of chondroprotective efficacy under inflammatory conditions and promoting efficient cartilage regeneration when utilizing the curcumin-loaded PGMs, we performed a cartilage defect animal experiment for *in vivo* assessment. A circular defect with a 5 mm diameter was created at the femoro-patellar grooves in rabbits, and the cell-free curcumin-loaded PGMs were implanted into the defect area, while pure PGMs were also transplanted as vehicle control (Figure 5A).

Eight weeks after the surgery, the tissue samples from the defect regions were collected and analyzed. Safranin-O staining results of the tissue sections among different groups showed that the curcumin-loaded PGMs significantly improved the regeneration of injured cartilage compared with both the vehicle PGMs and the blank

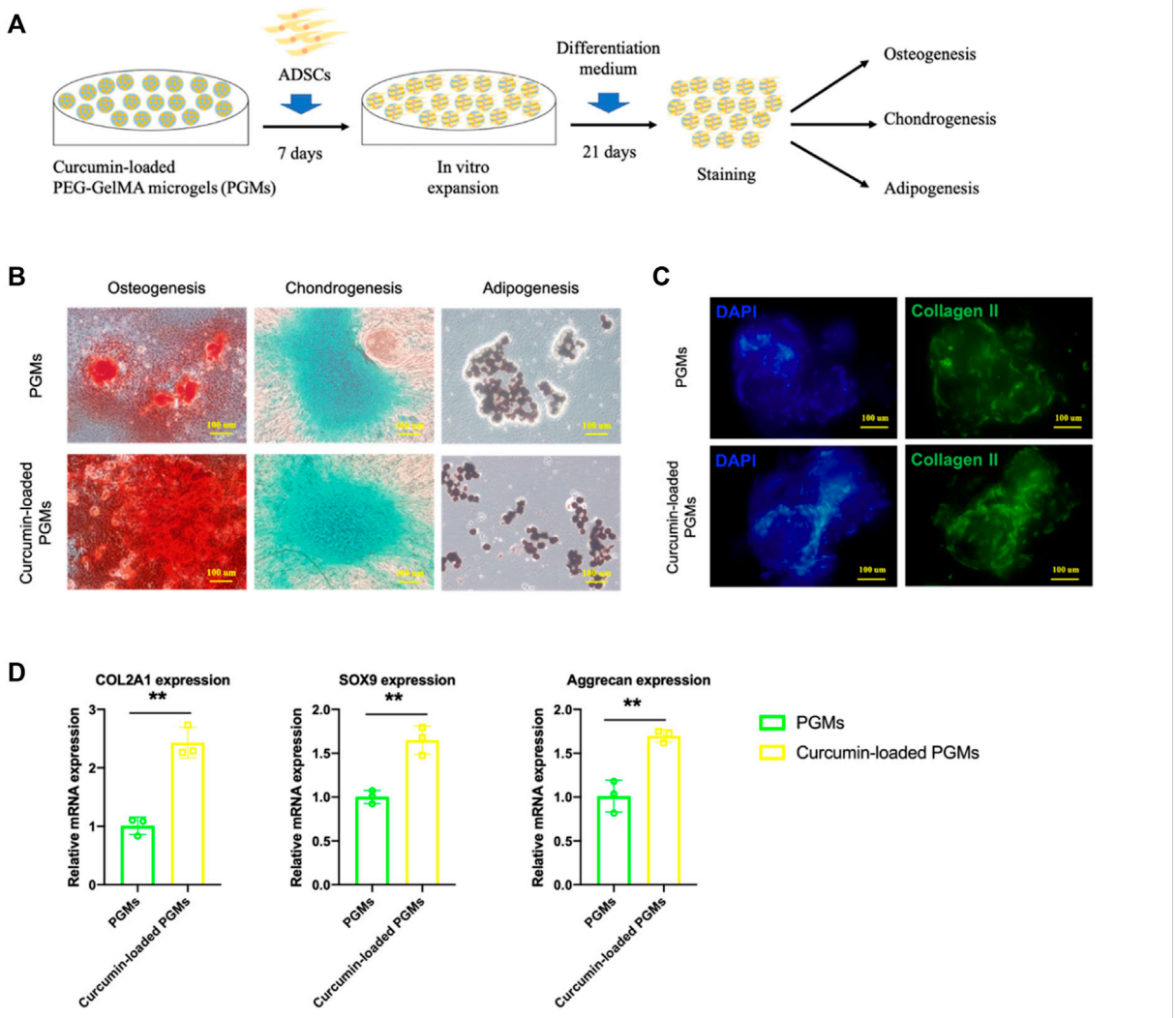

FIGURE 3
The chondrogenic bioactivity on ADSCs of curcumin-loaded PEG-GelMA microgel (PGMs). **(A)** Schematic of ADSCs culture on the curcumin-loaded PEG-GelMA microgel (PGMs) and further tri-lineage differentiation. **(B)** The level of osteogenesis, chondrogenesis, and adipogenesis of ADSCs was assessed by ARS staining, Alcian blue staining, and Oil Red staining, respectively. Scale bar = 100 μm. **(C)** Immunostaining of Collagen II protein expression in ADSCs cultured on the PGMs and curcumin (5 uM) -loaded PGMs, respectively. Scale bar = 100 μm. **(D)** Relative expression of chondrogenic marker genes (COL2A1, SOX9, Aggrecan) after chondrogenic induction for 21 days (Mean ± SD; $^{**}p < 0.01$; biological replicates $n = 3$ per group).

defect (Figure 5B). Further histological assessment of chondrocyte apoptosis and cartilage erosion that resulted from chronic inflammation showed a relatively lower level in response to the treatment of the curcumin-loaded PGMs, when compared to other groups (Figure 5C). Further immunohistochemical staining analysis on the expression of Collagen II, which is the hall-marker of chondrogenic differentiation, showed that the cartilage regeneration was enhanced by the curcumin-loaded PGMs (Figure 5D). The above results indicate that the injectable curcumin-loaded PGMs can effectively promote the cartilage regeneration either by the increased chondrogenic differentiation or the decreased level of local inflammation during the pathological degeneration.

Discussion

Osteoarthritis (OA) is featured for co-existence of chronic inflammation and cartilage degeneration, and current treatments targeting either aspect are difficult for covering the complex conditions at the same time (Lieberthal et al., 2015). In the middle and late stages of OA progression, neither anti-inflammatory drugs

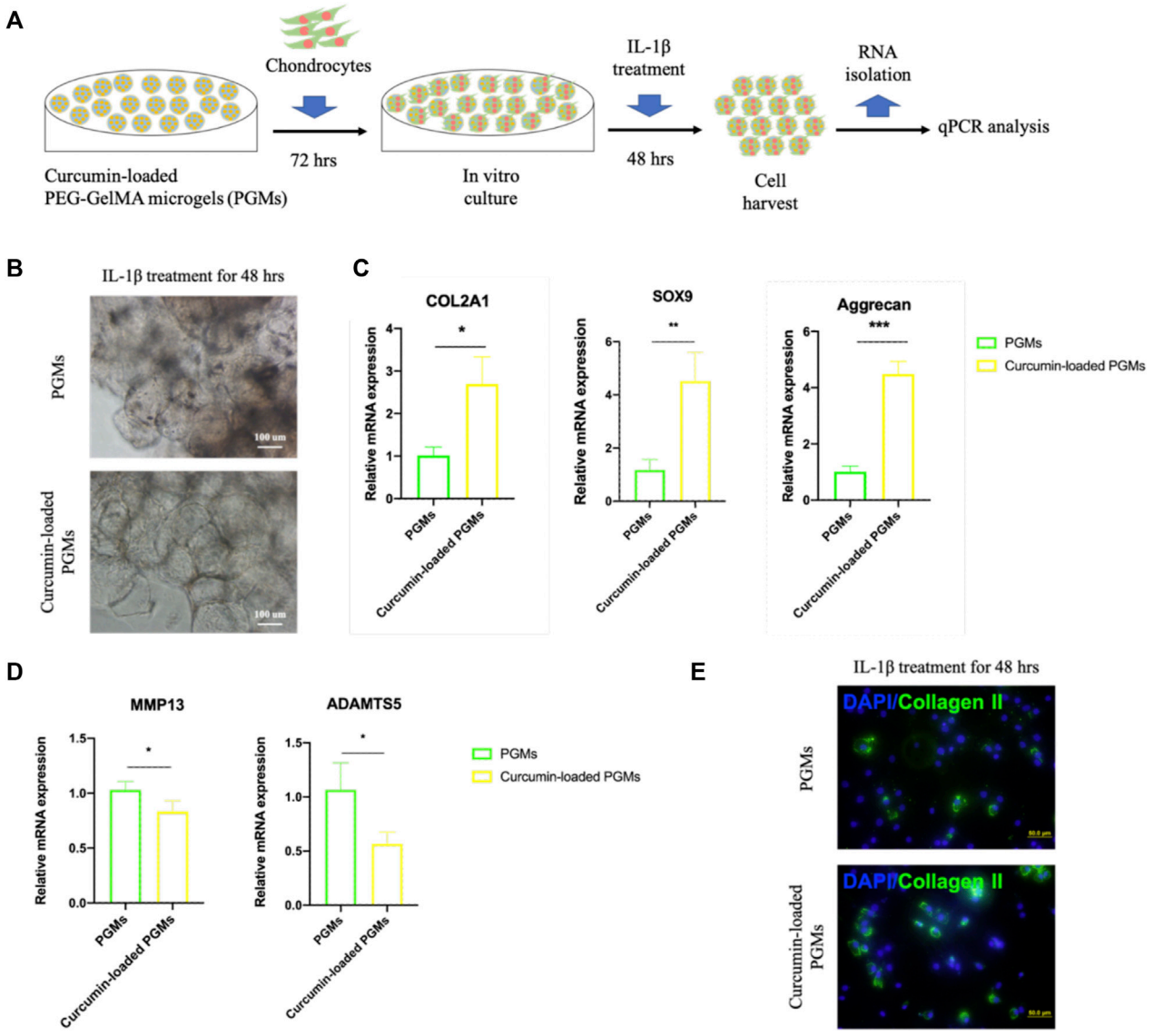

FIGURE 4
The amelioration of chondrocyte inflammation with curcumin-loaded PEG-GelMA microgel (PGMs). **(A)** Schematic of human chondrocytes cultured on the curcumin-loaded PEG-GelMA microgel (PGMs) for *in vitro* culture and further IL-1β stimulation (10 ng/ml). **(B)** The bright-field images of cultured chondrocytes after IL-1β treatment in the PGMs and curcumin (5 μM)-loaded PGMs groups, respectively. Scale bar = 100 μm. **(C)** Quantification of the expression of phenotypic genes (COL2A1, SOX9, Aggrecan) for chondrocytes, and **(D)** Quantification of the expression of inflammatory genes (MMP13, ADAMTS5) for chondrocytes. (Mean ± SD; $*p < 0.05$, $**p < 0.01$; $***p < 0.001$; biological replicates $n = 4$ per group). **(E)** Immunostaining of Collagen II protein expression of the chondrocytes (sub-cultured on cover slip for 2 days) after IL-1β treatment in the PGMs and curcumin-loaded PGMs, respectively. Scale bar = 50 μm.

nor small molecules that targeting specific molecular target alone cannot fully alleviate the pathological symptoms and prevent the progressive degeneration (An et al., 2021). This study illustrates a therapeutic strategy of the injectable curcumin-loaded PGMs with a dual role of promoting the chondroprotective efficacy under inflammatory conditions and inducing endogenous cartilage regeneration simultaneously.

The chronic inflammation during the OA development is still one of the most difficulties for the clinical treatment. Current pharmacological treatments provide symptomatic relief to joint pain and local inflammation, however, there is not a clear clinical effect on OA disease prevention or therapy. While most of the current efforts have been focused on developing novel molecular targets as well as their disease-modifying drugs, the

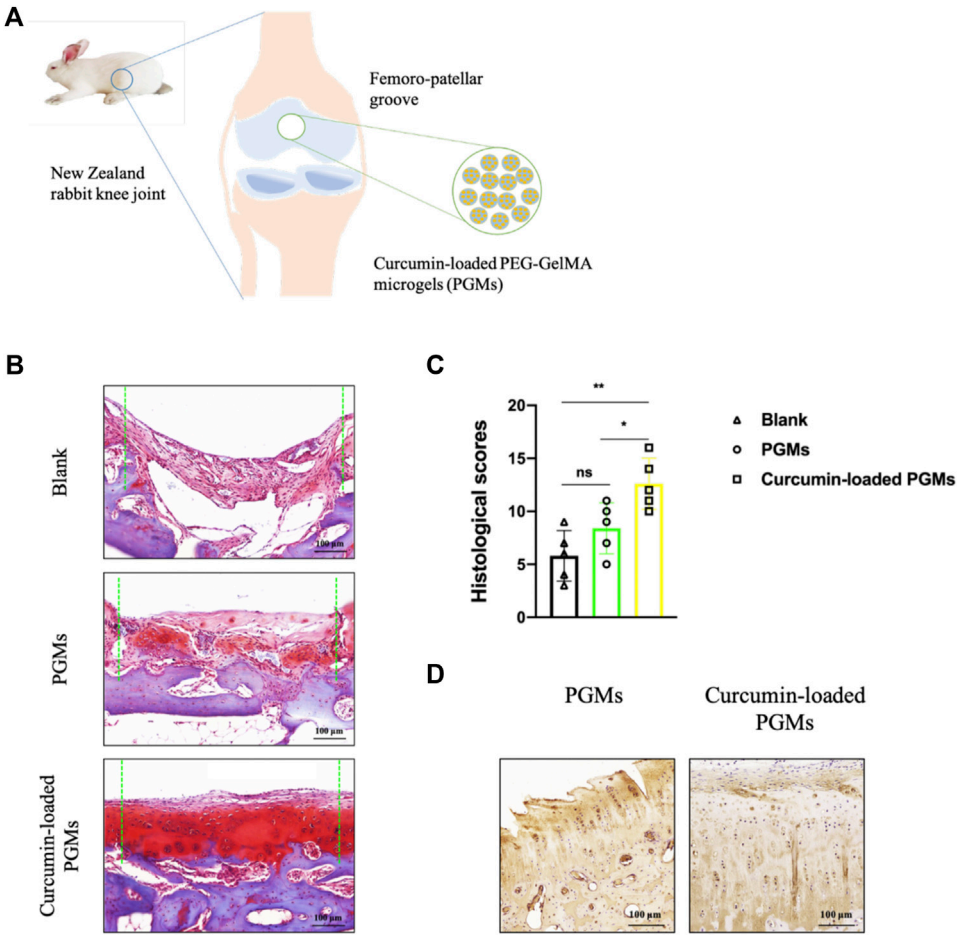

FIGURE 5
The amelioration of chondrocyte inflammation with curcumin-loaded PEG-GelMA microgel (PGMs). **(A)** Schematic of the implantation of curcumin-loaded PGMs for the repair of cartilage defects in a rabbit femoro-patellar groove. **(B)** The Safranin-O staining of the repaired cartilage tissues in Blank, PGMs and curcumin-loaded PGMs groups at 8 weeks post-surgery. Scale bar = 100 μm. **(C)** Quantification of the histological scores of cartilages under evaluation among Blank, PGMs and curcumin-loaded PGMs groups in Safranin-O staining results. (Mean ± SD; $*p < 0.05$, $**p < 0.01$; $n = 5$ per group). **(D)** The immunohistochemical staining of Collagen II in the repaired cartilage between PGMs and curcumin-loaded PGMs groups at 8 weeks post-surgery. Scale bar = 100 μm.

side-effects exist regarding the non-tissue-specific and long-term use of these treatments (Yang et al., 2021). Curcumin has been shown to mitigate the inflammatory process by decreasing the synthesis of inflammatory mediators such as interleukin (IL)-1β, tumor necrosis factor (TNF)-α, IL-6, IL-8, prostaglandin E2 (PGE2), and cyclooxygenase-2 (COX-2) (Zhang et al., 2016a; Sun et al., 2017; Sundar Dhilip Kumar et al., 2018). Moreover, curcumin suppresses the gene expression of matrix metalloproteinases (MMPs) (Zhang et al., 2016a; Mogharrabi et al., 2020) and nuclear factor kappa B (NF-kB) activation (Buhrmann et al., 2021), which play critical roles in the breakdown of the cartilage ECM. Due to the extremely limited oral bioavailability of curcumin (Ma et al., 2019), local application could provide effective delivery and absorption in treatment. More specifically, the bioavailability of curcumin at the disease site for OA treatment could be greatly enhanced by using injectable drug-delivery systems (Tiwari et al., 2017).

Nano-emulsion and nanoparticles were often taken as the promising approach for controlled release of curcumin in multiple situations (Young et al., 2014b; Zheng et al., 2015; Zhang et al., 2016a; Shi et al., 2016; Dende et al., 2017). However, the therapeutic effects are often impeded by the random distribution and extensive diffusion of drugs across the knee joint tissues. Surprisingly, the long-term toxicity profile of local distribution (Saifi et al., 2018) as well as the body wide non-targeting infiltration (Mohammadpour et al., 2019; Wu et al., 2019) of nanoparticles are still one of the most important concerns when drug-loaded nano-emusions or nanoparticles were intraarticularly injected. On the contrary, hydrogels spheroids at micro-scale were

TABLE 1 Primers used in the qRT-PCR assay.

Gene	Forward (5–3′)	Reverse (5–3′)
GAPDH	GGCAAGTTCAACGGCACAG	CGCCAGTAGACTCCACGACAT
SOX9	CTGACCGTGACCGTAGCAAGT	TGGATGTGGGCTTTGGACTCA
COL2A1	GTCTGTGACACTGGGACTGT	TCTCCGAAGGGGATCTCAGG
Aggrecan	CTGCAGACCAGGAGGTATGTGA	GTTGGGGCGCCAGTTCTCAAAT
MMP13	ATGCAGTCTTTCTTCGGCTTAG	ATGCCATCGTGAAGTCTGGT
ADAMTS5	ATCAC-CCAATGCCAAGG	AGCAGAGTAGGAGACAAC

proven to be more available for the direct release of cells, growth factors and drugs (Annamalai et al., 2019; Volpatti et al., 2021), and could provide as a dense barrier for inflammatory erosion and chondrocyte apoptosis (Wei et al., 2021; Han et al., 2022).

Actually, hydrophilic microgels have been used as microcarriers for *in vitro* cell culture and *in vivo* stem cell delivery system, both the long-term cell survival and microtissue formation were shown promising when applied *in vivo* (Luo et al., 2019). Furthermore, the delayed degradation of microgels and their enough surface for further resident adipose-derived stem cell proliferation are more important for the cartilage regeneration regarding the flexible intra-articular microenvironment. In our study, the curcumin-loaded PGMs not only filled up the irregular cartilage injury, but also enhanced the joint lubrication and provided enough surface for efficient endogenous stem cell migration and adhesion. These results together suggested that the curcumin-loaded PGMs system in this study better promotes the new cartilage formation when reduces the inflammatory effects by local delivery of curcumin at a low dosage and at the same time.

The injectability of the curcumin-loaded PGMs system in this study is another advantage for promising minimal-invasive application in OA treatment. Provided with the availability for application in response to the irregular-shaped and large-sized defects on joint cartilage surface in inflammatory OA, the *in vivo* delivery of anti-inflammatory drugs by PGMs is an alternative strategy for late-staged OA treatment. Even though, further investigations are still needed to clarify the main stem cell resources and subtypes, as well as their detailed contribution for the regeneration process of inflammatory cartilage injuries.

Conclusion

In summary, the curcumin-loaded PGMs at a relative low dosage was demonstrated to promote the proliferation and chondrogenic differentiation of mesenchymal stem cells *in vitro*. More importantly, the curcumin-loaded PGMs was shown to attenuate the inflammatory response of chondrocytes under IL-1β stimulation. Lastly, the *in vivo* application of the injectable PGMs significantly enhanced the repair of large-sized cartilage injury. These results suggest that the curcumin-loaded PGMs play a dual role in OA treatment by promoting the chondroprotective efficacy under inflammatory conditions and inducing efficient cartilage regeneration.

Materials and methods

Preparation of curcumin-loaded PEG-GelMA hydrogel microgels

The poly(ethylene glycol) dimethacrylate (PEGDMA, PEG)-gelatin methacrylate (GelMA) microgels were synthesized using microfluidic device as described in previous studies with minor modifications (Hutson et al., 2011; Gao et al., 2015). Briefly, curcumin powder (Sigma-Aldrich) was dissolved in 10 ml PEGDMA by stirring with a magnetic bar and heating in a boiling water bath to 100°C for 15 min until completely dissolved. After cooling, the curcumin-contained PEGDMA and GelMA were mixed together in PBS at 10% (w/v) and 5% (w/v), respectively (curcumin at a final concentration of 5 μM), in which PEGDMA did not contain curcumin was treated as vehicle control in the following experimental analysis. The aqueous phase was composed of PEG-GelMA hydrogel and 30 mg/ml photo-initiator 2-hydroxy-1 (4-(hydroxyethox)pheny)-2-methyl-1-propanone, and the continuous oil phase contained mineral oil. After starting the pumps, the aqueous and continuous phases were slowly injected into the syringes and the flow rate of the liquid in the channel is adjusted through injection pumps. Microgels were synthesized using PDMS flow-focusing devices and washed 3 times with a 1% BSA solution in PBS. The prepared hydrogel droplets were further solidified by photocrosslinking for 30 s under UV irradiation at the wavelength of 365 nm (6.9 mW/cm^2) wavelength. Lastly, the oil and active agent on the surface of PEG-GelMA microgels were removed by repeated washing with acetone and 75% ethanol, and purified by washing with PBS for 24 h. Size distribution of the microgels was determined *via* microscopy image analysis using ImageJ.

Mechanical testing

Samples were detached from the culture dish and incubated in PBS at room temperature. The mechanical test was performed with nano-indentation (Optics) according to the manufacturer's protocol.

The compressive modulus was determined as the slope of the linear region corresponding with 0%–10% strain.

Cell culture

Human adipose-derived mesenchymal stem cells (ADSCs) were obtained after digesting adipose tissues acquired from donors (68 years old) with written informed consent. In brief, fat pad pieces (1–2 mm^3) were digested with collagenase (Sigma-Aldrich) at 37°C for 2 h. The isolated cells were cultured in L-DMEM (Gibco) with 10% fetal bovine serum and 1% penicillin/streptomycin (Life Technologies) at 37°C and 5% CO2. The medium was changed every 3 days, and cells at passage 5 were used in this study.

Primary chondrocytes were obtained from patients undergoing total joint replacement surgery (aged 68–81 years) were cultured in F12 with 10% fetal bovine serum and 1% penicillin/streptomycin. F12 with 1% fetal bovine serum overnight were used for starvation prior to curcumin treatment. Chondrocytes were incubated with IL-1β (10 ng/ml, Sigma) for 48 h after incubation with curcumin-contained medium for 72 h (Zhang et al., 2016a). Cells were then lysed and RNA isolated for further analysis.

Cell live/dead staining

ADSCs that co-cultured with PEG-GelMA hydrogel microgels (PGMs) was tested by live/dead cytotoxicity kit. The ADSCs were co-cultured with PGMs at a density of 4×10^5 cells/mL. Then, the ADSC/PGMs suspension was mixed and seeded in a 24-well plate, and cultured in humidified incubator containing 5% CO_2 at 37°C. After culturing for 1, 3, 5, and 7 days, cells were stained with the live/dead cytotoxicity kit and imaged with a confocal laser scanning microscope (OLYMPUS IX83-FV1000).

Cell viability

ADSCs between passages 3–5 were cultured with PGMs at a density of 1×10^4 cells/disc in a 96-well plate. 33 μl medium containing microgel was added to each well, and then added complete medium to 200 μl. The proliferation of ADSCs were evaluated by the Cell Counting Kit-8 (CCK-8) testing. At 1, 3, 5, and 7 days, the medium was replaced with 180 μl of fresh complete medium and 20 μl of CCK-8 reagent (Dojindo, Japan) each well and incubated for 2 h at 37°C with 5% CO_2. Finally, the staining solution was collected and measured using a multi-plate reader at 450 nm.

Quantitative real-time PCR

Quantitative real-time PCR was carried out on 5 days to evaluate the expression of chondrogenic marker genes (SOX9, MMP13, and ADAMTS5) in cells co-cultured with PGMs and curcumin-loaded PGMs. Quantitative real-time PCR was performed with SYBR® Premix Ex Taq™ (Takara) using a ABI 7500 Sequencing Detection System (Applied Biosystems, Foster City, United States). GAPDH was used as a house-keeping. Data were analyzed using the comparison Ct ($2^{-\Delta\Delta Ct}$) method and expressed as fold changes compared to the control.

The sequences of the primers used are listed in Table 1.

Trilineage differentiation assays

For osteogenesis, the cells were cultured in osteogenic medium containing α-DMEM with 10% FBS supplemented with 0.1 μM dexamethasone, 0.2 mM L-ascorbic acid, and 10 mM glycerol 2-phosphate disodium salt hydrate. The medium was changed every 2 days. For chondrogenesis, the cells were resuspended at a concentration of 5×10^5 cells in 200 μl of growth media and plated as micro-mass. After 2 h at 37°C, the micro-mass were covered with chondrogenic medium containing DMEM with 10% FBS supplemented with 0.1 μM dexamethasone, 100 μg/ml sodium pyruvate, 40 μg/ml L-proline, 50 μg/ml L-ascorbic acid, 50 mg/ml ITS, and 10 ng/ml TGFβ1. The medium was changed every 2 days for 21 days. For adipogenesis, the confluent cells were cultured with adipogenic medium containing α-DMEM with 10% FBS supplemented with 10 μg/ml insulin, 100 μM indomethacin, 0.5 mM 3-iso- butyl-1-methylxanthine, and 0.1 μM dexamethasone. The medium was changed every 2 days.

Immunofluorescent staining

Cells cultured on PGMs system or cover slips were fixed with 4% paraformaldehyde (PFA) for 30 min and then permeabilized with 0.01% Triton X-100 for 10 min at room temperature. After washed with PBS for 3 times, cells were blocked with 1% bovine serum albumin for 1 h at room temperature. The primary antibody (Anti-Collagen II antibody, diluted 200-fold, ab34712, Abcam) was incubated at 4°C overnight. Cells were next incubated with secondary antibody (diluted 200-fold, G-Rabbit Alexa Fluor® 488, A11008; Invitrogen) for 1 h at room temperature. After incubation, the nuclei were lastly stained with 1 X DAPI. After staining, the cells were observed using a confocal microscope (OLYMPUS IX83-FV1000).

For alizarin red staining

Cells were washed with cold PBS and fixed with 4% PFA for 30 min on ice. Cells were washed with distilled water and stained with 2% alizarin red solution for 15 min. Cells were then washed thoroughly with distilled water and air dried before microscopic observation.

Alcian blue staining

After culture medium was removed, and cells were washed with PBS and fixed with 4% PFA for 30 min. Cells were stained for 30 min with 1% Alcian Blue solution 8GX (Sigma) in 3% acetic acid, pH 2.5, and washed three times with 0.1 N HCl and then washed three times with PBS.

Oil red staining

After culture medium was removed, and cells were washed with PBS and fixed with 4% PFA for 30 min at room temperature. Cells were rinsed again with PBS and stained for 30 min with Oil Red O working solution. Cells were then observed under a light microscope after three times of washes with PBS.

Animal experiments

All animals were treated according to standard guidelines approved by the Zhejiang University Ethics Committee (NO. ZJU20220320). Adult New Zealand white rabbits (3 kg, Male, 15 rabbits, 10 weeks old) were used in this study. All surgeries were performed under general anesthesia. The knee joint was opened with medial para-patellar approach. The patella was dislocated laterally and the surface of the femoro-patellar groove was exposed. Cartilage defects were created using a custom-made scalpel with a thickness of 2 mm. PGMs and curcumin-loaded PGMs were applied to the surface of the cartilage defects, separately (n = 5 rabbits in each group). The non-treated blank (n = 5 rabbits) was treated as control group. 8 weeks after surgery, animals were sacrificed and the joint cartilage samples were harvested for further analysis.

Histological analysis

Tissue samples were fixed in 4% paraformaldehyde and decalcified in 10% EDTA for 4 weeks. Paraffin sections were stained with Safranin-O staining and histological observations were performed under a light microscope. The repaired cartilage tissue was graded by an established histological scoring system, according to a modified O'Driscoll histology scoring (MODS) system (Kleemann et al., 2005).

Statistical analysis

The data of this study were averaged ±standard deviation (SD) of statistical data using SPSS software. At least three parallel samples (n = 3) were set for all experiments. Comparison between the two groups was analyzed by the independent t test, and $p < 0.05$ was considered statistically significant. * indicates $p < 0.05$, ** indicates $p < 0.01$, ***$p < 0.001$.

Data availability statement

The raw data supporting the conclusion of this article will be made available by the authors, without undue reservation.

Ethics statement

The studies involving human participants were reviewed and approved by Zhejiang University Ethics Committee. The patients/participants provided their written informed consent to participate in this study. All animals were treated according to standard guidelines approved by the Zhejiang University Ethics Committee (NO.20220320).

Author contributions

QS, BS, and ZQ contributed to the experimental concept and designed the research. QS and WY are responsible for the manuscript writing and data analysis. WY and CL prepared the materials; QS and WY contributed to all the cell experiment and data analysis; and QS and XR contributed to the animal experiment and histological analysis.

Funding

This study was supported by the Zhejiang Medical and Health Science and Technology Project (2022B12; 2017ZB003).

Conflict of interest

The authors declare that the research was conducted in the absence of any commercial or financial relationships that could be construed as a potential conflict of interest.

Publisher's note

All claims expressed in this article are solely those of the authors and do not necessarily represent those of their affiliated organizations, or those of the publisher, the editors and the reviewers. Any product that may be evaluated in this article, or claim that may be made by its manufacturer, is not guaranteed or endorsed by the publisher.

References

Alok, A., Singh, I. D., Singh, S., Kishore, M., and Jha, P. C. (2015). Curcumin - pharmacological actions and its role in oral submucous fibrosis: A review. *J. Clin. Diagn. Res.* 9 (10), ZE01–3. doi:10.7860/JCDR/2015/13857.6552

Ambrosi, T. H., Marecic, O., McArdle, A., Sinha, R., Gulati, G. S., Tong, X. M., et al. (2021). Aged skeletal stem cells generate an inflammatory degenerative niche. *Nature* 597 (7875), 256–262. doi:10.1038/s41586-021-03795-7

An, J. S., Tsuji, K., Onuma, H., Araya, N., Isono, M., Hoshino, T., et al. (2021). Inhibition of fibrotic changes in infrapatellar fat pad alleviates persistent pain and articular cartilage degeneration in monoiodoacetic acid-induced rat arthritis model. *Osteoarthr. Cartil.* 29 (3), 380–388. doi:10.1016/j.joca.2020.12.014

Annamalai, R. T., Hong, X., Schott, N. G., Tiruchinapally, G., Levi, B., and Stegemann, J. P. (2019). Injectable osteogenic microtissues containing mesenchymal stromal cells conformally fill and repair critical-size defects. *Biomaterials* 208, 32–44. doi:10.1016/j.biomaterials.2019.04.001

Beck, E. C., Barragan, M., Tadros, M. H., Gehrke, S. H., and Detamore, M. S. (2016). Approaching the compressive modulus of articular cartilage with a decellularized cartilage-based hydrogel. *Acta Biomater.* 38, 94–105. doi:10.1016/j.actbio.2016.04.019

Belk, J. W., Kraeutler, M. J., Houck, D. A., Goodrich, J. A., Dragoo, J. L., and McCarty, E. C. (2021). Platelet-rich plasma versus hyaluronic acid for knee osteoarthritis: A systematic review and meta-analysis of randomized controlled trials. *Am. J. Sports Med.* 49 (1), 249–260. doi:10.1177/0363546520909397

Buhrmann, C., Brockmueller, A., Mueller, A. L., Shayan, P., and Shakibaei, M. (2021). Curcumin attenuates environment-derived osteoarthritis by Sox9/NF-kB signaling Axis. *Int. J. Mol. Sci.* 22 (14), 7645. doi:10.3390/ijms22147645

Castro, L. M. M., Sequeira, A., Garcia, A. J., and Guldberg, R. E. (2020). Articular cartilage- and synoviocyte-binding poly(ethylene glycol) nanocomposite microgels as intra-articular drug delivery vehicles for the treatment of osteoarthritis. *ACS Biomater. Sci. Eng.* 6 (9), 5084–5095. doi:10.1021/acsbiomaterials.0c00960

Chubinskaya, S., Haudenschild, D., Gasser, S., Stannard, J., Krettek, C., and Borrelli, J., Jr. (2015). Articular cartilage injury and potential remedies. *J. Orthop. Trauma* 29 (12), S47–S52. doi:10.1097/bot.0000000000000462

Dende, C., Meena, J., Nagarajan, P., Nagaraj, V. A., Panda, A. K., and Padmanaban, G. (2017). Nanocurcumin is superior to native curcumin in preventing degenerative changes in Experimental Cerebral Malaria. *Sci. Rep.* 7, 10062. doi:10.1038/s41598-017-10672-9

Gao, G., Schilling, A. F., Hubbell, K., Yonezawa, T., Truong, D., Hong, Y., et al. (2015). Improved properties of bone and cartilage tissue from 3D inkjet-bioprinted human mesenchymal stem cells by simultaneous deposition and photocrosslinking in PEG-GelMA. *Biotechnol. Lett.* 37 (11), 2349–2355. doi:10.1007/s10529-015-1921-2

Gross, K. D., Niu, J. B., Stefanik, J. J., Guermazi, A., Roemer, F., Sharma, L., et al. (2011). Breaking the law of valgus: The surprising and unexplained prevalence of medial patellofemoral cartilage damage. *Arthritis Rheumatism* 63 (10), S634–S635.

Han, Z. Y., Bai, L., Zhou, J., Qian, Y. H., Tang, Y. K., Han, Q. B., et al. (2022). Nanofat functionalized injectable super-lubricating microfluidic microspheres for treatment of osteoarthritis. *Biomaterials* 285, 121545. doi:10.1016/j.biomaterials.2022.121545

He, Y., Yue, Y., Zheng, X., Zhang, K., Chen, S., and Du, Z. (2015). Curcumin, inflammation, and chronic diseases: How are they linked? *Molecules* 20 (5), 9183–9213. doi:10.3390/molecules20059183

Hutson, C. B., Nichol, J. W., Aubin, H., Bae, H., Yamanlar, S., Al-Haque, S., et al. (2011). Synthesis and characterization of tunable poly(ethylene glycol): Gelatin methacrylate composite hydrogels. *Tissue Eng. Part A* 17 (13-14), 1713–1723. doi:10.1089/ten.tea.2010.0666

Kleemann, R. U., Krocker, D., Cedraro, A., Tuischer, J., and Duda, G. N. (2005). Altered cartilage mechanics and histology in knee osteoarthritis: Relation to clinical assessment (ICRS grade). *Osteoarthr. Cartil.* 13 (11), 958–963. doi:10.1016/j.joca.2005.06.008

Kwon, H., Brown, W. E., Lee, C. A., Wang, D. A., Paschos, N., Hu, J. C., et al. (2019). Surgical and tissue engineering strategies for articular cartilage and meniscus repair. *Nat. Rev. Rheumatol.* 15 (9), 550–570. doi:10.1038/s41584-019-0255-1

Lei, Y. T., Wang, Y. P., Shen, J. L., Cai, Z. W., Zeng, Y. S., Zhao, P., et al. (2021). Stem cell-recruiting injectable microgels for repairing osteoarthritis. *Adv. Funct. Mat.* 31 (48), 2105084. doi:10.1002/adfm.202105084

Li, F. Y., Truong, V. X., Thissen, H., Frith, J. E., and Forsythe, J. S. (2017). Microfluidic encapsulation of human mesenchymal stem cells for articular cartilage tissue regeneration. *ACS Appl. Mat. Interfaces* 9 (10), 8589–8601. doi:10.1021/acsami.7b00728

Lieberthal, J., Sambamurthy, N., and Scanzello, C. R. (2015). Inflammation in joint injury and post-traumatic osteoarthritis. *Osteoarthr. Cartil.* 23 (11), 1825–1834. doi:10.1016/j.joca.2015.08.015

Liu, Y. Z., Peng, L. Q., Li, L. L., Huang, C. S., Shi, K. D., Meng, X. B., et al. (2021). 3D-bioprinted BMSC-laden biomimetic multiphasic scaffolds for efficient repair of osteochondral defects in an osteoarthritic rat model. *Biomaterials*, 279, 121216. doi:10.1016/j.biomaterials.2021.121216

Lopresti, A. L. (2018). The problem of curcumin and its bioavailability: Could its gastrointestinal influence contribute to its overall health-enhancing effects? *Adv. Nutr.* 9 (1), 41–50. doi:10.1093/advances/nmx011

Luo, C., Fang, H., Zhou, M., Li, J., Zhang, X., Liu, S., et al. (2019). Biomimetic open porous structured core-shell microtissue with enhanced mechanical properties for bottom-up bone tissue engineering. *Theranostics* 9 (16), 4663–4677. doi:10.7150/thno.34464

Ma, Z., Wang, N., He, H., and Tang, X. (2019). Pharmaceutical strategies of improving oral systemic bioavailability of curcumin for clinical application. *J. Control. Release* 316, 359–380. doi:10.1016/j.jconrel.2019.10.053

Makris, E. A., Gomoll, A. H., Malizos, K. N., Hu, J. C., and Athanasiou, K. A. (2015). Repair and tissue engineering techniques for articular cartilage. *Nat. Rev. Rheumatol.* 11 (1), 21–34. doi:10.1038/nrrheum.2014.157

Mogharrabi, M., Rahimi, H. R., Hasanzadeh, S., Dastani, M., Kazemi-Oskuee, R., Akhlaghi, S., et al. (2020). The effects of nanomicelle of curcumin on the matrix metalloproteinase (MMP-2, 9) activity and expression in patients with coronary artery disease (cad): A randomized controlled clinical trial. *ARYA Atheroscler.* 16 (3), 136–145. doi:10.22122/arya.v16i3.1938

Mohammadpour, R., Yazdimamaghani, M., Cheney, D. L., Jedrzkiewicz, J., and Ghandehari, H. (2019). Subchronic toxicity of silica nanoparticles as a function of size and porosity. *J. Control. Release* 304, 216–232. doi:10.1016/j.jconrel.2019.04.041

Munuera Martinez, L. (2010). Total arthroplasty: The other surfaces; wear and tear and osteolysis. *An. R. Acad. Nac. Med.* 127 (2), 371–380. discussion 381-7.

Nguyen, T. P. T., Li, F. Y., Shrestha, S., Tuan, R. S., Thissen, H., Forsythe, J. S., et al. (2021). Cell-laden injectable microgels: Current status and future prospects for cartilage regeneration. *Biomaterials* 279, 121214. doi:10.1016/j.biomaterials.2021.121214

Saifi, M. A., Khan, W., and Godugu, C. (2018). Cytotoxicity of nanomaterials: Using nanotoxicology to address the safety concerns of nanoparticles. *Pharm. Nanotechnol.* 6 (1), 3–16. doi:10.2174/2211738505666171023152928

Shi, D., Xu, X., Ye, Y., Song, K., Cheng, Y., Di, J., et al. (2016). Photo-cross-Linked scaffold with kartogenin-encapsulated nanoparticles for cartilage regeneration. *ACS Nano* 10 (1), 1292–1299. doi:10.1021/acsnano.5b06663

Shi, W. L., Sun, M. Y., Hu, X. Q., Ren, B., Cheng, J., Li, C. X., et al. (2017). Structurally and functionally optimized silk-fibroin-gelatin scaffold using 3D printing to repair cartilage injury *in vitro* and *in vivo*. *Adv. Mat.* 29 (29), 1701089. doi:10.1002/adma.201701089

Shu, C. C., Zaki, S., Ravi, V., Schiavinato, A., Smith, M. M., and Little, C. B. (2020). The relationship between synovial inflammation, structural pathology, and pain in post-traumatic osteoarthritis: Differential effect of stem cell and hyaluronan treatment. *Arthritis Res. Ther.* 22 (1), 29. doi:10.1186/s13075-020-2117-2

Sun, Y., Liu, W., Zhang, H., Li, H., Liu, J., Zhang, F., et al. (2017). Curcumin prevents osteoarthritis by inhibiting the activation of inflammasome NLRP3. *J. Interferon Cytokine Res.* 37 (10), 449–455. doi:10.1089/jir.2017.0069

Sundar Dhilip Kumar, S., Houreld, N. N., and Abrahamse, H. (2018). Therapeutic potential and recent advances of curcumin in the treatment of aging-associated diseases. *Molecules* 23 (4), 835. doi:10.3390/molecules23040835

Tiwari, N., Nawale, L., Sarkar, D., and Badiger, M. V. (2017). Carboxymethyl cellulose-grafted mesoporous silica hybrid nanogels for enhanced cellular uptake and release of curcumin. *Gels* 3 (1), 8. doi:10.3390/gels3010008

Veiseh, O., and Vegas, A. J. (2019). Domesticating the foreign body response: Recent advances and applications. *Adv. Drug Deliv. Rev.* 144, 148–161. doi:10.1016/j.addr.2019.08.010

Volpatti, L. R., Facklam, A. L., Cortinas, A. B., Lu, Y. C., Matranga, M. A., MacIsaac, C., et al. (2021). Microgel encapsulated nanoparticles for glucose-responsive insulin delivery. *Biomaterials* 267, 120458. doi:10.1016/j.biomaterials.2020.120458

Wei, W., Ma, Y. Z., Zhang, X. Z., Zhou, W. Y., Wu, H. W., Zhang, J. W., et al. (2021). Biomimetic joint paint for efficient cartilage repair by simultaneously regulating cartilage degeneration and regeneration in pigs. *ACS Appl. Mat. Interfaces* 13 (46), 54801–54816. doi:10.1021/acsami.1c17629

Wu, B., Li, Y., Nie, N., Xu, J., An, C., Liu, Y., et al. (2019). Nano genome altas (NGA) of body wide organ responses. *Biomaterials* 205, 38–49. doi:10.1016/j.biomaterials.2019.03.019

Yang, W., Sun, C., He, S. Q., Chen, J. Y., Wang, Y., and Zhuo, Q. (2021). The efficacy and safety of disease-modifying osteoarthritis drugs for knee and hip osteoarthritis-a systematic review and network meta-analysis. *J. Gen. Intern Med.* 36 (7), 2085–2093. doi:10.1007/s11606-021-06755-z

Young, N. A., Bruss, M., Gardner, M., Willis, W., Mo, X. K., Valiente, G., et al. (2014). Oral administration of nano-emulsion curcumin in mice suppresses inflammatory-induced NFkB signaling and macrophage migration. *Arthritis & Rheumatology* 66, S529.

Young, N. A., Bruss, M. S., Gardner, M., Willis, W. L., Mo, X., Valiente, G. R., et al. (2014). Oral administration of nano-emulsion curcumin in mice suppresses inflammatory-induced NFκB signaling and macrophage migration. *Plos One* 9 (11), e111559. doi:10.1371/journal.pone.0111559

Zhang, C., Cai, Y. Z., and Lin, X. J. (2016). Autologous chondrocyte implantation: Is it likely to become a saviour of large-sized and full-thickness cartilage defect in young adult knee? *Knee Surg. Sports Traumatol. Arthrosc.* 24 (5), 1643–1650. doi:10.1007/s00167-015-3643-3

Zhang, Y., Li, S. J., Jin, P. S., Shang, T., Sun, R. Z., Lu, L. Y., et al. (2022). Dual functions of microRNA-17 in maintaining cartilage homeostasis and protection against osteoarthritis. *Nat. Commun.* 13 (1), 2447. doi:10.1038/s41467-022-30119-8

Zhang, Z., Leong, D. J., Xu, L., He, Z., Wang, A., Navati, M., et al. (2016). Curcumin slows osteoarthritis progression and relieves osteoarthritis-associated pain symptoms in a post-traumatic osteoarthritis mouse model. *Arthritis Res. Ther.* 18 (1), 128. doi:10.1186/s13075-016-1025-y

Zheng, Z., Sun, Y., Liu, Z., Zhang, M., Li, C., and Cai, H. (2015). The effect of curcumin and its nanoformulation on adjuvant-induced arthritis in rats. *Drug Des. devel. Ther.* 9, 4931–4942. doi:10.2147/dddt.s90147

frontiers | Frontiers in Bioengineering and Biotechnology

TYPE Original Research
PUBLISHED 07 November 2022
DOI 10.3389/fbioe.2022.977159

Check for updates

OPEN ACCESS

EDITED BY
Bruce Alan Bunnell,
University of North Texas Health Science Center, United States

REVIEWED BY
Lin Wei,
Soochow University, China
David Dolivo,
Northwestern University, United States

*CORRESPONDENCE
Yuzhu Song,
yuzhusong@kust.edu.cn

SPECIALTY SECTION
This article was submitted to Tissue Engineering and Regenerative Medicine, a section of the journal Frontiers in Bioengineering and Biotechnology

RECEIVED 02 July 2022
ACCEPTED 26 October 2022
PUBLISHED 07 November 2022

CITATION
Wang G, Chen Z, Tian P, Han Q, Zhang J, Zhang A-M and Song Y (2022), Wound healing mechanism of antimicrobial peptide cathelicidin-DM.
Front. Bioeng. Biotechnol. 10:977159.
doi: 10.3389/fbioe.2022.977159

COPYRIGHT
© 2022 Wang, Chen, Tian, Han, Zhang, Zhang and Song. This is an open-access article distributed under the terms of the Creative Commons Attribution License (CC BY). The use, distribution or reproduction in other forums is permitted, provided the original author(s) and the copyright owner(s) are credited and that the original publication in this journal is cited, in accordance with accepted academic practice. No use, distribution or reproduction is permitted which does not comply with these terms.

Wound healing mechanism of antimicrobial peptide cathelicidin-DM

Guixi Wang[1], Zhizhi Chen[1], Pan Tian[1], Qinqin Han[1], Jinyang Zhang[1], A-Mei Zhang[1] and Yuzhu Song[1,2]*

[1]Research Center of Molecular Medicine of Yunnan Province, Faculty of Life Science and Technology, Kunming University of Science and Technology, Kunming, China, [2]School of Medicine, Kunming University of Science and Technology, Kunming, China

Background and Purpose: Chronic wound infections and the development of antibiotic resistance are serious clinical problems that affect millions of people worldwide. Cathelicidin-DM, an antimicrobial peptide from *Duttaphrynus melanostictus*, has powerful antimicrobial activity and wound healing efficacy. So, it could be a potential candidate to address this problem. In this paper, we investigate the wound healing mechanism of cathelicidin-DM to establish a basis for preclinical studies of the drug.

Experimental Approach: The effects of cathelicidin-DM on cell proliferation and migration, cytokines, and mitogen-activated protein kinase (MAPK) signaling pathways were examined. Then mice whole skin wound model was constructed to evaluate the wound healing activity of cathelicidin-DM, and further histological changes in the wounds were assessed by hematoxylin-eosin staining (H&E) and immunohistochemical assays.

Key Results: Cathelicidin-DM promotes the proliferation of HaCaT, HSF, and HUVEC cells in a concentration-dependent manner and the migration of HSF, HUVEC, and RAW.264.7 cells. Moreover,cathelicidin-DM can involve in wound healing through activation of the MAPK signaling pathway by upregulating phosphorylation of ERK, JNK, and P38. However, cathelicidin-DM didn't affect the secretion of IL-6 and TNF-α. At the animal level, cathelicidin-DM accelerated skin wound healing and early debridement in mice as well as promoted re-epithelialization and granulation tissue formation, α-SMA expression, and collagen I deposition in mice.

Conclusion and Implications: Our data suggest that cathelicidin-DM can be engaged in the healing of infected and non-infected wounds through multiple pathways, providing a new strategy for the treatment of infected chronic wounds.

KEYWORDS

antimicrobial peptide, cathelicidin-DM, wound healing, skin, infection

1 Introduction

As the first organ of the organism, the skin consists of two parts, the epidermis and the dermis. It is the first barrier against various microbial attacks and plays an important role in protecting the organism and maintaining the homeostasis of the internal environment (Baroni et al., 2012). Trauma inevitably occurred when the skin was exposed to the environment for long periods and was subjected to multiple factors and stresses. Following the onset of skin injury, the four phases of the wound healing processes will be sequentially initiated: hemostasis, inflammation, proliferation, and remodeling, with neighboring phases, linked and overlapping with each other (Wilkinson and Hardman, 2020). To a certain extent, the structural complexity and functional diversity of the skin determine that wound healing is a complex process that involves a variety of cells, cytokines, and various extracellular matrices to complete tissue repair. In the hemostatic phase, this phase is mainly concerned with coagulation and hemostasis, both to prevent massive blood loss that could damage organs and to provide an environment for later cell growth (Wang et al., 2018); in the inflammatory phase, neutrophils and macrophages infiltrate the wound site to engulf and remove cellular debris, bacteria, etc. to prevent bacterial infection (Eming et al., 2007; Tziotzios et al., 2012; Kloc et al., 2019); during the proliferative phase, the activated of keratin forming cells, fibroblasts, and endothelial cells proliferate and migrate together to complete re-epithelialization and granulation of tissue formation (Gonzalez et al., 2016; Wilkinson and Hardman, 2020); during the remodeling phase, collagen I is gradually replaced by collagen III and fibroblasts are converted to myofibroblasts, both of which together accomplish the contraction of the wound and scar (Almadani et al., 2021; Mathew-Steiner et al., 2021).

Chronic wounds caused by ubiquitous pathogens are a public safety problem worldwide and would also carry a huge economic burden. Damaged skin loses its barrier function and is at risk of infection (e.g., *Staphylococcus aureus*, *Pseudomonas aeruginosa*, etc.), as well as providing environmental conditions for the growth and colonisation of pathogens, thereby prolonging wound healing and threatening lives (Siddiqui and Bernstein, 2010). The theory that time can heal wounds will not be defeated (Martin, 2020). As drug resistance increases, so will the difficulty of treating such chronic wounds. Some researchers predict that by 2050, 10 million people worldwide will die from drug-resistant microbes (GradisteanuPircalabioru et al., 2021). Traditional therapeutic drugs also do not meet the real needs of society and the clinic and have major shortcomings. The use of intravenous antibiotics can be used to prevent or treat wound infections (Thapa et al., 2020), but this increases the local production of drug-resistant bacteria. In addition, topical antibiotics tend to cause discomfort and contact dermatitis. Therefore, it is necessary to develop novel drugs to manage such wounds.

Antimicrobial peptides are considered to be a new therapeutic strategy for infected non-healing wounds in need of a new treatment (de Souza et al., 2022), as well as an effective alternative to antibiotics (Magana et al., 2020). This is due to their powerful antibacterial and bactericidal activity, low drug resistance and wound healing activity. As a result, an increasing number of researchers are attracted to invest in the development and exploitation of antimicrobial peptides. In recent years, some antimicrobial peptides have also been found to enhance wound recovery (e.g., *Tylotion* (Mu et al., 2014), AH90 (Liu et al., 2014a), CW49(Liu et al., 2014b), Temporins A and B (Di Grazia et al., 2014), Tiger17 (Tang et al., 2014), cathelicidin-OA1 (Cao et al., 2018), cathelicidin-NV (Wu et al., 2018), DRGN-1 (Chung et al., 2017), LL-37 (Saporito et al., 2018; Yang et al., 2020),etc.), which provides better drug candidates for the treatment wounds. They are involved in certain processes of wound healing that play a role in accelerating wound repair which can be broadly summarised as: promotion of cell proliferation and migration, angiogenesis, immune regulation, collagen deposition, conversion of fibroblasts to myofibroblasts, etc (Table 1).

Cathelicidin DM is a bifunctional peptide (Shi et al., 2020). It kills a wide range of bacteria, and even inhibits clinical isolates. On the other hand, in a wound model of *E. coli* infection, the wound healing rate in mice treated with cathelicidin-DM was superior to that in the control and gentamicin groups. This paper aims to investigate the wound healing mechanism of cathelicidin-DM based on the wound healing process. It could provide preclinical data for its development as a drug for the prevention or treatment of wound infection and wound healing, or even for the treatment of chronic wounds with infection.

2 Material and methods

2.1 Material

Dulbecco's modified eagle medium (DMEM) and fetal bovine serum (FBS) respectively purchased from gibco in the US and Biological Industries in Israel. MAPK Family Antibodies Sampler Kit (Cat# 9926, RRID:AB_330797) and Phospho-MAPK Family Antibodies Sampler Kit (Cat# 9910, RRID: AB_330792) provided by Cell Signaling Technology. 4% paraformaldehyde, paraffin, phenylmethylsulfonyl fluoride, protein phosphatase inhibitors, etc., were purchased from China Soleibao Company.

Balb/c mice were purchased from Kunming Medical University. All cells were obtained from Kunming Institute of Zoology, Chinese Academy of Sciences. It was approved by the Experimental Animal Ethics Committee of Kunming University of Science and Technology for the work to be carried out.

TABLE 1 Natural and synthetic antimicrobial peptides in wound healing.

Name	Source	Wound healing features	References
Tylotoin	*Salamanders*	Immunomodulatory activity, the ability to promote cell migration and proliferation, and promote angiogenesis	Mu et al. (2014)
AH90	*Odorrana grahami*	Stimulation of TGF-β secretion, Keratinocyte migration, and fibroblast-to-myofibroblast transition	Liu et al. (2014a)
CW49	*Odorrana grahami*	Inhibits excessive inflammation and angiogenesis	Liu et al. (2014b)
Temporins A and B	*Rana temporaria*	Keratinocyte Proliferation and migration, promote angiogenesis	Di Grazia et al. (2014)
Tiger17		Stimulation of TGF-β and IL-6 secretion, Keratinocyte Proliferation and migration, fibroblast-to-myofibroblast transition	Tang et al. (2014)
Cathelicidin-OA1	*Odorrana andersonii*	macrophage recruitment, Keratinocyte proliferation and Fibroblast migration	Cao et al. (2018)
Cathelicidin-Nv	frog *Nanorana ventripunctata*	Keratinocyte and Fibroblast Proliferation, fibroblast-to-myofibroblast transition, collagen production in fibroblasts	Wu et al. (2018)
DRGN-1	*Varanus komodoensis*	granulation tissue formation, re-epithelialization, and keratinocyte proliferation/migration	Chung et al. (2017)
LL-37	human	Induction of cell proliferation, migration, and angiogenesis	Saporito et al. (2018), Yang et al. (2020)

2.2 Synthesis of cathelicidin-DM

Cathelicidin-DM, synthesized by Hangzhou DGpeptides, has been determined to have a molecular mass of 4,163.97 and a purity of >95% after Mass Spectrometry and High Performance Liquid Chromatography analysis.

2.3 Analysis of cell proliferation assay

The effect of cathelicidin-DM on the proliferation of human umbilical vein endothelial cells (HUVEC, RRID:CVCL_2959), human immortalized keratinocytes (HaCaT, RRID: CVCL_0038), and human skin fibroblasts (HSF, RRID: CVCL_9V78) were cultured with DMEM and used the CCK-8 assay. The concentrations of trypsin-digested resuspended cells were counted separately using hemocytometer plates and inoculated in 96-well plates (5×10^3 cells/well, 90 μl). After the cells were plastered, 10 μl of cathelicidin-DM was added at final concentrations of 0, 2, 5, 10, and 20 μg/ml and incubated in a 5% CO_2 incubator at 37°C for 16 h. Add 10 μl of CCK-8 to each well to continue the incubation for 1 h, keeping in mind that this step requires protection from light. The absorbance is measured at 450 nm, which reflects the number of cells.

2.4 Cell migration assay

The influence of cathelicidin-DM on the migration of HUVEC and HSF was examined using a cell scratch assay (Mu et al., 2014). The digested and counted HUVEC and HSF cells were spread out on the plate and left to culture until the cells reached about 90% melting. The serum-free DMEM was then replaced for cell starvation. After leaving for 24 h, the plates were scored with a 200 μl gun tip. After scoring, the plates were washed 3 times with PBS to remove the scoring cells and the serum-free medium was added for culture. Cathelicidin-DM at a final concentration of 20 μg/ml was also added and the control group was added to the serum-free medium, and the migration of cells was photographed and recorded at 0, 12, 24 and 48 h respectively. ImageJ and Photoshop were used to process the change in the scratch area and mark the location of cell migration respectively. Photographs were taken at the same location to ensure the reliability of the experiment.

2.5 Effects on macrophages *in vitro*

To further validate the biological function of cathelicidin-DM on macrophages, We used a transwell migration assay to examine the effect of cathelicidin-DM on the migration of mouse RAW264.7 cells (RRID:CVCL_0493) (Mi et al., 2018). The cells were starved for 10 h before preparing the cell suspension to reduce the effect of serum. Next, the chambers were equilibrated for 2 h using 200 μl of serum-free DMEM to hydrate the basement membrane. The cells were digested, counted, and adjusted to a cell concentration of 1.0×10^5 cells/ml. 200 μl of the cell suspension with PBS or cathelicidin-DM was added to the upper chamber of the transwell, while the lower chamber was added to a medium containing 20% FBS and incubated in a cell culture incubator. After 24 h of incubation, the transwell chambers were removed, washed with PBS (2 times), fixed with 4% paraformaldehyde for 15 min, washed with PBS 2 times, stained with 0.5% crystal violet (10 min), and washed with PBS 3 times, and the transwell chambers were placed upside

down on filter paper until they were air-dried and photographed under an inverted microscope.

2.6 Cytokine detection

RAW264.7 cells were digested at the logarithmic growth stage and grown in 96 well plates (180 μl, 1×10^5 cells/well). Then, the cells were treated with different final concentrations of cathelicidin-DM for 24 h. The supernatant was collected and the effect of cathelicidin-DM on the secretion of IL-6 and TNF-α was measured using an enzyme linked immunosorbent assay (ELISA) kit, refer to the instructions for details.

2.7 Mitogen-activated protein kinase signaling pathway assay

Cultured mouse RAW264.7 cells were digested, counted, inoculated into 6-well culture plates (2×10^6 cells/well), placed in a 5% CO_2 incubator at 37°C, and allowed to grow to 80% fusion, then transferred to serum-free DMEM and starved for 16 h. The cells were treated with different final concentrations (0, 2, 5, 10, and 20 μg/ml) of cathelicidin-DM for 3 h, then washed twice with pre-cooled PBS solution, and incubated for 30 min on ice with 250 μl of High-Performance RIPA Lysis Buffer containing 1% PMSF. Phosphorylated proteins also require the addition of dephosphorylation inhibitors. The lysate is scraped off using a cell scraper and transferred to a 1.5 ml centrifuge tube at 4°C for 20 min at 12000 rpm. The supernatant is transferred to a new 1.5 ml tube and the supernatant is the total protein. The supernatant was transferred to a new 1.5 ml centrifuge tube. The concentration of protein was determined using the BCA kit, refer to the instructions. The remaining proteins were separated and stored at −20°C.

The protein samples added with 5x loading buffer were placed in a 98°C metal bath and boiled for 10 min. The denatured protein samples were separated by 12% SDS-PAGE gel electrophoresis, and the separated proteins were transferred to a polyvinylidene fluoride membrane at the same time. PVDF was blocked with 5% BCA for 2 h at room temperature. After blocking, the membrane containing the target protein was washed three times with PBST buffer for 15 min each time. Select the corresponding primary antibody according to the desired target protein, and dilute the antibody with PBST at a ratio of 1:2000. The primary antibody was added to the incubation box and incubated overnight at 4°C. The next morning, the membrane was washed five times with PBST solution for 5 min each time, and then HRP-labeled goat anti-rabbit IgG (1:1000) was added, and incubated at 37°C for 1 h. The membrane was washed 5 times with PBST solution, 5 min each time, and developed with a developing instrument.

2.8 Construction of model of whole-layer trauma in mice

When the mice were purchased, they were kept in separate cages in the laboratory for 1 week to adapt to the environment and to ensure the reliability of the experiment. We randomly divided the mice into the control group and the experimental group ($n = 5$). The mice were anesthetized by intraperitoneal injection of sodium pentobarbital, removed their hair, and disinfected skin with 75% medical alcohol. A full skin trauma model of approximately 6 mm in diameter was made on the back of mice (He et al., 2019).

2.8.1 Construction of a non-infected model of whole-layer trauma in mice

The control and experimental groups were respectively treated with a sterile PBS solution and 300 μg/ml cathelicidin-DM at 12-h intervals. Photographs were taken of the mice on days 0, 2, 4, 6, 8, 10, and 12 days to record wound healing. The area was calculated using ImageJ software. Photographs were taken at the same location and at the same level to ensure the accuracy of the experiment.

2.8.2 Construction of an infection model for whole-layer trauma in mice

S. aureus (ATCC 25923) was used to infect mouse trauma sites to produce a mouse whole-layer trauma infection model. *Staphylococcus aureus* was first resuscitated by manipulation in a biological ultra-clean table. A single clone was picked and incubated in LB medium at 37°C and 200 rpm. When the logarithmic stage of growth was reached, the concentration of the bacterial solution was measured using an Ultraviolet-visible Spectrophotometer ($1OD = 1 \times 10^9$ cells/ml). The above *S. aureus* solution was adjusted to a concentration of 1×10^8 cells/ml to infect the wounds of mice. After *S. aureus* infection, the subsequent steps are the same as in 2.8.1.

2.9 Hematoxylin-eosin staining staining and immunohistochemical analysis

The method was modified slightly according to 2.8.1. Symmetrical full-thickness skin wounds of 6 mm were constructed on both sides of the back of the same mouse and treated with PBS and cathelicidin DM respectively. Wound tissue with a small amount of normal tissue was taken at the appropriate time and preserved in 4% paraformaldehyde solution for H&E staining and immunohistochemistry referring to the literature or instructions for the exact

10.3389/fbioe.2022.977159

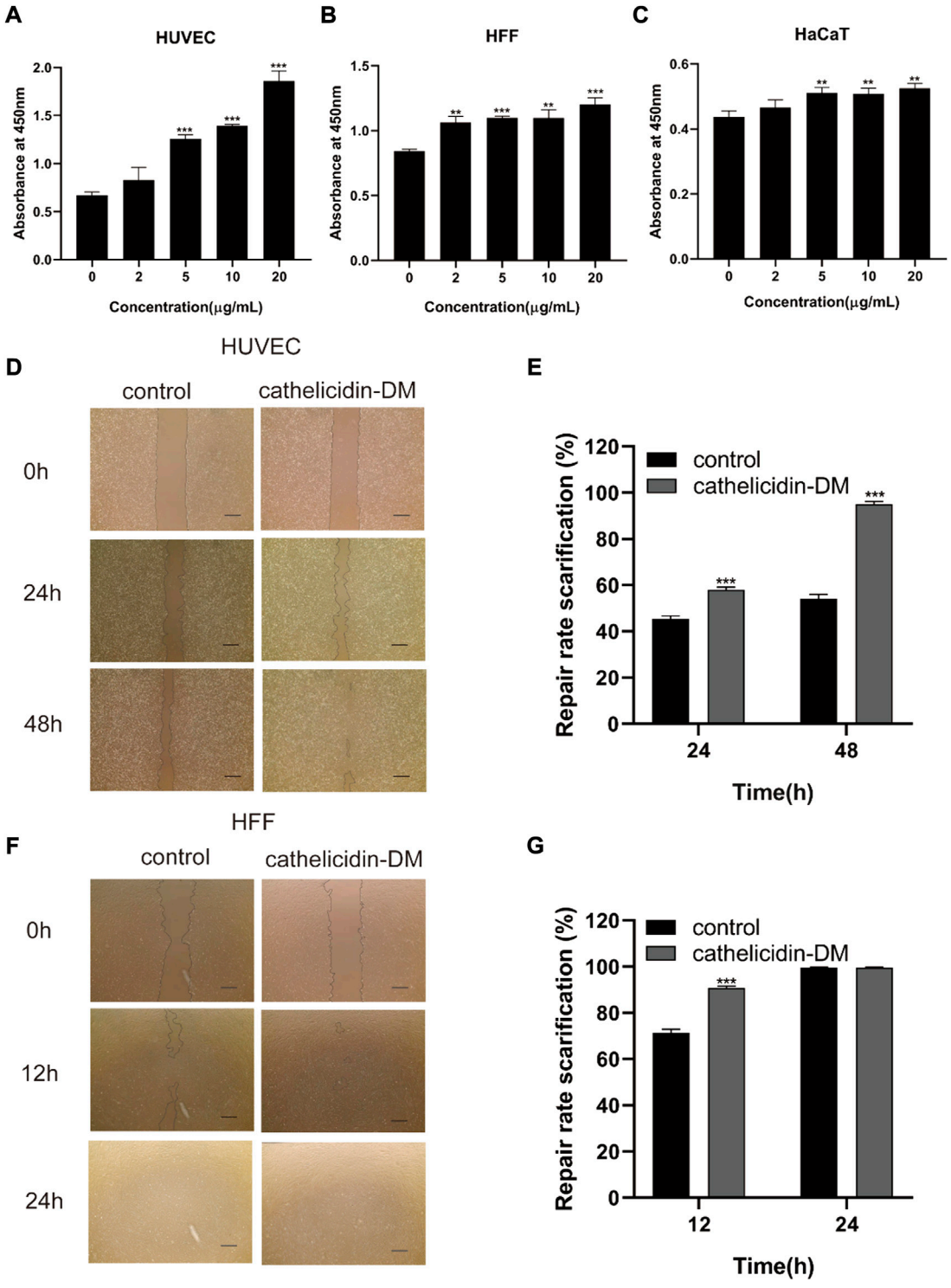

FIGURE 1
Effect of cathelicidin-DM on cell proliferation and migration. **(A-C)** The influence of different concentrations of cathelicidin-DM on the viability of HUVEC, HFF, and HaCaT cells at 0, 2, 5, 10, and 20 μg/ml, respectively. **(D,F)** Migration of HUVEC and HFF cells stimulated by 20 μg/ml cathelicidin-DM, Scale bar represents 200 μm. **(E,G)** The microscope images were quantified for analysis using ImageJ software and cell migration rates were calculated in the area of the cell scratches. All the experiments were repeated 3 times and the data are expressed as mean ± standard, $^{*}p < 0.05$, $^{**}p < 0.01$, $^{***}p < 0.001$.

procedure. Granulation tissue and epidermis in H&E stained sections were assessed using a semi-quantitative scoring system (Galeano et al., 2003; Liu et al., 2014a). The system uses a four-point scoring method to evaluate the formation of granulation tissue. one to four points represent a thin granulation layer, moderate granulation layer, thick granulation layer, and very thick granulation layer respectively. skin dermal and epidermal regeneration was evaluated by three-point scoring (1, little regeneration; 2, moderate regeneration; and 3, complete regeneration). Importantly, dermis and epidermis regeneration, and granulation tissue are quantified using Image Pro Plus. The immunohistochemical section was analyzed by ImageJ.

2.10 Statistical analysis

All data were analyzed using Student's t-tests or one-way ANOVA provided by GraphPad prism 8. Experimental results were expressed as mean ± standard deviation. $p < 0.05$ was considered statistically significant between the two groups.

3 Results

3.1 Cathelicidin-DM promoted the proliferation of HaCaT, HSF, and HUVEC cells

The skin is an organ based on keratinocytes, fibroblasts, vascular endothelial cells, and other cells whose proliferative and migratory activities are particularly important for wound repair. Studies have indicated that antimicrobial peptides can induce cell proliferation and migration to accelerate tissue healing, such as Cathelicidin-NV (Wu et al., 2018), SR-0379 (Tomioka et al., 2014), DRGN-1 (Chung et al., 2017), LL-37 (Koczulla et al., 2003; Carretero et al., 2008), etc. Therefore, we investigated the effect of different concentrations of cathelicidin-DM on HUVEC, HSF, and HaCaT cell viability using the CCK-8 assay. The results showed that cathelicidin-DM accelerated the proliferation of HUVEC, HSF, and HaCaT cells in a dose-dependent manner. As shown in Figures 1A–C, compared with the control group, the growth rates of HaCaT, HSF, and HUVEC cells were 16.27% and 19.92%, 30.5% and 42.58%, 107.32% and 177.17% at cathelicidin-DM concentrations of 10 μg/ml and 20 μg/ml, respectively.

3.2 Cathelicidin-DM facilitates the migration of HUVEC and HSF cells

Since cathelicidin-DM was more powerful in promoting the growth of HSF and HUVEC cells, we investigated the effect of cathelicidin-DM on the migration of HUVEC and HSF cells using a cell scratch assay. It was revealed that cathelicidin-DM significantly enhanced the migration of HUVEC (Figures 1D–G), while the effect on the migration of HSF cells was greater before 12 h and decreased with time. Cathelicidin-DM had 58.0% and 95.1% scratch repair rates for HUVEC cells at 24 and 48 h, whereas the control group only had 45.5% and 54.3%; the scratch repair rate for HSF cells treated with cathelicidin-DM was 90.4% and 99.6% at 12 and 24 h, while the scratch repair rate for the control group was 71.5% and 99.6%.

3.3 Cathelicidin-DM induced macrophage recruitment

Macrophages are involved in the entire process of wound healing, especially during the inflammatory phase, and also produce chemokines and growth factors such as TNF-α, IL-6 TGF-β1, and VEGF-α (Mi et al., 2018; Kloc et al., 2019), which promote cell proliferation and migration, and promote angiogenesis. Tiger17 from frogs and tylotoin from salamanders are chemotactic and recruit macrophages to the wound site to remove damaged tissue and antigens (Mu et al., 2014; Tang et al., 2014). As displayed in Figures 2A,B, cathelicidin-DM was able to promote the migration of mouse RAW264.7 cells *in vitro*, which improved cell migration performance by approximately 2.6-fold compared to the control group. Further, we examined the effect of cathelicidin-DM on the secretion of TNF-α and IL-6 by RAW264.7 cells using ELISA. As shown in Figure 2, 5, the results indicate that cathelicidin-DM had no significant effect on the secretion of TNF-α and IL-6 compared to the control group. (Figures 2C,D).

3.4 Cathelicidin-DM activates mitogen-activated protein kinase signaling pathway for injury healing

Since the MAPK signaling pathway has a role in wound healing and is closely related to cell proliferation, differentiation, and migration (Wu et al., 2018), we speculate that cathelicidin-DM activates the MAPK signaling pathway when it exerts its wound-healing function. As indicated in Figure 3A, we observed inducable extracellular regulated protein kinases (ERK), c-Jun N-terminal kinase (JNK), and P38 Mitogen-Activated Protein Kinase (P38) phosphorylation using western blot. Cathelicidin-DM regulated JNK phosphorylation in a concentration-dependent manner, and no concentration-dependent regulation was shown for ERK and P38, which were phosphorylated to the highest extent at a cathelicidin-DM concentration of 10 μg/ml (Figures 3B–D). In comparison with the control group, the phosphorylation levels of ERK, P38, and JNK were respectively up-regulated by 139.2%, 43.0%, and 348% at a cathelicidin-DM concentration of 20 μg/

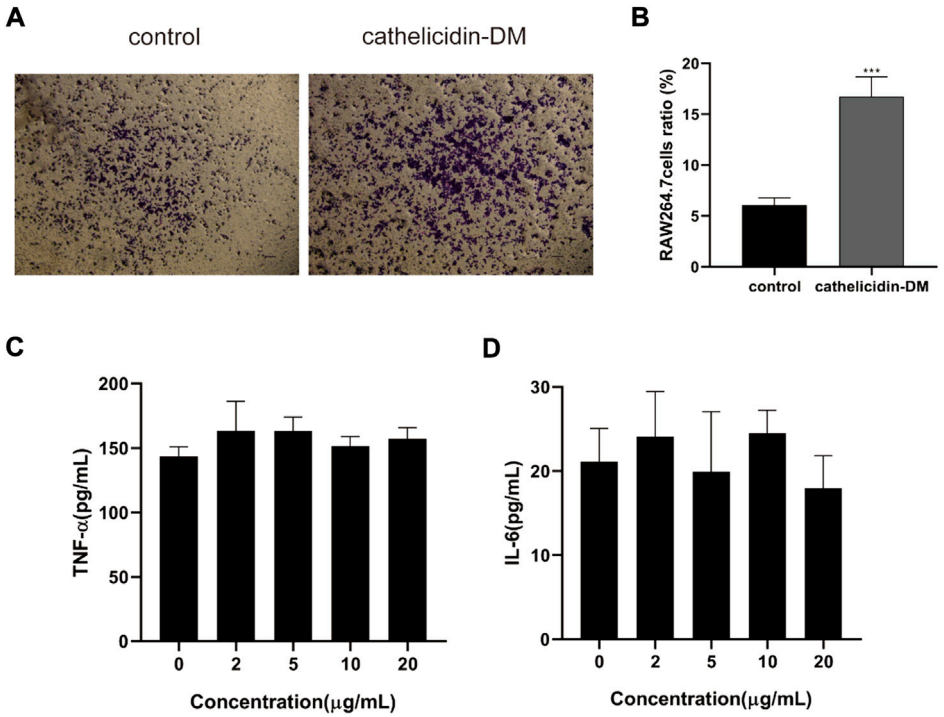

FIGURE 2
Effect of cathelicidin-DM on the migration of mouse RAW264.7 cells and secretion of TNF-α and IL-6. **(A)** The effect of 20 μg/ml cathelicidin-DM on the migratory activity of mouse RAW264.7 cells was assayed using Transwell chambers, Scale bar represents 100 μm. **(B)** Quantitative analysis of cells in **(A)** with ImageJ. **(C,D)** The effect of different concentrations of cathelicidin-DM on the secretion of TNF-α, IL-6. All the experiments were repeated 3 times and the data are expressed as mean ± standard, $*p < 0.05$, $**p < 0.01$, $***p < 0.001$.

ml. In conclusion, cathelicidin-DM activates phosphorylation of ERK, JNK, and P38 to activate MAPK signaling pathway to contribute to skin wound healing.

3.5 Cathelicidin-DM accelerated whole skin wound healing in mice

Previous work had demonstrated that caudal intravenous injection of cathelicidin-DM could therapeutic healing of *E. coli* infected wounds (Shi et al., 2020). And cathelicidin-DM could facilitate cell proliferation and migration. So we constructed a full-skin non-infected wound mice model to estimate the wound healing activity of topical cathelicidin-DM, observed the mice daily and photographed changes in wound area in mice. Figure 4A shows wound healing in mice at 0, 4, 8, and 12 days postoperatively, indicating that mice treated with topical cathelicidin-DM exhibited significant wound healing, much faster than the control group. We then analyzed the wound healing rates of the control and cathelicidin-DM treated mice and superimposed the wound tissue at different times, as shown in Figures 4B,C. It is clear that the wounds of the cathelicidin-DM treated mice were almost completely healed at 12 d. The results showed that the wound healing rate of mice treated with topical cathelicidin-DM reached 30%, 65%, and 91% at 4, 8, and 12 days post-trauma, respectively, compared to only 21%, 28%, and 66% in the control group, which indicates that the wounds of cathelicidin-DM treated mice were almost completely healed at 12 days. In another experiment, we found that topical application of cathelicidin-DM accelerated skin wound healing in *S. aureus*-infected mice compared with the control group (Figures 4C,D). 83.34% wound healing was achieved in the cathelicidin-DM-treated group at 12 d. In conclusion, cathelicidin-DM exerted therapeutic effects on both non-infected and S. aureus-infected wounds.

3.6 Hematoxylin-eosin staining dyeing analysis

Tissue re-epithelialization and granulation tissue formation are crucial aspects of the proliferative phase of wound healing. As shown in Figure 5, cathelicidin-DM promoted tissue re-epithelialization and granulation tissue formation in mice, while the wound length was less than that treated with PBS. On day 6 post-trauma, the cathelicidin-DM group had a thicker

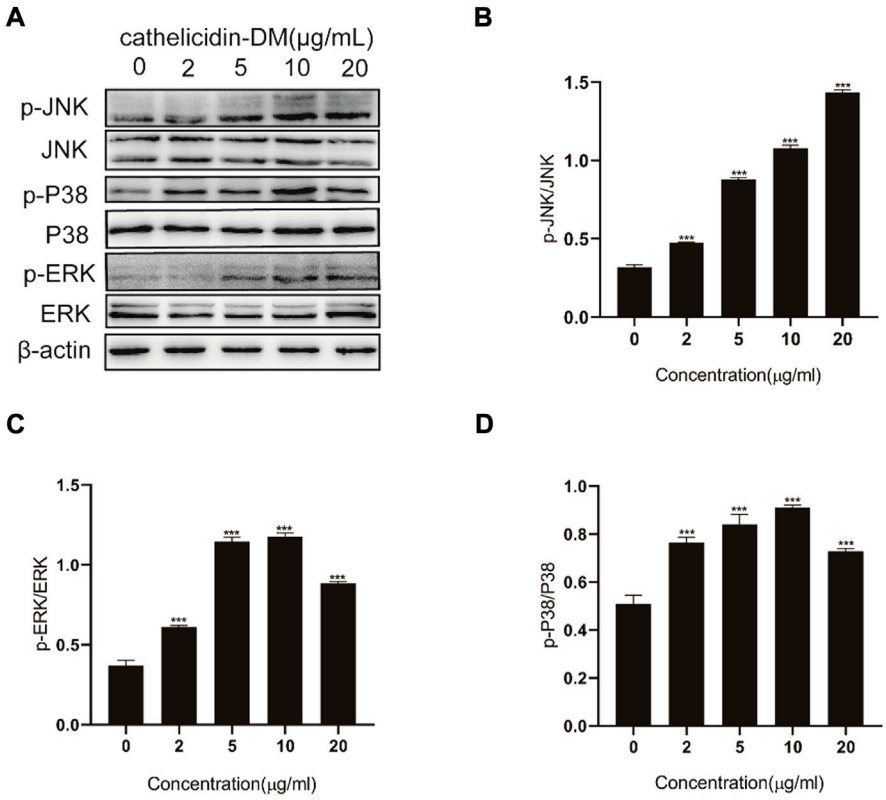

FIGURE 3
Effect of cathelicidin-DM on MAPK signaling pathway. **(A)** Western blot demonstrates the effect of cathelicidin-DM on the phosphorylation of JNK, ERK, and P38. **(B–D)** Relative greyscale analysis by ImageJ and relative activation by cathelicidin-DM of JNK **(B)**, ERK **(C)**, and P38 **(D)** expression. Values for the cathelicidin-DM treated group were significantly different from control groups. *$p < 0.05$, **$p < 0.01$ ($n = 3$).

epidermis and more abundant granulation tissue compared to the blank group. On the 8th day after wounding, mice in the cathelicidin-DM group still had more wound granulation tissue than the group treated with PBS, and the epidermis was thinner and changed to normal tissue.

3.7 Cathelicidin-DM facilitated the expression of α-smooth muscle actin and increased the deposition of collagen I

α-SMA is a symbol of differentiation of fibroblasts into myofibroblasts, which can traction wound contraction (Pfalzgraff et al., 2018). In previous studies, AH90 and tylotion exert wound healing effects through the conversion of fibroblasts to myofibroblasts, while Epinecidin-1 takes effect by increasing collagen formation (Liu et al., 2014a; Mu et al., 2014; Huang et al., 2017).

We extracted wound tissue from mice at 6 and 8 days post-trauma and further explored by immunohistochemistry whether cathelicidin-DM affects wound healing activity through α-SMA expression and collagen I deposition during the remodeling phase. The results showed that cathelicidin-DM promoted the expression of α-SMA and increased the deposition of collagen I (Figure 5). We found that the ratio of α-SMA positive area was 18% and 26.5% in the cathelicidin-DM treated group, respectively, compared to only 5.1% and 12.0% in the PBS group. The collagen-positive area was 3.6 and 2.2 times higher in the cathelicidin-DM group than in the control group at 6 and 8 d post-trauma respectively (Figures 5B,D).

4 Discussion

Cathelicidin-DM provides a better drug candidate molecule for the treatment of chronic wound infections (Shi et al., 2020). It shows strong antibacterial ability, which the MIC of cathelicidin-DM is as low as 6 μg/ml. This involves MDR and XDR, such as *Staphylococcus haemolyticus* (CI 1541410970016), *Enterococcus faecalis* (MDR 14U0445), *Staphylococcus aureus* (ATCC25923), *Escherichia coli* (MDR 13A10022), *K Pneumonia* (XDR 13A13361), etc. Antibacterial mechanism of cathelicidin-DM

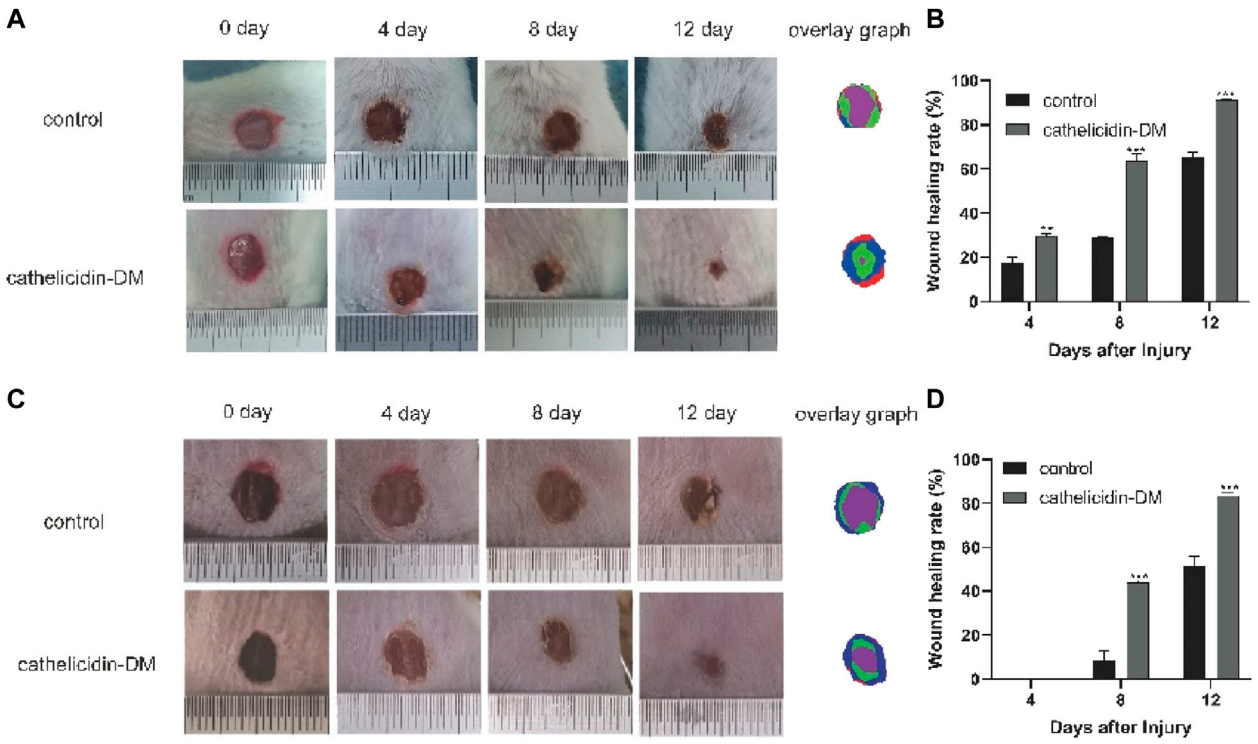

FIGURE 4
Cathelicidin-DM treatment accelerates wound closure in balb/c mice. **(A)** Graph of the healing effect of mouse trauma models treated with cathelicidin-DM, PBS on days 0, 4, 8, and 12 after trauma and superimposed maps of wound tissues from mice at 0, 4, 8, and 12 d processed by Photoshop, with red, blue, green and purple representing wound tissues from mice at 0, 4, 8 and 12 d post-trauma, correspondingly. **(B,D)** Quantitative analysis of wounds using ImageJ software and calculation of wound healing rates in the control and cathelicidin-DM groups. **(C)** Healing effects and wound overlays of a mouse S. aureus-infected wound model treated with cathelicidin-DM, PBS on days 0, 4, 8, and 12 post-wound. The value is shown as mean ± standard, $*p < 0.05$, $**p < 0.01$.

was confirmed to be related to the membrane permeability in the SYTOX green absorption experiment.

It also has the advantage of wound healing activity in the wound model of *E. coli* infection. . . *Staphylococcus aureus*, one of the common pathogens of community and hospital infection, widely exists in the natural environment and can cause a variety of serious infections. In addition, cathelicidin DM can treat wounds infected by *Staphylococcus aureus* (Figure 4).

Chronic wounds caused by pathogenic bacteria have always been a difficult area of medical treatment. Currently, wound medication is mainly used to prevent and treat wound infections with antibiotics, whose use is limited due to the rapid development of drug resistance. Some bifunctional peptides with antimicrobial and wound healing activities have great potential for the prevention and treatment of infectious wounds (Miao et al., 2021). Therefore, the wound-healing mechanism of cathelicidin-DM was investigated.

Cutaneous wound repair is a complex, conservative physiological process comprising four successive and overlapping phases of hemostasis, inflammation, proliferation, and remodeling, which work in harmony with each other to complete the repair of tissue and restore normal function (Barrientos et al., 2008; Sorg et al., 2017). The wound healing process is a cell-based repair process in which each cell performs different roles in the wound healing process. Macrophages participate in the entire phase of wound healing, especially during the inflammatory phase (Kim and Nair, 2019). During this phase, macrophages can be recruited to the wound and engulf apoptotic or dead cells, microorganisms, etc. which can be differentiated into M1 and M2 type macrophages to exert anti-inflammatory and pro-inflammatory effects (Kloc et al., 2019). *Tylotoin*, cathelicidin-OA1, AH90, and Tiger1 may facilitate macrophage recruitment or the release of factors involved in the inflammatory phase of wound healing. *In vitro*, experiments have shown that cathelicidin-DM promotes the migration of RAW264.7 cells, but does not affect the secretion of IL-6 and TNF-α (Figure 2).

During the proliferative phase of wound healing, keratinocytes are the structural cells of the healing process, in

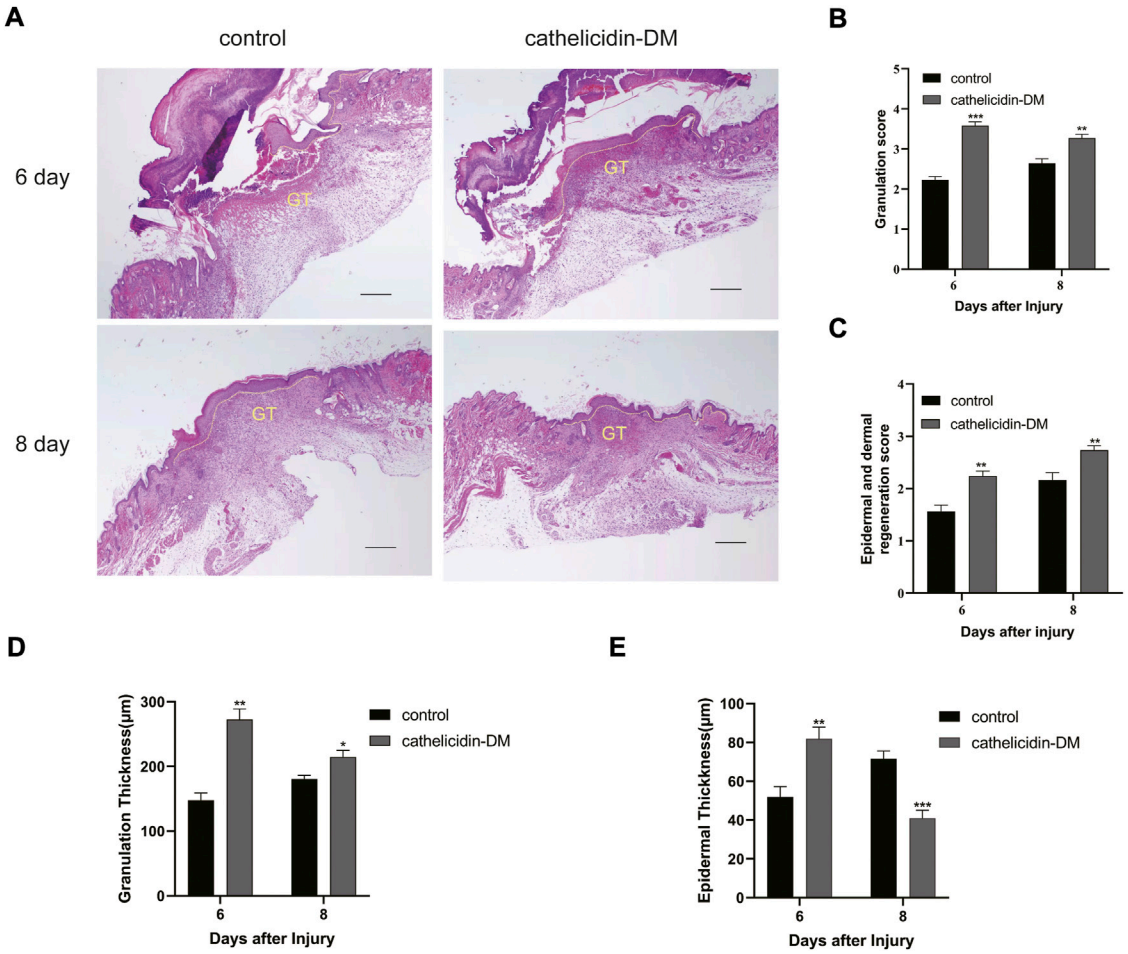

FIGURE 5
Histopathological examination of wounds in mice. **(A)** Effect of cathelicidin-DM on skin re-epithelialization and granulation tissue in mice (note: dashed line represents reepithelialization, GT represents granulation tissue, bars indicate 200 μm). **(B–E)** Histological scores of granulation thickness, epidermis and dermis regeneration; granulation and epidermal thickness of mice. Values represent means ± standard (n = 3). *p < 0.05, **p < 0.01.

case of skin injury, keratin-forming cells at the wound margin receive signals and promote proliferation and migration for re-epithelialization of the tissue (Sorg et al., 2017). Fibroblasts and vascular endothelial cells are a necessary part of the granulation tissue that fills the injured area. Vascular endothelial cells, which are stimulated by several factors to migrate and form capillaries, are important conduits for the transport of nutrients, oxygen, and other substances (Dulmovits and Herman, 2012; Sorg et al., 2018). Most wound healing peptides can be demonstrated, e.g., Temporins A, Tylotoin, Cathelicidin-OA1. Cathelicidin-DM facilitated the proliferation of HUVEC, HSF, and HaCaT cells and the migration of HUVEC and HSF cells (Figure 1). This in turn accelerated re-epithelialization and granulation tissue formation at the site of skin injury in mice. (Figure 5). Western blot showed that cathelicidin-DM upregulated the phosphorylation of JNK, ERK, and P38 in the MAPK signaling pathway to activate the MAPK signaling pathway in wound healing, which is involved in cell proliferation, and differentiation (Figure 3).

Two key features of the remodeling phase of wound healing are the differentiation of fibroblasts into myofibroblasts, which are responsible for wound contraction, and the conversion of collagen III into collagen I and its deposition (Broughton et al., 2006; Pazyar et al., 2014). To this end, cathelicidin-DM was examined to study if it plays a role in the remodeling phase. Immunohistochemical experiments showed that cathelicidin-DM stimulates the expression of α-SMA and the deposition of collagen I. The amount of α-SMA expression indicates the number of myofibroblasts (Figure 6). It suggests that cathelicidin-DM is capable of promoting the differentiation of fibroblasts into myofibroblasts, which may play a traction role in wound contraction.

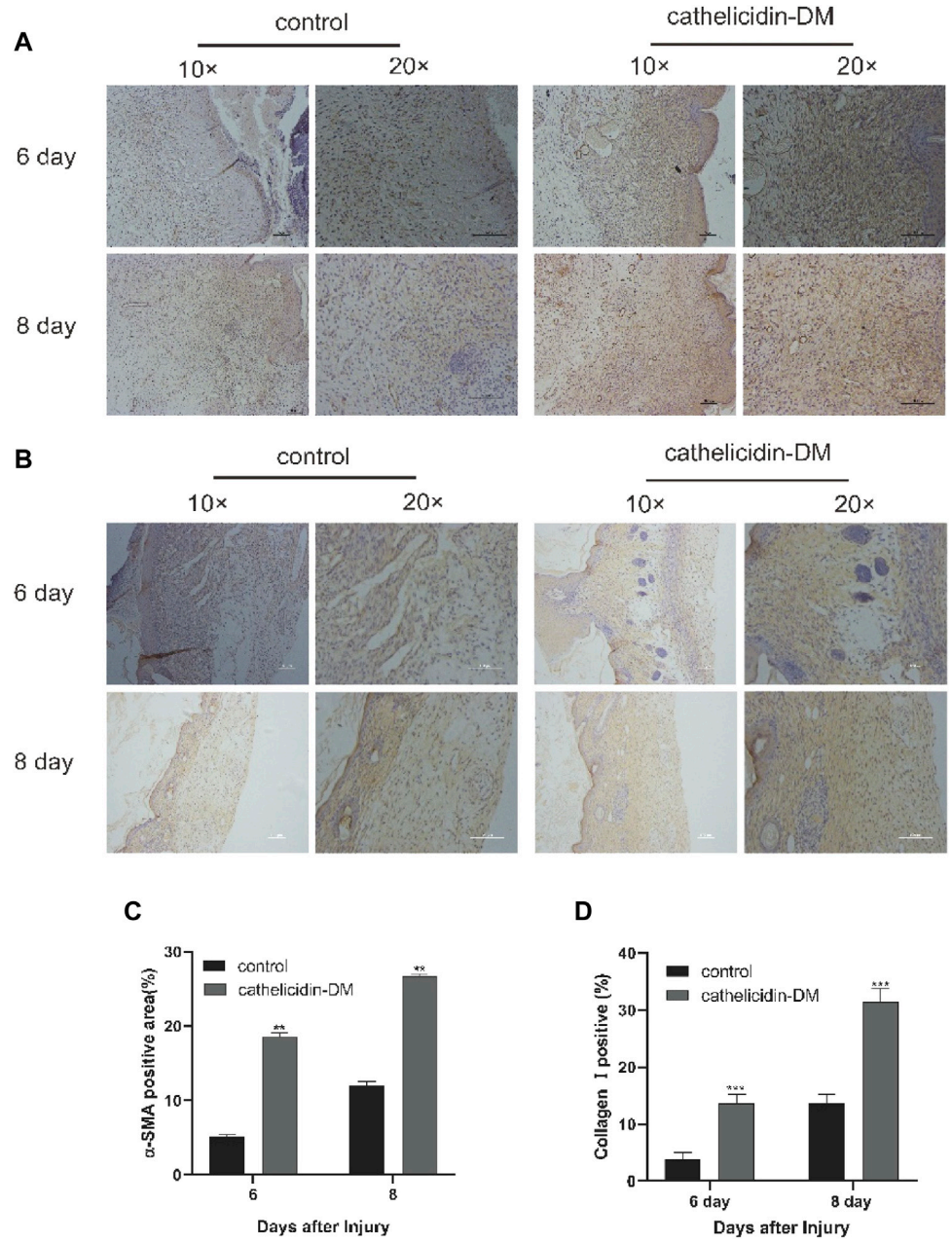

FIGURE 6
Cathelicidin-DM facilitated the expression of α-SMA and increased the deposition of collagen I. **(A)** Immunohistochemical picture of α-SMA-labelled skin tissue sections at 6 and 8 d post-trauma, with α-SMA staining in brown and scale representing 200 μm. **(B)** Images of wound skin sections stained with anti-collagen I at 6 and 8 d post-trauma, and stained brown with collagen I and scale representing 200 μm. **(C,D)** Positive rates for α-SMA **(C)** and collagen I **(D)** labeling immunohistochemistry were analyzed by ImageJ software. All data are presented as mean ± standard deviation compared to the control group, $*p < 0.05$, $**p < 0.01$ ($n = 3$).

AMPs application is also challenging in terms of inherent limitations. Current research on AMPs has focused on the identification of potent and selective peptides, as well as mechanisms and modes of action. The researchers found that they showed low stability and bioavailability when facing the local wound environment. In the future we will work in the following directions: 1. Direct targets of cathelicidin-DM and the relationship between structure and function; 2. Enhancement of cathelicidin-DM activity and stability by modifying and modifying peptides.

In summary, cathelicidin-DM is an antimicrobial-wound healing peptide that treats the healing of infected and non-infected wounds through multiple mechanisms. As such, it is expected to be developed as a wound-healing drug to be developed for the prevention or treatment of wound healing in infected skin wounds, offering a new strategy for the treatment of infected chronic wounds.

Data availability statement

The original contributions presented in the study are included in the article/Supplementary Material, further inquiries can be directed to the corresponding author.

Ethics statement

The animal study was reviewed and approved by the Kunming University of Science and Technology Laboratory Animal ethics committee.

Author contributions

GW, ZC, and PT contributed to experimental studies and data analysis. QH and JZ contributed to the data analysis. YS and GW wrote the manuscript. A-MZ played a major role in animal experiments. YS contributed to financial support and gave final approval for publication of the manuscript.

Funding

This study was supported by National Natural Science Foundation of China (31860607), and Yunnan Ten Thousand Talents Pan Young & Elite Talents Project and Major Science.

Conflict of interest

The authors declare that the research was conducted in the absence of any commercial or financial relationships that could be construed as a potential conflict of interest.

Publisher's note

All claims expressed in this article are solely those of the authors and do not necessarily represent those of their affiliated organizations, or those of the publisher, the editors and the reviewers. Any product that may be evaluated in this article, or claim that may be made by its manufacturer, is not guaranteed or endorsed by the publisher.

Supplementary material

The Supplementary Material for this article can be found online at: https://www.frontiersin.org/articles/10.3389/fbioe.2022.977159/full#supplementary-material

References

Almadani, Y. H., Vorstenbosch, J., Davison, P. G., and Murphy, A. M. (2021). Wound healing: A comprehensive review. *Semin. Plast. Surg.* 35 (3), 141–144. doi:10.1055/s-0041-1731791

Baroni, A., Buommino, E., De Gregorio, V., Ruocco, E., Ruocco, V., and Wolf, R. (2012). Structure and function of the epidermis related to barrier properties. *Clin. Dermatol.* 30 (3), 257–262. doi:10.1016/j.clindermatol.2011.08.007

Barrientos, S., Stojadinovic, O., Golinko, M. S., Brem, H., and Tomic-Canic, M. (2008). Perspective article: Growth factors and cytokines in wound healing. *Wound Repair Regen.* 16 (5), 585–601. doi:10.1111/j.1524-475X.2008.00410.x

Broughton, G., Janis, J. E., and Attinger, C. E. (2006). Wound healing: An overview. *Plastic Reconstr. Surg.* 117, 1–32. doi:10.1097/01.prs.0000222562.60260.f9

Cao, X., Wang, Y., Wu, C., Li, X., Fu, Z., Yang, M., et al. (2018). Cathelicidin-OA1, a novel antioxidant peptide identified from an amphibian, accelerates skin wound healing. *Sci. Rep.* 8 (1), 943. doi:10.1038/s41598-018-19486-9

Carretero, M., Escamez, M. J., Garcia, M., Duarte, B., Holguin, A., Retamosa, L., et al. (2008). *In vitro* and *in vivo* wound healing-promoting activities of human cathelicidin LL-37. *J. Invest. Dermatol.* 128 (1), 223–236. doi:10.1038/sj.jid.5701043

Chung, E. M. C., Dean, S. N., Propst, C. N., Bishop, B. M., and van Hoek, M. L. (2017). Komodo dragon-inspired synthetic peptide DRGN-1 promotes wound-healing of a mixed-biofilm infected wound. *NPJ Biofilms Microbiomes* 3, 9. doi:10.1038/s41522-017-0017-2

de Souza, G. S., de Jesus Sonego, L., Santos Mundim, A. C., de Miranda Moraes, J., Sales-Campos, H., and Lorenzón, E. N. (2022). Antimicrobial-wound healing peptides: Dual-function molecules for the treatment of skin injuries. *Peptides* 148, 170707. doi:10.1016/j.peptides.2021.170707

Di Grazia, A., Luca, V., Segev-Zarko, L. A., Shai, Y., and Mangoni, M. L. (2014). Temporins A and B stimulate migration of HaCaT keratinocytes and kill intracellular *Staphylococcus aureus*. *Antimicrob. Agents Chemother.* 58 (5), 2520–2527. doi:10.1128/aac.02801-13

Dulmovits, B. M., and Herman, I. M. (2012). Microvascular remodeling and wound healing: A role for pericytes. *Int. J. Biochem. Cell Biol.* 44 (11), 1800–1812. doi:10.1016/j.biocel.2012.06.031

Eming, S. A., Krieg, T., and Davidson, J. M. (2007). Inflammation in wound repair: Molecular and cellular mechanisms. *J. Invest. Dermatol.* 127 (3), 514–525. doi:10.1038/sj.jid.5700701

Galeano, M., Deodato, B., Altavilla, D., Cucinotta, D., Arsic, N., Marini, H., et al. (2003). Adeno-associated viral vector-mediated human vascular endothelial growth factor gene transfer stimulates angiogenesis and wound healing in the genetically diabetic mouse. *Diabetologia* 46 (4), 546–555. doi:10.1007/s00125-003-1064-1

Gonzalez, A. C., Costa, T. F., Andrade, Z. A., and Medrado, A. R. (2016). Wound healing - a literature review. *An. Bras. Dermatol.* 91 (5), 614–620. doi:10.1590/abd1806-4841.20164741

Gradisteanu Pircalabioru, G., Popa, L. I., Marutescu, L., Gheorghe, I., Popa, M., Czobor Barbu, I., et al. (2021). Bacteriocins in the era of antibiotic resistance: Rising to the challenge. *Pharmaceutics* 13 (2), 196. doi:10.3390/pharmaceutics13020196

He, X., Yang, Y., Mu, L., Zhou, Y., Chen, Y., Wu, J., et al. (2019). A frog-derived immunomodulatory peptide promotes cutaneous wound healing by regulating cellular response. *Front. Immunol.* 10, 2421. doi:10.3389/fimmu.2019.02421

Huang, H. N., Pan, C. Y., Wu, H. Y., and Chen, J. Y. (2017). Antimicrobial peptide Epinecidin-1 promotes complete skin regeneration of methicillin-resistant

Staphylococcus aureus-infected burn wounds in a swine model. *Oncotarget* 8 (13), 21067. doi:10.18632/oncotarget.15042

Kim, S. Y., and Nair, M. G. (2019). Macrophages in wound healing: Activation and plasticity. *Immunol. Cell Biol.* 97 (3), 258–267. doi:10.1111/imcb.12236

Kloc, M., Ghobrial, R. M., Wosik, J., Lewicka, A., Lewicki, S., and Kubiak, J. Z. (2019). Macrophage functions in wound healing. *J. Tissue Eng. Regen. Med.* 13 (1), 99–109. doi:10.1002/term.2772

Koczulla, R., von Degenfeld, G., Kupatt, C., Krotz, F., Zahler, S., Gloe, T., et al. (2003). An angiogenic role for the human peptide antibiotic LL-37/hCAP-18. *J. Clin. Invest.* 111 (11), 1665–1672. doi:10.1172/JCI17545

Liu, H., Duan, Z., Tang, J., Lv, Q., Rong, M., and Lai, R. (2014). A short peptide from frog skin accelerates diabetic wound healing. *Febs J.* 281 (20), 4633–4643. doi:10.1111/febs.12968

Liu, H., Mu, L., Tang, J., Shen, C., Gao, C., Rong, M., et al. (2014). A potential wound healing-promoting peptide from frog skin. *Int. J. Biochem. Cell Biol.* 49, 32–41. doi:10.1016/j.biocel.2014.01.010

Magana, M., Pushpanathan, M., Santos, A. L., Leanse, L., Fernandez, M., Ioannidis, A., et al. (2020). The value of antimicrobial peptides in the age of resistance. *Lancet Infect. Dis.* 20 (9), 216–230. doi:10.1016/S1473-3099(20)30327-3

Martin, R. F. (2020). Wound healing. *Surg. Clin. North Am.* 100 (4), 9–11. doi:10.1016/j.suc.2020.05.012

Mathew-Steiner, S. S., Roy, S., and Sen, C. K. (2021). Collagen in wound healing. *Bioeng. (Basel)* 8 (5), 63. doi:10.3390/bioengineering8050063

Mi, B., Liu, J., Liu, Y., Hu, L., Liu, Y., Panayi, A. C., et al. (2018). The designer antimicrobial peptide A-hBD-2 facilitates skin wound healing by stimulating keratinocyte migration and proliferation. *Cell. Physiol. biochem.* 51 (2), 647–663. doi:10.1159/000495320

Miao, F., Li, Y., Tai, Z., Zhang, Y., Gao, Y., Hu, M., et al. (2021). Antimicrobial peptides: The promising therapeutics for cutaneous wound healing. *Macromol. Biosci.* 21 (10), 2100103. doi:10.1002/mabi.202100103

Mu, L., Tang, J., Liu, H., Shen, C., Rong, M., Zhang, Z., et al. (2014). A potential wound-healing-promoting peptide from salamander skin. *FASEB J.* 28 (9), 3919–3929. doi:10.1096/fj.13-248476

Pazyar, N., Yaghoobi, R., Rafiee, E., Mehrabian, A., and Feily, A. (2014). Skin wound healing and phytomedicine: A review. *Skin. Pharmacol. Physiol.* 27 (6), 303–310. doi:10.1159/000357477

Pfalzgraff, A., Brandenburg, K., and Weindl, G. (2018). Antimicrobial peptides and their therapeutic potential for bacterial skin infections and wounds. *Front. Pharmacol.* 9, 281. doi:10.3389/fphar.2018.00281

Saporito, P., Vang Mouritzen, M., Lobner-Olesen, A., and Jenssen, H. (2018). LL-37 fragments have antimicrobial activity against Staphylococcus epidermidis biofilms and wound healing potential in HaCaT cell line. *J. Pept. Sci.* 24 (7), 3080. doi:10.1002/psc.3080

Shi, Y., Li, C., Wang, M., Chen, Z., Luo, Y., Xia, X. S., et al. (2020). Cathelicidin-DM is an antimicrobial peptide from *Duttaphrynus melanostictus* and has wound-healing therapeutic potential. *ACS Omega* 5 (16), 9301–9310. doi:10.1021/acsomega.0c00189

Siddiqui, A. R., and Bernstein, J. M. (2010). Chronic wound infection: Facts and controversies. *Clin. Dermatol.* 28 (5), 519–526. doi:10.1016/j.clindermatol.2010.03.009

Sorg, H., Tilkorn, D. J., Hager, S., Hauser, J., and Mirastschijski, U. (2017). Skin wound healing: An update on the current knowledge and concepts. *Eur. Surg. Res.* 58 (1-2), 81–94. doi:10.1159/000454919

Sorg, H., Tilkorn, D. J., Mirastschijski, U., Hauser, J., and Kraemer, R. (2018). Panta rhei: Neovascularization, angiogenesis and nutritive perfusion in wound healing. *Eur. Surg. Res.* 59 (3-4), 232–241. doi:10.1159/000492410

Tang, J., Liu, H., Gao, C., Mu, L., Yang, S., Rong, M., et al. (2014). A small peptide with potential ability to promote wound healing. *PLoS One* 9 (3), 92082. doi:10.1371/journal.pone.0092082

Thapa, R. K., Diep, D. B., and Tonnesen, H. H. (2020). Topical antimicrobial peptide formulations for wound healing: Current developments and future prospects. *Acta Biomater.* 103, 52–67. doi:10.1016/j.actbio.2019.12.025

Tomioka, H., Nakagami, H., Tenma, A., Saito, Y., Kaga, T., Kanamori, T., et al. (2014). Novel anti-microbial peptide SR-0379 accelerates wound healing via the PI3 kinase/Akt/mTOR pathway. *PLoS One* 9 (3), 92597. doi:10.1371/journal.pone.0092597

Tziotzios, C., Profyris, C., and Sterling, J. (2012). Cutaneous scarring: Pathophysiology, molecular mechanisms, and scar reduction therapeutics. *J. Am. Acad. Dermatol.* 66 (1), 13–24. doi:10.1016/j.jaad.2011.08.035

Wang, P. H., Huang, B. S., Horng, H. C., Yeh, C. C., and Chen, Y. J. (2018). Wound healing. *J. Chin. Med. Assoc.* 81 (2), 94–101. doi:10.1016/j.jcma.2017.11.002

Wilkinson, H. N., and Hardman, M. J. (2020). Wound healing: Cellular mechanisms and pathological outcomes. *Open Biol.* 10 (9), 200223. doi:10.1098/rsob.200223

Wu, J., Yang, J., Wang, X., Wei, L., Mi, K., Shen, Y., et al. (2018). A frog cathelicidin peptide effectively promotes cutaneous wound healing in mice. *Biochem. J.* 475 (17), 2785–2799. doi:10.1042/BCJ20180286

Yang, X., Guo, J. L., Han, J., Si, R. J., Liu, P. P., Zhang, Z. R., et al. (2020). Chitosan hydrogel encapsulated with LL-37 peptide promotes deep tissue injury healing in a mouse model. *Mil. Med. Res.* 7 (1), 20. doi:10.1186/s40779-020-00249-5

frontiers | Frontiers in Bioengineering and Biotechnology

TYPE Original Research
PUBLISHED 08 December 2022
DOI 10.3389/fbioe.2022.982894

Check for updates

OPEN ACCESS

EDITED BY
Bruce Alan Bunnell,
University of North Texas Health Science Center, United States

REVIEWED BY
Yong-Can Huang,
Peking University, China
Bin Li,
Soochow University, China

*CORRESPONDENCE
Liu Yang,
jointsurgery@163.com
Guangxing Chen,
cgx7676@hotmail.com
Cheng Chen,
ccljjff@163.com
Xiaoyuan Gong,
sliegxy@foxmail.com

†These authors share first authorship

SPECIALTY SECTION
This article was submitted to Tissue Engineering and Regenerative Medicine, a section of the journal Frontiers in Bioengineering and Biotechnology

RECEIVED 30 June 2022
ACCEPTED 28 November 2022
PUBLISHED 08 December 2022

CITATION
Song X, Wang X, Guo L, Li T, Huang Y, Yang J, Tang Z, Fu Z, Yang L, Chen G, Chen C and Gong X (2022), Etanercept embedded silk fibroin/pullulan hydrogel enhance cartilage repair in bone marrow stimulation.
Front. Bioeng. Biotechnol. 10:982894.
doi: 10.3389/fbioe.2022.982894

COPYRIGHT
© 2022 Song, Wang, Guo, Li, Huang, Yang, Tang, Fu, Yang, Chen, Chen and Gong. This is an open-access article distributed under the terms of the Creative Commons Attribution License (CC BY). The use, distribution or reproduction in other forums is permitted, provided the original author(s) and the copyright owner(s) are credited and that the original publication in this journal is cited, in accordance with accepted academic practice. No use, distribution or reproduction is permitted which does not comply with these terms.

Etanercept embedded silk fibroin/pullulan hydrogel enhance cartilage repair in bone marrow stimulation

Xiongbo Song[1†], Xin Wang[1†], Lin Guo[1], Tao Li[1], Yang Huang[1], Junjun Yang[1], Zhexiong Tang[1], Zhenlan Fu[1], Liu Yang[1*], Guangxing Chen[1*], Cheng Chen[2*] and Xiaoyuan Gong[1*]

[1]Center for Joint Surgery, Southwest Hospital, Third Military Medical University (Army Medical University), Chongqing, China, [2]College of Medical Informatics, Chongqing Medical University, Chongqing, China

Background: Bone marrow stimulation (BMS) is the most used operative treatment in repairing cartilage defect clinically, but always results in fibrocartilage formation, which is easily worn out and needs second therapy. In this study, we prepared an Etanercept (Ept) embedded silk fibroin/pullulan hydrogel to enhance the therapeutic efficacy of BMS.

Methods: Ept was dissolved in silk fibroin (SF)—tyramine substituted carboxymethylated pullulan (PL) solution and enzyme crosslinked to obtain the Ept contained SF/PL hydrogel. The synergistical effect of SF/PL hydrogel and Ept was verified by rabbit osteochondral defect model. The mechanism of Ept in promoting articular cartilage repair was studied on human osteoarthritic chondrocytes (hOACs) and human bone marrow mesenchymal stromal cells (hBMSCs) *in vitro*, respectively.

Results: At 4 and 8 weeks after implanting the hydrogel into the osteochondral defect of rabbit, histological analysis revealed that the regenerated tissue in Ept + group had higher cellular density with better texture, and the newly formed hyaline cartilage tissue was seamlessly integrated with adjacent native tissue in the Ept + group. In cellular experiments, Ept treatment significantly promoted both gene and protein expression of type II collagen in hOACs, while decreased the protein levels of metalloproteinase (MMP)-13 and a disintegrin and metalloprotease with thrombospondin motifs 5 (ADAMTS5); alcian blue staining, type II collagen and aggrecan stainings showed that addition of Ept significantly reversed the chondrogenesis inhibition effect of tumor necrosis factor alpha (TNF-α) on hBMSCs.

Conclusion: BMS could be augmented by Ept embedded hydrogel, potentially by regulating the catabolic and anabolic dynamics in adjacent chondrocytes and enhancement of BMSCs chondrogenesis.

KEYWORDS

etanercept, silk fibroin, pullulan, cartilage repair, bone marrow stimulation

Introduction

Osteoarthritis (OA), which associates with the dysfunction of adult articular cartilage, is the most common form of joint disease, and may result in arthralgia, joint deformation, and limited mobility in patients (Quicke et al., 2022). Among several risk factors (e.g. genetics, age, and obesity), articular cartilage injury caused by trauma or disease remains a high risk factor for OA. Due to the avascular and low cellularity nature of articular cartilage, intrinsic repair of defect is remarkably difficult *in vivo*, and surgical intervention is often required (DeFrate et al., 2019). Bone marrow stimulation (BMS) is a technique developed in the 1950s, and has been widely used in clinic to regenerate hyaline cartilage-like tissues from damaged articular cartilage (Makris et al., 2015; Kwon et al., 2019; Sahranavard et al., 2022). During the procedure, a physical conduit is created to connect vascularized subchondral bone marrow with the debrided cartilage lesion. Bone marrow substrates, including bone marrow mesenchymal stromal cells (BMSCs), growth factors, and cytokines are introduced into damaged articular cartilage, participating in the repair process. However, due to the inflammatory micro-environment of injured articular cavity, and insufficient mechanical support of bone marrow effusion, studies reported mechanically inferior collagen I/II fibrocartilage as the main outcome of BMS (Mithoefer et al., 2009).

Once injured, cartilage fragments are released into articular cavity, leading to the activation of immune cells such as macrophages and T cells, producing interleukin-1β (IL-1β) and tumor necrosis factor alpha (TNF-α) (Sharma et al., 2020). These inflammatory factors create chronic inflammatory micro-environment, and react upon chondrocytes to secrete metalloproteinases (MMPs) and a disintegrin and metalloprotease with thrombospondin motifs (ADAMTS), accelerating the degradation of type II collagen and aggrecans in cartilage matrix (Wang and He, 2018). Etanercept (Ept) is a recombinant soluble p75 TNF receptor, which has high affinity for TNF-α, preventing it from binding with its receptor (Garrison and McDonnell, 1999). Clinically, Ept is used as disease-modifying anti-rheumatic drugs (DMARDs), which could significantly alter disease progression (Smolen et al., 2017). In addition to the above descripted indication, an *in vivo* study demonstrated that subcutaneous injection of Ept promoted repair of osteochondral defects in the rabbit model (Kawaguchi et al., 2009). Application of the anti-TNF-α monoclonal antibody demonstrated reversal of cartilage degradation in polyarthritic TNF-α-overexpression mice (Shealy et al., 2002), indicating that Ept could serve as an inflammatory regulator to strengthen BMS in cartilage repair.

In addition to chemical environment, proper physical environments are required for migration, adhesion, and cartilaginous differentiation of BMSCs. The blood clot forms at the defect site post BMS operation is mainly composed of BMSCs, erythrocytes, leukocytes, and fibrinogen. Considering the poor mechanical property of blood colt, patients are advised to follow strict rehabilitation program to ensure gradual increase in mechanical stimulation postoperatively (Hurst et al., 2010), and stabilization of the clot by incorporating scaffold may improve the ensuing repair response. Recently, acellular bio-scaffolds have been fabricated to augment BMS (Armiento et al., 2018; Armiento et al., 2019). Bio-scaffolds with mechanical property similar to that of native articular cartilage provide suitable physical environment for the ingrowth, proliferation and chondrogenic differentiation of BMSCs. Simultaneously, the inflammatory microenvironment can be regulated by embedding immuno-modulatory elements in the bio-scaffolds (Glass et al., 2014; Tamaddon et al., 2020; Tong et al., 2020). Among different forms of acellular bio-scaffolds, hydrogels with good biocompatibility, proper degradation rates, and tissue-matched elasticity are widely used (Liu et al., 2020; Wagenbrenner et al., 2021; Huang et al., 2022). Previously, we prepared an enzymatically crosslinked silk fibroin/pullulan (SF/PL) hydrogel, and proved its feasibility for musculoskeletal tissue engineering (Li et al., 2018). Here, we assumed that clinical outcome of BMS could be enhanced by combination of SF/PL hydrogel and Ept.

In the present study, to enhance the current therapeutic effect of BMS, SF/PL hydrogel containing Ept was fabricated and performed with BMS. The synergistical effect of SF/PL hydrogel and continuously released Ept on articular cartilage repair was verified by rabbit osteochondral defect model. To investigate the mechanism of Ept in enhancing articular cartilage repair, human osteoarthritic chondrocytes (hOACs) and human bone marrow mesenchymal stromal cells (hBMSCs) were employed as *in vitro* model. The effects of Ept on catabolic and anabolic dynamics in hOACs, and on chondrogenetic differentiation in hBMSCs were analyzed, respectively.

Materials and methods

Preparation of Ept contained SF/PL hydrogel. Silk fibroin (SF) and tyramine substituted carboxymethyl pullulan (PL) were synthesized according to our previous study (Li et al., 2018). Ept contained SF/PL hydrogels were prepared by an enzyme-mediated polymerization strategy. In a typical procedure, 40mgEpt was dissolved in 2 ml of SF (30 mg/ml)—PL (6 mg/ml) solutions, the concentration of Ept used was mainly decided by converting equivalent dosage between rabbit and human according to body surface area (Nair et al., 2016; Nair et al., 2018). 10 μl of HRP solution (1000 U/mL) was added to 1 ml of SF and PL mixture solution, then 10 μl of H_2O_2 (1% v/v) was added and mixed by gentle pipetting. To obtain a proper size (200 ml mixture solution/hydrogel) for *in vivo* implantation, gel-forming procedure was carried out in a custom-made cylinder mold (3.2 mm in diameter, 4 mm in height). No flow within 1min upon inverting the vial was regarded as the gel state.

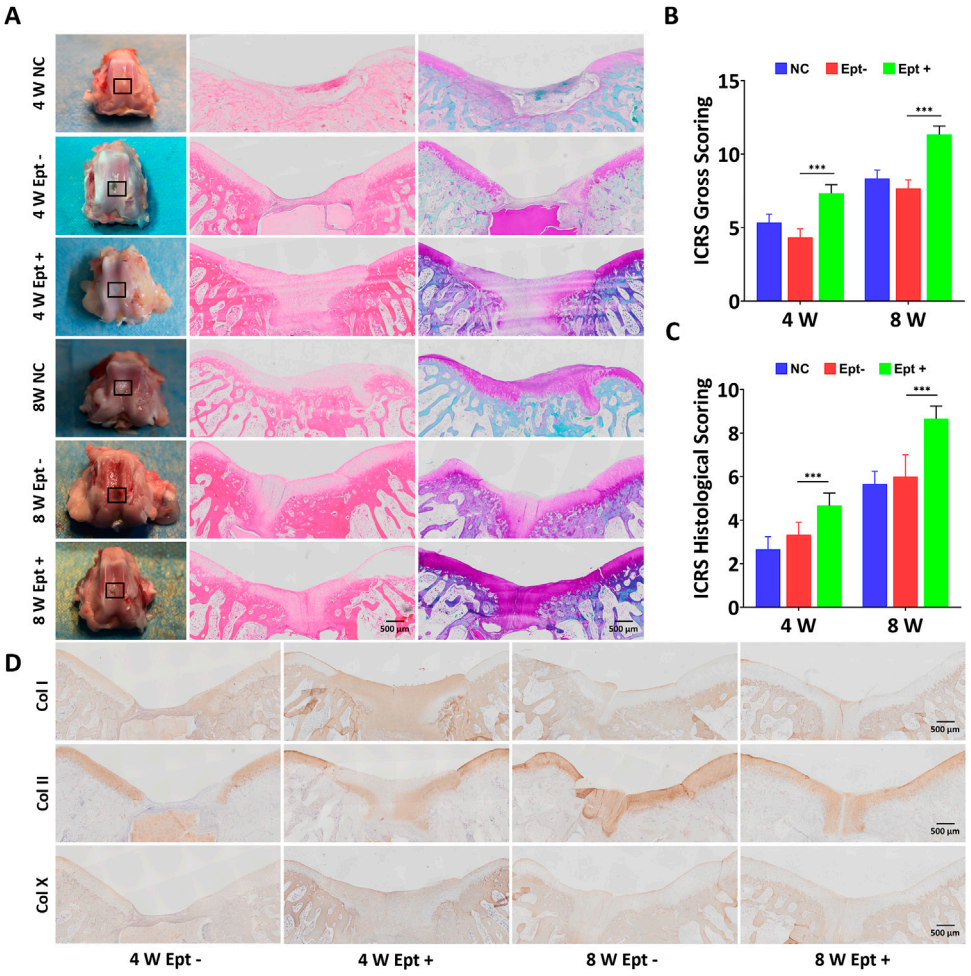

FIGURE 1
Comparison of osteochondral repair in the untreated group (NC), scaffold-only group (Ept−) and Ept loaded scaffold group (Ept+) at 4 and 8 weeks. **(A)** Macroscopic analysis, hematoxylin and eosin staining, and safranin O staining of the knee joints. Black rectangle indicates the osteochondral defects. **(B)** Macroscopic analysis for cartilage repair with the modified International Cartilage Repair Society (ICRS) gross grading (n = 3). **(C)** ICRS visual scoring based on panel D (n = 3). **(D)** The immunohistochemical staining against collagen (Col) types I, II and X of the regenerated tissue at 4 and 8 weeks. Mean ± SD.

Release curve of the Ept in the hydrogel in vitro. To quantify the release rate of Ept in the SF/PL hydrogel, the Ept embedded SF/PL Hydrogel was cultured in PBS in dialysis bag (3500 KDa) at 37°C. After culturing for 0.5 days, 1 day, 2 days, 3 days, 4 days and 5 days, the dialysate was collected and equal amount of PBS was supplemented. The content of Ept in the dialysate was detected through bicinchoninic acid (BCA) assay. All release experiments were conducted in triplicates.

Implantation of hydrogel into osteochondral defect in rabbit knee joint. All procedures were in accordance with the Guide for the Care and Use of Laboratory Animals, and were approved by the Institutional Animal Care and Use Committee of Third Military Medical University (Army Medical University, AMUWEC20211199). The operations were performed according to our previous study (Wang et al., 2019). Briefly, 18 skeletally mature New Zealand White rabbits (female, 2 kg) were randomly divided into untreated group (NC, n = 6), experiment group (Ept+, n = 6) and none Ept control group (Ept-, n = 6). Under anesthesia by pentobarbital sodium (50 mg/kg), BMS was simulated by creating osteochondral defect with a sterile electric drill (3.2 mm in diameter, 4 mm in depth) in the femoral trochlear groove of the left hind limb. Visible bleeding was observed to ensure that the defects reached subchondral bone (Figure 2A). For Ept+ and Ept- groups, defects were implanted with Ept contained SF/PL hydrogel (3.2 mm in diameter, 4 mm in height, n = 6) and SF/PL hydrogel alone (n = 6) respectively. At 4 and 8 weeks post implantation, animals were sacrificed (3 rabbits each time point) for histological observation.

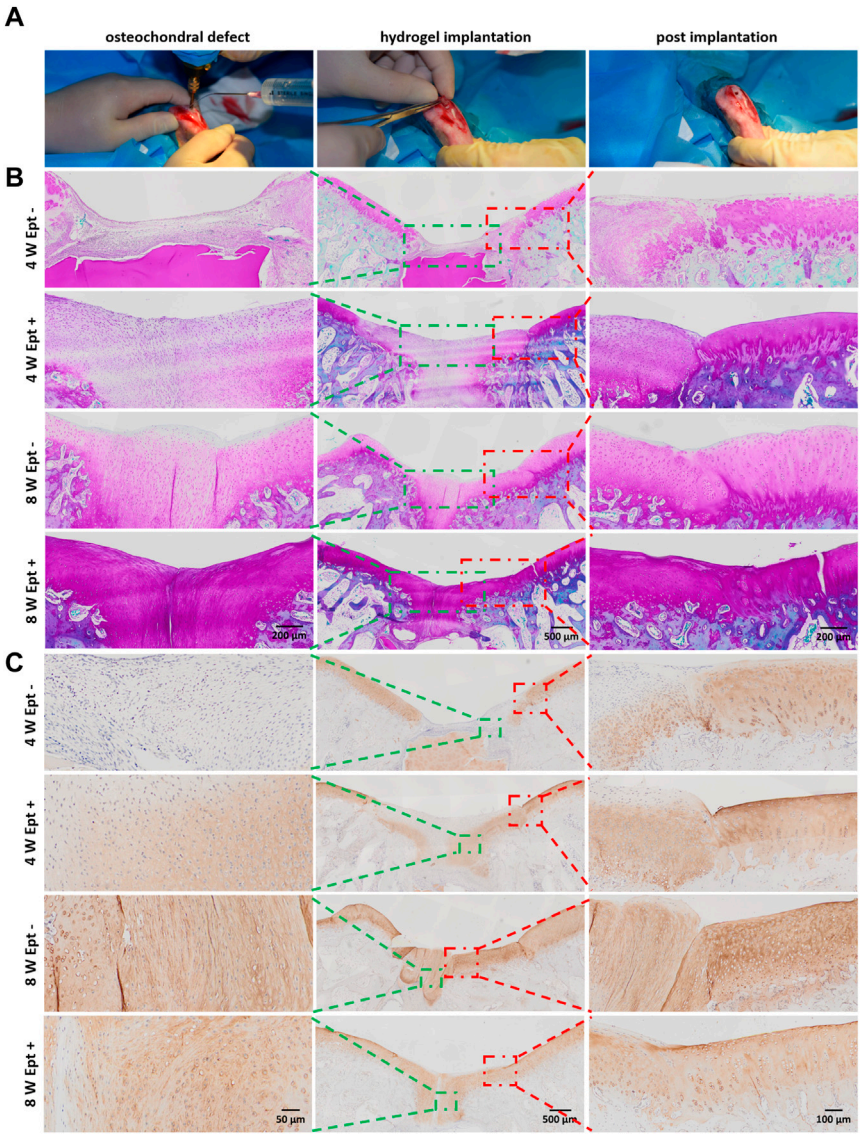

FIGURE 2
Detailed histological analysis indicated that Ept promoted osteochondral regeneration. **(A)** The creation process of chondral defect in trochlear groove and implantation of SF/PL hydrogel. **(B)** Safranin O staining of the knee joints 4 and 8 weeks postoperatively. **(C)** The immunohistochemical staining against Col II. Green rectangle indicates the center of regenerated tissue, red rectangle indicates the junction between regenerated tissue and adjacent articular cartilage.

Gross and histologic evaluation. For histologic analysis, specimens were fixed in 10% formaldehyde, decalcified in EDTA for 3–4 weeks, dehydrated in a graded ethanol series, and embedded in paraffin. Samples were cut in the sagittal plane into 4 mm-thick sections through the center of the defect. Paraffin sections were subjected to hematoxylin and eosin staining, safranin O staining, and immunohistochemical staining of collagen types I, II, and X. Cartilage regeneration was analyzed semi-quantitatively with the modified International Cartilage Repair Society (ICRS) gross grading scale (Wayne scoring system) and ICRS visual histologic assessment scale by 3 blinded observers (X.S., X.W., T.L.) (Mainil-Varlet et al., 2003; Wayne et al., 2005; Lee et al., 2018).

Cell culture of hBMSCs and hOACs. hBMSCs were purchased from American Type Culture Collection (ATCC) and expanded with human mesenchaymal stem cell growth medium (Cyagen, HUXMX-90011). Cells at passage 7 were used in the following experiments. Human osteoarthritic chondrocytes (hOACs) were obtained from primary knee OA patients undergoing total knee replacement after informed consent and approval from the Ethics

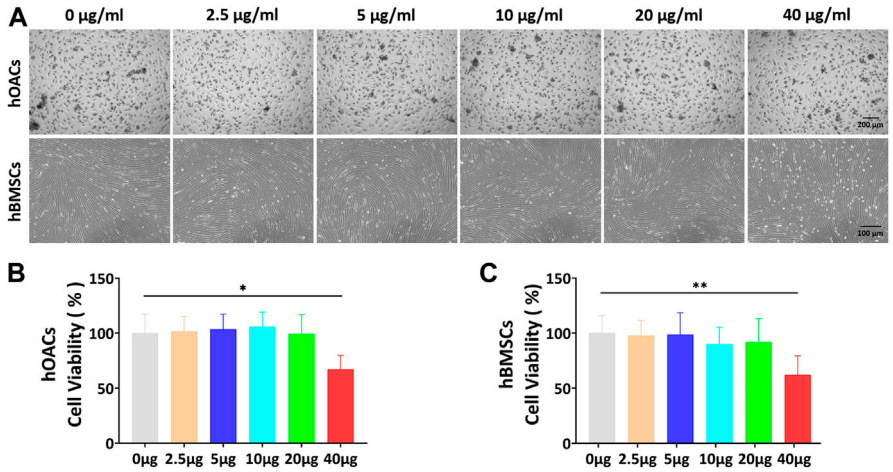

FIGURE 3
In vitro Ept concentration screening for hOACs and hBMSCs treatment. **(A)** Optical microscopy observation of Ept influenced cell viability in hOACs and hBMSCs. **(B and C)** The quantitative analyses of Ept influenced cell viability in hOACs and hBMSCs (n = 6). Mean ± SD, p^* < 0.05, p^{**} < 0.01.

Committee of Southwest Hospital (Chongqing, China). As previously described (Huang et al., 2017), cartilage specimens were washed in PBS three times and then diced. hOACs from the diced tissues were isolated by digesting the matrix overnight in high-glucose DMEM (Invitrogen) supplemented with 0.2% type II collagenase (Sigma). The resulting cell suspension was filtered through a 40-μm cell strainer; collected cells were centrifuged (1000rpm for 5 min), and resuspended in high-glucose DMEM supplemented with 10% FBS (Ausbian). The medium was changed every 2 days hOACs at passage 0 from three patients were used.

In vitro Ept concentration screening. Ept was dissolved in high-glucose DMEM to obtain final concentration of 2.5 μg/ml, 5 μg/ml, 10 μg/ml, 20 μg/ml, and 40 μg/ml hBMSCs or hOACs were seeded on 96-well plates (5× 10^3 cells/well, n = 6 each dosage) 12 h before the addition of Ept. Cell viability was analyzed with Cell Counting Kit–8 (Beyotime) after 48 h coculture. Equal amount of culture medium was used as control.

Effects of Ept on hOACs phenotype. hOACs were seeded on confocal Petri dish (1× 10^5 cells/dish), 30 mm cell-culture dish (1× 10^6 cells/dish), 100 mm cell-culture dish (5× 10^6 cells/dish) and 6-well plates (1× 10^6 cells/well) for immunofluorescent staining, mRNA expression level, protein expression level, and cytokines expression level detection, respectively. The hOACs cells cultured in high glucose DMEM culture medium served as control group (n = 3) and hOACs cultured in high glucose DMEM culture medium supplemented with 20 μg/ml Ept as experimental group (n = 3). After 48 h culture, cells were collected for analysis respectively, and cell culture medium of hOACs at 1, 3 and 7 days were collected for cytokines detection by enzyme-linked immunosorbent assay (ELISA).

Cartilaginous differentiation of hBMSCs. hBMSCs were seeded on confocal Petri dish (1× 10^5 cells/dish), 30 mm cell-culture dish (1× 10^6 cells/dish), and 100 mm cell-culture dish (5× 10^6 cells/dish) for immunofluorescent staining, and detection of mRNA expression level (n = 3), alcian blue staining (n = 5), and protein expression level, respectively. The hBMSCs cultured in chondrogenic differentiation medium were served as control group, chondrogenic differentiation medium with 50 ng/ml TNF-α as TNF-α group, chondrogenic differentiation medium with 20 μg/ml Ept as Ept group, chondrogenic differentiation medium with 50 ng/ml TNF-α and 20 μg/ml Ept as TNF-α+ Ept group. The specific culture medium was changed every day. Cells were collected for analysis after 14-day culture.

Alcian blue staining. According to the manufacturer's instruction, the 30 mm cell-culture dishes were washed twice with phosphate buffer saline (PBS) after removing culture medium. Then the cells were fixed with 4% paraformaldehyde (Biosharp) for 20 min followed by triple PBS wash (5 min each wash). Finally, the cells were incubated with alcian blue working solution (Cyagen, Guangzhou, China) for 30 min and washed with tap water for 5 min. Finally, staining was quantified by solubilizing the sample in 6 M guanidine hydrochloride for 8 h at room temperature (RT). The absorbance at 620 nm was measured by spectrophotometry (Varioskan Flash; Thermo Fisher Scientific) (Gong et al., 2019).

Immunofluorescent staining. Cells were washed with PBS and fixed with 4% formaldehyde for 20 min at RT. Then, the cells were washed three times with cold PBS and treated with Triton X-100 (Beyotime P0096) for 10 min at RT. The cells were washed again three times with Immunol Staining Wash Buffer (Beyotime P0106) and blocked for 1 h with Immunol Staining Blocking

10.3389/fbioe.2022.982894

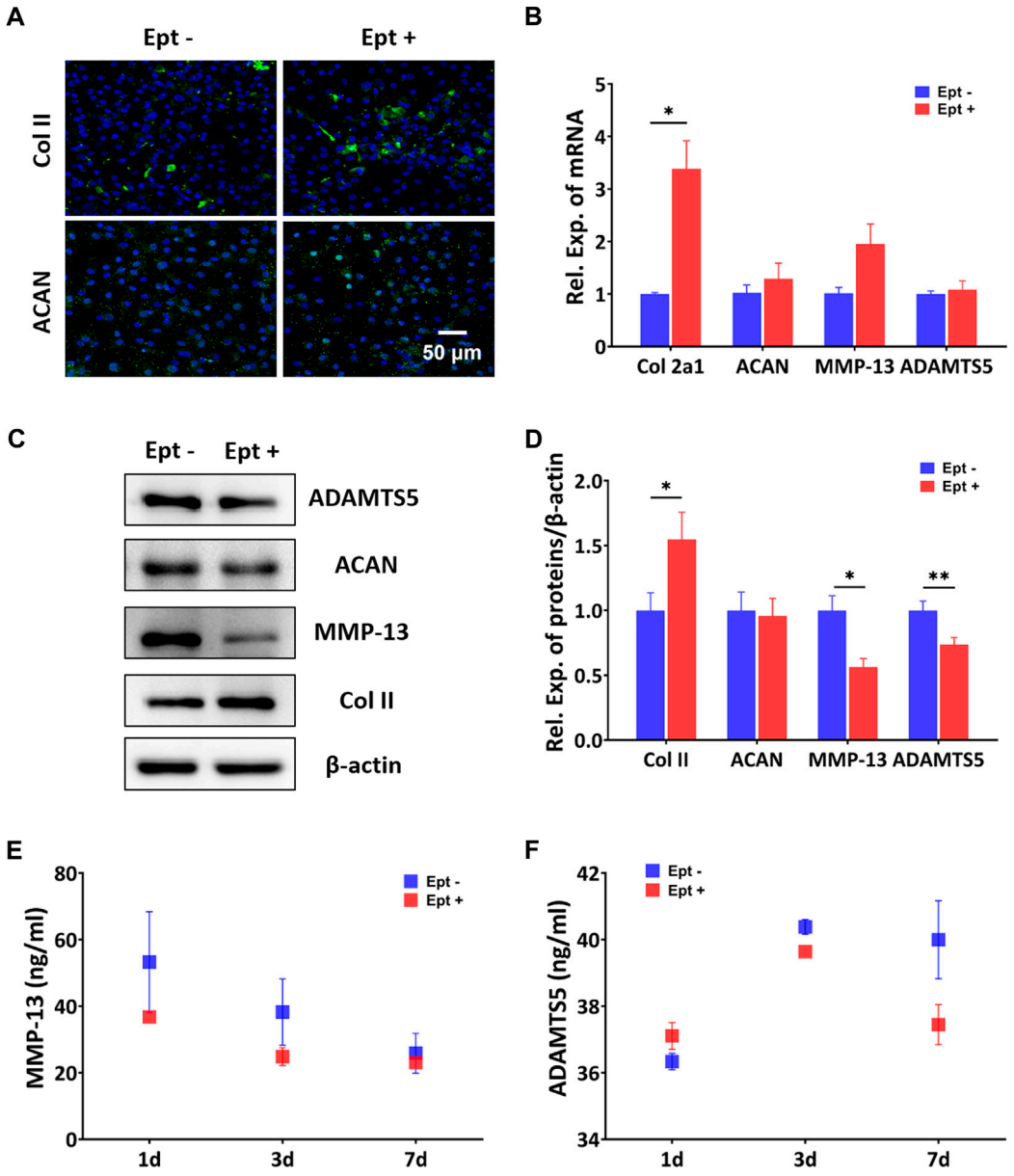

FIGURE 4
Regulatory effects of Ept on catabolic and anabolic dynamics in hOACs. **(A)** Immunofluorescent staining against Col II and aggrecan (ACAN) in Ept or vehicle treated hOACs. **(B)** PCR results of Col II, ACAN, MMP-13, and ADAMTS5 (n = 3). **(C)** Representative western blot detection of ADAMTS5, ACAN, MMP-13, Col II, and β-actin (n = 3). **(D)** Normalized quantitative data from western blot assay in Ept or vehicle treated hOACs. **(E and F)** Elisa detection of ADAMTS5 and MMP-13 levels in culture medium (n = 3). Mean ± SD, p^* < 0.05, p^{**} < 0.01.

Buffer (Beyotime P0102) at RT. Then hOACs were incubated with Collagen II Antibody (Novus NBP1-77795), Aggrecan Antibody (Novus NB600-504) at the dilution of 1:200, 1:200, respectively, and hBMSCs were incubated with Collagen I Antibody (Novus NB600-408), Collagen II Antibody (Novus NBP1-77795), Collagen X Antibody (Abcam ab182563), Aggrecan Antibody (Novus NB600-504), SOX9 Antibody (Abcam ab185966) at the dilution of 1:200 together, both in Immunol Staining Primary Antibody Dilution Buffer (Beyotime P0103) overnight at 4°C. Next, the cells were washed three times with Immunol Staining Wash Buffer and incubated with relative secondary antibody (Abcam ab150117 and Abcam ab150079) for 1 h at RT and DAPI (Beyotime, C1005) for 10 min at 37°C, washed again and imaged by fluorescence microscopy. To quantify the fluorescence intensity, at least three staining images from each group were analyzed using ImageJ (NIH).

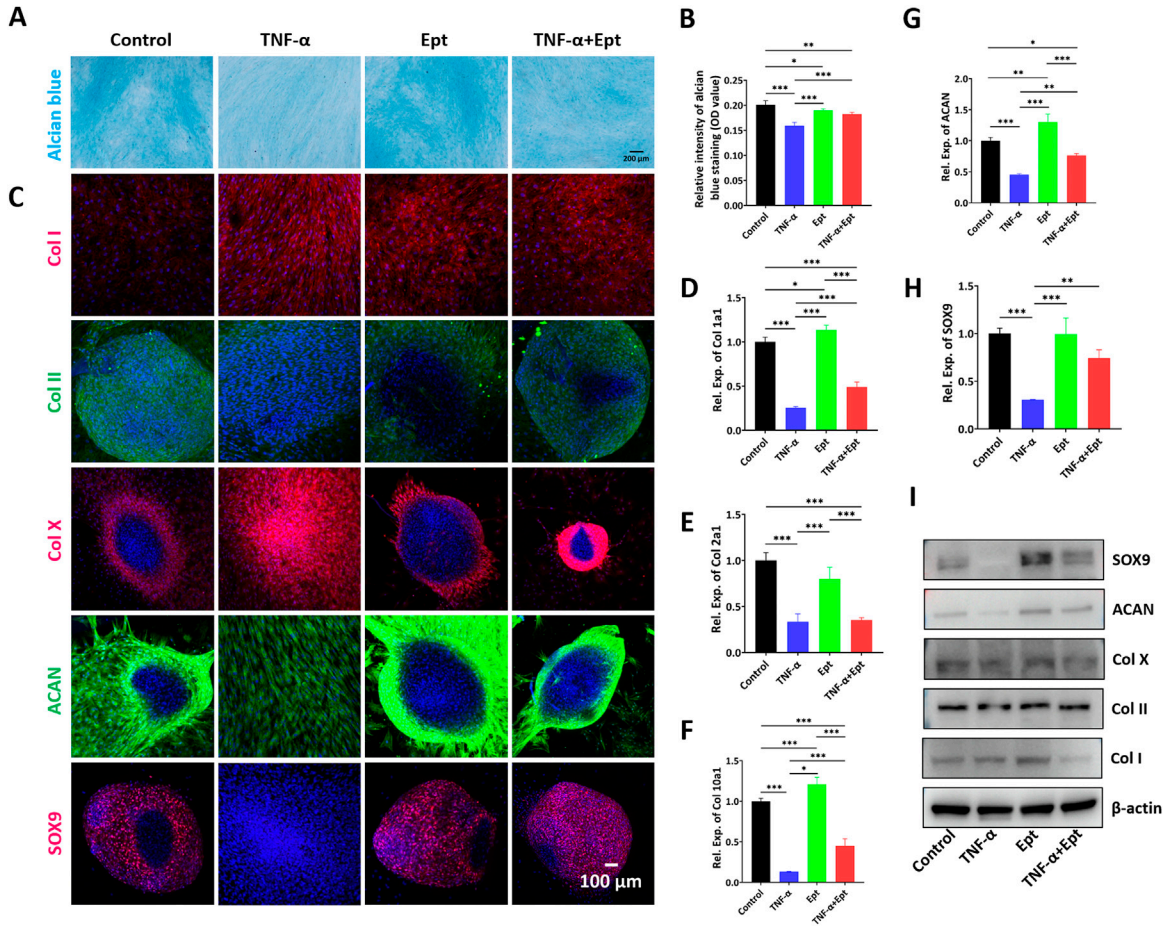

FIGURE 5
Effects of Ept on hBMSCs chondrogenesis. **(A,B)** Representative alcian blue staining and quantitative analysis (n = 5), **(C)** Representative immunofluorescence images of Col I (red color), Col II (green color), Col X (red color), ACAN (green color) and SOX9 (red color), **(D–H)** Relative mRNA expression of Col 1a1, Col 2a1, Col 10a1, ACAN and SOX9 (n = 3), **(I)** Representative western blot detection of Col I, Col II, Col X, ACAN and SOX9 in hBMSCs. Mean ± SD, $p^* < 0.05$, $p^{**} < 0.01$, $p^{***} < 0.001$.

The average fluorescence intensity was determined by dividing the corresponding cell area with the optical density (OD).

Quantitative real-time PCR. Total RNA was extracted from cells using TRIzol reagent (Invitrogen), and the RNA concentration was determined using a NanoDrop-2000 spectrophotometer (Thermo Scientific). Then, the RNA was reverse transcribed into cDNA using Transcriptor cDNA Synth. Kit 2 (Roche, Basel, Switzerland) according to the manufacturer's instruction. Quantitative real-time PCR based on FS Essential DNA Green Master (Roche) was performed using primers specific for Col1a1, Col2a1, Col10a1, SOX9, ACAN and GAPDH (Sangon, Shanghai, China). Primer sequences were as follows: Col1a1 forward, 5′-GCG AGAGCATGACCGATGGAT TC-3′, reverse, 5′-GCCTTCTTG AGGTTGCCAGTCG-3′, Col2a1 forward, 5′-TGCTGCCCAGAT GGCTGGAGGA-3′, reverse, 5′-TGCCTTGAAATCCTTGAG GCCC-3′, Col10a1 forward, 5′-GCCACCAGGCATTCCAGG ATTC-3′, reverse, 5′-GGAAGACCAGGCTCTCCAGAGTG-3′, SOX9 forward, 5′-GACTTCCGCGACGTGGAC-3′, reverse, 5′-GTTGGGCGGCAG GTACTG-3′ACAN forward, 5′-TCCTGG TGTGGCTGCTGTCC-3′, reverse, 5′-TCTGGCTCG GTGGTGAACTCTAG-3'. Each reaction contained 5 μLcDNA, 10 μLFS Essential DNA Green master mix, 3 μlwater (PCR grade), and 1 μL each of forward and reverse primers (10 μM). Reactions were performed in triplicate. Examination of the melting curve for non-specific peaks were performed to ensure specificity of PCR reactions, and mRNA levels were determined from Ct values according to a previously published method (Pfaffl, 2001). Briefly, the results were analyzed according to the 2−ΔΔ CT method and normalized to the housekeeping gene GAPDH. All data were expressed as mean ± standard deviation (SD) and analyzed by one-way ANOVA. Statistical significance was defined with $p < 0.05$.

Western blot. The cells were lysed in RIPA with PMSF (Beyotime, P0013B) on ice for 5 min and removed with a scraper. Then the lysate was centrifuged at 16,000 g for

15 min, and the supernatant was collected. The protein concentration was determined by BCA Protein Assay Kit (Beyotime, P0009). The samples were diluted with SDS-PAGE Sample Loading Buffer (Beyotime, P0015) and kept at 100°C for 10 min 20 μg of protein was loaded in 4–20% SurePAGE, Bis-Tris gels (GenScript, M00655) and run for 30 min at 200 V followed by transferring onto a PVDF membrane at 200 mA. The membrane was washed three times with 2% v/v TBST (tris-buffered saline with Tween-20). Then, the membrane was blocked with Western Blocking Buffer (Beyotime P0023B)for 1 h at RT, washed with TBST, and incubated with mouse monoclonal antibody anti-actin (Santa Cruz,sc-47778), Collagen I Antibody (Novus NB600-408), Collagen II Antibody (Novus NBP1-77795), Collagen X Antibody (Abcam ab182563), Aggrecan Antibody (Novus NB600-504), SOX9 Antibody (Abcam ab185966), MMP-13 Antibody (Novus NBP2-45887), ADAMTS5 Antibody (Novus NBP2-15286) diluted with Primary Antibody Dilution Buffer (Beyotime P0023A) at a dilution of 1:1000, 1:1000, 1:2000, 1:1000, 1:5000, 1:2000, and 1:5000, respectively overnight at 4°C shaker. Next, the membrane was washed four times with TBST for 10 min, incubated with the mouse anti-rabbit IgG-HRP (Santa Cruz, sc-2357, 1:10000), goat anti-mouse IgG-HRP (Santa Cruz, sc-2005,1:10000) for 1 h at RT, washed again four times, and visualized with Western ECL Substrate (Thermo Scientific) for chemiluminescence.

ELISA. The collected cell culture medium was centrifuged at 2000g for 15 min, then the supernatant was detected by ADAMTS5 ELISA kit (Cusabio, CSB-EL001312HU) and MMP-13 ELISA kit (Cusabio, CSB-E04674 h) according to the manufacture's instruction.

Statistical analysis. Statistical analyses were performed using Graphpad prism software (GraphPad Software, CA, United States, Version 6). Graphical results were displayed as means ± SD. All data were assessed for normality using the Kolmogorov-Smirnov test and for homoscedasticity using the F-test. The statistical significance differences between Ept+ and Ept- groups were determined by Student *t*-test for parametric data, and by Mann-Whitney test for non-parametric data. The Welch's correction was applied for variables with unequal variance. The statistical significance differences between multiple groups were determined by One-way ANOVA test and Fisher's LSD post-test for parametric data, and by Kruskal Wallis test and Dunn's multiple comparisons post-test for non-parametric data. In all cases, statistical significance was defined with $p < 0.05$.

Results

Gross and histologic evaluation

During the 8-week experiment, all surgical incisions in the rabbits healed well without any infection or death. At 4 weeks and 8 weeks after operation, rabbits were sacrificed by carbon dioxide suffocation, and the gross appearance of the joint samples were observed followed by histologic evaluation to assess the effect of Ept in promoting osteochondral defect repair of knee joint.

At 4 weeks postoperatively, the osteochondral defects in the Ept + group were almost completely covered with newly formed tissue while partially were covered in the Ept- group and NC group. At 8 weeks postoperatively, the osteochondral defects in all groups were completely covered with new cartilage tissue. The regenerated tissue in the Ept + group was similar to the surrounding native cartilage, indicating the formation of hyaline cartilage-like tissue, whereas the regenerated tissue in the Ept- group and NC group was irregular and the surrounding tissue was degenerated (Figure 1A). The macroscopic evaluation was confirmed by the averaged ICRS score. Both at 4 weeks and 8 weeks, the ICRS scores of the Ept + group were significantly higher ($n = 3$, $p < 0.001$) than those of Ept- group (Figure 1B).

Histologic analysis of osteochondral regeneration was carried out *via* hematoxylin and eosin staining and safranin O staining. At 4 weeks postoperatively, both staining showed distinct borders between repaired tissue and surrounding tissue, and the newly formed tissue in Ept + group was thicker than that in Ept- group. At 8 weeks, the surface of the defects became smooth in comparison with that at 4 weeks, and the tissue integration and thickness of Ept + group were superior to that in Ept- group and NC group (Figure 1A). As the ICRS visual histologic assessment showed (Figure 1C), better osteochondral defect repair was observed in Ept + group than that in the other two groups both at 4 weeks ($n = 3$, $p < 0.001$) and 8 weeks ($n = 3$, $p < 0.001$).

Qualitative analysis of type II, I, and X collagen expression was conducted upon immunohistochemical staining. No obvious difference in type I and type X collagen expression in regenerated cartilage between Ept+ and Ept- groups at 4 weeks and 8 weeks, as barely positive staining was found. Positive staining of type II collagen in the Ept + group was noticed at 4 weeks, but not in the Ept- group; at 8 weeks postoperatively, both groups showed strong staining for type II collagen with superior deposition and uniform texture in Ept + group (Figure 1D).

To further explore the mechanism of Ept in promoting osteochondral defect repair of rabbit knee joint, detailed differences in cytology and histology were analyzed by safranin O staining and immunohistochemical staining. At 4 weeks postoperatively, compared with Ept- group, intensive cell density in the newly formed cartilage tissue with strong safranin O staining was observed in Ept + group. At 8 weeks postoperatively, significant cartilage matrix deposition was found in the regenerated tissue of Ept + group, and the texture was close to that of native cartilage (Figure 2B, green rectangle). Differences were also found in the junction of regenerated tissue and native cartilage. The boundary between newly formed tissue and native cartilage was obvious in both groups at 4 weeks postoperatively. However, abnormal cellular

distribution with weak staining of cartilage matrix in adjacent cartilage of Ept- group was noticed. At 8 weeks postoperatively, compared with distinct boundary in Ept- group, uniform integration was found in Ept + group (Figure 2B, red rectangle). The trend of type II collagen expression was similar to proteoglycan at both defect sites and adjacent cartilage. At both 4 and 8 weeks postoperatively, stronger type II collagen expression was observed in Ept + group than Ept- group at defect sites (Figure 2C).

Influence of ept on anabolism and catabolism in hOACs

CCK-8 assay was used to screen the optimal dose of Ept for culturing hOACs and hBMSCs. After culturing hOACs or hBMSCs with different concentration of Ept (0 μg/ml, 5 μg/ml, 10 μg/ml, 20 μg/ml, and 40 μg/ml) for 48h, the morphological differences of the cells were observed under optical microscope (Figure 3A). For CCK-8 assay, the OD value of hOACs and hBMSCs treated with 40 μg/ml Ept was significantly lower than those in the other groups (Figure 3B and C, n = 6). These observation indicated the inhibitory effect of Ept on viability of hOACs and hBMSCs at 40 μg/ml. Immunofluorescent staining was performed on type II collagen and ACAN after 48 h treatment of Ept in hOACs. As shown in Figure 4A, stronger fluorescence was detected in Ept treated group. Cartilage matrix anabolic genes Col2a1 and ACAN, and cartilage matrix catabolic genes MMP-13 and ADAMTS5 were detected by PCR. As shown in Figure 4B (n = 3), Ept significantly promoted Col2a1 gene expression ($p = 0.011$), and other three genes showed a slight increase tendency of expression ($p > 0.05$). In protein level, Ept significantly promoted type II collagen synthesis (Figure 4C; Figure 4D, n = 3, $p = 0.018$), whereas decreased ACAN ($p = 0.15$), MMP-13 ($p = 0.012$) and ADAMTS5 ($p = 0.005$) protein synthesis (Figures 4C,D). Furthermore, based on ELISA assay, level of MMP-13 in culture medium was down-regulated at day 1 and 3, and ADAMTS5 was down-regulated at day 3 and 7 post Ept treatment (Figures 4E,F, n = 3). As the secretion of MMP-13 and ADAMTS5 after synthesis in chondrocytes was regulated by external environment (Chao et al., 2011; Nam et al., 2016), Figure 4E showed different statistic difference, but shared the same tendency that Ept treatment decreased the expression of MMP-13 and ADAMTS5 in hOACs.

Influence of ept on hBMSCs chondrogenesis

After chondrogenic inducing culture for 14 days, alcian blue staining was carried out to verify the cartilage matrix deposition in hBMSCs. As shown in Figure 5A, compared with control group, the TNF-α group showed the weakest staining intensity. Addition of Ept attenuated the negative effect of TNF-α on cartilage matrix deposition (Figure 5B). During 2-week chondrogeic induction, hBMSCs continuously secreted extracellular matrix, and spontaneously form pellet morphology. However, TNF-α inhibited the pellet formation in hBMSCs. The fluorescent intensity of type II collagen, ACAN and SOX9 was weaker in TNF-α group, while type I and type X collagen was stronger than the other three groups (Figure 5C). The chondrogenic markers were quantified by RT-qPCR (Figures 5D–H) and Western Blot (Figure 5I). In accordance with alcian blue and immunofluorescent stainings, the lowest gene expression of Col2a1, ACAN, and protein level of type II collagen, ACAN were observed in TNF-α group (Supplementary Figure S2). Ept attenuated the negative effect of TNF-α on chondrogenic markers. In addition, Ept alone promoted hBMSCs chondrogenic differentiation as Ept group showed the highest ACAN gene expression and type II collagen synthesis.

Discussion

In the present study, the Ept embedded SF/PL hydrogel was fabricated and utilized to verify the influence of inflammatory environment on the articular cartilage regeneration induced by BMS. The addition of Ept into SF/PL hydrogel during BMS was proven to promote articular cartilage regeneration in a rabbit osteochondral defect model. *In vitro* study showed that Ept improved the cartilaginous matrix deposition and restrain catabolism of hOACs, as well as promoted chondrogenesis of hBMSCs in the presence of TNF-α.

Due to the limited intrinsic healing capacity of articular cartilage, surgical intervention such as BMS is required for treatment of focal articular lesions, osteochondritis dissecans, and degenerative cartilage lesions (van Eekeren et al., 2012). During BMS, drilling into the debrided chondral bone induces hematoma effusion containing BMSCs, growth factors, and cytokines at surgical site. Considering the insufficient mechanical property of blood colt, scaffolds were employed to stabilize the colt during BMS in both clinical and laboratory studies (Hoemann et al., 2005). To enhance the outcome of BMS, the previously fabricated SF/PL hydrogel served as bio-scaffold for both BMSCs adhesion and gradual release of Ept in this study. SF is a natural biopolymer extracted from Bombyx mori cocoons, has been regarded as one of the most promising candidates for tissue engineering and regenerative medicine due to its good biocompatibility, excellent mechanical strength, and slow degradation (Huang et al., 2018; Zhou et al., 2018). Pullulan is a neutral, biodegradable and non-toxic polysaccharide and widely used in biomedical applications (Singh et al., 2017). In our previous study, SF and tyramine substituted carboxymethylated pullulan were enzyme crosslinked. The compressive modulus of fabricated SF/PL hydrogel was 71.4 ± 9.3 kPa, which was in the range of that of osteochondral tissue. Slow degradation of the hydrogel in protease XIV solution retained porous microstructure, which enabled BMSCs

ingrowth, chondrogenic differentiation and cartilage matrix deposition (Li et al., 2018).

The main purpose of this study was to evaluate the anti-inflammatory efficacy of Ept in promoting cartilage repair based on BMS. In order to simulate the BMS procedure, osteochondral defect in trochlear groove was created. The acute osteochondral injury induced by BMS significantly increased the expression of inflammatory cytokines in synovial fluid. Clinical evidence indicated that knees with osteochondral fracture had immediate increment in concentrations of TNF-α compared with knees without osteochondral fracture (Sward et al., 2014). During BMS procedure, bone marrow effusion, along with damage associated molecular patterns (DAMPs) that arose from tissue injury were released into articular cavity. Proinflammatory cytokines involved in traumatic reaction, such as IL-1β and TNF-α produced by chondrocytes, mononuclear cells, osteoblasts and synovial tissues, induce the production of a number of inflammatory and catabolic factors (Sahu et al., 2019). In a recent study, microfracture failure was found to have a positive correlation with TNF-α revealed by correlation analyses between the osteoarthritis research society international (OARSI) total score and the cytokines measurement (Danilkowicz et al., 2021). In our study, the ICRS Gross Scoring and the ICRS Histological Scoring results confirmed that addition of Ept in SF/PL hydrogel was beneficial to cartilage regeneration. To mimic the clinical practice, the concentration of Ept in SF/PL hydrogel was decided by converting equivalent dosage between rabbit and human according to body surface area. As the recommended dosage of Ept for adult is 50 mg/week, about 4 mg of Ept was needed for rabbit in the present study. The release experiment showed that the fabricated SF/PL hydrogel could continuously release about 85% of the embedded Ept in 5 days (Figure S1), which means the scaffold design (4 mg of Ept embedded in 200 ml SF/PL hydrogel) is suitable to antagonize the chronic proinflammatory effect of TNF-α in our rabbit model. Detailed histological analysis revealed that the cellular density in the regenerated tissue was higher in Ept + group, and most cells were spatially distributed in the newly formed lacuna-like structure. Moreover, as evidenced by safranin-O and IHC against type II collagen data, the newly formed hyaline cartilage tissue was seamlessly integrated with adjacent native tissue in the Ept + group, indicating that Ept might inhibit catabolism and promote anabolism of chondrocytes in an acute injury induced inflammatory microenvironment.

The negative effects of catabolic cytokines on cartilage have been well documented. Elevated levels of IL-6 and TNF-α in the injured cartilage were implicated in the IL-6 and TNF-α-mediated cartilage degradation (Sahu et al., 2019). To further illustrate the influence of TNF-α on BMS induced cartilage regeneration, the effect of Ept on chondrocyte phenotype, and on hBMSCs chondrognesis were assessed *in vitro*. Our data indicated that Ept treatment significantly promoted both gene and protein expression of type II collagen in hOACs, while decreased the protein levels of MMP-13 and ADAMTS5. The regulatory effect of Ept between catabolic and anabolic dynamics in chondrocyte might explain the superior integration in Ept + group from *in vivo* observation. The regeneration of articular cartilage induced by BMS was attributed to BMSCs chondrogenesis. Instead of chondrocytes migrated from adjacent articular cartilage, autoradiography using ^{3}H-thymidine and ^{3}H-cytidine showed that the repair was achieved by the differentiation of mesenchymal cells from the underlying bone marrow (Shapiro et al., 1993). Hence, the addition of Ept might have a positive effect on BMSCs chondrogenesis in the inflammatory microenvironment. In accordance with previous study (Heldens et al., 2012), TNF-α was found to inhibit hBMSCs chondrogenesis in control group. Whereas, addition of Ept significantly reversed the negative impact of TNF-α, as illustrated by alcian blue staining, type II collagen and aggrecan stainings. These results were complied with histological data, in which positive and uniform deposition of type II collagen was noticed in the Ept + group alone. However, significant increase in both type I and II collagen post Ept treatment alone was noticed in our data. As evidenced by previous study (Wu et al., 2021), this contradiction between gene and protein levels indicated posttranscriptional modification of these genes during chondrogenetic differentiation. In addition, we noticed that the spatial distribution of hypertrophic marker, type X collagen was different among groups. Although the gene expression level of type X collagen was elevated after Ept treatment (Figure 5F and I), the distribution was mainly in the peripheral area of deposited ECM in untreated and Ept treated hBMSCs. This observation along with previous studies (Knuth et al., 2019; Côrtes et al., 2021) suggested that ECM remolding by type X collagen was potentially required during hyaline cartilage matrix expansion (Figure 5C, COL II & ACAN).

Conclusion

In the present study, SF/PL hydrogel containing Ept was fabricated, and the synergistical effect of SF/PL hydrogel and Ept was verified by BMS simulation. The addition of Ept into SF/PL hydrogel was proven to promote articular cartilage regeneration *in vivo*, potentially attributed to regulation of catabolic and anabolic dynamics in adjacent chondrocytes and enhancement of BMSCs chondrogenesis. Our finding might provide novel strategy for BMS augmentation, and expand the indication of current pharmaceuticals.

Data availability statement

The original contributions presented in the study are included in the article/Supplementary Materials, further inquiries can be directed to the corresponding authors.

Ethics statement

The studies involving human participants were reviewed and approved by Ethics Committee of the First Affiliated Hospital of Army Medical University. PLA. The patients/participants provided their written informed consent to participate in this study. The animal study was reviewed and approved by Laboratory Animal Welfare and Ethics Committee of Third Military Medical University.

Author contributions

XS: Methodology, Investigation, Formal analysis, Writing—original draft. XW: Methodology, Investigation, Writing—original draft. LG: Conceptualization, Resources. TL: Investigation. YH: Methodology. JY: Investigation. ZT: Investigation. ZF: Investigation. LY: Conceptualization, Supervision. GC: Conceptualization, Supervision. CC: Conceptualization, Resources, Project Administration. XG: Conceptualization, Writing—original draft, Writing—review and editing, Supervision, Funding acquisition.

Funding

This work was supported by Nature Science Foundation of Chongqing (cstc2021jcyj-msxmX0135).

Acknowledgments

We thank DF, and RX for helpful suggestions. We thank the technical support in histologic staining offered by Knorigene Technologies.

Conflict of interest

The authors declare that the research was conducted in the absence of any commercial or financial relationships that could be construed as a potential conflict of interest.

Publisher's note

All claims expressed in this article are solely those of the authors and do not necessarily represent those of their affiliated organizations, or those of the publisher, the editors and the reviewers. Any product that may be evaluated in this article, or claim that may be made by its manufacturer, is not guaranteed or endorsed by the publisher.

Supplementary material

The Supplementary Material for this article can be found online at: https://www.frontiersin.org/articles/10.3389/fbioe.2022.982894/full#supplementary-material

References

Armiento, A. R., Alini, M., and Stoddart, M. J. (2019). Articular fibrocartilage - why does hyaline cartilage fail to repair? *Adv. Drug Deliv. Rev.* 146, 289–305. doi:10.1016/j.addr.2018.12.015

Armiento, A. R., Stoddart, M. J., Alini, M., and Eglin, D. (2018). Biomaterials for articular cartilage tissue engineering: Learning from biology. *Acta Biomater.* 65, 1–20. doi:10.1016/j.actbio.2017.11.021

Chao, P. Z., Hsieh, M. S., Cheng, C. W., Lin, Y. F., and Chen, C. (2011). Regulation of MMP-3 expression and secretion by the chemokine eotaxin-1 in human chondrocytes. *J. Biomed. Sci.* 18 (1), 86. doi:10.1186/1423-0127-18-86

Côrtes, I., Matsui, R. A. M., Azevedo, M. S., Beatrici, A., Souza, K. L. A., Launay, G., et al. (2021). A scaffold- and serum-free method to mimic human stable cartilage validated by secretome. *Tissue Eng. Part A* 27 (5-6), 311–327. doi:10.1089/ten.tea.2018.0311

Danilkowicz, R. M., Allen, N. B., Grimm, N., Nettles, D. L., Nunley, J. A., Easley, M. E., et al. (2021). Histological and inflammatory cytokine analysis of osteochondral lesions of the talus after failed microfracture: Comparison with fresh allograft controls. *Orthop. J. Sports Med.* 9 (10), 232596712110405. doi:10.1177/23259671211040535

DeFrate, L. E., Kim-Wang, S. Y., Englander, Z. A., and McNulty, A. L. (2019). Osteoarthritis year in review 2018: Mechanics. *Osteoarthr. Cartil.* 27 (3), 392–400. doi:10.1016/j.joca.2018.12.011

Garrison, L., and McDonnell, N. D. (1999). Etanercept: Therapeutic use in patients with rheumatoid arthritis. *Ann. Rheum. Dis.* 58 (1), I65–I69. doi:10.1136/ard.58.2008.i65

Glass, K. A., Link, J. M., Brunger, J. M., Moutos, F. T., Gersbach, C. A., and Guilak, F. (2014). Tissue-engineered cartilage with inducible and tunable immunomodulatory properties. *Biomaterials* 35 (22), 5921–5931. doi:10.1016/j.biomaterials.2014.03.073

Gong, X., Li, G., Huang, Y., Fu, Z., Song, X., Chen, C., et al. (2019). Synergistically regulated spontaneous calcium signaling is attributed to cartilaginous extracellular matrix metabolism. *J. Cell. Physiol.* 234 (6), 9711–9722. doi:10.1002/jcp.27657

Heldens, G. T., Blaney Davidson, E. N., Vitters, E. L., Schreurs, B. W., Piek, E., van den Berg, W. B., et al. (2012). Catabolic factors and osteoarthritis-conditioned medium inhibit chondrogenesis of human mesenchymal stem cells. *Tissue Eng. Part A* 18 (1-2), 45–54. doi:10.1089/ten.tea.2011.0083

Hoemann, C. D., Hurtig, M., Rossomacha, E., Sun, J., Chevrier, A., Shive, M. S., et al. (2005). Chitosan-glycerol phosphate/blood implants improve hyaline cartilage repair in ovine microfracture defects. *J. Bone Jt. Surg.* 87 (12), 2671–2686. doi:10.2106/jbjs.d.02536

Huang, J., Liu, F., Su, H., Xiong, J., Yang, L., Xia, J., et al. (2022). Advanced nanocomposite hydrogels for cartilage tissue engineering. *Gels* 8 (2), 138. doi:10.3390/gels8020138

Huang, S., Song, X., Li, T., Xiao, J., Chen, Y., Gong, X., et al. (2017). Pellet coculture of osteoarthritic chondrocytes and infrapatellar fat pad-derived mesenchymal stem cells with chitosan/hyaluronic acid nanoparticles promotes chondrogenic differentiation. *Stem Cell Res. Ther.* 8 (1), 264. doi:10.1186/s13287-017-0719-7

Huang, W., Ling, S., Li, C., Omenetto, F. G., and Kaplan, D. L. (2018). Silkworm silk-based materials and devices generated using bio-nanotechnology. *Chem. Soc. Rev.* 47 (17), 6486–6504. doi:10.1039/c8cs00187a

Hurst, J., Steadman, J., O'Brien, L., Rodkey, W., and Briggs, K. (2010). Rehabilitation following microfracture for chondral injury in the knee. *Clin. sports Med.* 29 (2), 257–265. viii. doi:10.1016/j.csm.2009.12.009

Kawaguchi, A., Nakaya, H., Okabe, T., Tensho, K., Nawata, M., Eguchi, Y., et al. (2009). Blocking of tumor necrosis factor activity promotes natural repair of osteochondral defects in rabbit knee. *Acta Orthop.* 80 (5), 606–611. doi:10.3109/17453670903350115

Knuth, C. A., Andres Sastre, E., Fahy, N. B., Witte-Bouma, J., Ridwan, Y., Strabbing, E. M., et al. (2019). Collagen type X is essential for successful mesenchymal stem cell-mediated cartilage formation and subsequent endochondral ossification. *Eur. Cell. Mat.* 38, 106–122. doi:10.22203/ecm.v038a09

Kwon, H., Brown, W. E., Lee, C. A., Wang, D., Paschos, N., Hu, J. C., et al. (2019). Surgical and tissue engineering strategies for articular cartilage and meniscus repair. *Nat. Rev. Rheumatol.* 15 (9), 550–570. doi:10.1038/s41584-019-0255-1

Lee, B. H., Park, J. N., Lee, E. J., Moon, Y. W., and Wang, J. H. (2018). Therapeutic efficacy of spherical aggregated human bone marrow-derived mesenchymal stem cells cultured for osteochondral defects of rabbit knee joints. *Am. J. Sports Med.* 46 (9), 2242–2252. doi:10.1177/0363546518780991

Li, T., Song, X., Weng, C., Wang, X., Wu, J., Sun, L., et al. (2018). Enzymatically crosslinked and mechanically tunable silk fibroin/pullulan hydrogels for mesenchymal stem cells delivery. *Int. J. Biol. Macromol.* 115, 300–307. doi:10.1016/j.ijbiomac.2018.04.046

Liu, Y., Xu, L., Hu, L., Chen, D., Yu, L., Li, X., et al. (2020). Stearic acid methyl ester promotes migration of mesenchymal stem cells and accelerates cartilage defect repair. *J. Orthop. Transl.* 22, 81–91. doi:10.1016/j.jot.2019.09.008

Mainil-Varlet, P., Aigner, T., Brittberg, M., Bullough, P., Hollander, A., Hunziker, E., et al. (2003). Histological assessment of cartilage repair: A report by the histology endpoint committee of the international cartilage repair society (ICRS). *J. Bone Jt. Surgery-American Volume* 85-A (2), 45–57. doi:10.2106/00004623-200300002-00007

Makris, E., Gomoll, A., Malizos, K., Hu, J., and Athanasiou, K. (2015). Repair and tissue engineering techniques for articular cartilage. *Nat. Rev. Rheumatol.* 11 (1), 21–34. doi:10.1038/nrrheum.2014.157

Mithoefer, K., McAdams, T., Williams, R. J., Kreuz, P. C., and Mandelbaum, B. R. (2009). Clinical efficacy of the microfracture technique for articular cartilage repair in the knee: An evidence-based systematic analysis. *Am. J. Sports Med.* 37 (10), 2053–2063. doi:10.1177/0363546508328414

Nair, A., Morsy, M. A., and Jacob, S. (2018). Dose translation between laboratory animals and human in preclinical and clinical phases of drug development. *Drug Dev. Res.* 79 (8), 373–382. doi:10.1002/ddr.21461

Nair, A. B., Jacob, S., and Pharmacy, C. (2016). A simple practice guide for dose conversion between animals and human. *J. Basic Clin. Pharm.* 7 (2), 27–31. doi:10.4103/0976-0105.177703

Nam, D. C., Kim, B. K., Lee, H. J., Shin, H. D., Lee, C. J., and Hwang, S. C. (2016). Effects of prunetin on the proteolytic activity, secretion and gene expression of MMP-3 *in vitro* and production of MMP-3 *in vivo*. *Korean J. Physiol. Pharmacol.* 20 (2), 221–228. doi:10.4196/kjpp.2016.20.2.221

Pfaffl, M. (2001). A new mathematical model for relative quantification in real-time RT-PCR. *Nucleic acids Res.* 29 (9), e45–e45. doi:10.1093/nar/29.9.e45

Quicke, J., Conaghan, P., Corp, N., and Peat, G. (2022). Osteoarthritis year in review 2021: Epidemiology & therapy. *Osteoarthr. Cartil.* 30 (2), 196–206. doi:10.1016/j.joca.2021.10.003

Sahranavard, M., Sarkari, S., Safavi, S., Ghorbani, F., Ms, F., Sarkari, S., et al. (2022). Three-dimensional bio-printing of decellularized extracellular matrix-based bio-inks for cartilage regeneration: A systematic review. *Biomater. Transl.* 3 (2), 105–115. doi:10.12336/biomatertransl.2022.02.004

Sahu, N., Viljoen, H. J., and Subramanian, A. (2019). Continuous low-intensity ultrasound attenuates IL-6 and TNFα-induced catabolic effects and repairs chondral fissures in bovine osteochondral explants. *BMC Musculoskelet. Disord.* 20 (1), 193. doi:10.1186/s12891-019-2566-4

Shapiro, F., Koide, S., and Glimcher, M. J. (1993). Cell origin and differentiation in the repair of full-thickness defects of articular cartilage. *J. Bone Jt. Surg.* 75 (4), 532–553. doi:10.2106/00004623-199304000-00009

Sharma, N., Drobinski, P., Kayed, A., Chen, Z., Kjelgaard-Petersen, C. F., Gantzel, T., et al. (2020). Inflammation and joint destruction may be linked to the generation of cartilage metabolites of ADAMTS-5 through activation of toll-like receptors. *Osteoarthr. Cartil.* 28 (5), 658–668. doi:10.1016/j.joca.2019.11.002

Shealy, D. J., Wooley, P. H., Emmell, E., Volk, A., Rosenberg, A., Treacy, G., et al. (2002). Anti-TNF-alpha antibody allows healing of joint damage in polyarthritic transgenic mice. *Arthritis Res.* 4 (5), R7. doi:10.1186/ar430

Singh, R. S., Kaur, N., Rana, V., and Kennedy, J. F. (2017). Pullulan: A novel molecule for biomedical applications. *Carbohydr. Polym.* 171, 102–121. doi:10.1016/j.carbpol.2017.04.089

Smolen, J., Landewé, R., Bijlsma, J., Burmester, G., Chatzidionysiou, K., Dougados, M., et al. (2017). EULAR recommendations for the management of rheumatoid arthritis with synthetic and biological disease-modifying antirheumatic drugs: 2016 update. *Ann. Rheum. Dis.* 76 (6), 960–977. doi:10.1136/annrheumdis-2016-210715

Sward, P., Struglics, A., Englund, M., Roos, H. P., and Frobell, R. B. (2014). Soft tissue knee injury with concomitant osteochondral fracture is associated with higher degree of acute joint inflammation. *Am. J. Sports Med.* 42 (5), 1096–1102. doi:10.1177/0363546514524924

Tamaddon, M., Gilja, H., Wang, L., Oliveira, J. M., Sun, X., Tan, R., et al. (2020). Osteochondral scaffolds for early treatment of cartilage defects in osteoarthritic joints: From bench to clinic. *Biomater. Transl.* 1 (1), 3–17. doi:10.3877/cma.j.issn.2096-112X.2020.01.002

Tong, W., Zhang, X., Zhang, Q., Fang, J., Liu, Y., Shao, Z., et al. (2020). Multiple umbilical cord-derived MSCs administrations attenuate rat osteoarthritis progression via preserving articular cartilage superficial layer cells and inhibiting synovitis. *J. Orthop. Transl.* 23, 21–28. doi:10.1016/j.jot.2020.03.007

van Eekeren, I. C., Reilingh, M. L., and van Dijk, C. N. (2012). Rehabilitation and return-to-sports activity after debridement and bone marrow stimulation of osteochondral talar defects. *Sports Med.* 42 (10), 857–870. doi:10.2165/11635420-000000000-00000

Wagenbrenner, M., Mayer-Wagner, S., Rudert, M., Holzapfel, B. M., and Weissenberger, M. (2021). Combinations of hydrogels and mesenchymal stromal cells (MSCs) for cartilage tissue engineering-A review of the literature. *Gels* 7 (4), 217. doi:10.3390/gels7040217

Wang, T., and He, C. (2018). Pro-inflammatory cytokines: The link between obesity and osteoarthritis. *Cytokine Growth Factor Rev.* 44, 38–50. doi:10.1016/j.cytogfr.2018.10.002

Wang, X., Song, X., Li, T., Chen, J., Cheng, G., Yang, L., et al. (2019). Aptamer-functionalized bioscaffold enhances cartilage repair by improving stem cell recruitment in osteochondral defects of rabbit knees. *Am. J. Sports Med.* 47 (10), 2316–2326. doi:10.1177/0363546519856355

Wayne, J. S., McDowell, C. L., Shields, K. J., and Tuan, R. S. (2005). *In vivo* response of polylactic acid-alginate scaffolds and bone marrow-derived cells for cartilage tissue engineering. *Tissue Eng.* 11 (5-6), 953–963. doi:10.1089/ten.2005.11.953

Wu, C. L., Dicks, A., Steward, N., Tang, R., Katz, D. B., Choi, Y. R., et al. (2021). Single cell transcriptomic analysis of human pluripotent stem cell chondrogenesis. *Nat. Commun.* 12 (1), 362. doi:10.1038/s41467-020-20598-y

Zhou, Z., Zhang, S., Cao, Y., Marelli, B., Xia, X., and Tao, T. H. (2018). Silk materials: Engineering the future of silk materials through advanced manufacturing (adv. Mater. 33/2018). *Adv. Mat.* 30, 1870250. doi:10.1002/adma.201870250

Frontiers in
Bioengineering and Biotechnology

Accelerates the development of therapies, devices, and technologies to improve our lives

A multidisciplinary journal that accelerates the development of biological therapies, devices, processes and technologies to improve our lives by bridging the gap between discoveries and their application.

Discover the latest Research Topics

See more →

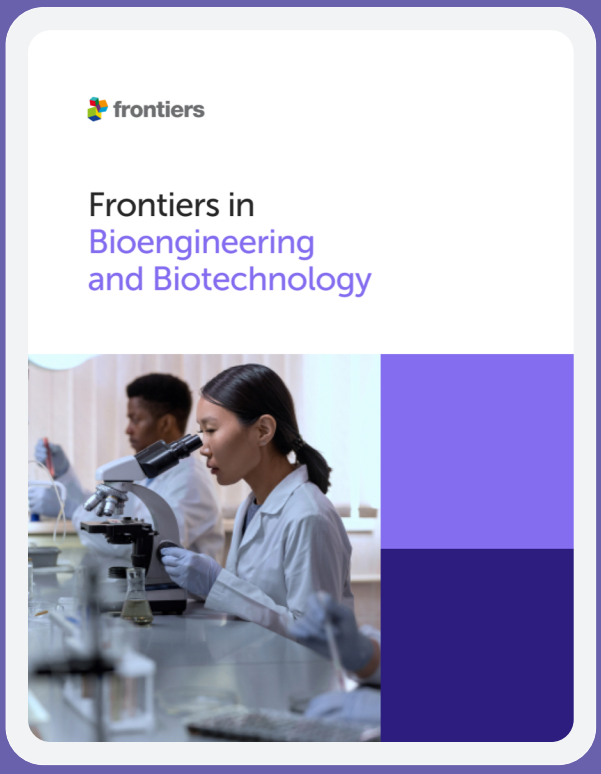

Frontiers

Avenue du Tribunal-Fédéral 34
1005 Lausanne, Switzerland
frontiersin.org

Contact us

+41 (0)21 510 17 00
frontiersin.org/about/contact